ION IMPLANTATION DAMAGE IN SEMICONDUCTORS AT LOW TEMPERATURES

by

ROBERT SULIS WALKER, B.Sc., M.Eng.

A Thesis

Submitted to the Faculty of Graduate Studies

in Partial Fulfilment of the Requirements

for the Degree Doctor of Philosophy

McMaster University

July 1977.

DOCTOR OF PHILOSOPHY (1977)
(Electrical Engineering)

McMASTER UNIVERSITY
Hamilton, Ontario.

TITLE: Ion Implantation Damage in Semiconductors at Low Temperatures

AUTHOR: Robert Sulis Walker, B.Sc. (Acadia University)
M.Eng. (McMaster University)

SUPERVISOR: Dr. D.A. Thompson

NUMBER OF PAGES: xxiv, 305

ABSTRACT

This thesis reports on a systematic investigation of the ion implantation damage in Si, Ge, GaP and GaAs at ≤50K. The damage has been measured "in-situ" using the channeling-backscattering technique. Implantation energies have ranged from 10-250 keV with Z_1 in the interval $2 \leq Z_1 \leq 81$.

The study has been divided into two parts, depending on Z_1. For low Z_1 ($Z_1 \lesssim 30$), the damage profiles in Si, GaP and GaAs have been extracted at 50K. Discrepancies from the theoretical profiles are evident and can be accounted for in terms of the previously reported Z_1-oscillations in the electronic stopping powers. The radial distribution of displaced atoms is examined in these three materials by systematically introducing small misalignments ($\psi \leq 0.36\ \psi_1$) between the analyzing beam direction and crystal axis. This "Off-Axis" effect is examined as a function of Z_1, ion dose, and depth. Significant atom relaxations are concluded to extend perpendicular to the channel row by up to $\sim$ 40% of the channel radius. While atom relaxations do not contribute to the measured damage at low ion doses, they can account for up to 50-70% of the measured damage at high ion doses. A quantitative model of the damage-dose behaviour has been developed, in which the atom relaxation component is incorporated as being directly proportional to the measured damage.

The number of displaced atoms/ion is found to be greater than the prediction derived from collision theory by up to an order of magnitude for high-Z_1 bombardment. Therefore, the second section of the thesis contains

a detailed study of the effect for $7 \leq Z_1 \leq 81$ in Si and Ge at 35K. The deviation is not an artifact of the channeling-backscattering technique. It is concluded that an "energy-spike" may be initiated by the high-Z_1 bombardments; the energy-spike induces a local amorphous zone in the semiconductor, thereby accounting for the increased damage. A semi-empirical model of the data is developed, which divides the damage into collisional and energy-spike components. Extensive use is made of molecular ion bombardments, since they provide a simple method of varying the individual ion-induced collision cascade energy density; this allows for a test of the energy-spike concepts. It is concluded that spikes will influence the damage up to energies corresponding to a lower energy density limit of 0.1 eV/atom in Si and 0.01 eV/atom in Ge. The lower energy limit for spike effects is evidently << 10 keV. In Si it appears that the amorphization process is best described by a thermal-spike mechanism, whereas in Ge, it is inferred that the athermal collapse of the unstable lattice is more probable. To support the arguments and concepts of the energy-spike, a Monte Carlo computer code has been written to simulate the collision cascade and provide insight into the parameters of the individual ion-induced cascades.

TABLE OF CONTENTS

LIST OF FIGURES

2.7 Iso-density contours for distribution of energy into atomic processes for 40 keV As^+-Si.

2.8 Isothermals following a 100 eV Cu recoil in Cu at (a) $t = 3.27 \times 10^{-13}$ sec, (b) $t = 9.9 \times 10^{-13}$ sec, from initiation of the cascade. The figures represent the two-dimensional display of a 10 x 10 x 10 atom array.

2.9 Sputtering yields of Au for 45 keV ions, normalized to the yield of 45 keV Ar^+-Au (from ref. 60). Solid line from Sigmund.[20]

3.1 Monte Carlo deposited energy histograms for 80 keV Te^+-Ge, showing recoil energy transport. $E_d = 25$ eV, $U = 0$.

3.2 Comparison of the deposited energy distributions from the WSS and Monte Carlo methods. The displaced atom distribution from the Monte Carlo method is included. (a) 80 keV Te^+-Ge, (b) 40 keV N^+-Si.

3.3 Normalized Monte Carlo deposited energy histograms for 80 keV Te^+-Ge. $E_d = 25$ eV. Solid line, $U = 0$. Dashed line, $U = E_d$.

3.4 Comparison of $\nu(E)/E$ values for WSS (solid line) and Monte Carlo (points) for $E_d = 25$ eV, $U = 0$.

3.5 The fraction, $\xi U/E$, of energy lost to the lattice during atom displacement. $U = E_d$. Monte Carlo (solid lines). Eq. (3.13) (dashed lines).

3.6 Proportionality factor, ξ, for the four cases listed in the text. Bi^+-Si, solid points. N^+-Si, open points.

LIST OF TABLES

TABLE OF SYMBOLS

		Page No.
a	- Thomas-Fermi screening radius	11
a_o	- first Bohr radius	11
A	- channel area accessible to the analyzing beam	100
b	- collision diameter	11
	- surface channel of backscattered spectrum	88
b'	- channel in which damaged layer ends	88
c	- proportionality constant in damage-dose model	156
C	- numerical fitting constant in Lindhard potential	75
	- scaling constant in semi-empirical single scattering dechanneling	93
C_{ms}	- scaling constant for multiple scattering dechanneling	98
C_{ps}	- scaling constant for plural scattering dechanneling	98
C_{ss}	- scaling constant for single scattering dechanneling	98
d	- interatomic spacing	34
D_s	- diameter of amorphous zone created by the energy-spike	200
e	- electronic charge	
E	- incident ion energy in Laboratory System	9
E'	- energy in C.G. System	9
E_o	- incident beam energy	79
E_1	- energy of particle scattering from target surface	79
E*	- energy below which energy transfer of at least T_{min} occurs at every interatomic distance	164

		Page No.
E_1	- energy at which $\psi_1 = a/d$	77
$E_\perp$	- transverse energy of analyzing beam	73
E_d	- threshold displacement energy	25
ΔE	- energy width of channel in backscattered spectrum	82
ΔE_d	- energy resolution of detector	82
$\Delta E'_\perp$	- increase in transverse energy due to multiple scattering	131
ΔE_s	- amount of total energy into sub-threshold collisions	55
	- multiple scattering energy spread of analyzing beam	82
$f_{R.S.}$	- function in continuum approximation of string potential	76
$F(\vec{r},E)$	- spatial distribution function	17
$F(x,y,z)$	- normalized analyzing beam flux distribution	100
F_D	- fractional damage in collision cascade volume	172
$G(x,y,z)$	- normalized radial distribution of displaced atoms	100
k	- dimensionless electronic stopping coefficient	15
	- elastic scattering kinematic factor	80
k_L	- Lindhard's value for electronic stopping coefficient	127
K	- electronic stopping coefficient	44
K_{kp}	- $dN_{kp}/d\nu(E)$	183
K_s	- fitting parameter in semi-empirical model of damage	184
m	- parameter defining power cross-section approximation	12
m_e	- mass of electron	
M_1	- atomic mass of ion	
M_2	- atomic mass of target	
n_i	- yield of particles in aligned component of analyzing beam that directly backscatter from displaced atoms	87

		Page No:
N	- target atom density	
$N(E)$	- number of Frenkel pairs created by recoil of energy, E	25
$N_d(z)$	- measured number of displaced atoms at depth, z	100
N_D	- total measured displaced atoms per unit bombardment area	88
N_D^*	- measured number of displaced atoms/ion at low dose	103
N_{kp}	- number of displaced atoms predicted using the Kinchin-Pease type boundary condition	26
N_r	- number of replacement collisions	61
N_t	- total number of displacement collisions	61
N_s	- energy-spike component of damage	183
N_{sat}	- saturation damage level	142
N_v	- number of target atoms in cascade volume	170
p	-impact parameter	9
r_{min}	- minimum approach distance of channeled particle to row	72
r_o	- channel radius	137
R_d	- total damage depth	91
$s_e(\epsilon)$	- reduced electronic stopping cross-section	15
$s_n(\epsilon)$	- reduced nuclear stopping cross-section	14
S_A	- aligned electronic stopping power	85
S_{AV}	- proportionality factor between energy and depth scales	82
$S_n(E)$	- nuclear stopping cross-section	14
S_R	- random electronic stopping power	85
t	- Lindhard's reduced independent parameter	12
	- target thickness	81
t_{max}	- reduced parameter for maximum energy transfer	41

		Page No.
t_{min}	- reduced parameter for minimum energy transfer	41
T	- recoiling atom energy	9
T_m	- maximum recoiling atom energy	9
Δt	- target thickness corresponding to one energy channel	82
Δt_d	- depth resolution of detector	91
u_1	- one-dimensional thermal vibrational amplitude	77
u_2	- two-dimensional thermal vibrational amplitude	78
U	- energy expended at each displacement collision	19
U(r)	- string potential	72
U_{min}	- minimum string potential in the channel	131
$U_{R.S.}$	- static continuum approximation to the string potential	76
ΣU	- total energy expended in all displacement collisions	47
v	- ion velocity	9
v_B	- velocity of first Bohr orbital electron	9
V(r)	- interaction potential	9
V_i	- individual cascade volume	65
$V_{i,av}$	- average individual cascade volume	65
V, V_s	- statistical cascade volume	65
V_R	- ratio of individual to statistical cascade volumes	65
x	- parallel direction to surface of target	
x_d	- mean distance between collisions that transfer at least E_d at every interatomic distance	34
x_f	- final x location of ion in Monte Carlo cascade	64
$\langle x^2 \rangle$	- transverse second moment of distribution $F(\vec{r},E)$ in x-plane	65
y	- parallel direction to surface of target	
$y_A(i)$	- yield in channel i for aligned spectrum after bombardment	86

		Page No.
y_f	- final y location of ion in Monte Carlo cascade	64
$y_N(i)$	- yield in channel i for non-aligned spectrum	87
$y_R(i)$	- yield from random component of aligned beam	87
$y_V(i)$	- yield in channel i for aligned spectrum before bombardment	91
$\langle y^2 \rangle$	- transverse second moment of distribution $F(\vec{r},E)$ in y-plane	65
Σy_s	- yield in aligned spectrum due to surface oxide	93
z	- normal direction to surface of target	
z_f	- final z location of ion in Monte Carlo collision cascade	64
$\langle \Delta z^2 \rangle$	- longitudinal second moment of distribution $F(\vec{r},E)$	65
Z_1	- atomic number of ion	
Z_2	- atomic number of target atoms	

Greek Symbols

χ_{min}	- normalized minimum yield for aligned beam	75
χ'	- dechanneled fraction of aligned beam	88
ϵ	- Lindhard's reduced energy	11
ϵ_o	- ϵ/E	34
δ	- one-dimensional cascade volume ratio	67
$n(E)$	- inelastic energy deposition	18
γ	- fractional maximum energy transfer	9
λ	- mean free path between collisions	43
	- fitting parameter in numerical approximation to Thomas-Fermi cross-section	12
λ_m	- fitting parameter in power cross-section approximation	12
$\nu(E)$	- elastic energy deposition	18

		Page No.
ν_1	- fitting parameter in semi-empirical model of damage	183
ϕ	- azimuthal scattering angle	43
	- angle between incident beam direction and detector	81
	- ion dose per unit bombardment area	151
$\phi(r/a)$	- Thomas-Fermi screening function	11
ϕ_A	- tilt angle under aligned conditions	88
ϕ_i	- tilt angle under implant conditions	88
ψ	- angle between analyzing beam direction and lattice row	72
$\psi(x)$	- digamma function	26
ψ_c	- critical angle for channeling	72
ψ_{in}	- angle between incident beam direction and best-alignment	131
ψ_{coll}	- half-angular divergence of incident analyzing beam	139
ψ_1	- critical angle at low temperature in high-energy approx.	76
$\psi_{1/2}$	- half-angular width of yield for channeling angular scan	74
ρ	- reduced range parameter	14
$d\sigma_n$	- nuclear differential scattering cross-section	9
θ	- scattering angle in C.G. System	9
θ_1	- scattering angle of scattered particle in Lab System	42
θ_2	- scattering angle of recoiling atom in Lab System	42
$\bar{\theta}_\nu$	- energy density	168
τ	- energy-spike lifetime	32
τ_o	- slowing-down time of ion	173
$\xi(m)$	- proportionality factor for N_{kp}, related to the cross-section	26

CHAPTER I

INTRODUCTION

During the last decade, ion implantation has been shown to be a viable commercial method of doping semiconductors (cf. ref. 1). Unlike conventional diffusion, ion implantation is not controlled by the process temperature or the impurity solubility limit. Rather, unique and reproducible dopant concentration profiles can be attained by control of the ion energy and integrated beam current.

With the increasing technological interest in ion implantation, the necessity for a comprehensive picture of the lattice disorder produced along the ion tracks has become apparent.[1] This is required since the electrical properties of the implanted layer may often be determined by radiation damage effects, rather than by properties of the dopant atom itself. Under certain conditions, most of the radiation damage will recover, or anneal, at temperatures lower than those necessary in the diffusion process; however, any remaining defects act as traps reducing the carrier concentration, recombination centers, which reduce the carrier lifetime, and scattering centers which reduce the free carrier mobility. The entire anneal behaviour depends in a complex manner on the initial damage concentration and its microscopic structure.

Investigations of the radiation damage in semiconductors have been as varied as are the possible combinations of implantation conditions. The amount and distribution of damage has been observed to be affected by ion species, energy, implantation temperature, dose and dose rate,

and properties of the semiconductor itself. Considerable data now exist from which empirical predictions of the damage behaviour can often be deduced. However, attempts to develop a theoretical basis for the explanation of experimental observations are frustrated by the difficulty in isolating the competing processes of damage accumulation and recovery. This has resulted since the implants have generally been performed at temperatures where the defects are mobile as they are produced; both annealing and nucleation can then occur. Thus, the isolation and study of the damage mechanism itself requires the measurement of damage at temperatures low enough that these recovery processes are inhibited.

More fundamentally, the study of ion implantation damage offers a unique examination of the present level of understanding of the basic atomic collisions phenomena. A theory of both the spatial distribution[2] and amount[3] of damage resulting from ion bombardment has been developed, based on a linear transport model of the ion-induced collision cascade. As long as mechanisms which alter the initial defect concentration, such as defect annealing, are prevented, a comparison of the predicted and measured damage is a valid test of the theory. Again, this points to the necessity of low temperature damage measurements.

For these reasons, this thesis reports on a systematic investigation of ion implantation damage in the semiconductors at low temperatures. The four materials of primary technological interest have been studied, namely: the elemental semiconductors, silicon and germanium, and the III-V compound semiconductors, gallium phosphide and gallium arsenide. Implantation energies range from 10-250 keV, with the ion atomic mass varying from 2 to 200. The target temperature is maintained at $\leq$50K,

and the damage is measured "in-situ" using the channeling-backscattering technique.

In Chapter II, the linear collision theory relevant to the spatial distribution and amount of ion-induced damage is presented. Possible solid-state related effects which progress on a time scale comparable to the slowing-down time ($\sim 10^{-13}$ sec) of the ion and that may influence the measured damage are outlined. In particular, a "thermal-spike" mechanism[4] appears consistent with recent observations of non-linear effects in heavy-ion sputtering yields. This suggests that a detailed knowledge of the energy deposition process within the individual cascade volume may be necessary in understanding the damage behaviour. Therefore, the relationship between the individual cascade dimensions and those resulting from the statistical approach is developed in Chapter III. A Monte Carlo computer code that simulates the collision cascade has been written to obtain the necessary information. The code is also compared to the results of Chapter II so that some of the approximations inherent in the statistical model of the collision cascade are examined.

The application of the channeling-backscattering technique to measurement of damage is presented in Chapter IV. The methods of damage profile extraction and determination of the total damage are also given. The quantitative interpretation of these measurements is critically examined. The coupled accelerator system by which the "in-situ" ion bombardment and channeling-backscattering measurements may be performed is discussed in Chapter V. The provisions necessary for cryogenic cooling of the target material are outlined.

In Chapter VI, three aspects of the ion-induced damage in Si,

GaP and GaAs at 50K are studied:

(i) the relationship between the measured and predicted damage profiles;

(ii) the radial distribution of displaced atoms across the channel. The study is accomplished by introducing a small misalignment of the channel axis to the beam direction. Both the ion mass and depth dependence of the "Off-Axis" effect are examined.

(iii) the amorphization process of the implanted layer as a function of ion mass and ion dose.

It will also be shown in Chapter VI that the total amount of damage is not predicted by the linear collision theory except in the case of very light mass ions. As the ion mass increases, the measured damage increasingly exceeds the predicted value, with the discrepancy being greater than an order of magnitude for the heaviest ions used. Chapter VII contains a systematic study of this effect in Si and Ge at 35K. It will be shown that the measured damage is consistent with an "energy-spike" model of the energy deposition. The "energy-spike" appears to initiate a local stable highly-disordered, or amorphous, region within the cascade volume, thereby accounting for the increased damage. Possible mechanisms by which the energy-spike initiates the local amorphization are discussed. Extensive use is made of molecular ion bombardment, since it offers a convenient method of varying the cascade energy density without significantly affecting the cascade dimensions. Some comparison is made with room temperature damage measurements.

CHAPTER II

THE COLLISION CASCADE

2.1 Introduction

When an energetic ion strikes the atoms of a solid, a chain of atomic collisions will result in which several generations of recoiling atoms can be generated. This collision sequence is referred to as the collision cascade, and its analytical description is obviously necessary in the study of ion-induced damage and the damage distribution. In general, the energy loss processes are randomized in the sense that one cannot predict "a priori" the exact nature of the collision cascade associated with each individual ion, i.e.: the final ion location, the number of collision events, etc. cannot be predicted. However, in cases where a great many particles are involved, such as in ion implantation (typically 10^{12}-10^{16} ions/cm^2), a statistical description of the cascade is sufficient. This is possible as long as the physical parameters which define the collisions are known. Of particular interest to the research of this thesis is the average spatial distribution of energy deposited into atomic scattering events; both the distribution and amount of damage are assumed related to this quantity.

In Sec. 2.2, collision theory is reviewed with regard to the assumptions involved and the parameters that define the energy loss processes. The general linear transport equations, leading to the determination of the distributions of interest, are described. Also, the asymptotic solution of the transport equation for the total number of

displaced atoms is discussed. A comparison of the theory is made with published experimental measurements of cascade-related parameters, e.g.: range and damage distributions, sputtering coefficients, and the number of displaced atoms.

The above comparison will show that the collision theory can be inadequate in predicting the magnitude of the final lattice disorder following energetic ion irradiation. Therefore, in Sec. 2.3, models which have been proposed to account for the resultant behaviour of the solid after the collision cascade has been generated are reviewed. In particular, a "thermal-spike"[4] concept appears of relevance to the work of the thesis, and experimental evidence that has been reported in support of the model is presented.

2.2 Collision Theory

The following discussion of collision theory shall be restricted to ion energies typical of the ion implantation process, i.e.: energies from a few keV to several hundred keV. In this energy regime, a unified theory of the atomic and electronic stopping has been given by Lindhard et. al.[5,6,7] (referred to as the LSS theory). Winterbon et. al.[2,8] have applied the LSS theory to the determination of the spatial distribution of ion ranges and energy deposition (referred to as the WSS theory).

2.2.1 Assumptions

The collision between a keV ion (or recoiling atom) and atoms of the target is generally subject to the following simplifications:

(i) The collision can be described classically and is non-relativistic.

(ii) The collision is binary. For keV ions, the impact parameter for significant energy transfer is generally << the interatomic spacing.

(iii) The struck atom can be considered stationary during the collision. This will be valid as long as the particle energy >> the thermal energy of the atom.

As the particle gives up more and more of its energy, the last two assumptions may eventually break down; while this will affect the spatial distributions of ion range and energy deposition in only a small way, it may dramatically influence the final state of lattice disorder (viz. displacement or thermal-spike mechanisms, which will be discussed in Sec. 2.3).

A moving particle gives up its energy through two principle mechanisms, i.e.: atomic and electronic scattering. The processes are correlated[9] since the amount of electronic scattering depends on the distance of approach of the moving particle to the atom in the same manner as does the atomic scattering. However, in the LSS theory, it is shown adequate to approximate the quasi-elastic scattering by separate elastic scattering and path-independent inelastic scattering.[10] Winterbon[11] has shown that correlated stopping has little effect on the gross structure of the collision cascade.

Figure 2.1 shows the basic features of the elastic scattering of a moving particle and stationary atom. The problem of describing the collision is more readily solved in the center-of-gravity system, for which the scattering angle, θ, is given by (cf. ref. 12):

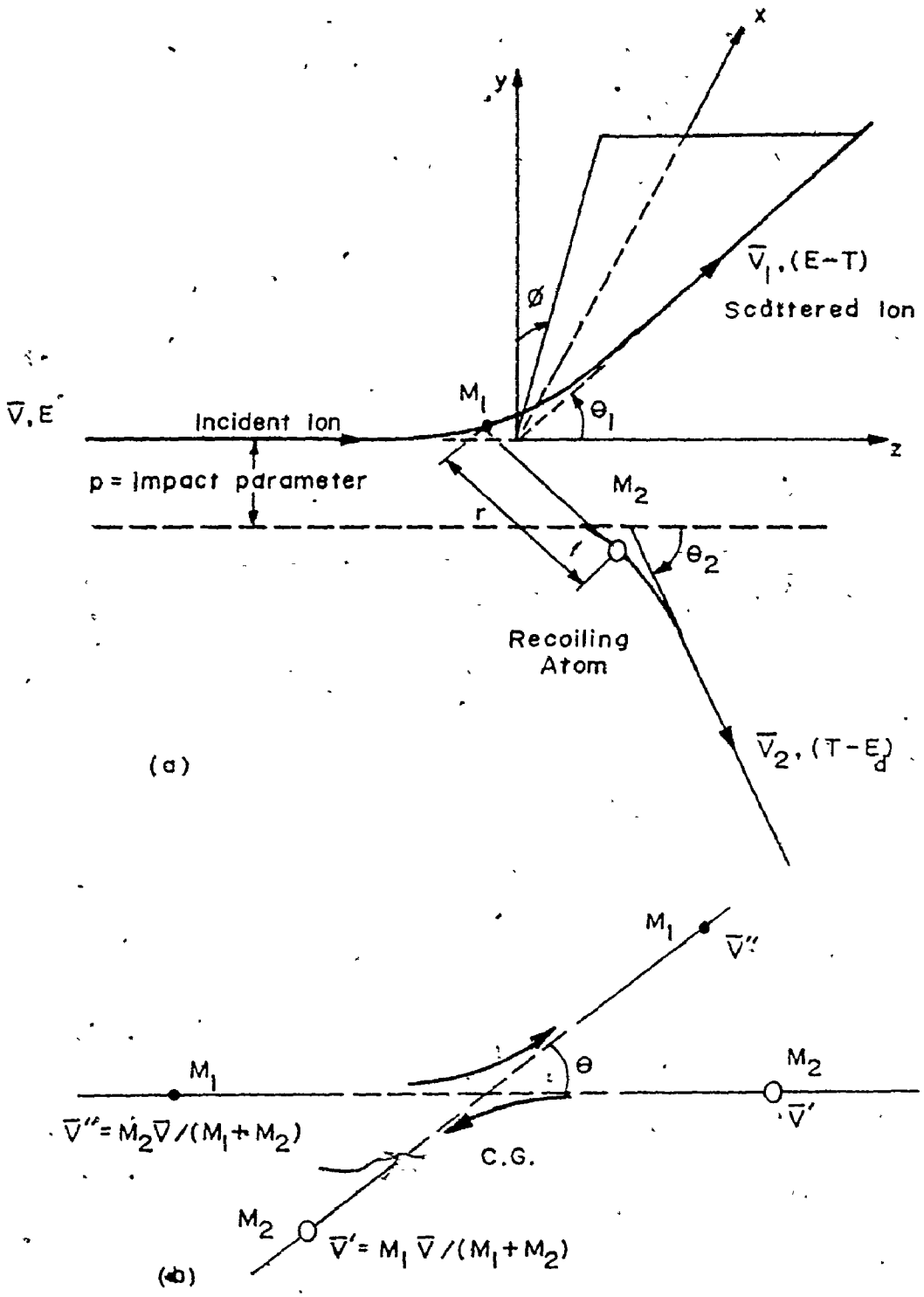

Fig. 2.1: (a) Binary collision in Laboratory Coordinate System.

(b) Binary collision in C.G. Coordinate System.

$$\theta = \pi - 2p\int_0^{u_o} du/[1 - V(u)/E' - p^2u^2]^{1/2} \quad , \qquad (2.1)$$

where

p = the impact parameter,

$E' = M_2E/(M_1 + M_2)$,

$u = 1/r$,

$u_o = 1/r_o$,

r_o = the distance of closest approach,

$V(u)$ = the interaction potential, and

E = the incident particle energy.

For an elastic collision, the recoiling atom energy, T, is:

$$T = T_m \sin^2\theta/2 \quad , \qquad (2.2)$$

where

$$T_m = \gamma E = 4M_1M_2 \cdot E/(M_1 + M_2)^2 \quad . \qquad (2.3)$$

A particularly useful concept is the differential cross-section, which defines the probability that a particular event will occur. For the particle-atom scattering, the nuclear differential cross-section, $d\sigma_n$, becomes:

$$d\sigma_n = d\sigma_n(\theta) = 2\pi pdp \quad , \qquad (2.4)$$

such that all particles falling on an area $2\pi pdp$ at an impact parameter, p, will be scattered by an angle between θ and $\theta + d\theta$. A cross-section for inelastic scattering can be similarly defined.

Three regions of inelastic stopping can be differentiated. When the ion velocity, $v \sim v_B Z_1^{2/3}$, where v_B is the velocity of the first Bohr

orbital electron, a resonant coupling of the ion and atom electrons occurs and the stopping is a maximum. For $v > v_B Z_1^{2/3}$, the coupling becomes weaker and the stopping decreases. For $v < v_B Z_1^{2/3}$, the stopping is predicted to be proportional to v;[10] this is the velocity range appropriate to keV ion implantations.

2.2.2 The Interaction Potential

As two like atoms approach each other from an infinite separation, they will experience an increasing attractive force that will exhibit a maximum near the equilibrium lattice spacing, d. As the approach continues, the force will quickly become repulsive as the nuclear forces begin to dominate the interaction. The magnitude of the repulsion depends on the ability of the orbital electrons to screen the nuclear charge; for very close approach distances, the screening is removed and the interaction is simple Coulombic.

For keV ion-atom scattering, a wide range of impact parameters are possible. A complex Hartree-Foch treatment[13] is necessary to completely describe the interaction, and V of Eq. (2.1) will depend on Z_1, Z_2 and r. Thus, the scattering angle will be a function of four independent variables:

$$\theta = \theta(Z_1, Z_2, E', p) \qquad (2.5)$$

The exact solution of the scattering must then be performed for all possible ion-target combinations.

To reduce this complexity, a number of approximate potentials have been developed to treat a particular range of r. For $r \lesssim d$, the Born-Mayer potential[14] can be used; for $r \ll d$, potentials due to

Bohr,[15] Lindhard,[16] Moliere[17] have been proposed. One convenient potential having a sufficient range of validity to describe the interaction appropriate to ion implantation results from the Thomas-Fermi statistical model of the atom[18] where:

$$V(r) = Z_1 Z_2 e^2/r \cdot \phi(Z_1/Z_2, r/a) \quad , \tag{2.6}$$

and ϕ is a tabulated[19] screening function that tends to unity as $r \to 0$ (simple Coulomb scattering) and to zero as $r \to \infty$. The parameter, a, is the Thomas-Fermi screening length:

$$a = 0.8853\ a_o Z_2^{-1/3} \quad , \tag{2.7}$$

where a_o is the first Bohr radius, $a_o = \hbar^2/me^2$. The use of the Thomas-Fermi potential gives:

$$\theta = \theta(Z_1/Z_2, b/a, p/a) \quad , \tag{2.8}$$

where $b = 2Z_1 Z_2 e^2/E'$ and is referred to as the collision diameter. The parameter, a/b, appears often in the theory and is referred to as the reduced energy, ϵ:[7]

$$\epsilon = a/b = aE'/Z_1 Z_2 e^2 \quad . \tag{2.9}$$

Lindhard et. al.[7] have shown that the dependence of θ on Z_1 and Z_2 can be adequately incorporated by redefining the screening radius, a, as an effective screening radius:

$$a = 0.8853\ a_o (Z_1^{2/3} + Z_2^{2/3})^{-1/2} \quad , \tag{2.10}$$

such that θ is now:

$$\theta = \theta(\epsilon, p/a) \quad . \tag{2.11}$$

Eq. (2.1) has been solved by perturbation theory, valid for small θ, and the result extrapolated to large θ.[7] This has been shown to reduce the parametric dependence to one independent variable, t:

$$t = e^2 T/T_m = e^2 \sin^2 \theta/2 \quad , \tag{2.12}$$

and the scattering cross-section may be adequately approximated by:[7]

$$d\sigma_n = \pi a^2 (dt/2t^{3/2}) f(t^{1/2}) \quad . \tag{2.13}$$

While the wide-angle extrapolation introduces a significant error in the cross-section at large θ, the simplicity of the expression combined with the strong forward peaking of the cross-section outweigh its limitations. The function, $f(t^{1/2})$, is a universal screening function, which can be calculated numerically using the Thomas-Fermi treatment. An adequate numerical approximation to the function is:[8]

$$f(t^{1/2}) = \lambda t^{1/6} (1 + (2\lambda t^{2/3})^{2/3})^{-3/2} \quad . \tag{2.14}$$

The parameter, $\lambda = 1.309$ was determined by best fitting. The function is plotted in Fig. 2.2.

A convenient approximation to $f(t^{1/2})$ is known as the power cross-section approximation,[7] i.e.:

$$f(t^{1/2}) = \lambda_m t^{1/2-m} \quad , \tag{2.15}$$

where $0 \leq m \leq 1$. Three commonly chosen values of m are: $m = 1$, corresponding to simple Coulomb scattering ($\lambda_1 = 1/2$); $m = 1/2$, corresponding to $V(r) \propto r^{-2}$ ($\lambda_2 = 0.327$); and $m = 1/3$, corresponding to $V(r) \propto r^{-3}$ ($\lambda_3 = 1.309$). These three approximations are shown in Fig. 2.2. For low particle energies (at small $t^{1/2}$), the Thomas-Fermi approach over-

estimates the cross-section and the Born-Mayer potential is more appropriate. A reasonable power cross-section approximation to the latter is achieved by taking $m = 0$ and $\lambda_0 = 24$.[20]

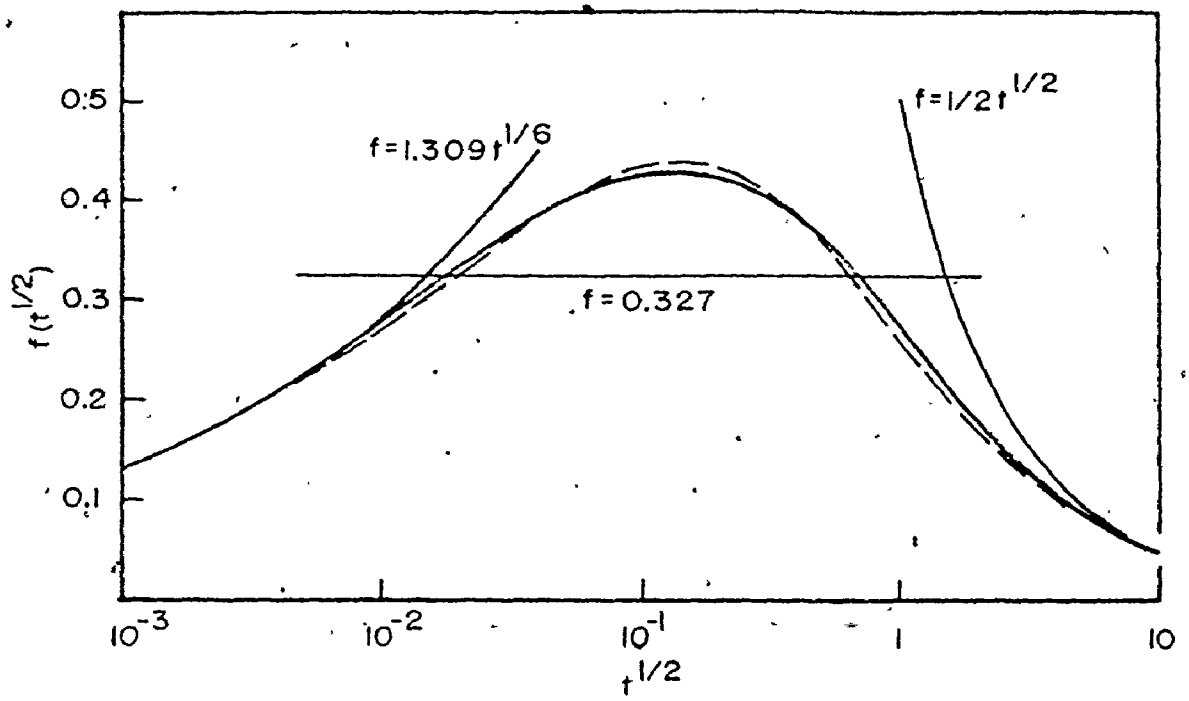

Fig. 2.2: The universal screening function, $f(t^{1/2})$ calculated from the Thomas-Fermi Potential (thick solid line). The numerical approximation to $f(t^{1/2})$, Eq. (2.14) (dashed line). Power cross-section approximation, Eq. (2.15), for m = 1/3, 1/2, 1 (thin solid lines). From ref. 8.

2.2.3 The Stopping Powers

In the previous sections, the energy loss processes have been separated into elastic (or nuclear) and inelastic (or electronic) components. Thus, the total stopping power, dE/dR, will be the sum of the nuclear and

electronic stopping powers, i.e.:

$$dE/dR = (dE/dR)_n + (dE/dR)_e \quad . \tag{2.16}$$

(i) Nuclear stopping power, $(dE/dR)_n$

The nuclear stopping power will be defined by the nuclear differential scattering cross-section of the previous section:

$$(dE/dR)_n = -NS_n(E) = -N\int_0^{T_m} T d\sigma_n \quad , \tag{2.17}$$

where N is the target atom density and $S_n(E)$ is, by definition, the nuclear stopping cross-section. Application of Eq. (2.13) gives:

$$(dE/dR)_n = \frac{-N\pi a^2 T_m}{e^2}\int_0^e d(t^{1/2}) f(t^{1/2}) \quad . \tag{2.18}$$

It proves convenient to introduce a dimensionless range parameter, ρ:[5]

$$\rho = N\pi a^2 \gamma R \quad . \tag{2.19}$$

A universal nuclear stopping cross-section, $s_n(e)$, then results:

$$(de/d\rho)_n = -s_n(e) = -1/e\int_0^e f(t^{1/2}) d(t^{1/2}) \quad , \tag{2.20}$$

which is valid for all possible ion-target combinations (within the limitations imposed by the assumptions of the previous sections).

For the power cross-section approximation to $f(t^{1/2})$, $s_n(e)$ becomes:

$$s_n(e) = \lambda_m t^{1-2m}/2(1 - m) \quad . \tag{2.21}$$

The function $s_n(e)$ is plotted in Fig. 2.3, along with the power cross-section approximations for m = 1/2, 1/3. Note that for m = 1/2, $s_n(e)$ is a constant, 0.327.

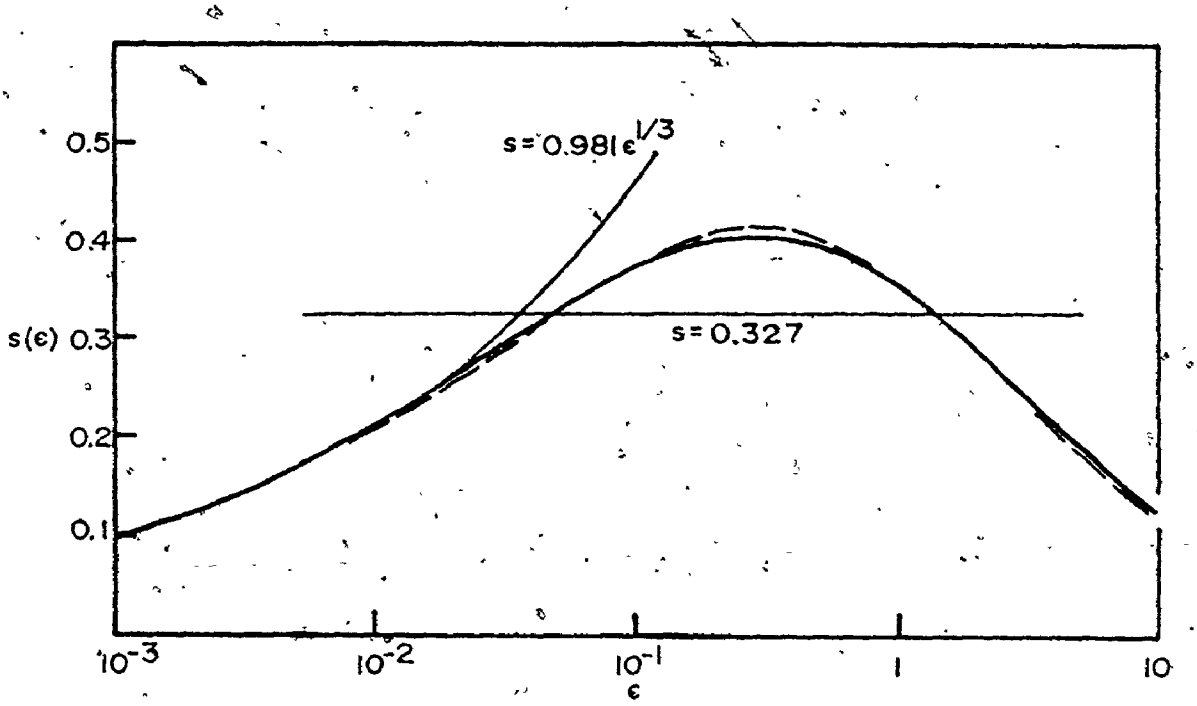

Fig. 2.3: Universal nuclear stopping cross-section calculated from the Thomas-Fermi Potential (thick solid line). Numerical approximation to $s_n(\epsilon)$, Eq. (2.13) (dashed line). Power cross-section approximation for m = 1/3, 1/2 (thin solid lines). From ref.8.

(ii) Electronic stopping power, $(dE/dR)_e$

In the energy region where the electronic stopping is proportional to particle velocity, the electronic stopping cross-section, $s_e(\epsilon)$, can be approximated by:[10]

$$s_e(\epsilon) = -(d\epsilon/d\rho)_e = k\epsilon^{1/2} \qquad (2.22)$$

However, a universal $s_e(\epsilon)$ does not exist, since $k = k(M_1, M_2, Z_1, Z_2)$. Fortunately, it is a slowly varying function of these parameters, and

is often of the order of 0.1 to 0.2. Shown in Fig. 2.4 is a comparison of electronic stopping, for k = 0.15 and 1.5, and the nuclear stopping cross-section.

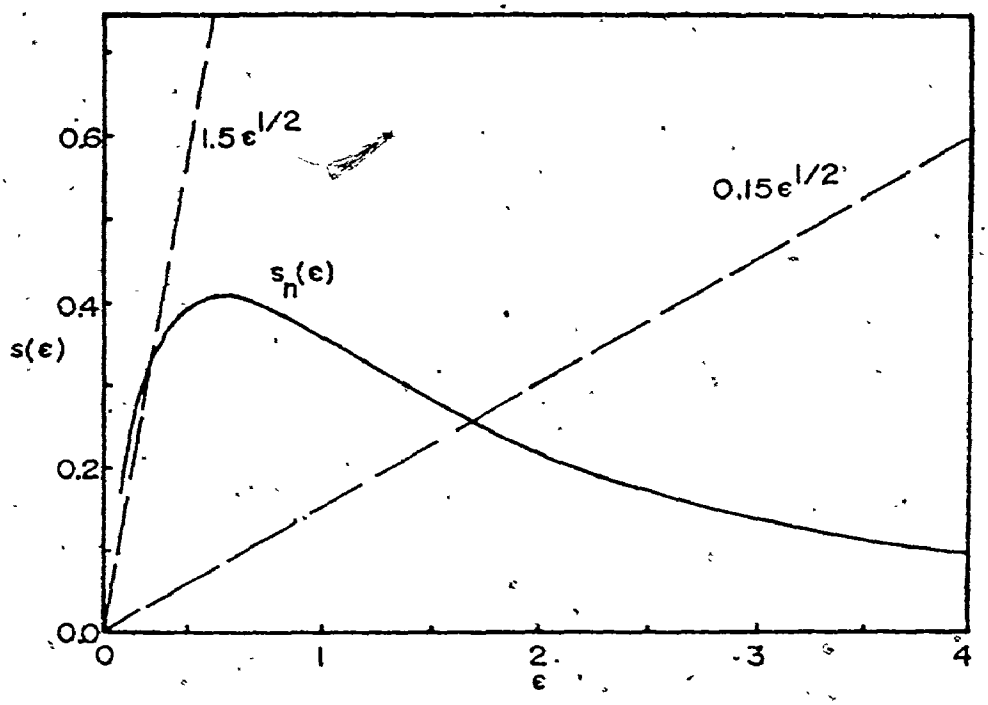

Fig. 2.4: Nuclear and electronic stopping powers in reduced units. Nuclear stopping power (full solid line). Electronic stopping power for k = 0.15 and 1.5 (dashed line).

2.2.4 Range and Energy Deposition Distributions

In the statistical description of the collision cascade three average spatial distributions are of interest, i.e.: the distribution of (1) the end position of the implanted ions (i.e., range), (2) the

energy deposited into atomic processes (i.e., damage), and (3) the energy deposited into inelastic processes (i.e., ionization). With a knowledge of these distributions (and their volume integrals), one may calculate such secondary effects as the reflection coefficient, sputtering coefficient, ionization efficiency, etc. The use of the expressions "damage" and "ionization" is more figurative than literal in that they indicate the influence that the atomic and inelastic energy distributions will have on the target. The quantitative relation between the distribution of atomic energy deposition and the actual distribution of displaced atoms is examined in the next chapter.

In the standard approach to obtaining these distributions, a random, uniform and infinite medium is assumed, in which the target surface is merely a reference plane. This may introduce a sizeable error in the distributions near the surface, since particles are permitted to cross the surface plane more than once. A surface correction[21] may be applied to attempt to correct for this when quantities sensitive to the distributions near the surface, e.g.: reflection or sputtering coefficients, are required. In the following development, the LSS theory is assumed to describe the energy loss processes. For higher energies, Brice[22] has tabulated information related to the distributions.

If $F(\vec{r},E)$ is the distribution function which describes one of the above three spatial distributions, the spatial moments are defined by:

$$\langle r^n \rangle = \int r^n F(\vec{r},E) d^3r \quad . \tag{2.28}$$

For n = 0, one obtains the normalization for F. For range, this is 1, i.e.: the particle must come to rest at some point. For damage, the normalization

is to the total energy deposited in atomic motion, which is defined as $\nu(E)$. For ionization, the total inelastic energy deposition is referred to as $\eta(E)$. Since energy is conserved:

$$E = \nu(E) + \eta(E) \quad , \tag{2.24}$$

where the normal boundary condition is $\nu(E) \to E$ as $E \to 0$.[7] This separation into ν and η can be qualitatively justified since (1) once energy is given to the electrons, it can be transferred back to atomic motion only extremely slowly and in small amounts, due to the large mass ratio, and (2) in the limit of $E \to 0$, sufficiently slow moving atoms no longer excite electrons and the energy must be dissipated further by atom vibrations alone. In Fig. 2.5, $\nu(E)/E$ is plotted for various ions in silicon for $E \lesssim 200$ keV. A rapid increase in $\nu(E)/E$ must occur for $E \ll 10$ keV in order that $\nu(E)/E \to 1$. However, for keV ions a significant fraction of the energy ($\sim$30-70%) goes into inelastic stopping.

A linear Boltzmann transport equation will describe $F(\vec{r},E)$ if the assumptions of Sec. 2.2.1 are valid, i.e.; for $Z_1 = Z_2$:

$$F(\vec{r},E) = N\delta r\int d\sigma_{n,e}[F(\vec{r} - \delta\vec{r},E - T_n - \sum_i T_{ei}) + F(\vec{r} - \delta\vec{r},T_n - U) + \sum_i F_e(\vec{r} - \delta\vec{r},T_{ei} - U_i)] + (1 - N\delta r\int d\sigma_{n,e})F(\vec{r} - \delta\vec{r},E), \tag{2.25}$$

where $F(\vec{r},E)$ for the particle at $\vec{r}$ is equated to the F-values of the particle, struck atom and ejected electrons at $\vec{r} - \delta\vec{r}$, averaged over the probability of occurance of the individual processes. In Eq. (2.25):

$N\delta r d\sigma_{n,e}$ = the probability that the particular collision occurs in δr,

T_n = the energy transferred to the recoiling atom,

T_{ei} = the energy transferred to the i^{th} electron,

U = the energy lost to the lattice at each displacement in order to break the atom bonds and overcome the potential minimum in which the lattice atom is located,

U_i = the ionization energy of the i^{th} electron, and

F_e = the distribution function for the electrons.

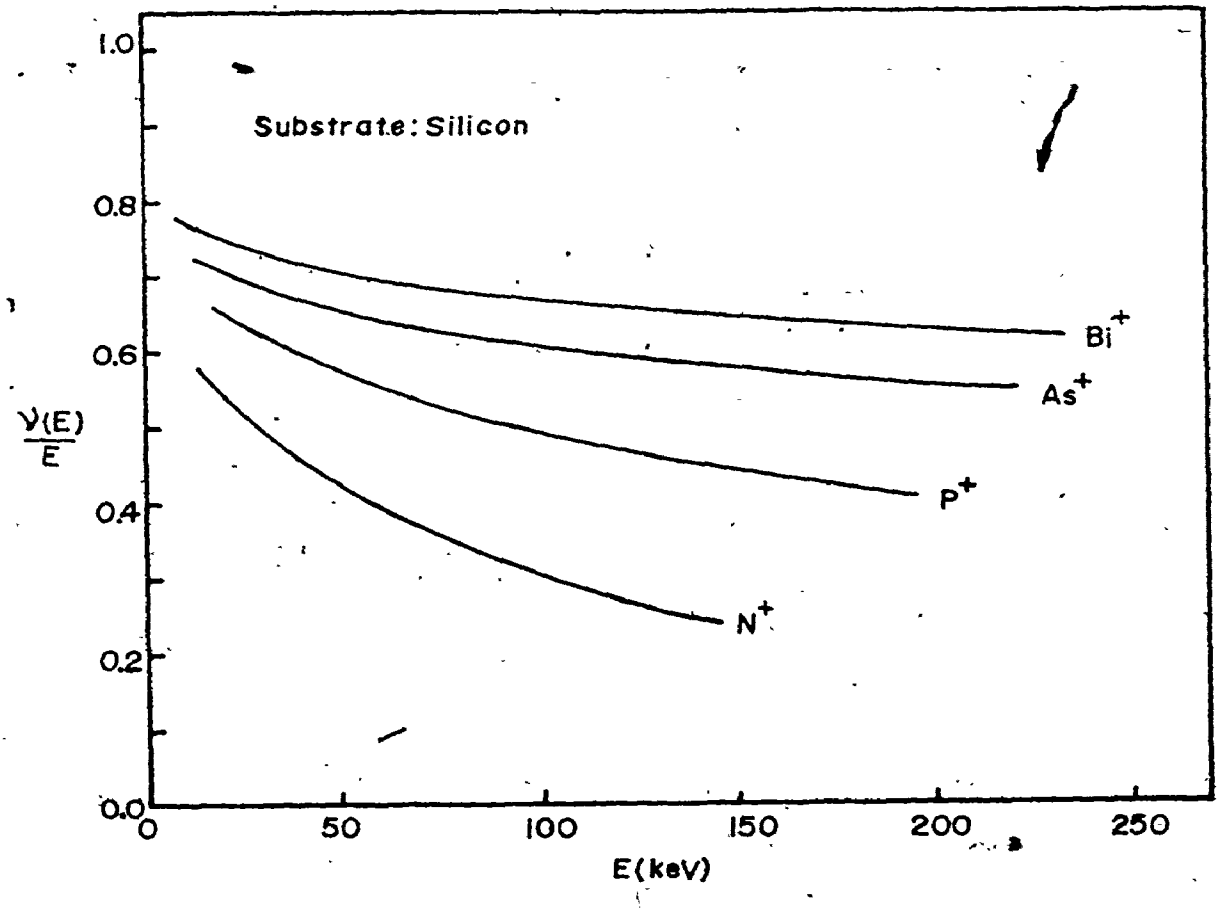

Fig. 2.5: The fraction of incident ion energy going into atomic processes, $\nu(E)/E$, for various ions in Si. Calculated from ref. 2.

In keeping with the LSS theory, the atomic and electronic stopping are assumed separable. Moreover, $\sum T_{ei}$ is assumed $<< E - T_n$ such that $F(\vec{r},E - T_n - \sum_i T_{ei}) = F(\vec{r},E - T_n) + \sum T_{ei} \frac{\partial}{\partial E} F(\vec{r},E)$. Finally, since electrons are not given sufficient momentum to displace an atom, the term containing $\sum F_e$ is neglected. Then in the limit of $\delta r \to 0$:

$$\frac{\vec{v}}{v} \frac{\partial}{\partial \vec{r}} F(\vec{r},E) = N\int d\sigma_n [F(\vec{r},E - T_n) - F(\vec{r},E) + F(\vec{r},T_n - U)]$$

$$- NS_e \frac{\partial}{\partial E} F(\vec{r},E) \quad , \tag{2.26}$$

where $\vec{v}/v = \delta\vec{r}/\delta r$, and $d\sigma_n$ and S_e are defined in Sec. 2.2.2 and 2.2.3 respectively.

In the generalization to $Z_1 \neq Z_2$, $F(\vec{r},T_n - U)$ must be replaced by $\bar{F}(\vec{r},T_n - U)$, where the bar indicates that the recoil atom may be a different species than the incident particle, and will satisfy another equation like Eq. (2.26), for which $Z_1 = Z_2$. For the range distribution, it is not necessary to follow the recoiling atom, and $\bar{F}(r,T_n - U)$ is removed. The result is a general transport equation:

$$- \frac{\vec{v}}{v} \frac{\partial}{\partial \vec{r}} F(\vec{r},E) = N\int d\sigma_n [F(\vec{r},E) - F(\vec{r},E - T_n) - \xi \bar{F}(\vec{r},T_n - U)]$$

$$+ NS_e \frac{\partial}{\partial E} F(\vec{r},E) \quad , \tag{2.27}$$

where $\xi = 0$ for range distributions, 1 for damage and ionization.

It is generally assumed that $T_n >> U$, and that the energy lost to the lattice during the atom displacement can therefore be neglected. While this will have little influence on the spatial energy distribution,[8] it may significantly effect the volume integral, $\nu(E)$. The effect is

examined in the next chapter.

The exact solution of the above transport equation has proved impossible unless further simplifying approximations are made. However, if Eq. (2.27) is multiplied by r^n and integrated by parts, a recursive expression for the spatial moments (defined in Eq. (2.23)) will result.[5,8] The exact calculation of the moments is possible, and the problem reduces to developing the distribution from a finite number of the generated moments. Winterbon[2] has tabulated the first four longitudinal moments for the three required distributions, as well as the second transverse moment, for several ion-target combinations in the range $\epsilon \lesssim 20\text{-}50$. An interpolation procedure is outlined to obtain the moments for other mass ratios.

In theory, an infinite number of moments are required in order to develop the distribution exactly. However, various procedures exist to allow an adequate approximation of the distribution with a limited number of moments, provided the distribution is continuous and near-symmetrical. Procedures commonly used are: an orthogonal polynomial expansion such as the Edgeworth expansion,[23] the Pearson distributions,[24] or the inverse Fourier transform method.[2] The Edgeworth expansion is particularly useful in ion implantation studies since: (1) its formulation is simple, and (2) it is a weighted-Gaussian function and the range and energy distributions are often near-Gaussian. For ion injection normal to the target surface (along the z-axis), the Edgeworth series expansion of the longitudinal distributions is (for the first four moments, μ_n, n = 1-4):

$$F(z,E) = \frac{\tilde{g}}{(2\pi)^{1/2}\mu_2^{1/2}} \exp(\frac{-\xi^2}{2}) f(\xi) \quad , \tag{2.28}$$

where

$$f(\xi) = 1 - (\frac{\mu_3}{6\mu_2^{3/2}})\cdot(3\xi - \xi^3) + \frac{1}{24}(\frac{\mu_4}{\mu_2^2} - 3)\cdot(3 - 6\xi^2 + \xi^4)$$

$$- (\frac{\mu_3^2}{72\mu_2^3})\cdot(15 - 45\xi^2 + 15\xi^4 - \xi^6) \quad ,$$

and

$$\xi = \frac{z - \langle z\rangle}{\mu_2^{1/2}} \quad ,$$

$$\mu_n = \langle (z - \langle z\rangle)^n \rangle \quad ,$$

$\tilde{g} = 1$ for range, $\nu(E)$ for damage and $n(E)$ for ionization.

A detailed discussion of the behaviour of the various moments and distributions is not necessary here. Sufficient insight may be obtained from Fig. 2.6, where the three distributions have been developed using the above expansion for the case of high M_2/M_1 (N^+-Ge) and for low M_2/M_1 (Bi^+-Ge) at E = 40 keV.

For normal incidence, the distributions will exhibit a rotational symmetry about the z-axis. If the transverse second moment is $\langle x^2\rangle$, the Edgeworth series expansion in two dimensions becomes:

$$F(z,x,E) = \frac{\tilde{g}\cdot\exp(-\xi^2/2 - x^2/(2\langle x^2\rangle))}{(2\pi)^{3/2}\mu_2^{1/2}\langle x^2\rangle}\cdot f(\xi) \quad , \tag{2.29}$$

where $\tilde{g}$, ξ, μ_n and $f(\xi)$ are defined above. Iso-density contours of constant F can be generated by solving Eq. (2.29) for x with F and z known. Plotted in Fig. 2.7 is the iso-density contour for the atomic

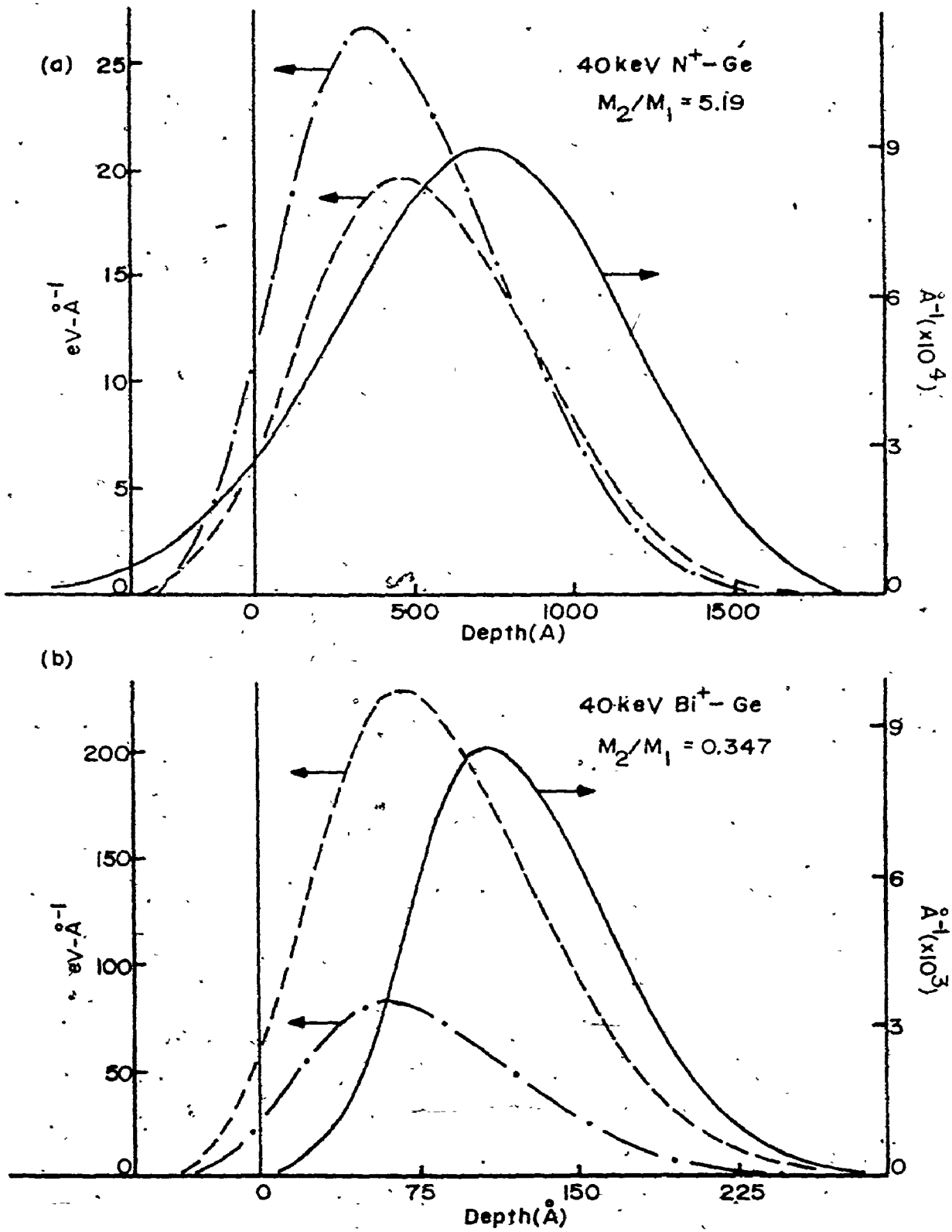

Fig. 2.6: Distributions obtained from Edgeworth series expansion of first four longitudinal moments: range (solid line), damage (dashed line), ionization (dot-dash line). (a) 40 keV N^+ on Ge, (b) 40 keV Bi^+ on Ge. Distributions are normalized via Eq. (2.23) for n = 0.

energy deposition distribution for 40 keV As^+ on silicon. The contour units of eV/atom are obtained by dividing Eq. (2.29) by N, the atom density. By rotating the plot about the z-axis, iso-density surfaces are generated.

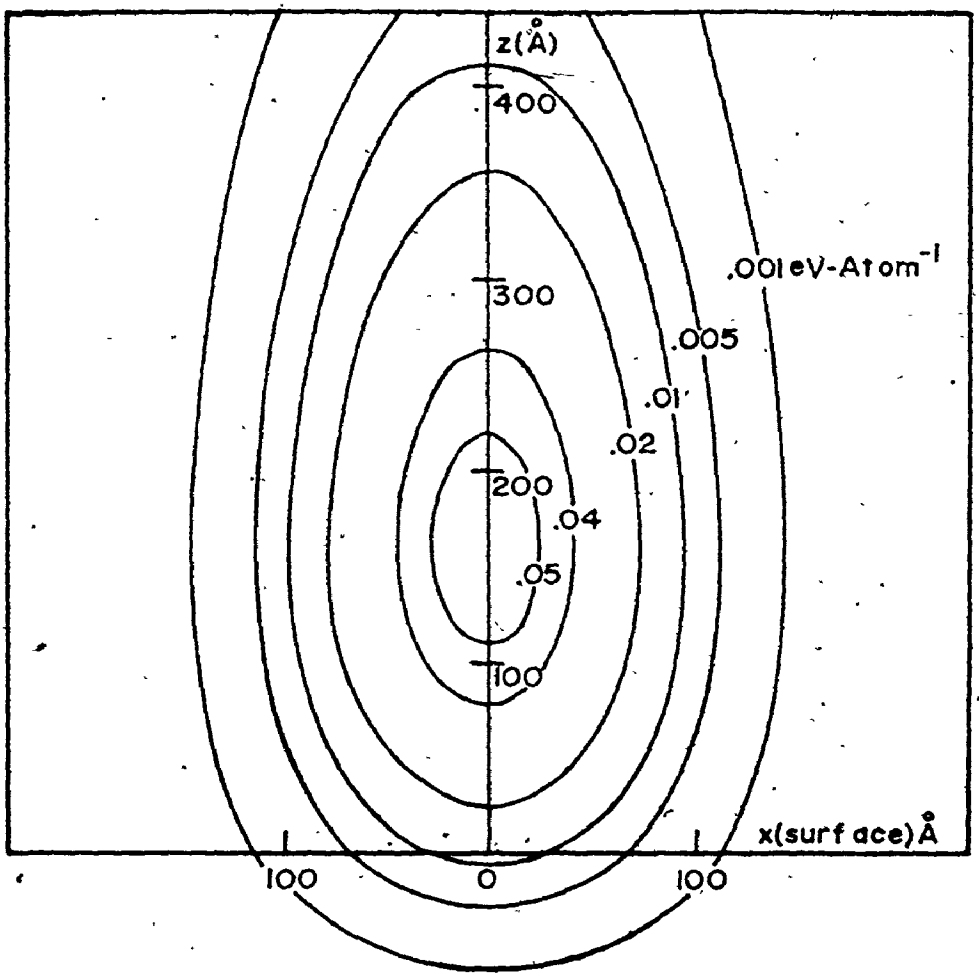

Fig. 2.7: Iso-density contours for distribution of energy into atomic processes for 40 keV As^+-Si.

There is a fundamental distinction between the range and energy distributions. For an individual ion, the single range distribution is a delta function whereas the energy distribution is spread over some

volume. The calculated distributions are the averages over an infinite number of ions. The range distribution then reflects the probability distribution of final ion positions. The energy distributions may bear little relation to the energy distribution of an individual cascade. Some attempts[25,26] have been made to relate the sizes of the individual cascades to the averaged distributions by using correlation calculations. However, since the problem of defining the individual cascade structure is of major significance to this research, a Monte-Carlo approach has been adopted and is described in the following chapter.

2.2.5 The Number of Displaced Atoms

Of particular interest in damage studies is the average number of displaced atoms that result from the collision cascade. When an atom is scattered, the interstitial atom and remaining vacancy are referred to as a Frenkel pair. A linear transport equation describing the average number of Frenkel pairs, N(E), created by a primary recoil of energy, E, can be developed along arguments similar to those of the previous section:

$$\int_0^E \frac{d\sigma_n}{dT} [N(E) - N(E - T) - N(T)]dT = 0 \quad , \tag{2.30}$$

where T is the recoil energy. Electronic stopping has been neglected for now. Within the model of Kinchin and Pease,[27] N(E) obeys the boundary condition:

$$N(E) = \begin{cases} 0 \text{ for } E < E_d \\ 1 \text{ for } E_d < E \leq 2E_d \end{cases} \quad , \tag{2.31}$$

where E_d is a threshold displacement energy necessary to disrupt the atom bonds and move the recoiling atom to a stable location relative to

the remaining vacancy.

If the atoms are considered as hard spheres, the approximate solution of Eq. (2.30), subject to the above boundary condition on N(E), is:[27]

$$N_{kp}(E) \sim E/2E_d \quad , \quad \text{for } E >> E_d \quad , \tag{2.32}$$

and $N_{kp}(E)$ is linear in energy. The subscript, kp, indicates that the Kinchin-Pease boundary condition, Eq. (2.31), is imposed.

Robinson[28,29] has considered more appropriate cross-sections, and for the power-cross-section approximation, finds the asymptotic solution for fixed m to be:

$$N_{kp}(E) \sim \xi(m)E/2E_d \quad , \quad \text{for } E >> 2E_d \quad , \tag{2.33}$$

where: $\xi(m) = 2(2^m - 1)/[\psi(1) - \psi(1 - m)]$ and $\psi(x)$ is the digamma function, $\psi(x) = \frac{d}{dx} \ln\Gamma(x)$. The parameter, $\xi(m)$ decreases from $\xi = (12/\pi^2)\ln 2 = 0.84$ at $m = 0$, to 0 at $m = 1$. Since m will vary as the ion and recoils lose energy, it would appear that $\xi(m)$ will vary, and a non-linearity in energy will appear. However, Sigmund[30] has argued that since it is the number of near-threshold collisions of the higher generations of recoil atoms which primarily determines N(E), the appropriate value of m should correspond to $E \sim 2E_d$, i.e.: $m = 0$ and $\xi = 0.84$. The effect of electronic stopping can be included[31] by replacing E with $\nu(E)$ in Eq. (2.33) and:

$$N_{kp}(E) \sim 0.84\ \nu(E)/2E_d \quad , \quad \text{for } E >> 2E_d \quad , \tag{2.34}$$

This is referred to as the modified Kinchin-Pease equation. The above has also been derived by a treatment of the recoil density.[31]

2.2.6 Comparison with Experiment

The most easily studied distribution is the ion range. Satisfactory predictions of the measured range distributions have been found for many ion-target systems (cf. ref. 5). However, two principle sources of discrepancy have been noted:

(1) it is known that the electronic stopping does not exhibit the exact velocity-proportionality that is predicted in the LSS theory.[32] For amorphous targets, "Z_1-oscillations" in the electronic stopping produce deviations of up to perhaps 20-50%.[2] It has been shown[33] in high-e implants, where the electronic component is of relatively high importance an adjustment of the constant, k, in the electronic stopping of Eq. (2.22) is necessary to match the range distributions.

(2) At very low e, the Thomas-Fermi approach to the nuclear scattering begins to overestimate the cross-section. Larger ion ranges[34] and range straggling[35] have been noted for $e << 0.02$.

The experimental verification of the energy distributions proves more difficult; in fact, no experimental measurement of the ionization distribution has been made. The atomic energy deposition distribution can, in certain instances, be inferred. In materials such as the semiconductors, where the atoms displaced in the atomic scattering process are relatively stable, the damage distribution should be directly related to the energy distribution. The channeling-Rutherford backscattering

technique is a convenient method of measuring the damage distribution (see Chapter IV). Such measurements of radiation damage in semiconductors have yielded satisfactory agreement with the theory.[36] However, discrepancies similar to those noted in the range measurements have been observed.[37,38] This will be discussed in more detail in Chapter VI, where these measurements are presented.

Collision theory can be examined experimentally by the measurement of secondary effects that result from the collision cascade, such as reflection and sputtering yields. Sigmund[20] has developed a comprehensive theory of the sputtering of amorphous targets, based on the LSS and WSS theories. It has been shown to adequately predict sputtering yields for a wide range of ion-target systems. As well, time-of-flight measurements of sputtered particles reveal that their energy spectra generally agree with that predicted by the theory (cf. ref. 39). However, deviations in both the sputtered yields and energy spectra have been observed under certain conditions; the discussion of these are deferred until the following section.

Perhaps the greatest discrepancy between collision theory and experiment occurs when the modified Kinchin-Pease equation is used to predict the final number of defects. In the metals, the approach often overestimates the observed N(E) by as much as an order of magnitude.[40] Also, the energy dependence of N(E) has been found quadratic rather than linear.[41]

Contrary to this, channeling-backscattering measurements of N(E) in semiconductors following heavy-ion irradiation have found Eq. (2.34) to underestimate the observed N(E) by $\gtrsim$ an order of magnitude.[42-44]

As well, electron microscopy examination of the defect structure following low-dose ion irradiations have revealed the presence of small amorphous zones.[45,46]

In comparing the collision theory with experimental quantities, it is important to differentiate between discrepancies that result from: (1) inadequacies in the theory, and (2) external influences on the measured quantity. For instance, a high target temperature may cause a smearing of the ion range distribution due to diffusion or annealing of the lattice damage with a resultant distortion of the damage distribution. Channeling effects, as discussed in Chapter IV, may cause anomolous ion penetration.

Discrepancies discussed earlier in ion range measurements are obviously of the first kind. External influences such as are often related to target temperature or target structure can be both easily defined and controlled. However, the nature of the discrepancies in the sputtering and damage experiments are more difficult to separate. In fact, many of the observations may result from the breakdown of the linear collision theory at small particle energies, combined with the behaviour of the particular solid when this breakdown occurs. Such effects are the topic of the next section.

2.3 Solid State Considerations

In this section, we are concerned with the local rearrangements of the crystal which can occur as the collision cascade terminates. These rearrangements may be roughly divided into athermal and thermal processes; the former is a consequence of the defect density within the cascade

volume, while the second results from effects related to the eventual dissipation of the initial ion energy. These processes are not due to the thermal activation of the crystal at its ambient temperature, but will have gone to completion in a comparatively short time ($\sim 10^{-11}$ sec), after the cascade has ended ($\sim 10^{-13}$ sec).

2.3.1 Athermal Rearrangements

Athermal rearrangement of the defects remaining after the collision cascade may produce very different results in different materials. In the metals, the defects have a relatively large recombination volume, i.e.: if an interstitial comes to rest near enough to an existing vacancy (or vice-versa) the defects may coalesce without a thermal activation being required. This large volume is evidenced by the relatively high threshold displacement energies (20-30 eV) that are characteristic of the metals. In the semiconductors $E_d \sim 10$-15 eV, and is mainly the energy necessary to break the atom bonds. Therefore, as various branches of the cascade overlap, significant spontaneous recombination may occur in the metals, thereby reducing the initial concentration of Frenkel pairs. Then the number of stable defects will depend on the volume of the primary damage and will have little connection to the Kinchin-Pease equation (Eq. (2.34)). Sigmund[31] has shown that the athermal recombination will also predict the E^2 dependence of the defects, as has been reported experimentally.[41]

In the semiconductors, the weaker covalent bonding and more open lattice spacing will result in more stable defects, and spontaneous recombination will be less probable. As well, the amorphous phase can

be readily formed by prolonged ion bombardment (cf. ref. 47). At the microscopic level, the meta-stability of the amorphous phase has led to the prediction of the local collapse of the crystal lattice into an amorphous zone when a certain local critical defect concentration has been attained. The value of this critical concentration is subject to controversy, and predictions range from 2%[48] to 50%.[49]. This point will be discussed further in Chapters VI and VII. Athermal rearrangement of the unstable lattice could account for the presence of amorphous zones observed by electron microscopy in ion-bombarded semiconductors.

2.3.2 Thermal Rearrangements

As the collision cascade subsides, a local heating effect will result as the initial ion energy is dissipated through thermal atom motion. This has been envisaged as a result of the breakdown of the linear energy transport theory once the particle energies approach thermal energies, and effectively many atoms will be put in motion by the back-and-forth energy transfers. Such a region in the crystal has been referred to as a thermal-spike.[4]

In order to discuss what effect the thermal spike may have on the lattice rearrangement, the methods of energy transfer and the time scales involved in the transfers must be considered. The cascade is essentially generated in the time necessary to bring the ion to rest, i.e.: $\sim 10^{-13}$ sec. The atoms then communicate in times of the order of the lattice vibration times ($\sim 10^{-13}$ sec) so that after $\sim 10^{-12}$-10^{-13} sec, the energy distribution will begin to approximate the Maxwell-Boltzmann distribution and the concept of local temperature and heating becomes

practical. Fig. 2.8 shows the isothermal contours generated by computer simulation[50] of the cascade of a 100 eV recoil in copper. The times are 3.27×10^{-13} sec and 9.9×10^{-13} sec from initiation of the cascade and effective temperatures have been defined by dividing the atom kinetic energy by $3k/2$. Significant local heating is evident. The same procedure can be applied to the iso-density contours of Fig. 2.7. However, to define the isothermal contours by this method one assumes that no thermal dissipation has occured until the energy distribution is established.

The initial ion energy will be shared between the lattice atoms and electrons; therefore, energy can be transmitted via three types of collisions: atom-atom, electron-electron, and atom-electron. For 1 eV electrons, electron collisions occur in $\sim 5 \times 10^{-16}$ sec, while for 1 eV atoms, atom-atom collisions take $\sim 10^{-13}$ sec. Therefore, the electronic energy should be dissipated long before the thermal spike is important. Atom-electron collisions are very inefficient at transferring energy because of the large mass ratio involved. Collisions between "hot" atoms and "cool" electrons would require more than $(M_2/4m_e)$, i.e.: between 10^4 and 10^5 collisions to cool the atom system. Thus, at least 10^{-11} sec are necessary for energy to pass between the two systems. Classical theory of heat conduction shows that the cooling time by atom-atom collisions $< 10^{-11}$ sec and will therefore dominate the energy dissipation process. Sigmund[51] has treated the spike lifetime, τ, more quantitatively; his treatment will be discussed in some detail in Chapter VII.

The thermal effects will likely be material dependent, as are the athermal effects discussed above. In the metals, where the crystal lattice has a greater capability to reorder, the spike may cause some

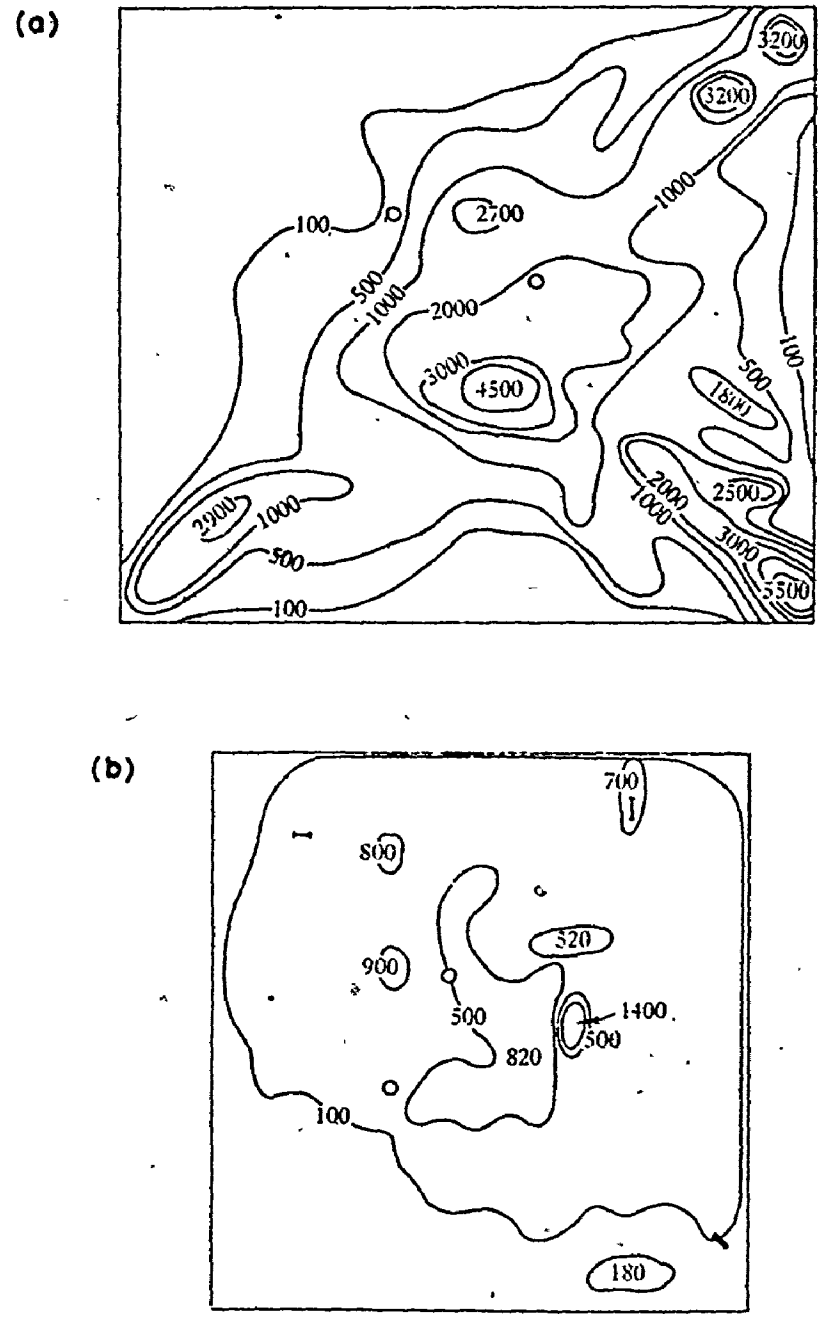

Fig. 2.8: Isothermals following a 100 eV Cu recoil in Cu at (a) $t = 3.27 \times 10^{-13}$ sec and (b) $t = 9.9 \times 10^{-13}$ sec from initiation of recoil. The Figures represent the two-dimensional projection for a 10 x 10 x 10 atom array. From ref. 50.

defect migration that results in annihilation and clustering. However, in the semiconductors, the effect may be quite the opposite, and a local zone with a high degree of disorder may be quenched in as the spike dies out. Computer simulation[52] of the influence on the silicon lattice due to spike heating and cooling indicates the formation of a local amorphous phase is possible. This suggests another mechanism by which the amorphous zones present in ion bombarded semiconductors could be formed.

Closely connected in origin to the thermal-spike is the "displacement-spike". As the particle loses energy, its atomic collisions will eventually no longer be binary, but the particle will interact simultaneously with several atoms. Thus, linear collision theory will again be invalid. Atoms will be thrown out of a region surrounding the end of the ion track, producing a vacancy rich core surrounded by an interstitial rich shell. Brinkman[53] has defined the displacement-spike as occuring when the mean distance, x_d, travelled between collisions that transfer more energy than E_d reaches the interatomic spacing, d. Then:

$$x_d = 1/N\Sigma_d \quad , \tag{2.36}$$

where

$$\Sigma_d = \int_{E_d}^{T_m} \frac{d\sigma_n}{dE}\, dE \quad .$$

For the power cross-section approximation of Sec. 2.2.2, and m = 1/2:

$$x_d = \frac{\pi a^2 \lambda_{1/2} \gamma^{1/2}}{\epsilon_o (E E_d)^{1/2}} \quad , \tag{2.37}$$

where $\epsilon_o = \epsilon/E$ and $\gamma = T_m/E$. Then the characteristic energy, E_D, when when $x_d = d = N^{-1/3}$ is:

$$E_D = \frac{\pi^2 a^4 \lambda_{1/2}^2 \gamma N^{2/3}}{e_o^2 E_d} \quad . \tag{2.38}$$

Eq. (2.38) shows that E_D increases very rapidly in moving through the periodic table, from ∿1 keV for Si recoils in Si to ∿100 keV for Bi ion in Si. Therefore, displacement spikes will influence most keV heavy ion irradiations. Note that the displacement spike will not cause an increase in the number of displacements in itself. However, the displacement and thermal spike processes are closely connected, in that the former will serve to put many atoms of both sub-threshold and threshold energies in motion. It will therefore act to initiate the thermal-spike.

Collision theory has so far assumed a random, uniform medium, whereas in experiment a single crystal target is often used. Computer simulation[54] of the collision cascade in the lattice and measurement[55] of the angular dependence of the sputtering yields from crystalline targets have revealed that the lattice structure can influence the energy transport mechanisms. The channeling of recoils and focussed collision sequences along densely packed atom strings are the main effects. These will be stronger in the metals, where the less-open lattice structure is more conducive to their occurence. As well, the gross disruptive nature of high -Z_1 implantation in the semiconductors by the spike mechanisms discussed above will diminish their importance.

2.3.3 Experimental Evidence for Thermal-Spikes

From the above discussion, one rearrangement process which appears likely to affect the ion-induced damage in the semiconductors is the thermal-spike. The most striking evidence for existence of thermal-spikes

comes from sputtering experiments, since these deal with the dynamic behaviour of the cascade. In time-of-flight measurements of sputtered atoms,[56] a thermal component in the energy spectrum has been observed. The magnitude of the thermal component increases with ion and target mass and with target temperature as well.[57] A thermal-spike model has been used to satisfactorily explain the observations. Systematic deviations from Sigmund's sputtering theory[20] have been observed for high $-Z_1$ irradiation of heavy targets.[58-60] For example, shown in Fig. 2.9 are the sputtering yields for various 45 keV ions in gold, normalized to the Ar^+ sputtering yield.[60] The theory consistently underestimates the yields for large Z_1. Comparison of sputtering yields for diatomic ions, the latter having the same atom energy as the monatomic ion, have revealed that significant non-linearities can exist. Table 2.1 shows the results of the investigations of the sputtering "molecular effect" for various ion-target combinations.[58-60] Linear collision theory would predict a "molecular effect" of unity. However, values greater than unity appear, the magnitude of the effect increasing with both ion and target mass. Recent measurements of the non-linearity for polyatomic ion bombardment in Ag suggest the effect may even exceed an order of magnitude.[61] Anderson et. al.[62] and Sigmund[51] have argued that the non-linear behaviour is a consequence of the thermal-spike. Spike effects will increase in importance as Z_1 and Z_2 increase, since as the cascade volume diminishes the energy density within the individual volume will increase. Calorimetric measurements[62] of the total energy of the sputtered atoms performed for atomic and molecular Se^+ and Te^+ on lead at 34 keV per atom have revealed no significant difference in the

total sputtered energy. This indicates that the surplus atoms which contribute to the non-unity "molecular-effect" must be of comparatively low (thermal) energies.

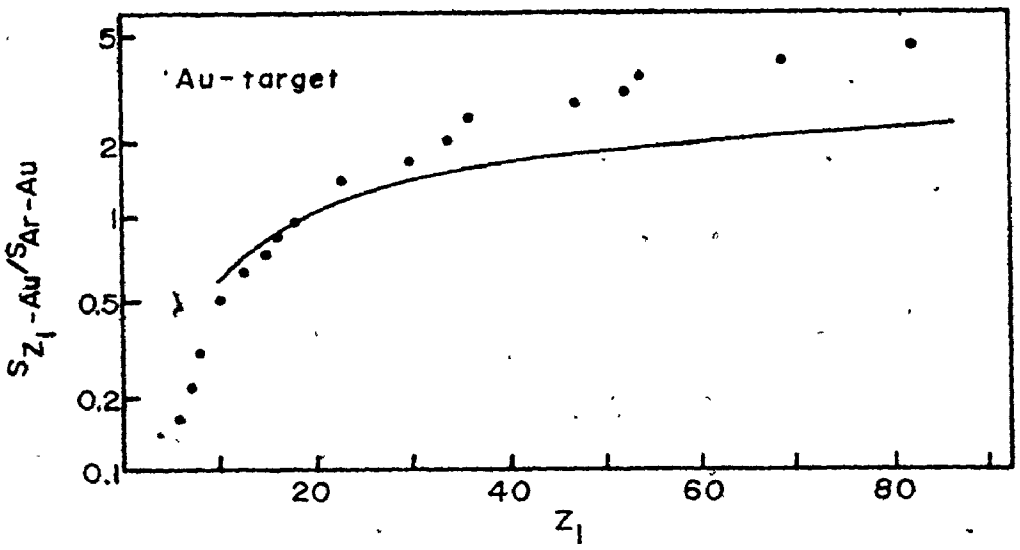

Fig. 2.9: Sputtering yields of Au for 45 keV ions, normalized to the yield of 45 keV Ar-Au (from ref. 60). Solid line from Sigmund[20].

Table 2.1: Ratios[60] between sputtering yield per atom for molecular and atomic ion bombardment for different ion-target combinations.

Projectiles	Targets		
	Si	Ag	Au
$Cl\text{-}Cl_2$	-	1.09	-
$Se\text{-}Se_2$	1.15	1.44	1.44
$Te\text{-}Te_2$	1.30	1.67	2.15

The interpretation of observed physical changes as due to thermal-spikes is difficult because other feasible explanations of the observations may exist. However, phase transformations in iron compounds following proton irradiation have been explained[63] as resulting from the creation of thermal spikes by heavy atom recoils having sufficient temperature to initiate the transformations.

Thus, it appears that there is a good deal of experimental evidence for the existence of thermal-spikes. We have suggested how the spike may influence the final amount of disorder following ion implantation of the semiconductors. As well, local collapse of the lattice in regions of high defect density may occur. No detailed experimental investigation of the effects have been performed to date. Such an investigation is the topic of Chapter VII. It becomes obvious that the investigation will require a detailed knowledge of the individual cascade structure, including its dimensions, local energy density, and local defect density. While this information can be difficult to obtain from the statistical approach of Sec. 2.2, it is possible to program a computer to simulate the generation of the individual cascade. The latter is referred to as the Monte Carlo approach and the method is developed and discussed in the following chapter.

CHAPTER III

MONTE CARLO SIMULATION OF THE COLLISION CASCADE

3.1 Introduction

In the previous chapter, it was seen that the statistical description of the collision cascade is often inadequate in describing the final amount of lattice disorder in the semiconductors following energetic ion bombardment. Further, it appears that in order to discuss the source of the discrepancy a detailed knowledge of the individual cascade structure is required. One can obtain some information analytically[25,26] on the individual cascade parameters by using correlation theory. However, it is possible to program a computer to simulate the collision cascade. By averaging the results of many simulated cascades, one should obtain the same information as derived from the statistical approach of Sec. 2.2. This computer simulation is referred to as the Monte Carlo technique.[64,65] The interesting feature of the simulation is that it allows the direct study of the individual cascade as well.

This chapter describes a Monte Carlo computer code which has been developed to simulate the collision cascade as would result from keV ion implantation of an amorphous target. In Sec. 3.2, the principles of the code are defined and the method outlined. In Sec. 3.3, the code output is compared to the results of the statistical treatment of the previous chapter. The features of the individual cascade which can be studied by the Monte Carlo approach are discussed in Sec. 3.4.

3.2 The Simulation Method

When attempting to simulate the collision cascade on a computer, one must decide at the outset whether or not the target will be assumed to have a lattice structure. The simulation principles depend critically on this assumption; for a crystal model, the ion trajectory is randomized in its initial conditions,[64,65] i.e.: its entry location in the lattice. From then on, the lattice structure will combine with the energy loss processes to define the cascade generation. For the non-crystalline or random model,[66] the initial conditions are constant. Rather, the randomization of the cascade is introduced by weighting the nuclear scattering cross-section and path length between collisions by a given probability distribution. The choice of model depends on the objectives. For example, the crystal model gives information on lattice-structure-related effects such as channeling, focussed collision sequences, defect configurations, etc. Since in this thesis we deal with the implantation of crystalline targets, the crystal model would appear more appropriate. However, in the keV energy range, the main features of collision cascade have generally been found to be insensitive to the lattice structure.[67,68] As well, the random model is analogous to the statistical treatment of Chapter II. Therefore, the much simpler random model has been chosen here. In the same manner as the statistical treatment, the collisions shall be assumed binary, with the struck atom being stationary before collision.

In order to follow the spatial development of the collision cascade, it is necessary to define the polar and azimuthal scattering angles in the center-of-gravity system at each collision (see Fig. 2.1), as well as the distance travelled between collisions. These angles

can then be translated to scattering angles in the laboratory system (cf. ref. 12).

1) The polar scattering angle, θ. By definition of the nuclear differential cross-section, the probability that an incident particle will scatter between θ and $\theta + d\theta$ is:

$$p(\theta)d\theta = d\sigma_n(\theta,E)/\int_{\theta_{min}}^{\pi} \frac{d\sigma_n(\theta)}{d\theta}\, d\theta \quad , \tag{3.1}$$

where the denominator provides the normalization of the total probability to unity. In a binary collision, θ_{min} should be zero, corresponding to an infinite impact parameter. Since the nuclear cross-section diverges for large impact parameter, the computation becomes impossible unless a maximum impact parameter is introduced.[69] In a solid, it is introduced conveniently, since in a binary collision model the particle cannot be further than half the interatomic distance, d, from the atom with which it collides. In terms of the reduced parameter, $t = \epsilon^2 T/T_{max}$, introduced in Sec. 2.2, Eq. (3.1) becomes:

$$p(t)dt = d\sigma_n(t)/\int_{t_{min}}^{t_{max}} \frac{d\sigma_n}{dt}\, dt \quad , \tag{3.2}$$

where t_{max} corresponds to the maximum energy transfer, T_{max}. Since we are mainly interested in the energy transfers which produce an atom displacement, it is convenient to have t_{min} correspond to the displacement energy, E_d. This value of t_{min} will always correspond to an impact parameter of <1/2 d. The cut-off of the cross-section at E_d means that energy loss through collisions below the displacement threshold will be ignored. The

sub-threshold component is generally small provided $E_d << E$. This point will be considered further in the next section.

For a collision involving a transfer of energy, t, integration of Eq. (3.2) gives:

$$\int_{t_{min}}^{t} \frac{d\sigma_n(t)}{dt}\, dt \Big/ \int_{t_{min}}^{t_{max}} \frac{d\sigma_n(t)}{dt}\, dt = p_1 \quad , \tag{3.3}$$

where p_1 will be a fraction between 0 and 1. In the Monte Carlo technique, p_1 is chosen as a random number between 0 and 1 so that the problem becomes finding the appropriate value of t such that Eq. (3.3) is satisfied. For the numerical approximation to $d\sigma_n(t)$ in Eq. (2.14), the integral of $d\sigma_n(t)$ may be calculated numerically and tabulated for various values of t. Then for a given random number, a value for the integral is obtained and a table search and interpolation will yield t. This procedure is used for $t \gtrsim 10^{-4}$. For smaller values of t, Fig. 2.2 reveals that the power-cross-section approximation with m = 1/3 is an accurate fit to the numerical expression and Eq. (3.3) may be evaluated analytically. This method is used for $t < 10^{-4}$ and greatly reduces the computational effort. Once t has been obtained, θ is defined, i.e.:

$$t = \epsilon^2 \sin^2 \theta/2 \quad ,$$

and the scattering angles for the scattering and recoil atoms, θ_1 and θ_2, in the lab system are:[12]

$$\tan\theta_1 = \frac{M_2}{M_1} \frac{\sin\theta}{\left(1 + \frac{M_2}{M_1}\cos\theta\right)} \quad ,$$

$$\tan\theta_2 = \frac{\sin\theta}{(1 - \cos\theta)} \quad . \tag{3.4}$$

2) The azimuthal scattering angle, ϕ. The choice of ϕ is arbitrary since the scattering in the azimuthal plane is isotropic. It will be defined by a second random number, p_2, between 0 and 1, such that:

$$\phi = 2\pi p_2 \quad , \tag{3.5}$$

where $\phi_{max} = 2\pi$.

3) The distance between collisions, ℓ. The mean free path, λ, between collisions can be defined as:

$$\lambda = 1/N\Sigma(E,T) \quad , \tag{3.6}$$

where

$$\Sigma(E,T) = \int_{E_d}^{T_{max}} d\sigma_n(T) \quad ,$$

and N is the atom density of the target. The above definition of λ is consistent with the random model since it preserves the lattice density while ignoring the lattice structure. The mean free path may now be randomized by assuming an exponential distribution of free path, with λ as the average.[70] It is straightforward to show that the distance, ℓ_i, travelled between the i^{th} and $(i + 1)^{th}$ collisions becomes:

$$\ell_i = -\Sigma_i(E_i)\ln p_3 \quad , \tag{3.7}$$

where E_i is the energy after the i^{th} collision and p_3 is a random number between 0 and 1. The above development implicitly assumes that the energy loss to inelastic scattering between collisions is small enough that the change in nuclear cross-section in travelling distance ℓ_i can be ignored.

In the LSS model of path-independent, velocity proportional

electronic stopping:

$$(dE/dR)_e = -KE^{1/2} \quad , \tag{3.8}$$

where K is the constant of Eq. (2.22), only not in dimensionless e-ρ units. On integration of the above equation, the electronic loss, ΔE_{ei}, between the i^{th} and $(i+1)^{th}$ collisions is:

$$\Delta E_{ei} = E_i - (E_i^{1/2} - \frac{K\ell_i}{2})^2 \quad , \tag{3.9}$$

where ℓ_i is defined by Eq. (3.7). A constraint must be imposed on the maximum ΔE_{ei}, i.e.: $\Delta E_{ei} \leq E_i$ or $\ell_i \leq 2E_i^{1/2}K$. Note that in the definition of ℓ_i it is assumed that $\Delta E_{ei} << E_i$; obviously the necessity of the above constraint suggests that at low E_i, the condition can break down. However, it will have little influence on the spatial distribution, since the range of the particle when $\Delta E_{ei} \sim E_i$ will be small.

At small E_i, the correlated nature of the electronic stopping requires consideration; this has been attempted by Torrens and Robinson.[67,68] Basically, the inclusion of correlated scattering will cut off the electronic stopping at small E[2] so that the boundary condition on the total energy into atomic processes, $\nu(E)$, is satisfied, i.e.: $\nu(E) \to 1$ as $E \to 0$. Winterbon[2] has shown that as long as the cross-section at small E is fitted by a power cross-section of $m \geq 1/4$, the cross-section is strong enough that $\nu(E) \to 1$ anyway. As well, it has been shown that correlated scattering will have minor effect on the cascade dimensions.[11] This is due to the fact that the shape of the cascade is primarily determined by the high-energy part of the cascade where correlated scattering need not be considered. We shall assume that the extension of the description of

the electronic energy loss at large E used in the Monte Carlo approach to small E will have little influence on the results. This is examined in the next section. The implication of not incorporating correlated scattering is that the Monte Carlo approach should not be extended to cross-sections approximated by a power cross-section having $m < 1/4$.

The code has been developed for both range and damage calculations. Since it is the latter which is of direct interest, we will concentrate on those aspects of the code. The procedure is to follow an incident ion of energy E injected at an arbitrary angle to the surface, collision by collision, until its energy falls below some minimum cut-off energy, E_f. Likewise, all subsequent generations of recoils are followed until no particle in the collision cascade has energy greater than E_f. In keeping with the Kinchin-Pease[27] model of the cascade (see Sec. 2.2.5), it is assumed that the particle is at rest once its energy falls below $E_f = 2E_d/\gamma$, since it will no longer be able to transfer sufficient energy to create a further displacement. For large M_2/M_1, an adequate description of the spatial energy deposition can be obtained by ignoring the energy transport of the recoils, or by considering at most only the primary recoils. However, the code has been generalized to follow all recoils. This enables a measure of the total number of displaced atoms for comparison with the modified Kinchin-Pease Eq. (2.33) and Eq. (2.34). The effects of ignoring recoil energy transport are examined in the next section.

At any collision, if the recoiling particle has energy less than E_f, the defect count is incremented, since only collisions of $T > E_d$ have been allowed. However, when the scattered particle has energy less than E_d, it will take the place of the recoiling atom with no net increase in

the number of defects. This is referred to as a replacement collision. If the number of collisions is counted and compared to the number of defects, the fraction of defects lost to replacement collisions can be obtained.

In order to follow the spatial development of the cascade, the scattering angles of the collision partners are converted to the original laboratory axes relative to the target surface by a simple coordinate transformation. This is necessary since the scattering angles are referenced to the axis system of the incident particle. The computer has been programmed to follow the recoiling atom at each collision while six pieces of information are stored for the scattered particle, i.e.: its collision coordinates, scattering angles and energy. When a recoil falls below E_f, the information on the previous scattered particle is retrieved and the storage area made available again. Thus, an array containing the information on the scattered particles will dynamically increase and decrease in size as the cascade develops. This technique will allow for a minimal storage space in the computer and therefore removes one restriction on the size of cascade that can be simulated. In particular, the array area will be dimensioned at (n,6) with six pieces of information being required for each scattered particle. The parameter, n, is the maximum number of generations of recoils. A value of n = 10 is considered adequate in the ion-target combinations studied, although it has been arbitrarily set at n = 100 in the code.

At each displacement collision, an amount of energy, U, must be expended[8] in breaking the atom bonds and overcoming the potential minimum in which the atom is located. In the statistical treatment of

of the previous chapter, U has been assumed to be zero. However, if a finite value of U is considered, the energy balance (Eq. (2.24)) for the ion of initial energy, E, becomes:

$$E = \nu(E) + \eta(E) + \Sigma U \quad , \tag{3.10}$$

where ΣU is $n \times U$, n being the total number of displacement collisions which occur. $\nu(E)$ and $\eta(E)$ are the elastic and inelastic energy deposition components respectively. Since the presence of ΣU will alter the integrals, $\nu(E)$ and $\eta(E)$, of the energy deposition distributions, the option of subtracting a chosen U from the recoil energy has been included. It also allows for the examination of whether a finite U will affect the spatial distributions themselves. We note at this point that no consideration has been made as to where the energy, ΣU, eventually ends up. For example, in the semiconductors, most of U would be expected to be converted to inelastic energy in the bond breaking process. However, it will be discussed in Chapter VII that with regard to lattice stability, ΣU may well be intimately involved in determining the final amount of damage, and so should be combined with the atomic displacement energy component. It is obvious that this division will eventually become somewhat arbitrary, and is why ΣU has been included in Eq. (3.10) as a separate component.

The Monte Carlo code is a modified and extended version of a code written recently[71] to be run on a CDC 6400 computer. The present code has been developed to run on a PDP-15 minicomputer, having 32K 18-bit words of memory, and an extra 20K words for common storage. Mass storage is on a fixed-head disk. A link structure has been implemented using the disk, in order to overcome the limitation of available space. To

follow a 10-100 keV ion cascade to termination requires typically 1-3 minutes. A listing and documentation of the code are available in the addendum to this thesis.

3.3 Comparison of the Statistical and Monte Carlo Collision Cascades

The LSS theory has been used to define the energy loss processes in both the statistical and Monte Carlo approaches to describing the collision cascade. Therefore, the descriptions should be essentially identical, provided the Monte Carlo results are averaged over a statistically large number of cascades. A comparison of the averaged results will provide a sufficient check on the formulation of the code. It has been developed to generate range, atomic energy deposition and damage distributions; the latter two developments basically contain the range information, as well as being of more interest to the research of the thesis. The comparison will concentrate on the damage parameters only.

In the following analysis, the choice of a displacement energy, E_d, has been necessary. In terms of the Monte Carlo code, the choice is not critical, since its results have been found to be insensitive to E_d, at least in the energy interval, $\sim 10 \text{ eV} \lesssim E_d \lesssim 35 \text{ eV}$. Therefore, an E_d of 25 eV has been used consistently, rather than the realistic E_d ($\sim$13 eV in Si and Ge), to save on the computer running time.

The code permits the choice of following all recoil generations, only the primary recoils, or none of the recoils. When it is decided not to follow a recoiling atom, the recoil energy is deposited into the distribution of $\nu(E)$ at the collision coordinates. Otherwise, the recoil is assumed to come to rest at the collision location where its energy

falls below the cut-off energy, E_f. Although E_f may be set arbitrarily, it is commonly left at $E_f = 2E_d/\gamma$, i.e.: at the minimum energy necessary to produce an additional displaced atom. When the particle energy falls below E_f, its energy is deposited into $\nu(E)$ at the collision location. An amount of energy, U, lost to the lattice during the atom displacement, may be subtracted from the recoil energy at each collision. Two values of U have been used in the following comparisons: (1) U = 0, after the MARLOWE code of Robinson and Torrens,[67,68] and (2) $U = E_d$, after the model proposed by Synder and Neufeld.[72] In the WSS treatment of the collision cascade in Sec. 2.2.4, U was assumed zero, and corresponds to the first of the above cases.

3.3.1 The Spatial Distributions

In the Monte Carlo simulation of ion range, none of the recoils need be followed. For large M_2/M_1, where relatively high recoil energies are unlikely, the shape of the distribution of $\nu(E)$ is adequately defined by depositing the recoil energy at the collision coordinates. However, as M_2/M_1 decreases, it becomes necessary to follow at least the primary recoil as well. Shown in Fig. 3.1 are the Monte Carlo deposited energy histograms resulting from 80 keV Te^+ bombardment of Ge for the three options that have been discussed above for treating the recoils. E_d = 25 eV has been used, with U = 0. When no recoils are followed, the histogram is skewed towards the surface. For the other cases, the histograms peak at a greater depth, indicating the significance of the forward energy transport of the recoils. Following only the primary recoils appears to give essentially the same distribution as when all the recoils are followed. However, the total $\nu(E)$ values differ. This

reflects the fact that when the recoil energy is deposited into $\nu(E)$, a fraction of the energy is no longer available to be lost in inelastic scattering.

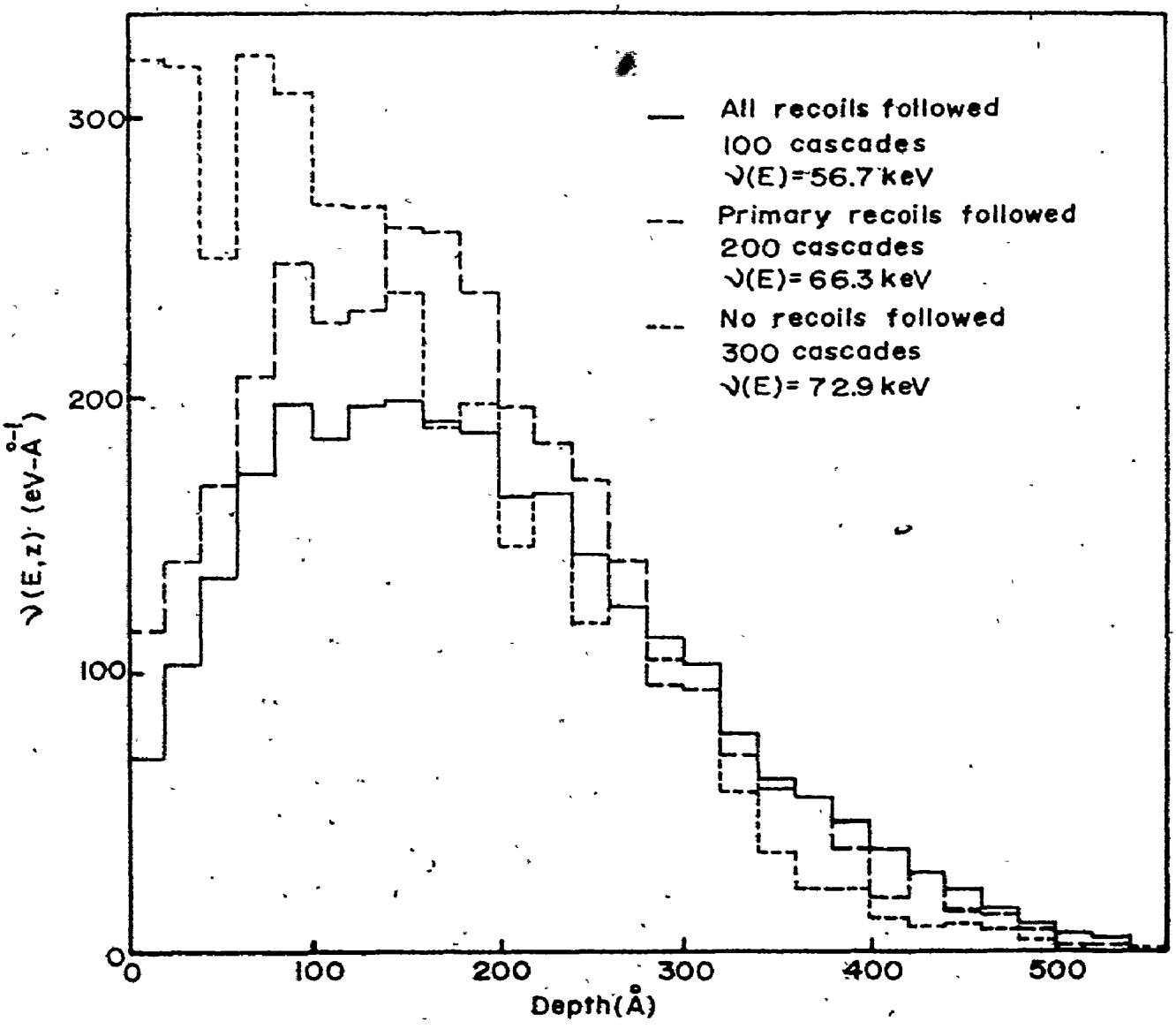

Fig. 3.1: Monte Carlo deposited energy histograms for 80 keV Te^+-Ge, showing recoil energy transport. E_d = 25 eV, U = 0.

Ion-Target	Mass Ratio (M_2/M_1)	Energy (keV)	Mean Damage Range (Å)		Longitudinal Straggling (Å)		Transverse Straggling (Å)	
			WSS	Monte Carlo	WSS	Monte Carlo	WSS	Monte Carlo
$^{83}Bi^{+}$-Si	0.134	20	79.8	85.3	44.3	46.0	24.2	26.3
		80	214.	216.	119.	120.	66.0	70.2
$^{33}As^{+}$-Si	0.375	20	115.	127.	68.6	74.5	43.4	47.5
		80	350.	377.	205.	199.	122.	133.
$^{7}N^{+}$-Si	2.01	20	399.	409.	233.	260.	166.	167.
		80	1640.	1680.	820.	802.	533.	526.
$^{52}Te^{+}$-Ge	0.567	20	67.4	68.5	41.0	40.5	27.5	28.0
		80	181.	183.	109.	115.	71.0	80.0
$^{15}P^{+}$-Ge	2.34	20	140.	145.	92.8	93.9	72.1	74.2
		80	480.	484.	293.	288.	218.	222.

Table 3.1: Comparison between WSS and Monte Carlo deposited energy distributions. For the Monte Carlo results, E_d = 25 eV.

In Table 3.1, three moments of the spatial distribution of $\nu(E)$ are compared for five ion-target combinations, each at two energies. The WSS moments have been obtained by interpolation of tabulated values.[2] Agreement in the straggling is generally within the estimated statistical error of ±5%. The mean depths agree within this error, although the Monte

Carlo depths are consistently deeper. This behaviour is expected because the WSS distributions extend beyond the surface, and will weight the first moment slightly in that direction. The overall distribution shapes are compared in Fig. 3.2(a),(b) for 80 keV Te^+-Ge and 40 keV N^+-Si (E_d = 25 eV, U = 0). Again, the agreement is satisfactory. Included in the figure are the spatial distributions of the final locations of the displaced atoms. The term, interstitial distribution, is avoided since it has little meaning in a non-crystalline material. As was inferred in the previous chapter, it is found that the damage distribution is directly proportional to the distribution of $\nu(E)$.

It was assumed in the statistical description of the collision cascade that the inclusion of a finite U would not affect the spatial deposited energy distribution.[8] This assumption is examined in Fig. 3.3 where the normalized distributions of $\nu(E)$ are compared for 80 keV Te^+-Ge with U = 0 and U = E_d (E_d = 25 eV). No significant difference is evident.

No accommodation can be made in the random code for athermal recombination of defects or for the influence of existing defects on the collision cascade. However, the code does allow for the examination of the proportionality between the deposited energy and damage distributions with effects such as replacement collisions and a finite value of U included. These comparisons shall be made in Sec. 3.3.2 and 3.3.3.

3.3.2 The Integral of the Energy Deposition Distribution

It can be seen in Fig. 3.2 that as long as the Monte Carlo simulation follows all recoil generations to termination, both the resultant

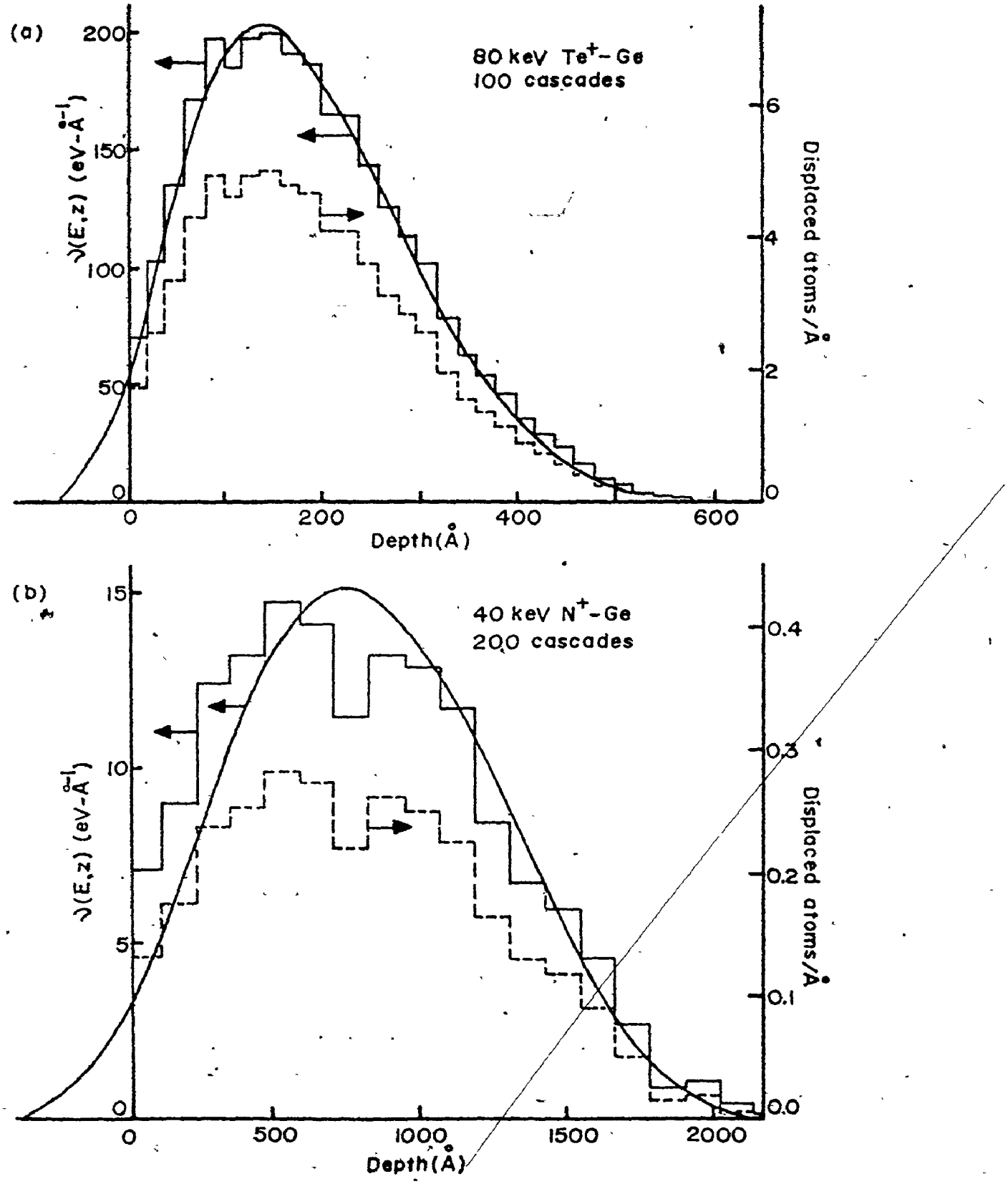

Fig. 3.2: Comparison of the deposited energy distributions from the WSS and Monte Carlo methods. The displaced atom distribution from the [illegible] is

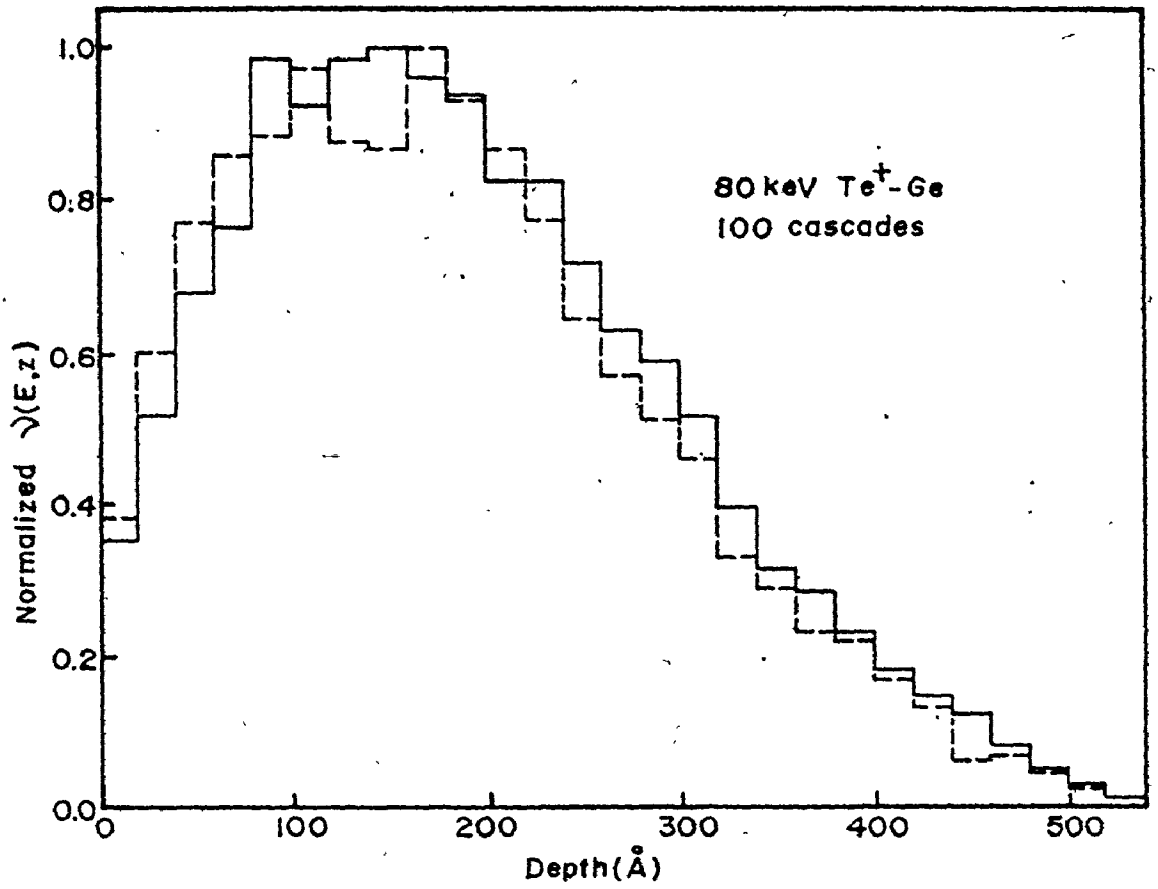

Fig. 3.3: Normalized Monte Carlo deposited energy histograms for 80 keV Te^+-Ge. E_d = 25 eV. Solid line, U = 0. Dashed line, U = E_d.

distribution of energy deposition and its integral, $\nu(E)$, agree with the results of the statistical approach. The values of $\nu(E)$ obtained by the two methods are compared in Fig. 3.4 for the case of Bi^+-Si and N^+-Si (U = 0, all recoils followed). The values agree within <5%, despite some basic differences in what $\nu(E)$ includes in each method:

(i) In the WSS approach, the nuclear scattering cross-section extends to zero transferred energy (i.e.: infinite impact parameter) and

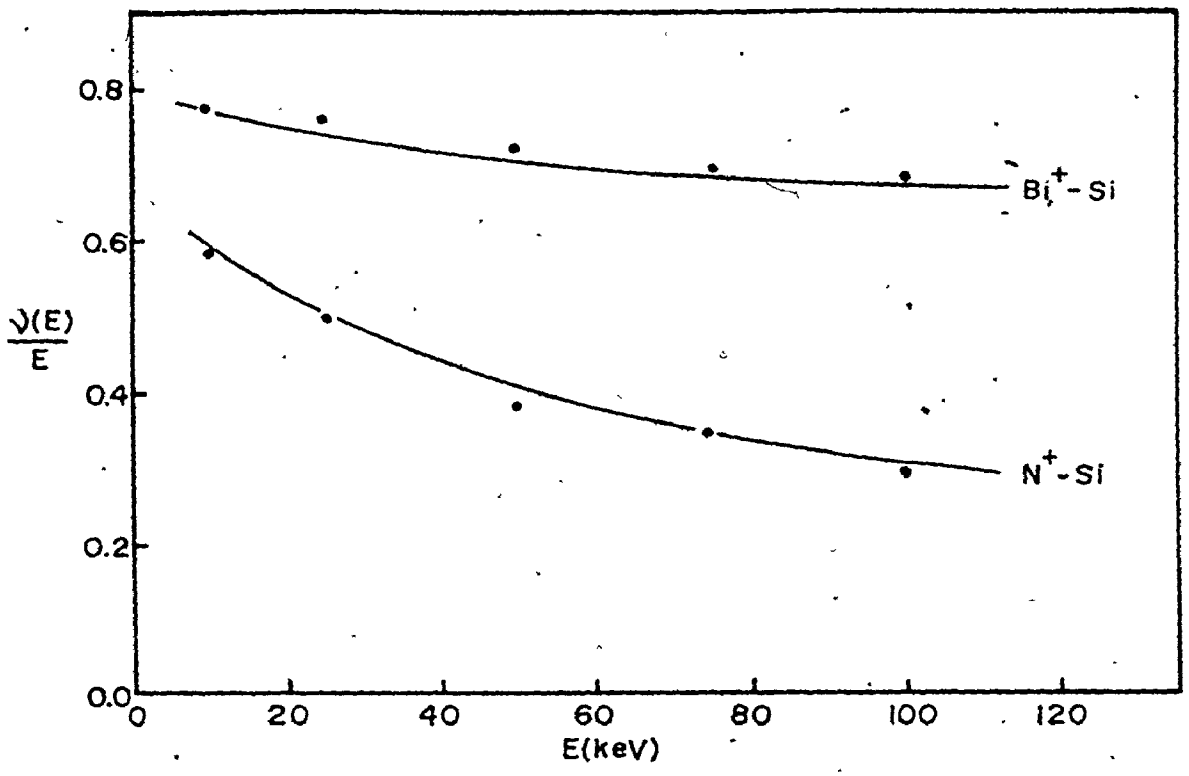

Fig. 3.4: Comparison of $\nu(E)/E$ values for WSS (solid line) and Monte Carlo (points) for E_d = 25 eV, U = 0.

therefore includes sub-displacement-threshold energy transfers in $\nu(E)$. Such collisions have been excluded in the Monte Carlo approach, where T_{min} is fixed at E_d. However, the sub-threshold energy component is comparatively small; Sigmund[30] has estimated the amount of energy, ΔE_s, into sub-threshold collisions for the power cross-section approximation as:

$$\Delta E_s/E = \frac{1}{m} \left(\frac{E_d}{E}\right)^{1-m} \quad . \qquad (3.11)$$

For m = 1/3 and E_d = 25 eV, $\Delta E_s/E$ varies from ~5% to only 1% as E varies from 10 to 100 keV.

(ii) The statistical method assumes the target is infinite with the result that a portion of $\nu(E)$ extends beyond the surface plane. In reality, the energy beyond the surface corresponds to energy into sputtered particles. While this energy is included in the WSS value of $\nu(E)$, such is not the case for the Monte Carlo value. However, for the ion-target combinations considered here, the discrepancy amounts to <1%.

Since the above differences in the definition of $\nu(E)$ are small, the close agreement in the values derived by the statistical and Monte Carlo methods is further verification of the correctness of the latter formulation. We can now examine the influence on $\nu(E)$ of a non-zero U; for the case of $U \neq 0$, $\nu(E)$ may be lowered significantly because of the presence of ΣU in the energy balance Eq. (3.10). It is possible to estimate ΣU; Sigmund[31] has given the total number of atoms that recoil with energy in the interval (E_0, dE_0) in a collision cascade initiated by an atom of energy, E, by:

$$F(E,E_0)dE_0 = \frac{mEdE_0}{(\psi(1) - \psi(1-m))(E_0 + U)^{1-m}E_0^{1+m}}, \quad E >> E_0 >> U, \quad (3.12)$$

where

$$\psi(x) = \frac{d}{dx} \ln\Gamma(x) = \text{digamma function.}$$

$F(E,E_0)dE_0$ is referred to as the recoil density. Eq. (3.12) is the asymptotic solution for the power cross-section approximation. Electronic losses have been neglected.

ΣU becomes:

$$\Sigma U = U\int_{E_d}^{E} F(E,E_o)dE_o = \frac{[(1 + U/E_d)^m - 1]E}{\psi(1) - \psi(1 - m)} \quad , \; U << E_d << E. \qquad (3.13)$$

Although the above solution requires $U << E_d$, we shall examine the solution for $U = E_d$ as has Sigmund.[31] Then, for $m = 0$, $\Sigma U/E = 0.42$, and for $m = 1/3$, $\Sigma U/E = 0.34$. Similarly, from the Monte Carlo approach, $\Sigma U = nE_d$ (for $U = E_d$), where n is the number of displacement collisions. Compared in Fig. 3.5 is the ratio, $\Sigma U/E$, using both the Monte Carlo code and Eq. (3.13). Since the Monte Carlo code uses the power cross-section approximation with $m = 1/3$ at low particle energies, its results should only be compared to those of Eq. (3.13) for $m = 1/3$. In the former method, $\Sigma U/E$ is not a constant, but is dependent on both the ion energy and mass ratio, with ΣU varying from ∿15% of E to more than 45% of E. However, these dependences are found to be incorporated if one considers instead the ratio, $\Sigma U/\nu(E)$, i.e.: $\Sigma U/\nu(E) = 1.30 \pm 0.01$.

It is noted that if ΣU is combined with $\nu(E)$ in the energy balance Eq. (3.10), such that:

$$E_s = \nu(E) + \Sigma U = 2.3\nu(E) \; , \qquad (3.14)$$

the resultant E_s agrees within <10% with the value of $\nu(E)$ obtained when $U = 0$. This observation will prove useful in Chapter VII when it becomes necessary to define the amount of incident ion energy which goes into establishing the final lattice disorder.

3.3.3 The Integral of the Damage Distribution

It was predicted in Sec. 2.2.5 that the integral, N_{kp}, of the damage distribution is proportional to $\nu(E)$ and inversely proportional

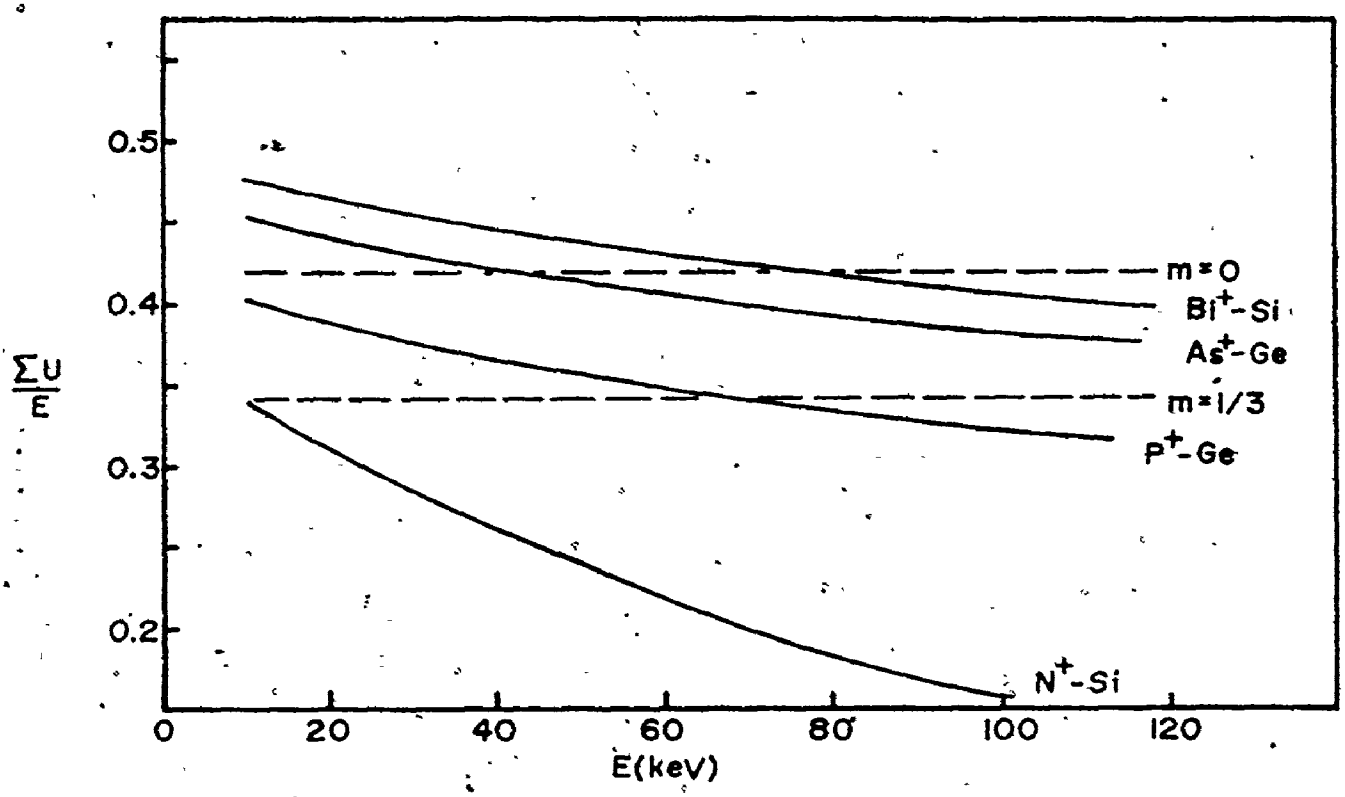

Fig. 3.5: The fraction, $\Sigma U/E$, of energy lost to the lattice during atom displacement. $U = E_d$. Monte Carlo (solid lines). Eq. (3.13) (dashed lines).

to E_d. The proportionality factor, $\xi(m)$, is dependent on the nuclear cross-section appropriate for $E \sim 2E_d$ and can take on values between 0 and 1. In the Monte Carlo formulation, the cross-section at low energies corresponds to the power cross-section approximation with $m = 1/3$. Then $\xi(m = 1/3) \sim 0.7$. The derivation of Eq. (2.33) has allowed for replacement collisions due to its Kinchin-Pease type boundary condition, Eq. (2.31). The identical proportionality factor results from integration of the recoil density, Eq. (3.12), with the assumption that replacement

collisions do not occur, but with a non-zero U ($U = E_d$).

The proportionality of N_{kp} to both $\nu(E)$ and $(2E_d)^{-1}$ has been verified using the Monte Carlo method. For instance, shown in Fig. 3.6 is the ratio, ξ:

$$\xi = N_{kp} \cdot (2E_d)/\nu(E) \quad , \tag{3.15}$$

as a function of E (E_d fixed at 25 eV) for Bi^+-Si and N^+-Si. Four different constant values of ξ are evident, depending on the following conditions:

(1) U = 0, no replacement collisions; $\xi = 1.72$.

(2) U = 0, replacement collisions; $\xi = 1.24$.

(3) $U = E_d$, no replacement collisions; $\xi = 1.20$.

(4) $U = E_d$, replacement collisions; $\xi = 0.97$.

In the last two cases, where $U = E_d$, the value of $\nu(E)$ used in the ratio, Eq. (3.15), corresponds to the value for U = 0, so that $\nu(E)$ is consistent throughout the comparison. For cases (2) and (3), the ratios are almost identical, in agreement with the above observation regarding the proportionality factor of the two asymptotic solutions. However, a large difference is evident in the magnitude of ξ (~45% discrepancy for case (2)). At least two weaknesses in the asymptotic solutions could account for the difference:

(i) The solution, Eq. (2.33), for N_{kp} has employed a Kinchin-Pease type boundary condition, which effectively segments the energy into units of $2E_d$. Since $\xi(m)$ cannot exceed unity, the upper limit on N_{kp} becomes $0.5\ \nu(E)/E_d$. In reality, the segment unit would be an average between E_d and $2E_d$, weighted by the nuclear cross-section. In the power cross-section approximation with m = 1/3, the average becomes $\sim 1.42E_d$, so that

the upper limit on N_{kp} would be $0.70\nu(E)/E_d$. It is seen that for the corresponding case above, case (2), the upper limit is not exceeded.

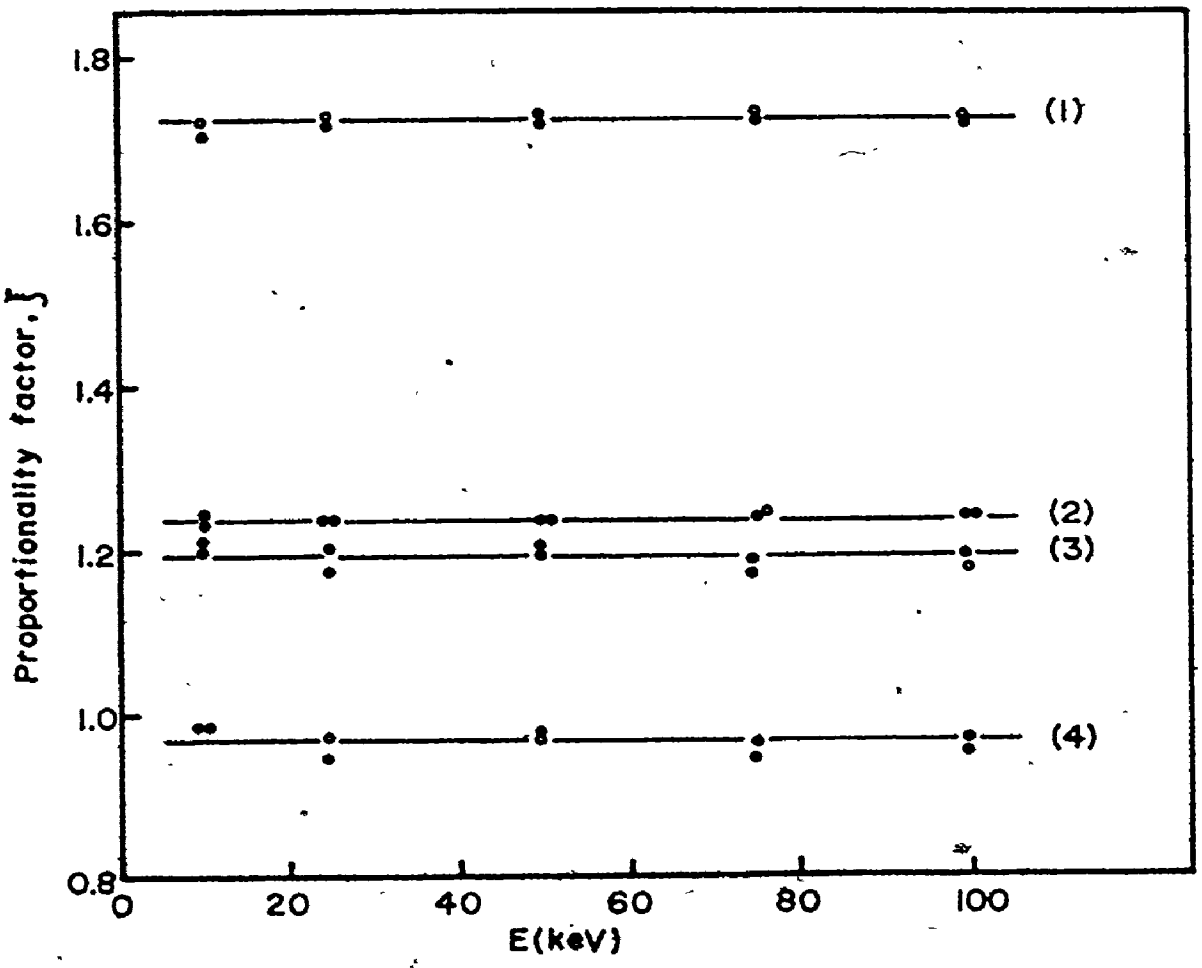

Fig. 3.6: Proportionality factor, ξ, for the four cases listed in the text. Bi^+-Si, solid points. N^+-Si, open points.

(ii) An assumption implicit in the various asymptotic solutions is that $E >> E_d$. Obviously, this condition is invalid for many of the higher generation recoils.

The case considered most valid has $U = E_d$ and replacement colli-

$\xi =$ if Eq. 33) is to

N_{kp}, an error of possibly ~30% may exist.

Sigmund[3] has attempted to account for replacement collisions by defining the probability, $F(E,E_o,E_1)$, of producing a recoil in $E_o + dE_o$ and leaving the scattered particle with $E_1 + dE_1$. For $U = 0$, the asymptotic value in the power cross-section approximation is:

$$F(E,E_o,E_1) = \frac{mE}{[\psi(m) - \psi(1-m)](E_o + E_1)^2 E_o} , \tag{3.16}$$

and the number, N_r, of replacement collisions is:

$$N_r = \int_0^{E_d} dE_1 \int_{E_d}^{E} dE_o F(E,E_o,E_1)$$

$$= \frac{m}{[\psi(m) - \psi(1-m)]} (1 - \ln 2) \frac{E}{E_d} . \tag{3.17}$$

Inelastic scattering has been ignored. The total number, N_t, of collisions can be obtained by integration of the recoil density, Eq. (3.12). With $U = 0$, N_t becomes:

$$N_t = \frac{m}{[\psi(m) - \psi(1-m)]} \frac{E}{E_d} . \tag{3.18}$$

Then the fraction, f_r, of collisions which are replacement collisions is $f_r = \ln 2 = 0.3$. Note that this result is independent of the power cross-section. From the Monte Carlo method, the replacement fraction is found in close agreement with this value; for $U = 0$, $f_r = 0.28 \pm 0.005$. When a finite U is included, the fraction decreases; for $U = E_d$, $f_r = 0.19 \pm 0.005$. A significant portion of the replacement events occur when recoils of energy between E_d and $2E_d$ undergo subsequent collisions; when $U = E_d$,

these recoils are assumed at rest, and can no longer contribute to f_r.

Thus, there appears to be general agreement between the statistical and Monte Carlo descriptions of the collision cascade.. While some deviation is observed in the damage distribution integrals, their parameter dependences are identical. In the next section, we shall use the Monte Carlo code to study the features of the individual ion cascade.

3.4 The Individual Cascade

It was noted in the previous chapter that the statistical deposited energy distribution is the result of summing the energy deposition of an infinite number of individual ions. This was verified in the last section, where the Monte Carlo distribution, averaged over many cascades, was found to reproduce the statistical distribution. However, the spatial dimensions of the statistical cascade may differ by a large amount from the dimensions of each individual cascade. For large M_2/M_1, the trajectory of the ion can undergo large fluctuations, so that the volume containing the damage resulting from many ions with the same entry position may greatly exceed the damage volume for a single ion. As M_2/M_1 decreases, the heavier ion deviates less from its direction at entry into the material, and the statistical volume better describes the individual volume.

Shown in Fig. 3.7 is the qualitative relationship between the statistical and individual volumes as the mass ratio is varied. The isodensity contours have been generated using Eq. (2.29), and have been chosen arbitrarily as the contours at which the statistical energy distributions have fallen to $1/10^{th}$ their maximum value. Superimposed on each contour plot is a representative cascade as generated using the Monte Carlo

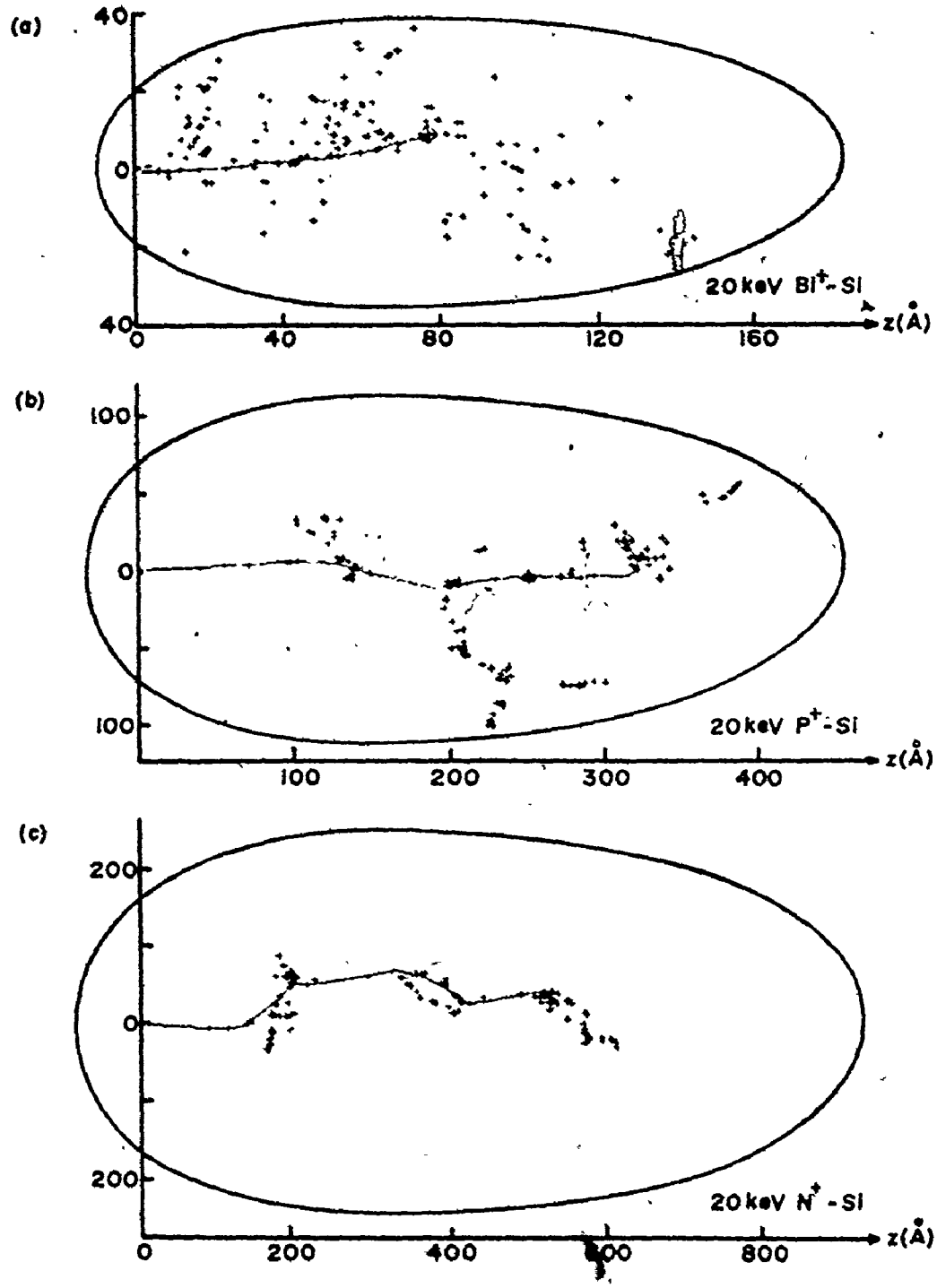

Fig. 3.7: Relationship between individual and statistical cascade dimensions for three ions in Si. $1/10^{th}$ maximum iso-energy-density contours from Eq. (2.29) (solid lines). Displaced atom final location in Monte Carlo cascade (+). The ion trajectory and its final location are indicated for the Monte Carlo cascade. E_d = 25 eV, E_F = 150 eV.

code. Each "+" indicates the final location of a displaced atom. E_f has been set at 150 eV so that plots contain a reasonable number of points. Then each point shows the energy deposition of something less than 150 eV. As one moves up the figure, corresponding to decreasing M_2/M_1, the individual cascade appears to fill a greater portion of the area enclosed by the iso-density contour. As well, sharp changes in the ion trajectory diminish as the probability of wide-angle elastic scattering reduces.

The volume relationship can be developed quantitatively by introducing a definition of the individual cascade dimensions in the following manner. Let (x_i,y_i,z_i) be the coordinates of the particular collision that produces a primary recoil, where z is normal to the target surface. If j displaced atoms result in the collision sub-cascade of the i^{th} primary recoil, and k primary recoils occur in total, the second moments in each dimension can be defined by:

$$\langle x^2 \rangle = \frac{\sum_{i=1}^{k} \sum_{\ell=1}^{j} (x_\ell - x_i)^2}{n} \cdot \frac{z_f}{(x_f^2 + z_f^2)^{1/2}} , \tag{3.19}$$

$$\langle y^2 \rangle = \frac{\sum_{i=1}^{k} \sum_{\ell=1}^{j} (y_\ell - y_i)^2}{n} \cdot \frac{y_f}{(y_f^2 + z_f^2)^{1/2}} , \tag{3.20}$$

$$\langle \Delta z^2 \rangle = \frac{\sum_{i=1}^{n} z_i^2 - (\sum_{i=1}^{n} z_i)^2/n}{n} \cdot \frac{(x_f^2 + y_f^2 + z_f^2)^{1/2}}{z_f} , \tag{3.21}$$

where n is the total number of displaced atoms in the cascade, and (x_f,y_f,z_f) are the coordinates of the final location of the incident

particle. The terms that contain these coordinates attempt to adjust each moment so that it is defined with respect to the mean direction of ion motion, rather than to the surface normal. The individual volume, V_i, for the i^{th} ion can be represented as a spheroid having axes defined by the above moments, i.e.:

$$V_i = \frac{4\pi}{3} (\langle x^2 \rangle_i \langle y^2 \rangle_i \langle \Delta z^2 \rangle_i)^{1/2} \quad . \tag{3.22}$$

The average individual volume, $V_{i,av}$, after n ions then becomes:

$$V_{i,av} = \sum_{i=1}^{n} V_i/n \quad . \tag{3.23}$$

Likewise, the statistical cascade volume, V_s, can be described as a spheroid having major and minor axes determined by the second moments $\langle \Delta z^2 \rangle$, $\langle x^2 \rangle$ of the statistical distribution resulting from the n cascades, i.e.:

$$V_s = \frac{4\pi}{3} (\langle \Delta z^2 \rangle^{1/2} \langle x^2 \rangle) \quad . \tag{3.24}$$

The volume ratio, $V_R = V_{i,av}/V_s$, defines the fraction of the statistical cascade volume filled on average by an individual cascade. While, the above definitions of volume in terms of the second moments are somewhat arbitrary, the volume ratio will be less sensitive to this choice.

The volume ratio, V_R, has been determined using the Monte Carlo code for various energy ions in both Si and Ge. Some of these data are shown in Fig. 3.8. For 50 cascades, the statistical uncertaintly in V_R $\sim$ 10-20%. V_R is observed to span several orders of magnitude for a factor of 10-20 change in M_2/M_1. For $V_R \gtrsim 0.05$, the volume ratio appears to be independent of energy over the energy interval examined (10-100 keV).

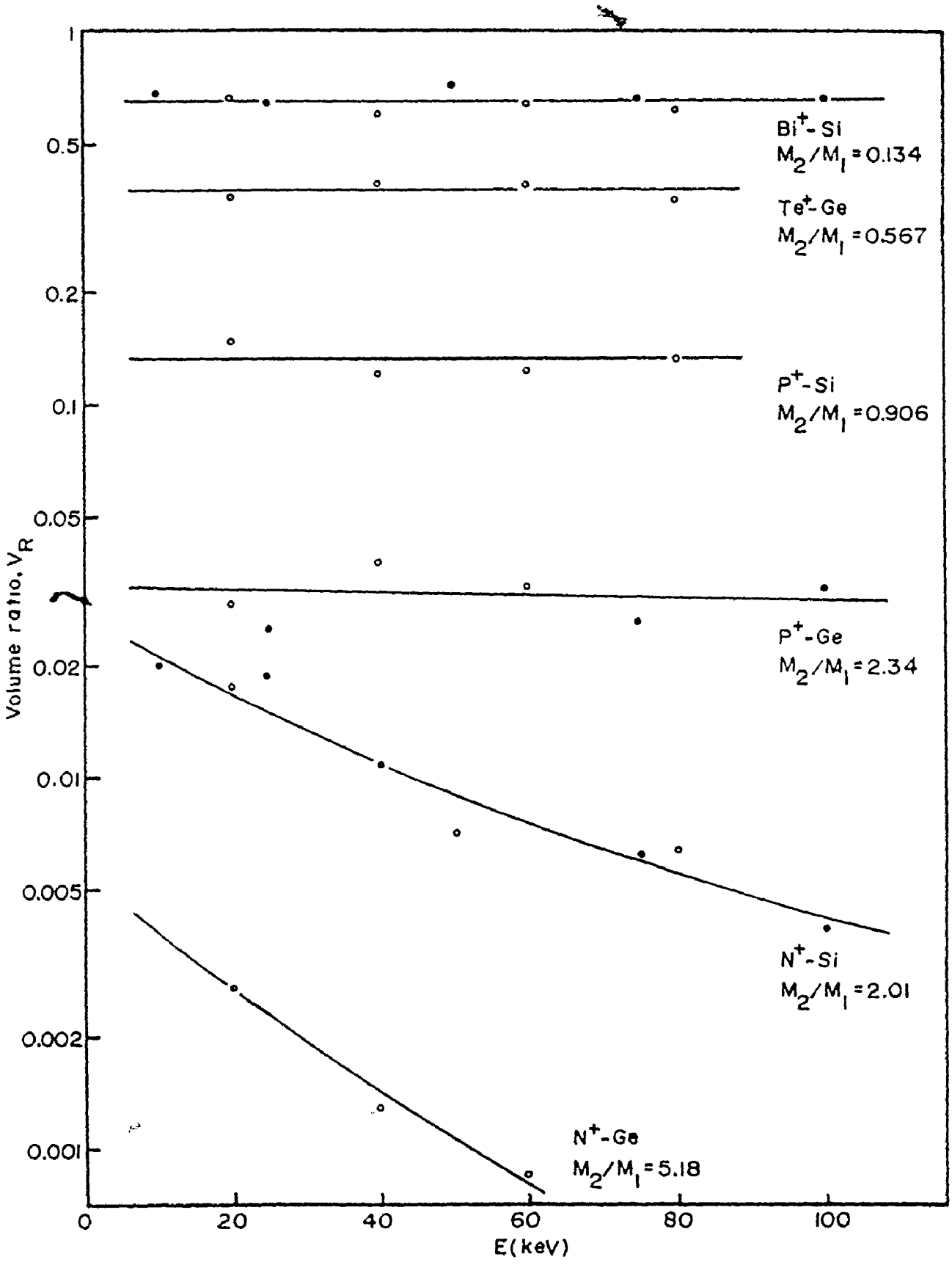

Fig. 3.8: Ratio, V_R, of individual to statistical cascade volume for various ion-target combinations. 50-100 cascades (open points). 20 cascades

However, once V_R drops below $V_R \lesssim 0.05$, an energy dependence becomes evident. For example, for N^+-Si, V_R decreases by a factor of $\sim$5 between 10 and 100 keV.

Figure 3.8 reveals that although V_R decreases in a particular target as M_2/M_1 increases, there is also a dependence on M_2. In particular, V_R for P^+-Ge exceeds that for N^+-Si, even though the mass ratio for the former combination is larger. This dependence is given in Fig. 3.9, where $\delta = V_R^{1/3}$ is plotted versus M_2/M_1. The term, δ, is the average one-dimensional cascade ratio, assuming the effect is identical in the longitudinal and transverse planes. In the calculation of δ using the Monte Carlo values of V_R, the energy dependence of V_R has been ignored. The error bars indicate the standard deviation spread in the data over the energy interval, 10-100 keV. Values for both Si and Ge are given. The dashed line is due to Sigmund et. al.;[25] it was generated using correlation theory and the power cross-section approximation with $m = 1/2$. V_R asymptotes to unity as $M_2/M_1 \to 0$ for both the Monte Carlo and correlation calculations. However, the results of correlation theory are consistently greater than the Monte Carlo results. In fact, correlation theory predicts δ will saturate at $\delta = 0.5$ in the limit of large M_2/M_1. Such behaviour is not apparent with the Monte Carlo method, and values of δ as low as 0.1 are reported. Saturation of δ is considered physically unreasonable; actually, it is expected that the definition of the individual cascade volume given by Eqs. (3.19)-(3.21) will even overestimate V_i at very large M_2/M_1 where subcascades will be formed at mutually large separations. A volume definition which considers separately the individual subcascades would then be more appropriate.

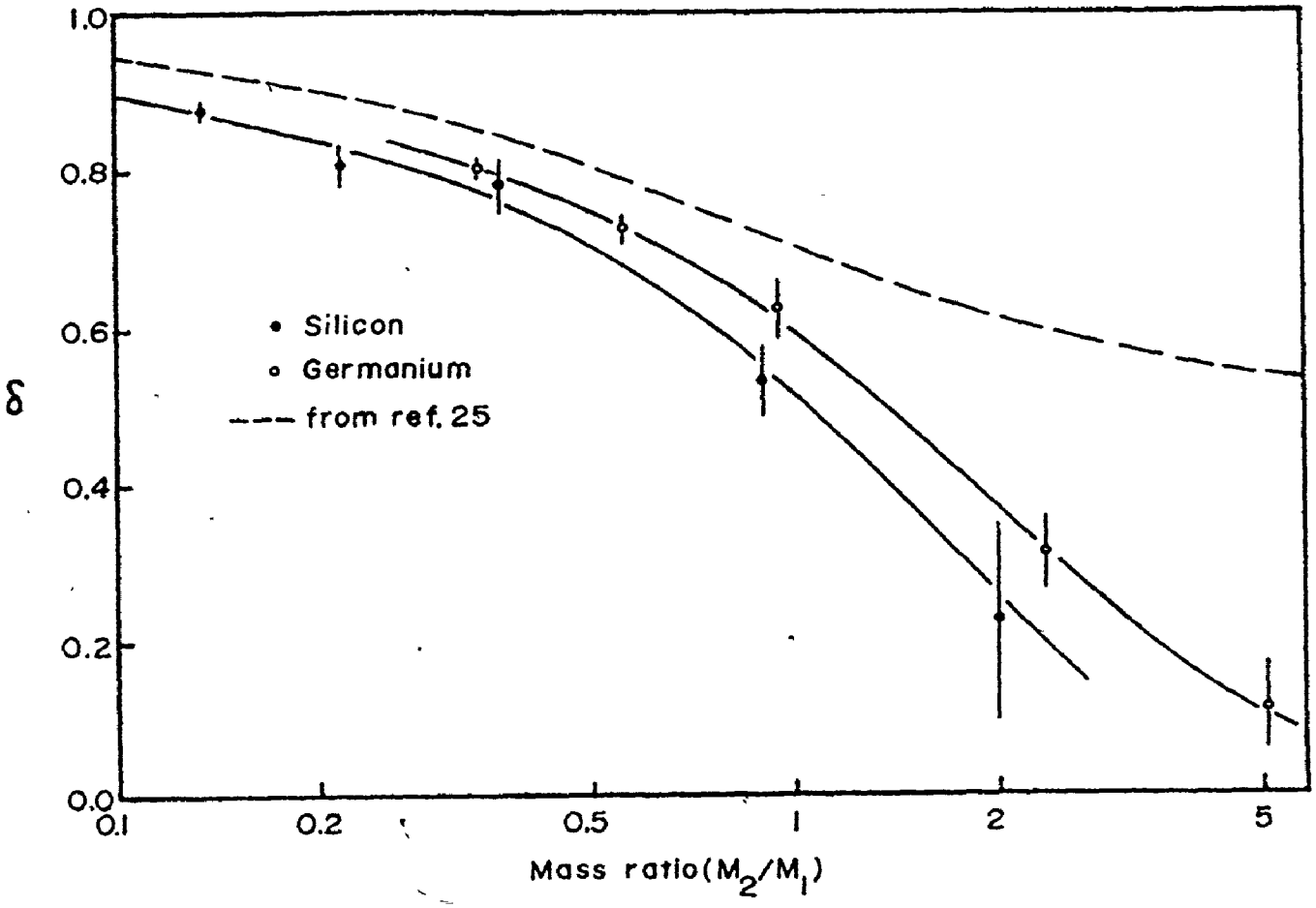

Fig. 3.9: One-dimensional cascade ratio, δ, as a function of mass ratio. Dashed line from ref. 25. Points are Monte Carlo results.

In Fig. 3.9, the Monte Carlo values of δ for Ge lie above those for Si. For constant energy and mass ratio, the movement from Si to Ge corresponds to a decrease in the reduced energy, ε, as defined by Eq. (2.9). Under these conditions, an increase in the nuclear stopping cross-section will occur, and an overall reduction in the cascade dimensions results. Qualitatively, such a reduction could account for the increase in δ. In terms of the power cross-section appr[illegible] a [illegible] in ε

a reduction in m. For Si-Si, m = 1/2 is the appropriate power cross-section approximation over most of the energy interval of Fig. 3.8, while for Ge-Ge, m = 1/3. Sigmund et. al.[25] have calculated that at $M_1 = M_2$, δ will increase by about 0.06 as m decreases from m = 1/2 to m = 1/3. This is of the order of the observed shift in δ between Si and Ge at $M_1 = M_2$.

The above discussion has made it evident that the individual cascade dimensions may vary dramatically from the predictions of the WSS theory. As well, for increasing mass ratio (M_2/M_1) the concept of a homogeneous energy deposition within the cascade volume breaks down as an isolated subcascade structure becomes more prevalent. The consequences of these observations will be presented in Chapter VII, where the significance of the local cascade energy density is discussed.

CHAPTER IV

ANALYSIS TECHNIQUES

4.1 Introduction

Many techniques have been developed to study the defects present in materials that have undergone energetic ion bombardment. For example, electron microscopy, EPR and optical absorption all give direct information on the microscopic defect structure. However, such information is often of a specific nature and methods such as channeling-Rutherford backscattering[73] are required for more quantitative measure of the damage. Since the latter technique tends to relate only the gross average aspects of the damage, it has often proved useful to combine it with complementary methods, such as those listed aboye, to obtain a complete microscopic and macroscopic description. Examples of the use of the more common methods can be found in ref. 74.

With regard to the ion implantation of the semiconductors, we are interested in the quantitative measure of the resultant damage and damage distribution. The analytical tool chosen as most directly giving this information (within the limitations outlined in Sec. 4.3.3) is the channeling-Rutherford backscattering technique. The present chapter contains a discussion of both its application to damage analysis and the procedures necessary to extract meaningful information.

In Sec. 4.2, the basic principles of the channeling of light energetic (MeV) ions in a crystalline material are reviewed. The characteristics of the backscattering of such particles are

the influence of the channeling effect. In Sec. 4.3, the application of the technique to measurement of the total damage and damage profiles in the semiconductors is developed. Various dechanneling models are considered; a semi-empirical approach appears most satisfactory. Finally, the assumptions implicit in the application are critically examined and the limitations noted.

As stated above, the channeling-backscattering technique gives the gross average damage features. Therefore, in Chapters VI and VII, where the results of the damage measurements are presented, the discussion shall be complemented, where possible, by consideration of published electron microscopy measurements of ion implantation damage.

4.2 Channeling-Rutherford Backscattering

4.2.1 Channeling of Light MeV Ions

When a beam of energetic ions is incident on a monocrystalline target, the interaction between the ions and target atoms depends strongly on the relative orientation of the beam and target. Under certain orientations, the repulsive forces between the ion and atom cores can act to gently steer the ion along an oscillatory trajectory through the lattice; this effect is referred to as "channeling". Although the possibility that channeling might exist was pointed out in 1912,[75] it was not until the early 1960's that it was actually verified experimentally.[76,77] Since then, work in the area has progressed rapidly and the channeling effect has been more and more applied to a variety of diverse problems, e.g.: measurements of radiation damage and nuclear lifetimes, and location of impurity in the ive of and

its applications have been recently written by Gemmel[78] and Morgan[79].

The basic principles of the channeling of an ion beam are illustrated in Fig. 4.1, in which is depicted the approach of an ion of incident energy, E, to a lattice row. The perpendicular distance from the ion to the row is r. Provided the angle, ψ, between the beam and crystal row is less than some small critical angle, ψ_c, the increasing electrostatic repulsion between the ion and screened field, U(r), as the ion approaches the row, will cause a smooth deflection of the ion away from the row by a series of correlated small angle scatterings. The transverse energy, $E_\perp$, of the beam will be conserved in the process; therefore, the criterion for channeling may be defined by the energy balance:

$$E_\perp = E\psi^2 \geq U(r_{min}) \quad ,$$

or (4.1)

$$\psi \leq \psi_c = \left(\frac{U(r_{min})}{E}\right)^{1/2} \quad ,$$

where r_{min} is the minimum approach distance.

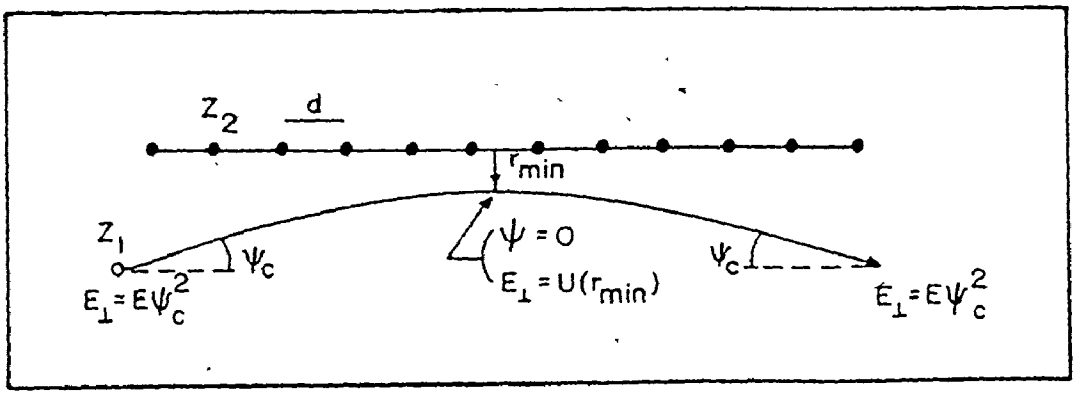

Fig. 4.1: Schematic diagram illustrating how a correlated sequence of collisions with an aligned row of atoms can gently steer (channel) a particle. The transverse energy, $E_\perp$, is conserved

It is convenient to categorize the channeling effect according to the mass and energy of the ion. For relatively slow moving heavy ions (M_1(a.m.u.) $\gtrsim$ 10 and $v \lesssim v_B$, the Bohr velocity) the quantitative prediction of channeling behaviour is nearly impossible because of the strong influence on the channeling of variable external factors, e.g.: radiation damage, surface contamination, etc. (cf. ref. 80). For high velocity light ions, such as MeV He ions or protons, the influence of such external factors is minimal, and a sound theoretical framework exists for describing channeling.[16] It is the latter regime which is of interest in the solid state applications of channeling, and will therefore be considered in the remainder of the section.

Shown in Fig. 4.2a are the three basically different trajectories which an ion can have. For an ion incident at an angle, θ, to the channel direction, the following may occur:

(i) For $\theta < \psi_c$, the ion follows a channeled trajectory, A. Note that the particle is effectively prevented from entering a forbidden cylinder of radius, r_{min}, (typically 0.1-0.2 A) about the lattice row.

(ii) For $\theta >> \psi_c$, the correlated small angle scattering cannot occur, and a trajectory, C, similar to that in an amorphous material, results. For now, we shall refer to such a trajectory as random, although the use of the term in connection with a crystalline material is somewhat vague.

(iii) For θ only slightly greater than ψ_c (trajectory B), the average atom density which the ion sees is actually greater than that for the random trajectory, owing to the increased time spent near the lattice row during the oscillatory motion. The ion is then said to be "quasi-channeled".

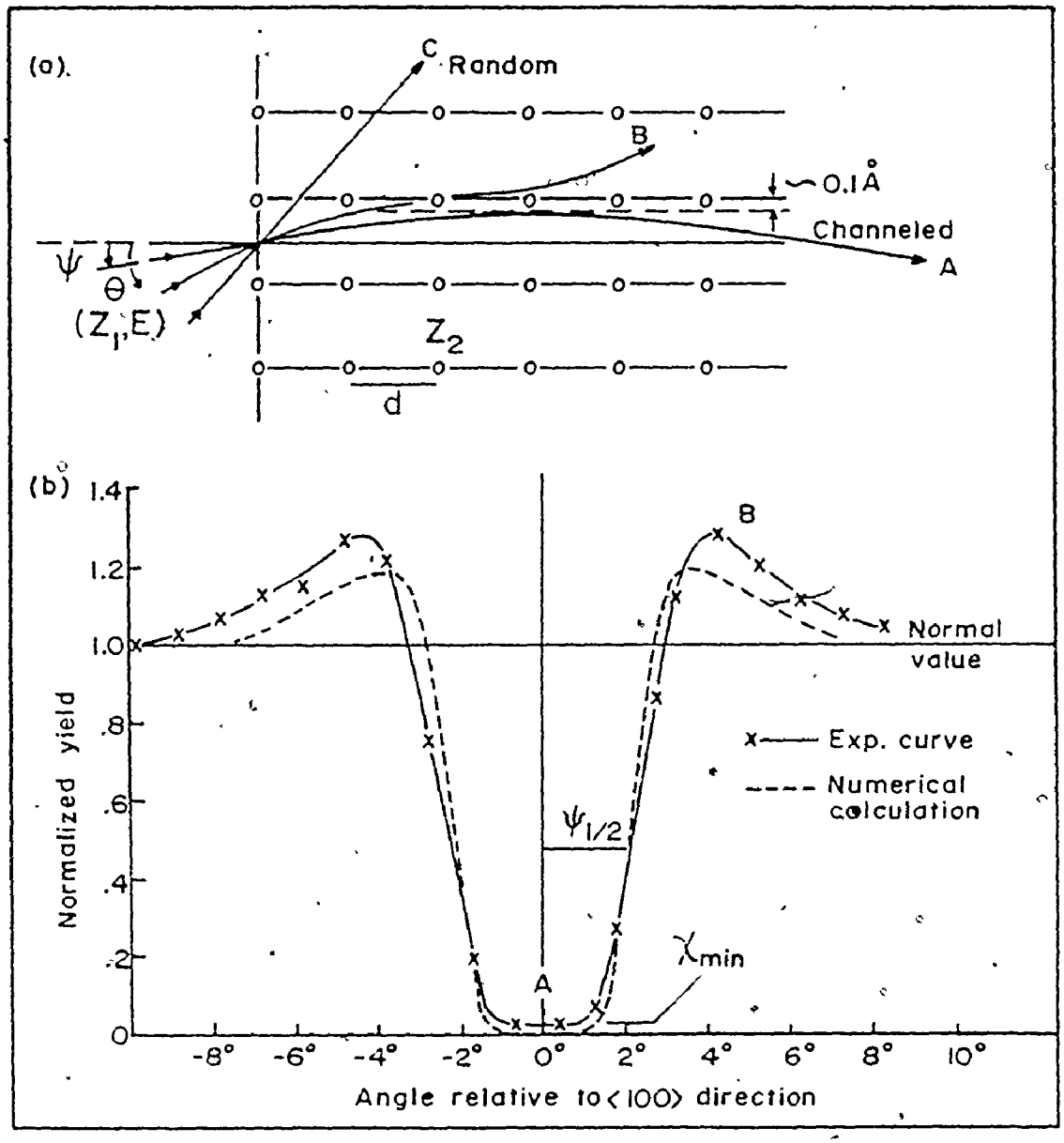

Fig. 4.2: (a) Ion trajectories for three typical values of the angle, θ, between the incident beam and lattice row.

(b) Experimental (x) and calculated (dashed line) angular dependence of the yield of a typical close encounter process (RBS of 480-keV protons in <100> tungsten). From ref. 81.

The description of ion trajectories leads to the angular dependence of any physical process which requires an impact parameter $\leq r_{min}$. Rutherford backscattering, nuclear reactions, inner-shell X-ray production and Coulomb excitation are common examples of such processes. The normalized yields from these events characteristic of the trajectories of Fig. 4.2a are labelled in Fig. 4.2b (from ref. 81). For $\psi = 0$, the yield is not zero but has a minimum yield, χ_{min}. This is mainly due to the small fraction of the incident beam that strikes the crystal within the forbidden area πr_{min}^2, at the end of the row, and enters a random trajectory. For trajectory B, the denser atom array that is experienced by the beam produces a yield greater than that typical of the random path. Included in Fig. 4.2b, is the predicted[16,81] orientation dependence of the yield. Excellent agreement is seen to exist with the measured results.

Both axial and planar channeling are possible. Since axial channeling is of more importance in the application of channeling to the measurement of radiation damage, the parameters basic to it will be considered briefly.

The channeling criterion, Eq. (4.1), requires a knowledge of the interatomic potential, U(r). Lindhard[16] has approximated the Thomas-Fermi potential, Eq. (2.6), by:

$$V(r) = Z_1 Z_2 e^2 \phi(\frac{r}{a})/r$$

$$\approx \frac{Z_1 Z_2 e^2}{r} \ln[(\frac{Ca}{r})^2 + 1] \quad , \qquad (4.2)$$

where the parameter, a, is the Thomas-Fermi screening radius, Eq. (2.10), and $\phi(r/a)$ is the Thomas-Fermi screening function. C is a numerical fitting

constant, $C \approx 3^{1/2}$. In the static-continuum approximation for axial channeling, Lindhard[16] has defined an average row potential, $U_{R.S.}$ (the subscript R.S. indicates row-static) as:

$$U_{R.S.}(r) = \frac{1}{d}\int_{-\infty}^{\infty} V(r^2 + z^2)^{1/2} dz$$

$$\simeq \frac{2Z_1 Z_2 e^2 f_{R.S.}(\frac{r}{a})}{d} \quad , \tag{4.3}$$

where

$$f_{R.S.}(\frac{r}{a}) = \frac{1}{2} \ln[(\frac{Ca}{r})^2 + 1].$$

For the continuum model to be valid, the ion must pass a large number of atoms while undergoing the collision with the atom string. This requirement can be shown to place a limit on the minimum approach distance, i.e.:

$$r_{min} >> \psi d.$$

The equality, $r_{min} = \psi d$ serves as a useful definition of r_{min}, and the channeling criterion, Eq. (4.1) can be obtained. Two approximations of the criterion are commonly made:

(1) For small r/a (high-energy approximation):

$$f_{R.S.}(r/a) \simeq \ln(\frac{Ca}{r}) \quad .$$

Eq. (4.1) becomes, with $r_{min} = \psi d$:

$$\psi \leq \psi_1 = (\frac{2Z_1 Z_2 e^2}{Ed})^{1/2} \quad , \tag{4.4}$$

provided $\psi_1 \leq a/d$.

(2) For large r/a (low-energy approximation):

$$f_{R.S.}(r/a) \simeq \frac{1}{2}(\frac{Ca}{r})^2 \quad ,$$

and the criterion is:

$$\psi \leq \left(\frac{\psi_1 Ca}{2^{1/2} d}\right)^{1/2} , \tag{4.5}$$

provided $\psi_1 > a/d$. The energy, E_ψ, at which $\psi_1 = a/d$ is:

$$E_\psi = 2Z_1 Z_2 e^2 d/a^2 . \tag{4.6}$$

For He^+ on Si<110>, $E_\psi \sim 0.1$ MeV. In the application of channeling to damage measurement, $E >> 0.1$ MeV; therefore, the high-energy approximation of the channeling criterion is most appropriate here.

Since lattice vibration times are typically three orders of magnitude longer than the ion deflection time, the assumption of a static atom row is valid. However, if the thermal vibration amplitude, u_1, is $\gtrsim a$, the vibrations will likely perturb significantly the channeled trajectory. Barrett[82] has found that $\psi_{1/2}$ (see Fig. 4.2b) can be reasonably described by:

$$\psi_{1/2} = k\left(f_{R.S.}\left(\frac{mu_1}{a}\right)\right)^{1/2}\psi_1 . \tag{4.7}$$

Values of $k = 0.83$ and $m = 1.2$ have given best fits of Eq. (4.7) to his Monte Carlo simulation results. In actual experiments, $\psi_{1/2}$ is more easily obtained than the critical angle, ψ_c, defined earlier. Lindhard[16] has suggested that:

$$\psi_{1/2} = \alpha_R \psi_1 , \tag{4.8}$$

with α_R taking on values between 1 and 2.

From a simple geometrical consideration, the minimum yield, χ_{min}, for axial channeling may be approximated by:

$$\chi_{min} = Nd\pi(a^2 + u_2^2) \quad . \tag{4.9}$$

N is the target atom density and u_2 is the two-dimensional thermal vibrational amplitude, $u_2^2 = 2u_1^2$. Eq. (4.9) has been found to fit a wide range of experimental χ_{min}'s if modified to the following form:[82]

$$\chi_{min} = Nd\pi(C_1a^2 + C_2u_2^2) \quad , \tag{4.10}$$

where $C_1 = 0.5$ and $C_2 \approx 3$. Typical values of axial χ_{min}'s are 0.01-0.03.

In practice, additional factors such as surface contamination, lattice strain, non-zero beam divergence, etc. will increase the experimental χ_{min}. Therefore, a direct measure of χ_{min} gives information on the crystal perfection, surface preparation, etc.

4.2.2 Rutherford Backscattering

For an ion-target system having $t \gtrsim 100$, where $t = \epsilon^2 T/T_m$, (ϵ is Lindhard's reduced energy as defined by Eq. (2.9)) the appropriate differential cross-section, $d\sigma/d\omega$, is that given by Rutherford (see Fig. 2.2), i.e.:

$$d\sigma/d\omega = (Z_1Z_2e^2/4E)^2(1 + \gamma^2)\sin^3\theta/\sin^3\phi/(\gamma\cos\phi + 1)/\sin^4\theta/2. \tag{4.11}$$

θ and ϕ are the scattering angles in the center-of-mass and laboratory systems respectively, E is the ion energy and $\gamma = T_m/E$ which is the maximum fractional energy transfer. For wide angle scattering, such that $t \sim \epsilon^2$, $t \gtrsim 100$ for He^+-Si when $E \gtrsim 27$ keV, while for H^+-Si when $E \gtrsim 12$ keV. Its small impact parameter ($\lesssim 10^{-3}$A) and large cross-section therefore make Rutherford backscattering an ideal tool for channeling studies using MeV light ions.[78,79]

Figure 4.3 illustrates the fundamental features of an experimental arrangement for investigating the yield of backscattered particles in crystalline materials: 1) collimation apertures to reduce the beam divergence to $\lesssim 0.1°$, 2) a double-axis goniometer for crystal orientation with respect to the beam direction, and 3) a suitable detector of the backscattered particles. For MeV light ion scattering, a surface-barrier solid state detector is most often used. Wide-angle backscattering ($\phi \to 180°$) is commonly employed because of the relative constancy of the cross-section for large ϕ, and of the comparative ease of implementation.

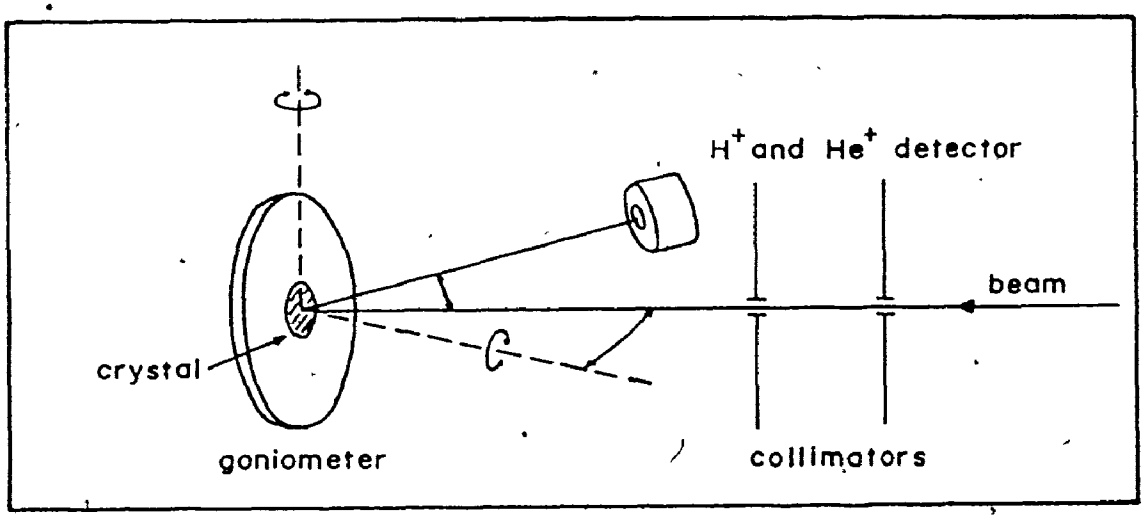

Fig. 4.3: Schematic diagram of the experimental assembly for a channeling-backscattering experiment.

Figure 4.4a shows the energy spectrum of backscattered He for 1 MeV He^+ on Si, for particles following a random trajectory (curve labelled "random"). Its characteristics can be explained with reference to Fig. 4.5. When a particle of energy, E_0, strikes the target surface, it may

backscatter with energy, E_1, through angle, ϕ, to the detector. Since the collision is elastic, energy and momentum are conserved and $E_1 = k^2 E_o$. k is the kinematic factor:

$$k = M_1\cos\phi/(M_1 + M_2) + \{[(M_1\cos\phi/(M_1 + M_2)]^2 + (M_2 - M_1)/(M_1 + M_2)\}^{1/2} , \quad (4.12)$$

For He^+-Si and $\phi = 150°$, k = 0.585.

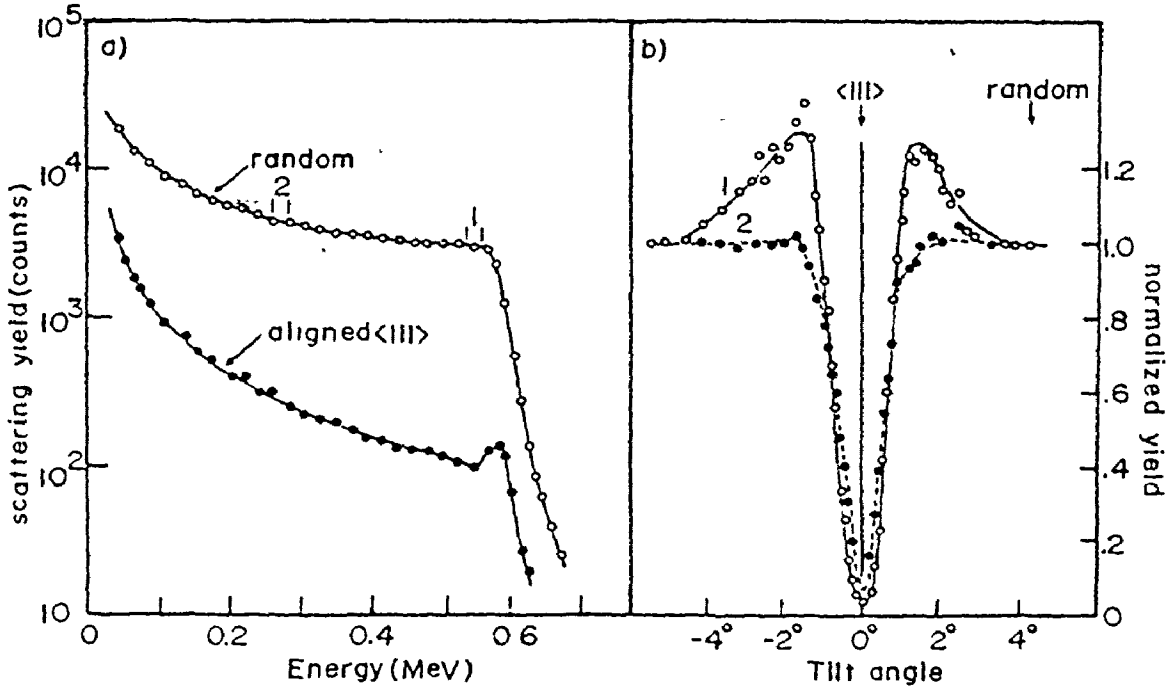

Fig. 4.4: (a) Backscattered energy spectra for 1.0 MeV He^+ incident Si for aligned <111> and non-aligned (random) direction of incidence. (b) Orientation dependence of the normalized yield obtained for energy regions 1 and 2 in (a), i.e.: from depths of 0.1 and 0.6 μm respectively.

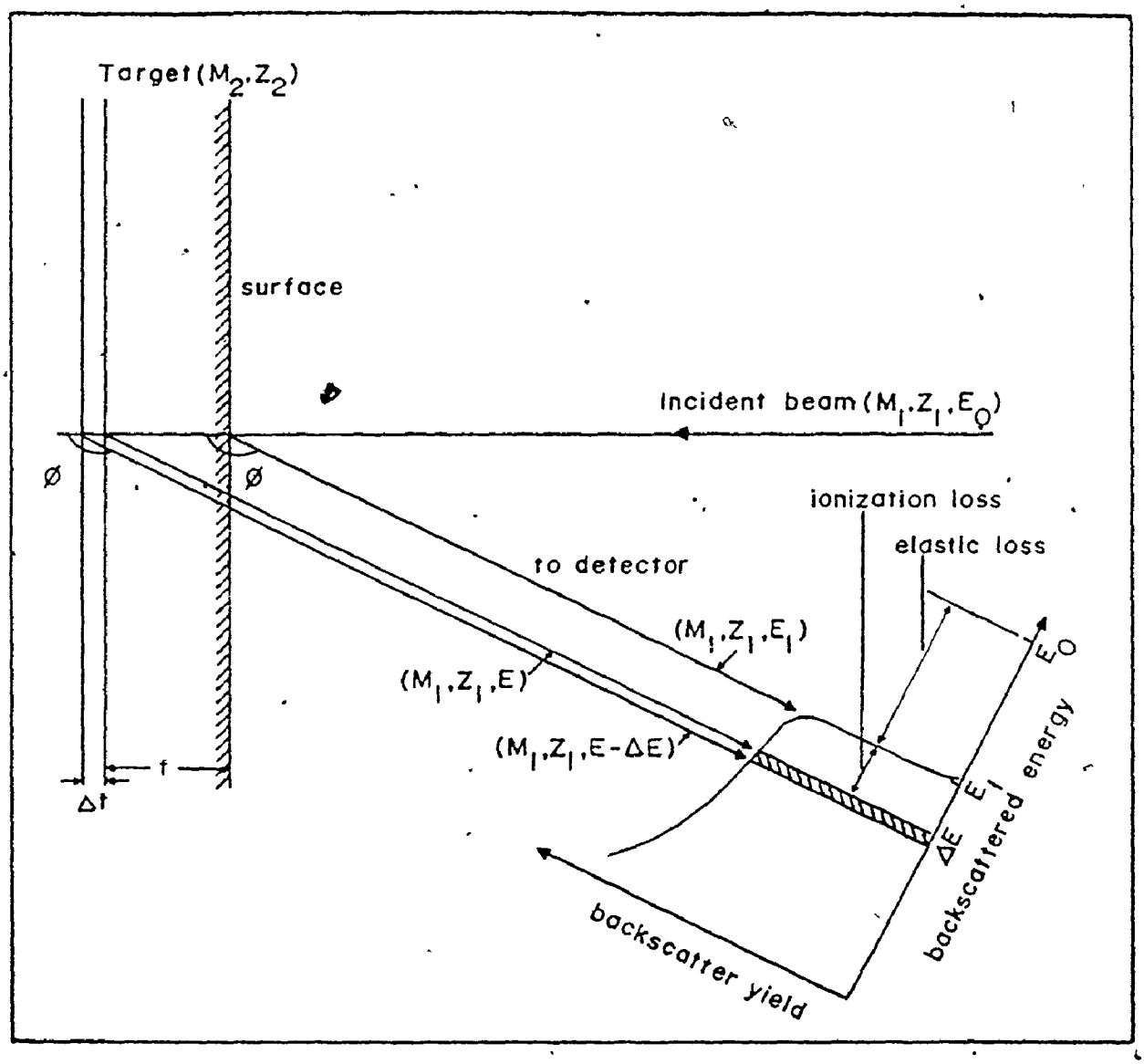

Fig. 4.5: Principles of elastic scattering experiments.

When a particle penetrates the surface and subsequently backscatters at depth, t, it will lose energy to ionization and excitation of the target atoms before and after scattering. If S(E) is the electronic stopping power, a continuous spectrum of backscattered particles will result for $E < E_1$, where:

$$E(t) = k^2(E_o - \int_o^t S(E)dt) - \int_{t/\cos\phi}^{o} S(E)dt \quad . \qquad (4.13)$$

For energies and depths typically involved in backscatter experiments ($E \gtrsim$ MeV, $t \lesssim$ 1-10 μm), S(E) is relatively constant, and Eq. (4.13) can be adequately approximated by:

$$E(t) = k^2E_o - t(S(E_o)k^2 + S(E_1)/\cos\phi) \quad . \qquad (4.14)$$

The energy scale of Fig. 4.4a then converts to a depth scale such that one energy channel, ΔE, becomes a depth increment, Δt:

$$\Delta t = \Delta E/(S(E_o)k^2 + S(E_1)/\cos\phi) = \Delta E/S_{AV} \quad . \qquad (4.15)$$

The random spectrum exhibits an increasing yield for decreasing energy, reflecting the E^{-2} dependence of the cross-section of Eq. (4.11). The spectrum can be normalized to the yield at the surface (at $E = E_1$), i.e.: the yield, y(i), in the i^{th} energy channel is related to the yield, y'(i), before normalization by:

$$y(i)/y'(i) = (1 - (1 - E/E_1)/(1 + S(E_1)/(k^2S(E_o)\cos\phi))^2. \qquad (4.16)$$

The resolution, ΔE_d, of the detection system is revealed in the finite slope of the surface edge in the spectrum at $E = E_1$. For a surface barrier detector $\Delta E_d \sim$ 15 keV (FWHM). This will translate to a depth resolution through Eq. (4.15). For 1 MeV He^+-Si and $\phi = 150°$, $\Delta t \sim 250$Å. Energy straggling due to multiple scattering is generally not important; Matsumura and Furukawa[83] have given the energy straggling, ΔE_s, for He-Si by the empirical relationship, $\Delta E_s(\text{keV}) \sim t(\text{Å})^{1/2}/11$. At t = 1000Å, $\Delta E_s \sim 3$ keV $\ll \Delta E_d$.

Figure 4.4a considers backscattering from a monatomic target. For

a binary target having elements M_{21} and M_{22}, where the mass difference is such that $(k^2_{M_{21}} - k^2_{M_{22}})E_o >> \Delta E_d$, the spectrum will have steps at $k^2_{M_{21}}E_o$ and $k^2_{M_{22}}E_o$. The relative yields from the components is roughly proportional to Z^2, as seen in Eq. (4.11).

Shown also in Fig. 4.4a is the backscatter yield when the beam is incident along a low-index crystallographic axis - in this case the <111>. The strong influence of channeling on the backscatter yield is evident. The small peak on the high energy edge of the aligned spectrum is due to backscattering both from disordered silicon in the surface oxide and from the first atom of every lattice row. The spectrum yield is a direct measure of the random component of the beam. At the surface, the yield, normalized to that of the random spectrum, is given by Eq. (4.10). For increasing depths, the interaction of the channeled component with lattice vibrations, electrons, etc. will cause some portion of the component to scatter or dechannel into the random fraction, such that the normalized yield increases. Fig. 4.4b compares the orientation dependence of the normalized yield at the surface and at ~0.6 μm. The increase in χ_{min} due to dechanneling is apparent. Also, the shoulder region resulting from quasi-channeled trajectories has disappeared in the deeper angular scan.

While a particle in a channeled trajectory experiences a lower atom density than in a random trajectory, it likewise sees a reduced electron density. In such a case, $S(E_o)$ of Eq. (3.16) becomes that for the channeled particle (typically 0.5 → 0.9 of the random value),[84] and an uncertainty is introduced in the depth scale for the aligned spectrum. In many instances, the uncertainty ≲10% if the random value is used. This shall be discussed later with regard to application of channeling to damage

profiling.

Since the backscatter yield is so strongly dependent on the relative orientation of the beam and target, the measure and definition of a "random" spectrum in a single crystal requires consideration. A technique[85] which has been found to give spectra reproducible to ≤2% is to rotate the crystal in the azimuthal plane while at a tilt angle ~$10\times\psi_{1/2}$ relative to the major crystal axis. Provided the rotation period << the spectrum acquisition time, the speed of rotation is not important (we have used ~5°/sec). As long as the detector lies in the tilt-beam plane, no correction for target geometry is necessary when comparing spectra. From now on, spectra acquired in this manner will be referred to as being "non-aligned", rather than random. This avoids the confusion in the definition of a random trajectory in a crystal, as well as emphasizing the averaging effect of the rotation technique.

4.3 Damage Analysis by Channeling-Rutherford Backscattering

4.3.1 The Approach

As an energetic ion comes to rest in a crystal, a cascade of displaced atoms will be created along its path, both by direct collision with the ion or collision with recoiling atoms. For the ion-solid systems typical to the ion-implantation process, this damage layer will extend over ≤ a few thousand angstroms, i.e.: much less than the several μm ranges of MeV He ions or protons. When the latter are subsequently channeled along a major crystal axis of the target, they will backscatter normally from the displaced atoms that lie in the channel, while back-scatter from lattice atoms is suppressed in the manner characteristic of

the channeling effect. Therefore, the channeling-backscattering technique is a powerful analytical method of investigating both the damage and damage distribution in ion implanted crystals.

Figure 4.6 shows the backscatter spectra taken at 50K, both aligned and non-aligned, for an unirradiated Si sample, as well as the spectrum after 40 keV N^+ irradiation. The peak in the latter spectrum relates to the enhanced backscattering of the channeled ions from the displaced atoms in the implanted layer. For both aligned spectra the small surface peak, mainly due to the surface oxide (see Fig. 4.4a), has been subtracted. Also, the spectra have been normalized to the backscatter yield at the surface by correcting the yields for the energy dependence of the Rutherford cross-section via Eq. (4.16). Stopping powers have been taken from the semi-empirical values tabulated by Zeigler and Chu.[86] As has been recently suggested,[84b] the random stopping powers, S_R, have been used for the aligned spectra. It was noted earlier that the aligned stopping powers, S_A, in undamaged crystals are somewhat lower than the non-aligned values. For instance, for 1 MeV He^+ in Si,[84] $S_A\langle 111\rangle/S_R \sim 0.8$ and $S_A\langle 110\rangle/S_R \sim 0.6$. The choice of the appropriate S(E) for a given channeled particle will depend strongly upon both the electron and ion flux distributions across the channel. In the case of a well ordered crystal, the channeled particle flux has been shown to be peaked towards the region of lowest interatomic potential.[87] Since this region also contains a lower electron density, there results an "on-average" S_A lower than S_R. However, the presence of defects in the channel will increase the mean transverse energy of the beam and quickly smear any flux peaking. Therefore, as defects are introduced, S_A will rapidly approach S_R.

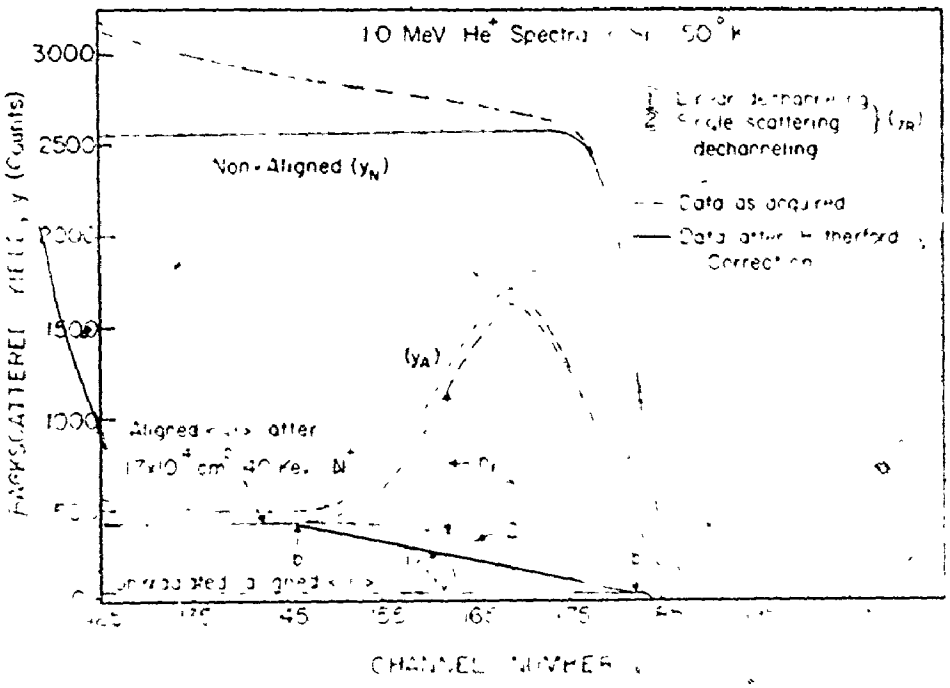

Fig. 4.6: Backscatter spectra for 1.0 MeV He^+ incident on Si at 50K for non-aligned and aligned <111> analyzing beam before and after irradiation with 40 keV N^+.

The analytical procedure by which the backscatter peak is related to the damage is described with reference to Fig. 4.6. The basic assumption is that at some depth, t, below the crystal surface the incident aligned beam consists of an aligned (or channeled) component and a random (or dechanneled) component.[88] In any energy channel, i, the backscatter yield, $y_A(i)$, in the aligned spectrum after irradiation is then composed

of two separate contributions:

(a) The yield, n_i, of particles in the aligned component that directly backscatter from the displaced atoms, N'(i), that are located in the target layer corresponding to the i^{th} energy channel.

(b) The yield, $y_R(i)$, of particles in the random component that backscatter normally from all target atoms.

While transitions from the random component to the aligned component are considered negligible, the reverse may occur because of scattering from displaced atoms, electrons, the surface layer, surface oxide and lattice vibrations. The latter transition is referred to as dechanneling. In implanted targets, dechanneling via scattering from the lattice disorder usually dominates the dechanneling mechanisms.

The difference in energy between the random and aligned components of the beam at depth, t, caused by different stopping powers, is assumed negligible as far as ion-atom scattering is concerned, i.e.: the scattering cross-section for the aligned component at depth, t, is the same as for the random component. For the time being, the radial distributions of displaced atoms and of the channeled beam will be assumed constant across the channel. The consequences of relaxing this assumption will be examined in Sec. 4.3.3.

For the above conditions, the aligned yield in the i^{th} channel is:

$$y_A(i) = y_R(i) + n_i = y_R(i) + (y_N(i) - y_R(i))N'(i)/N(i) , \qquad (4.17)$$

where $y_N(i)$ is the non-aligned yield and N(i) the atom areal density in the target layer corresponding to the i^{th} channel. Then:

$$N'(i)/N(i) = (y_A(i) - y_R(i))/(y_N(i) - y_R(i)) \qquad (4.18)$$

$$= (y_A(i)/y_N(i) - \chi'(i))/(1 - \chi'(i)) \quad , \qquad (4.19)$$

where $\chi'(i) = y_R(i)/y_N(i)$ and is the random or dechanneled fraction of the beam. The total number of displaced atoms, N_D, per unit bombardment area becomes:

$$N_D = \sum_{k=b'}^{b} N'(k)\Delta t(k)$$

$$= \sum_{k=b'}^{b} N(k)\Delta t(k)(y_A(k) - y_R(k))/(y_N(k) - y_R(k))$$

$$= N\Delta E/S_{AV} \sum_{k=b}^{b} (y_A(k) - y_R(k))/(y_N(k) - y_R(k))\cos(\phi_A - \phi_i), \quad (4.20)$$

where b is the surface channel, and b' the channel where the damage ends. ϕ_A is the aligned tilt angle and ϕ_i the tilt during implant. $\cos(\phi_A - \phi_i)$ therefore corrects the depth scale so that it is parallel to the implant direction. Δt is the target thickness corresponding to the channel energy width ΔE. The stopping power has been assumed constant such that Eq. (4.15) is valid and $\Delta t \propto \Delta E$. In this case, application of the Rutherford correction to the non-aligned spectra should give a constant yield. This is found to be the case over a wide energy range (see Fig. 4.6). Therefore, the Rutherford correction is useful since:

(i) it provides a check on the knowledge of both the beam energy and stopping powers as well as checking the validity of using a constant S(E) in the depth scale conversion;

(ii) it simplifies Eq. (4.21) by replacing $y_N(k)$ with a

constant; this also avoids problems in the summation near b, where the non-aligned yield is particularly strongly smeared due to the finite detector resolution.

4.3.2 Dechanneling

From Eq. (4.19) it is evident that the quantitative analysis of the backscatter yield requires a knowledge of the dechanneled fraction, $\chi'(i)$, of the aligned beam. In radiation damage measurements, the dechanneling is often dominated by scattering from the lattice disorder; evaluation of this component has most often been approached[89-92] by application of realistic scattering models[16,93,94] developed to describe the scattering of energetic particles in amorphous materials. Whatever the dechanneling model, three basic boundary conditions should be satisfied:

(i) Beyond the damage layer, the damage should return to zero, i.e.: $y_R(b') = y_A(b')$.

(ii) The dechanneling line should merge continuously with the dechanneling beyond the damage layer. This is valid whenever a smoothly varying damage distribution exists.

(iii) The dechanneling at the surface should be the same as in the unirradiated crystal.

The success of the various amorphous scattering models at satisfying these boundary conditions has been very limited. One reason for this is that the channeled beam is sensitive to the lattice distortion that accompanies the ion-induced damage. Thus, an additional dechanneling component may be present due to correlated scattering from the lattice

strains. Secondly, if defect annealing can occur, the defects may arrange into more complex defect structures, e.g.: dislocation loops, stacking faults, etc. Such complexes have been shown to exhibit specific dechanneling behaviour[95] that is characteristic to the particular complex. Obviously, the amorphous scattering models cannot, and should not, be expected to account for such dechanneling processes that are peculiar to channeling alone. The greatest success of the amorphous models at describing dechanneling has been in the analysis of low temperature high-disorder irradiations,[91] where the conditions under which the models were developed are best approximated.

Since the majority of the work of the thesis has dealt with "in-situ" damage measurements at $\lesssim$50K, complications in the dechanneling calculation due to defect annealing should be minimal. The strain contribution to the dechanneling can be present; however, its direct calculation can often be avoided by noting:

(i) As shown in Fig. 4.6, the contribution of the dechanneled fraction of the beam to the total peak area often comprises $\lesssim$20%.

(ii) N_D is not a strong function of $\chi'(i)$, since it appears in both the numerator and denominator of Eq. (4.19).

Then, if the dechanneling line is arbitrarily forced to meet the boundary conditions, the above arguments indicate that the extracted disorder profile should become relatively insensitive to the shape of the line that is determined by the particular scattering model used. This semi-empirical approach to the dechanneling correction has been used in the analysis of

all the data of the thesis. However, two different methods of applying the dechanneling have been chosen, depending on the ion-target system being studied. When the depth resolution, Δt_d, is a sufficiently small fraction of the total damage depth, R_d, the damage is well enough resolved that a channel-by-channel approach to the analysis can be made (and a damage profile extracted). When Δt_d is large compared to R_d, the profile shape is sufficiently smeared such that a profile extraction cannot be attempted. Unfolding the detector resolution function from the spectra by a deconvolution procedure (cf. ref. 96) would theoretically remove this limitation. In practice it has been found that the uncertainty in knowledge of this function, inadequate statistics, and insufficient conversion gain rule out the unfolding technique. The delineation between the two methods occurs roughly at $R_d \sim 5\Delta t_d$.

(i) $\underline{R_d \lesssim 5\Delta t_d}$

For shallow damage layers, where the resolution controls the shape of the peak, the use of the second boundary condition becomes impractical. Therefore, the first and third conditions are most easily satisfied by a linear dechanneling correction. Fig. 4.7 shows the linear dechanneling line on an aligned spectrum following 45 keV Te^+ irradiation of Si at 35K. In such a case, the dechanneling correction becomes:

$$\sum_{k=b'}^{b} y_R(k) = \frac{n}{2}\left(y_A(b') - y_V(b)\right) \quad , \tag{4.22}$$

where $y_V(b)$ is the surface yield from the unirradiated sample, neglecting the surface peak, and $n = b - b'$. Then N_D is given by:

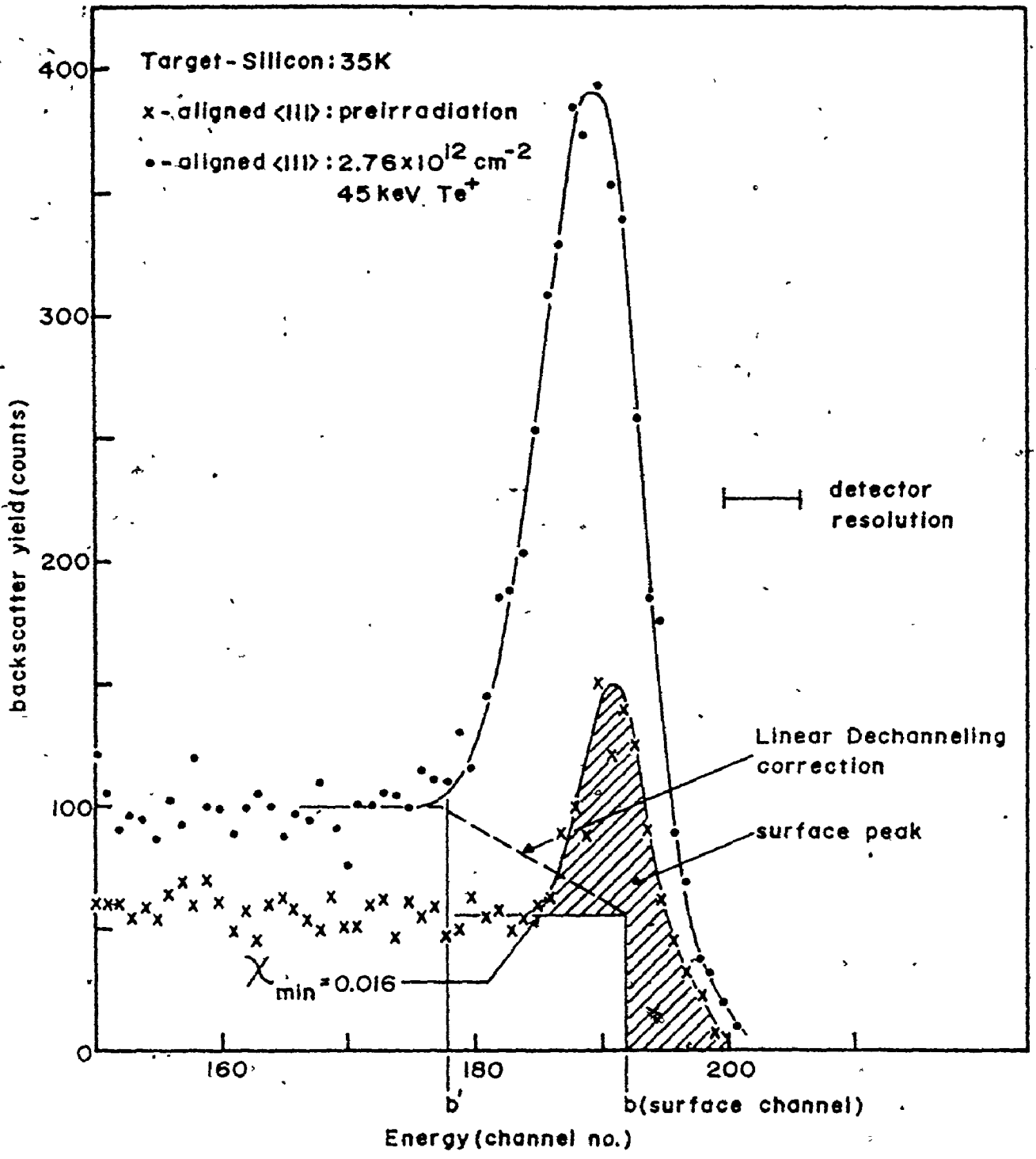

Fig. 4.7: Backscatter spectra for 1.0 MeV He^+ incident on a Si single crystal at 35K for aligned <111> analyzing beam before and after irradiation with 45 keV Te^+.

$$N_D = \sum_{k=b'}^{b} N''(k)\Delta t(k)$$

$$= \frac{N\Delta E/S_{AV}\left(\sum^{n'} y_A(k) - n/2(y_A(b') - y_V(b)) - \Sigma y_S\right)\cos(\phi_A - \phi_i)}{y_N - 1/2(y_A(b') - y_V(b))} \quad (4.23)$$

Σy_S is the yield due to the surface peak (shaded area in Fig. 4.7). The summation must extend over n' channels ($n' > n$) to account for the finite resolution.

The maximum error in N_D due to the use of a linear dechanneling correction in Eq. (4.23) is estimated at <5%.

(ii) $\underline{R_d > 5\Delta t_d}$

The effect of the resolution on the analysis shall be ignored for now.

The first boundary condition can be met by scaling the calculated dechanneling line such that $y_R(b') = y_A(b')$.[36] However, depending on the scaling technique and amount of scaling required, the other conditions may not be met. The following scaling[97,37] method has been found to satisfy all three conditions.

Dechanneling by the defects is assumed to occur by single scattering deflections greater than some critical angle for channeling. The only assumption made of the scattering probability is that it is a constant over the implant layer, i.e.: the number of channeled particles, n_i, that backscatter from displaced atoms in the i^{th} channel has a constant proportionality to the number dechanneled by these displaced atoms. The yield from dechanneled particles becomes:

$$y_R(i) = \sum_{k=i+1}^{b} Cn_k + \frac{1}{2} n_i C + y_V(i) \quad , \quad (4.24)$$

where C is the constant of proportionality.

The term $\frac{1}{2} n_i C$ attempts to keep the dechanneling in step with the displaced atoms causing the scattering by compensating for the additional dechanneling from defects in the i^{th} channel. $y_V(i)$ accounts for dechanneling due to scattering from lattice vibrations, electrons, and surface disorder. Then n_i is given by:

$$n_i = y_A(i) - y_R(i)$$

$$= (y_A(i) - \sum_{k=i+1}^{b} Cn_k - y_V(i))/(1 + C/2) \quad . \tag{4.25}$$

Beyond the damage peak, $n_i(i \geq b') = 0$. The first boundary condition will be satisfied provided:

$$C = (y_A(b') - y_V(b')/\sum_{k=b'}^{b} n_k \quad . \tag{4.26}$$

The procedure requires making a first estimation of C by using a linear dechanneling correction to estimate $\sum_{k=b'}^{b} n_k$ in Eq. (4.26). This value is applied to Eq. (4.25) and a new value for C again determined by Eq. (4.26). The procedure is repeated until C converges to some arbitrary limit; three or four iterations are adequate. Once C has been obtained, application of Eq. (4.21) will give the damage profile.

The dechanneling line calculated by the semi-empirical procedure is shown in Fig. 4.6 (curve labelled "single-scattering dechanneling"). All the boundary conditions are met. The linear dechanneling line has been included for comparison. The extracted profiles using both dechanneling methods are shown in Fig. 4.8. The differences in profile shapes are small and the total damage differs by ~5%. The influence of the analyzing beam energy on the profiles extracted by this method is demonstrated in Fig. 4.9

where a 60 keV N^+ irradiation of Si has been analyzed using 1-2 MeV He. The profiles agree satisfactorily.

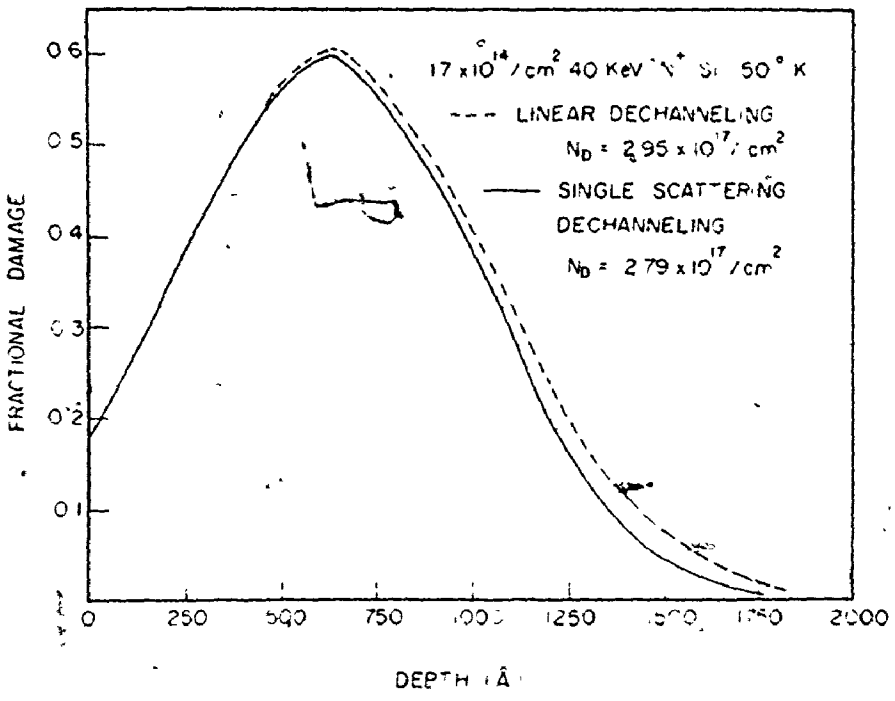

Fig. 4.8: The extracted damage profiles for 40 keV N^+ bombarded Si obtained using linear and single scattering dechanneling.

One convenience of the above approach is that it requires no knowledge "a priori" of the scattering probability function. Another iterative scaling method[98] that we have found satisfactory, is to include the scaling constant within the particular scattering probability function. This method can be applied to any of the amorphous scattering models, i.e.: single, plural,[93,94] or multiple[16] scattering. When used with single

scattering the results are identical to those from the above technique. However, the procedure is somewhat more difficult to implement since the appropriate probability function must now be calculated.

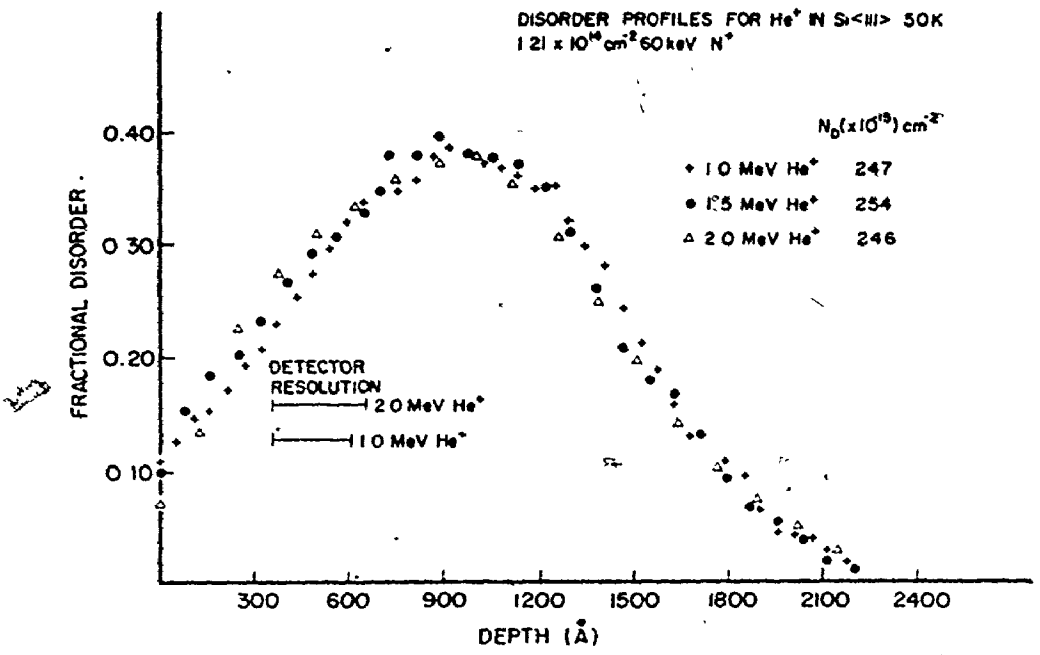

Fig. 4.9: Extracted damage profiles for 60 keV N^+ bombarded Si obtained using the semi-empirical single scattering dechanneling. Analyzing energies of 1.0, 1.5 and 2 MeV have been used.

The scaling constant, C, of Eq. (4.26), depends on the system gain through the term $(y_A(b') - y_R(b'))$. Thus, one advantage of the latter

scaling technique is that the scaling constants are independent of the gain. They may then be used as a measure of the inability of the various amorphous scattering models to fully describe the dechanneling in a particular ion-target system. To examine this further, the channeling data of Chapter V has been analyzed by this approach. These data include <111> and <110> "in-situ" analysis by 1-2 MeV He^+ of the damage introduced in each of Si, GaAs, and GaP at 50K by 20-40 keV light ions ($He^+ \rightarrow Ne^+$). Plotted in Fig. 4.10 are the scaling constants for single, plural and multiple scattering as a function of N_D.[98] The general observations are:

(i) plural scattering requires the least scaling, owing to it having the greatest generality in its development;

(ii) the constants appear to be only a function of N_D. This is not surprising at low temperature where formation of defect complexes is inhibited;

(iii) single and multiple scattering scaling constants saturate beyond $N_D \gtrsim 4 \times 10^{17}$ cm^{-2}, while that for plural scattering continues to decrease. The latter agrees with the observation that $C_{PS} \sim 1$ for $N_D \sim 1.5 \times 10^{18}$ cm^{-2};[91]

(iv) the N_D values found for each of the three scattering models can be compared by moving vertically along Fig. 4.10. The deviations are typically $\lesssim$5%.

It is emphasized that these constants should not be interpreted as weighting any parameter contained explicitly in the various probability functions. There is no fundamental weakness in the amorphous scattering

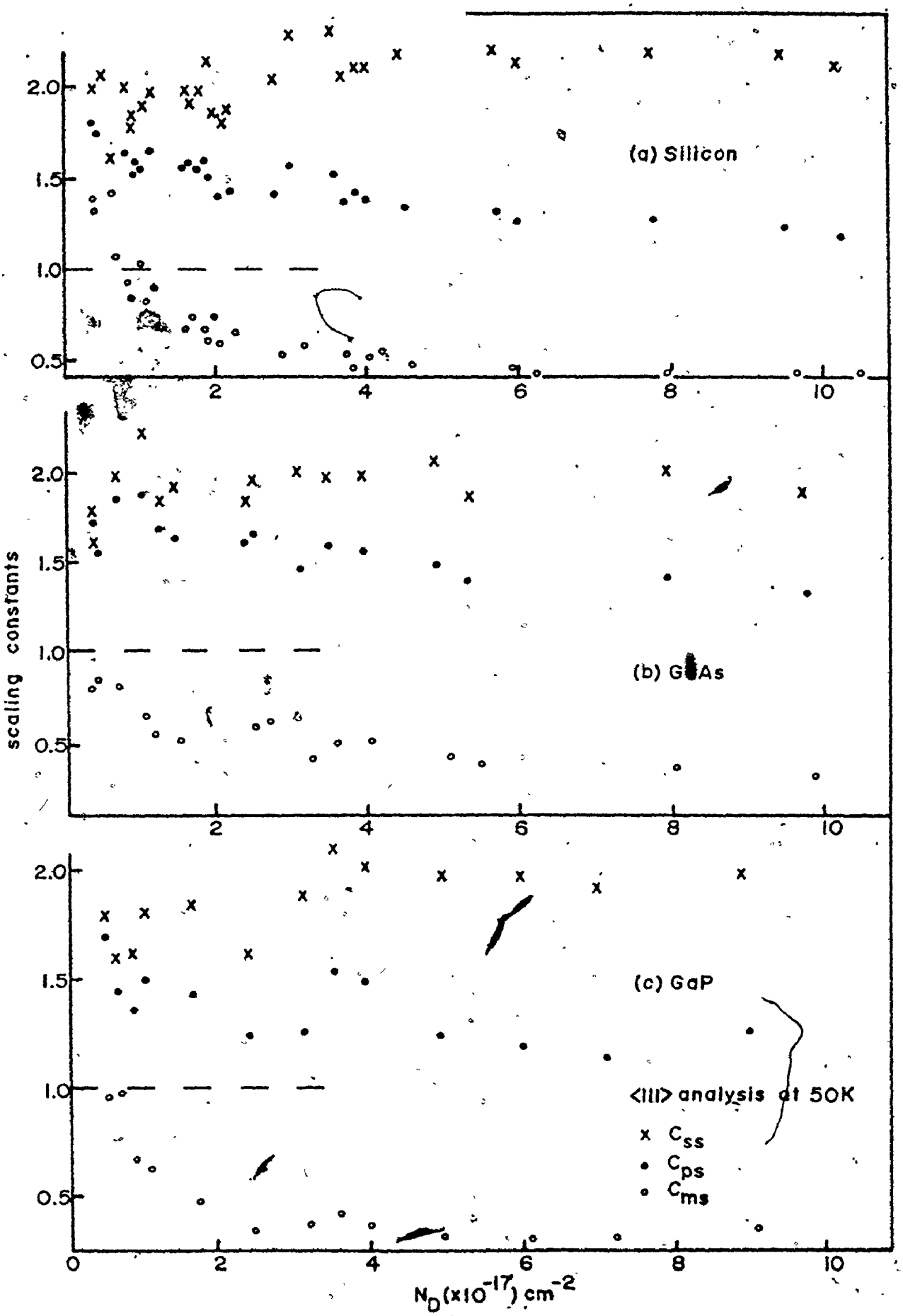

Fig. 4.10: The scaling constants for single (C_{ss}), plural (C_{ps}) and multiple (C_{ms}) scattering as a function of the dam N_D

models; rather, the difficulty lies in the fact that fundamentally different scattering mechanisms can be present in the channeling experiments.

The effect of the finite detector resolution on the analysis procedure is twofold. Firstly, the semi-empirical approach requires a judgement decision as to the where the damage ends. For the data analyzed by this technique, the depth resolution is typically $\lesssim$10-15% of the damage depth; the smearing effect of the resolution places a maximum uncertainty in the end channel of 2-4 channels. The variation in N_D for this variation in the end channel is $\lesssim$2%. Secondly, the finite resolution will distort the surface edge of the spectrum and those counts that "spill" beyond the surface channel are ignored. These lost counts typically amount to $\sim$1-5% of the peak area, depending on the ion-target system. The total cumulative error in N_D as determined by the semi-empirical approach is estimated at $\lesssim$5-10%.

The computer codes that have been written to perform the various analyses presented in this section are documented in the addendum to the thesis.

4.3.3 Limitations in the Technique

The analysis of the channeling-backscattering spectra for damaged crystals requires a well-resolved backscatter peak for the analysis that is described in the previous section to be attempted. Semiconductors are particularly suited since direct backscatter from the defects is indeed observed. In metals, such is not the case and the backscatter spectra are characterized by a rapid dechanneling rate with no discernable peak. Even in the semiconductors there is a practical lower limit on the amount of

disorder that can be observed by the technique. For single alignment, the limit is ~5% and is primarily determined by the underlying crystal quality, i.e.: χ_{min}, and the rate of dechanneling. However, it is possible to doubly align the crystal so that the out-going ion path to the detector corresponds to a major crystal axis. The sensitivity to the damage is increased by reducing the factors which limit the single alignment experiments. Then the much higher analyzing beam dose required for adequate statistics becomes the limiting effect.[36]

Some of the assumptions made in Sec. 4.3.1 require more careful consideration. Eq. (4.18) was derived on the assumption that the radial flux and damage distributions are uniform across the channel. In fact, the number of displaced atoms, $N_d(z)$, actually obtained from the backscatter spectra is given by:

$$\frac{N_d(z)}{N} = \int_A G(x,y,z)F(x,y,z)dxdy \quad , \tag{4.27}$$

where $G(x,y,z)$ is the distribution of scattering centers across the channel at depth, z, and $F(x,y,z)$ is the corresponding distribution of the channeled beam. A is the channel area accessible to the beam.

(i) Flux peaking

It has been shown both theoretically[87] and experimentally[99] that in a well-ordered crystal, the channeled beam distribution will become peaked towards the region of low potential, this region often being near mid-channel. This results from the focussing effect the string potential has on the flux. In some lattice location studies (cf. ref. 99), backscatter yields from interstitial impurities near the channel center have been

enhanced by factors of 2-3 due to flux peaking. In terms of the damage analysis, if G(x,y,z) is non-uniform as well, flux peaking will make the unfolding of the actual displaced atom distribution from Eq. (4.27) very difficult indeed. Therefore, the question becomes whether flux peaking can exist to any great extent in a damage measurement.

Firstly, flux peaking is an equilibrium process which requires a few thousand angstrom depth to become fully established. This depth is often greater than that of the damage layer. Secondly, flux peaking is extremely sensitive to any scattering mechanism, of which radiation damage is a strong example. The presence of defects should therefore work to destroy flux peaking. This would be particularly true for low energy heavy ions where the damage exists as highly-disordered zones within the bombarded volume.

(ii) Strain effects

As the lattice atoms rearrange to accommodate the ion-induced defects, they may relax into the channel sufficiently (i.e. $\gtrsim$0.1Å) that the beam can interact with them in much the same manner it would with lattice vibrations. Such effects would mainly act to enhance the dechanneling, viz. the correlated scattering dechanneling mechanism discussed in Sec. 4.3.2. However, direct backscatter may still occur if the relaxations are large enough. For example, it has been estimated[100] that the average atomic relaxation surrounding a divacancy in silicon is 0.25Å. As compared to the interstitial, the divacancy would then be expected to contribute $\sim$15%[101] to the backscatter yield.

It is noted that flux peaking and strain effects will not work

together to enhance the backscatter yield, i.e.: the flux is dramatically reduced by flux peaking in the region of the channel where the strains are dominant. As well, arguments given above suggest that flux peaking will be of minor importance in most damage analyses. If $F(x,y,z)$ is assumed constant, the measured damage will represent an average displaced atom distribution over the area sampled by the beam. This observation will be used in Chapter VI to estimate $G(x,y,z)$ and so infer the relative importance of the strain effects.

(iii) Channeling and lattice disorder

The use of channeling as an analytical tool requires a well defined crystal structure. In damage analysis by the channeling technique, the parameter being measured, i.e.: the defects, is also serving to destroy the technique itself. If the damage is extensive enough, an ambiguity will exist as to what is actually being measured. For instance, let us assume the damage is introduced fairly homogeneously across the implant area as in, say, light ion irradiation. As the ion dose increases, eventually 50% of the atoms in the damage layer will become displaced as a direct result of the collision cascade. In terms of channeling, one atom in two being displaced would certainly indicate the lattice could not support channeling and a backscatter yield characteristic of an amorphous layer would be expected. One could argue that in such an instance the lattice is no longer defined and this is exactly the effect that should be observed. Therefore, at high ion doses, the channeling technique indicates only the relative lattice disorder and care must be exercised in quantitatively interpreting the N_D values.[102] These arguments are not

far removed from those concerning strain effects.

If one wishes to use the channeling technique to measure the number of displaced atoms, N_D^*, per incoming ion, it must be done at as low a damage level as possible to avoid the above complications. Channeling should yield the most accurate measure of N_D^* in low-damage high-Z_1 irradiations, for it is under these conditions that the development in Sec. 4.3.1 would be expected to be most valid.

(iv) Quasi-channeling

It has been assumed that the channeled beam can be separated into a random and aligned component. Near the surface, the separation may not be distinct as a series of so-called quasi-channeled trajectories can exist for ions that enter the channel near the minimum approach distance, r_{min}, to the row (see trajectory B in Fig. 4.2a). Such trajectories will exhibit an oscillatory backscatter yield[82] as the quasi-channeled particle moves between the open channel and lattice row (note that the approach distance to the row < r_{min}). The effect will die out after a few oscillations as the particles scatter out of the trajectory. Oscillations at shallow depths in the backscatter yield have been observed in planar channeling, where the oscillatory trajectory is in one-dimension. For axial channeling, the effect is much more difficult to observe.

It has been argued that these backscatter oscillations may add to the damage peak for shallow damage layers.[103] However, the oscillations have not been observed in any of the aligned unirradiated spectra of the thesis. While the effect may slightly enhance the surface peak, the latter has been measured in all cases prior to irradiation and subtracted

from the damage peak (see Eq. (4.23)). Therefore, quasi-channeling should not influence the results significantly.

CHAPTER V

EXPERIMENT

5.1 Introduction

In this chapter, a detailed discussion of the experimental apparatus and techniques is given. A coupled accelerator system described in Sec. 5.2 is used to carry out 10-150 keV ion implantations and in-situ damage analysis by the channeling-backscattering technique. The target chamber and sample manipulator designs are presented in Sec. 5.3. Emphasis is placed on the provisions made for cryogenic cooling of the target. In Sec. 5.4, the Data Acquisition System and methods of accurate current measurement are discussed. A minicomputer has been incorporated for pulse-height analysis and data manipulation. Outlined in Sec. 5.5 are the various considerations made when performing the damage analysis, e.g. the reasons for the particular choice of analyzing beam, beam current, and dose. The technique of calibrating the analysis beam and of aligning the crystal for channeling are included here. In Sec. 5.6, the target materials and preparation are specified.

5.2 Accelerators and Beam Transport

The research of the thesis involves the investigation of the radiation damage induced by the ion implantation process in the semiconductors. In order to minimize annealing effects, low temperature irradiations and "in-situ" damage analysis are necessary. A coupled accelerator system

has been developed that utilizes a 150 kV ion accelerator for the implantations and a 3.5 MV Van de Graaff accelerator for the disorder analysis using the channeling-backscattering technique. Fig. 5.1 is a schematic of the system. The beam from either accelerator may be brought into the target chamber via the common analyzing magnet, thereby allowing the "in-situ" damage measurement. Energy stabilization of ≤0.2% is attained for both accelerators by monitoring the beam current striking slits placed after the analyzing magnet. A feedback circuit adjusts the energy of the beam so that the currents are equalized.

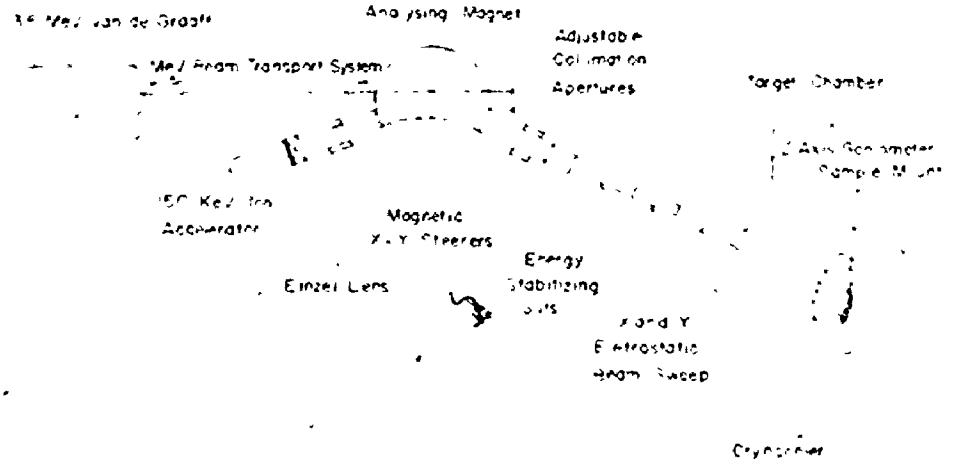

Fig. 5.1: Schematic of the coupled accelerator system.

The channeling-backscattering analysis is undertaken with 1-2 MeV He^+ ions from the Van de Graaff accelerator. The analyzing beam is collimated to 0.037° half-angular divergence by 0.75 mm. diameter apertures. Since critical angles (ψ_c) beyond which channeling cannot occur are of the order of 1 degree, this beam divergence is small enough that its effect on the channeling will be minimal. The collimation apertures are moveable vertically (resettable to $\leq$0.01 mm) to allow analysis at various positions on the target.

The ion implantation accelerator is a Texas Nuclear Corporation model 9509 Cockroft-Walton neutron generator that has been modified to accommodate a Danfysik 911A universal ion source. This is a hot cathode source having an auxillary heating filament so that solid, as well as gaseous, source materials may be employed. Depending on its melting point and vapour pressure, the solid is placed in one of three holders which determine the distance from the heating filament. A carrier gas (typically Ar) is used to achieve the discharge. The ovens and carrier gas are eliminated when the source material is gaseous. Between extraction and acceleration, the beam is focussed by an Einzel Lens assembly.

During implantation, the collimation apertures are replaced by 2 mm and 4 mm apertures, the former being nearest the analyzing magnet. Between these apertures are two pairs of electrostatic beam sweep plates to allow for horizontal and vertical deflection of the beam. The implanted area ($\sim$0.5 cm^2) on the target is defined by electrostatically sweeping the beam across the 4 mm aperture. Uniformity of the implant ($\leq$5%) is achieved by using a triangular sweep voltage waveform. Peak-to-peak voltage is

between 0 and 500 V. Typical vertical sweep frequency is ∿3 Hz, while for the horizontal sweep it is ∿15 Hz; the large frequency difference avoids implant non-uniformity due to the possible harmonic coupling of the frequencies. Average target currents range from 0.5-50 nA/cm^2.

Obviously, an accurate measure of the implant dose is necessary. Since the dose is determined by measuring the integrated charge (see Sec. 5.4), the neutral component of the beam at the target should be minimal. To accomplish this, the 2 mm aperture is placed ∿4 mm off-axis vertically, such that a direct path from the magnet to the target does not exist. The beam is steered on target by applying a d.c. voltage (0-500 V) to the vertical deflection plates. This ensures that ions neutralized between the magnet and beam sweep system cannot strike the target. The fraction of the beam neutralized after the sweep system has been estimated as typically ≤0.01, by observing the secondary electron emission at the target with the charged component deflected by the electrostatic plates. This component will be distributed almost uniformly across the implanted area when beam sweeping is performed.

The vacuum in each accelerator is maintained by Hg diffusion pumps having liquid nitrogen cooled vapour traps. The beam lines are equipped with ion pumps. The base system pressure is $\leq 1 \times 10^{-6}$ Torr.

5.3 Target Chamber and Sample Manipulator

Figure 5.2 shows schematically the details of the interior of the target chamber. To achieve the low target temperatures, a two-stage compressed-helium cryogenic refrigerator (Air Products model CSW-202) is used. The heat capacity at the second stage of the cryocooler is 2 Watts

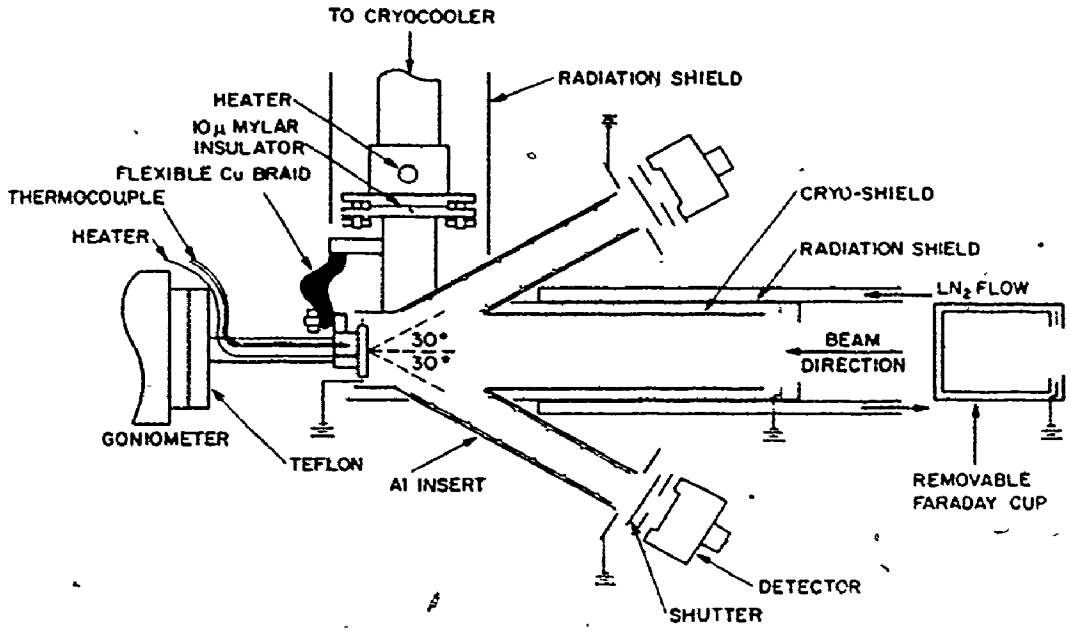

Fig. 5.2: Schematic of the target chamber geometry.

at 20K. The copper target mount is attached to the second stage by a flexible copper braid, and to a goniometer stage having two degrees of rotation. The angular resolution of the goniometer is <0.025°. Thermal isolation of the target mount from the goniometer is achieved by a thin-walled stainless steel tube and teflon washer. The flexible braid permits the target to be cooled while allowing sufficient manipulation, i.e.: the target can be tilted with respect to the incident beam direction (+45° to -20°) and rotated about an axis parallel to the incident beam direction (220° of rotation possible). The target mount is surrounded almost entirely by a copper shield that is also attached to the second stage of the

cryocooler. This target-shield arrangement acts as a Faraday cup for beam current measurement. It also takes advantage of the strong cryo-pumping action at low temperatures to reduce the effective pressure in the vicinity of the target. The base temperature as measured by Au (0.03 at .% Fe) - Chromel thermocouples, is 18K at the cryocooler second stage, 25K at the copper shield, and 35K at the target. At 25K, the partial vapour pressure of all gases except H_2, He and Ne is $<10^{-10}$ Torr. Therefore, in the vicinity of the target the effective pressure should be $<10^{-10}$ Torr.

Possible target surface contamination arises from the direct line of sight from the target to the poorer vacuum in the chamber outside the inner shield. This exposure is due to the finite beam and detector tube apertures and amounts to $\sim$0.05 sr. Since the chamber vacuum is $\sim 2 \times 10^{-7}$ Torr when the cryocooler is operating, the upper limit for the surface contamination rate would be $\sim 4 \times 10^{15}$ atoms/cm^2·h. No contamination related effects have been observed in the backscattering spectra. However, when the entire system is at room temperature, a significant carbon build-up on the target surface is soon observed.

To minimize the radiative heat load on the cryocooler second stage, it is surrounded by a radiation shield that is attached to the cryocooler first stage ($\sim$45K). Another radiation shield, that is cooled directly by a flow of liquid nitrogen, encloses the greater part of the inner shield.

A 2.5 W nichrome heater in the target mount allows the target to be heated to $\sim$100K. The entire target-shield temperature can be varied up to 300K by a heater in the second stage cold head.

The target chamber vacuum is maintained by a Hg diffusion pump with a liquid nitrogen cooled vapour trap. Without the cryocooler operating,

the base chamber pressure is 2-4 x 10^{-6} Torr. With the cryocooler on, the pressure reduces to ~2 x 10^{-7} Torr.

In the early stages of this research, a somewhat different target chamber geometry was used[37] in which the cryocooler was a single-stage compressed-helium unit (Malaker Corp. Mark VII-C Cryomite). The base target temperature was ~50K.

5.4 Data Acquisition System

The implant dose is determined by measuring the integrated charge at the target over the course of the implant. Since it is required to know this dose precisely, certain considerations have been made in the target chamber geometry to ensure the current measurement is accurate (see Fig. 5.2). Firstly, the target mount and copper shield are electrically isolated from the cryocooler by a 10μ Mylar film and from the goniometer by a Teflon washer. This target-shield arrangement acts as a Faraday cup. Secondary electron suppression rings exist at the beam and detector tube entrances, and on a Teflon ring that fits on the circumference of the target mount itself. A suppression voltage of -100 V has been found adequate to eliminate secondary electron losses. A removeable Faraday cup is placed in front of the target-shield system for initial beam set-up and for accurate current measurement. The difference between the current at the target and Faraday cup is <0.5%. Also, backscatter measurements of the concentration of high mass impurities, e.g.: As, Te, implanted into silicon have verified the dosimetry to better than 5%.

In the damage analysis, the backscattered He particles are detected by a standard silicon surface-barrier detector (FWHM ~ 15 keV). Detectors are mounted perpendicular to the goniometer tilt-beam plane and at a

backscattering angle of 150°. Shutters that are controlled from outside the target chamber may be positioned in front of the detectors during implantation in order to reduce their deterioration from radiation damage. With the long detector tubes of the present system, scattering of the backscattered He from the tube walls to the detector must be considered. For 1.0 MeV He^+ on silicon, the yield of low energy He (<100 keV) reaching the detector increases by up to 30% when the detector tubes are employed. The scattering has been eliminated by lining the tubes with an aluminum insert. The inner surface of the insert has a series of ridges that are spaced so as to prevent the single scattering events to the detector.

Figure 5.3 is a block diagram of the detector-data acquisition system. A unique feature is the incorporation of a PDP 11/05 minicomputer. It has been programmed to perform the pulse-height analysis, as well as various data manipulation operations. For example, the data may be displayed on a Textronix model 602 display unit, stored on a Dec RX-11 "floppy" disk, or printed on the teletype. These operations may be done concurrently with the data acquisition. Other special features include: software simulation of the operation of a single channel analyzer-scaler combination, and a software ratiometer, the use of which will be described in Sec. 5.5. A listing of this program is available in the addendum to the thesis. Data may also be transferred to a PDP-15 computer via a high speed data link. The latter has been programmed to perform the various analyses that are discussed in Sec. 4.3.

An Ortec model 439 current digitizer measures the beam current at the target or Faraday cup. This is the only operation required during the implantation. However, during the channeling-backscattering analysis

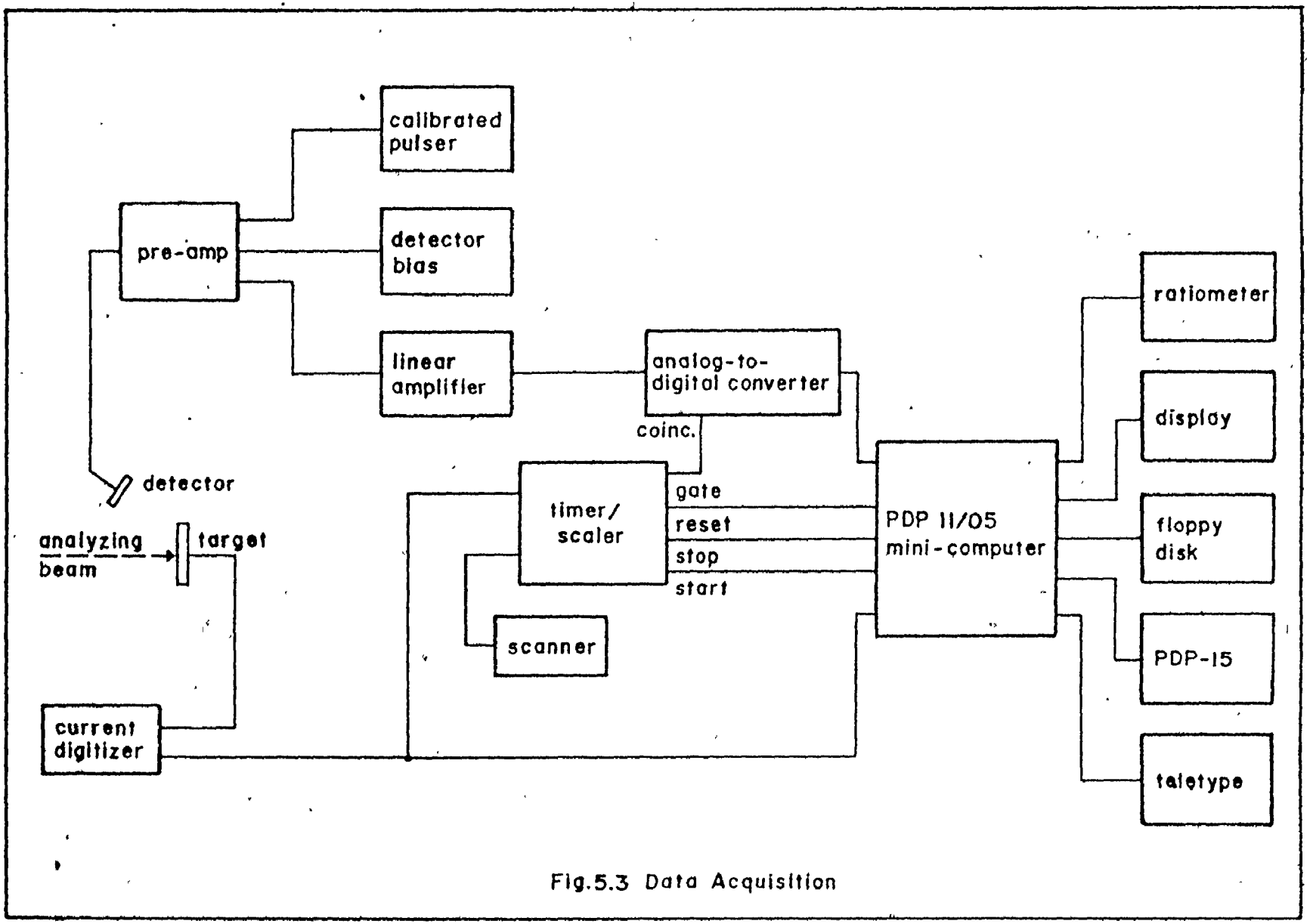

Fig. 5.3: Block diagram of the Data Acquisition System.

the digitizer feeds a Canberra model 1492 timer/scaler, which acts as a control unit for the data acquisition. It is normally preset to stop counting the digitizer output at a given integrated charge. Simultaneously, it will stop the pulse-height analysis by gating the analog-to-digital converter (ADC) coincidence-mode input. Therefore, a normalization of the various backscatter spectra to the same integrated beam charge is accomplished. A controller has also been developed to automatically perform the stop-reset-start sequence on the timer/scaler.

When a backscattered He particle reaches the solid-state detector, an energy-proportional pulse is generated. The pulse is passed through a Canberra model 1408 pre-amplifier and Tennelec model 213 linear amplifier. It is then digitized in the Northern Scientific 621 8192-channel ADC. Standard conversion gain is 256 channels, since the detector resolution rules out the advantage of further quantization. The current digitizer is tied to the minicomputer by a "queued interrupt" method. This means that the computer's interrupt service routines cannot interfere with the digitizer count rate. However, the ADC must wait for the computer to store each digitized output before the next can be processed. The service time is ~75 μsec and primarily determines the losses that occur at a particular backscattering count rate. For 1% losses, or "dead time", the allowed rate is 130 counts/sec.

5.5 Measurement Considerations

Various factors must be considered in choosing the damage analysis parameters, i.e.: the analyzing particle and energy, beam current and dose. The parameters should match the detector-data acquisition system; for example, the "dead time", energy resolution and statistics should be

optimized. At the same time, the analysis must not introduce significant effects in the target material. The analyzing beam will create disorder by atomic collisions. It has also been suggested that the enhanced ionization density due to the beam can stimulate either lattice disordering[104] or defect annealing.[105] Since it is the lattice disorder due to only the ion implantation process which we require to measure, such effects will introduce major analysis complications.

1-2 MeV He^+ has been chosen as the most suitable analyzing beam. Its backscatter yield is high enough that sufficient statistics are readily obtained while the total cross-section is low enough that beam-induced effects can be avoided. For these energies, the electronic stopping is near maximum, so that the depth resolution is optimized. The electronic stopping powers for He have been taken from the semi-empirical values tabulated by Zeigler and Chu.[86] For the compound semiconductors, the Bragg Additivity Rule[106] has been applied to determine the effective stopping power. The average stopping power, S_{AV}, as defined by Eq. (4.15), is given in Table 5.1 for the beam energies most commonly used. These values of S_{AV} will translate the energy resolution of the detection system to a depth resolution ~200-300Å.

Table 5.1: Average stopping power, S_{AV}, for He and ϕ = 150°. S_{AV} is defined by Eq. (4.15).

Target	S_{AV} (keV/10^{15}atom/cm^2)	
	1 MeV He	1.5 MeV He
Si	0.120	0.105
Ge	0.162	0.154
GaAs	0.162	0.154
GaP (Ga only)	0.142	0.133

Beam currents used when acquiring the aligned spectra are: ~20 nA/mm^2 in Si and ~2-4 nA/mm^2 in Ge, GaP and GaAs. For these currents the "dead-time" is ≲1% and dose-rate effects are not observed. Integrated doses for the aligned spectra are typically: ~10 $\mu C/mm^2$ in Si and 2 $\mu C/mm^2$ in the other materials. As discussed below, these values have been chosen to compromise between statistics and beam induced lattice disorder. The currents and doses used for the non-aligned spectra are ≲20-30% of the above.

For the channeled beam measurements, the doses quoted above are ~one-tenth those found necessary for there to be what can be considered a significant increase in the lattice disorder at 35K, i.e.: for a $\Delta\chi_{min}$ ~ 0.005. When more than one aligned spectrum is required, the practice has been to move the analysis position on the target to a previously un-analyzed area by adjusting the collimation apertures. The doses required for the non-aligned spectra are sufficient at low temperatures that significant lattice disorder is caused. Therefore, these spectra have been acquired only after all the channeling measurements have been made.

Crystal alignment for channeling has been achieved by the method proposed by Andersen et.al.[107] The basic operation is to observe the backscattered yield to the detector as a function of the goniometer settings. When the beam is incident within some small critical angle (~1°) on a low-index crystallographic plane or axis, a dramatic reduction in the yield will result. In practice, the azimuthal angle corresponding to a particular planar dip is plotted as a function of tilt (up to, say, 10°) on a standard stereogram. The intersection of lines drawn through two such planes then gives the axial direction. All crystals used have <111> orientation, meaning the intersecting planes are (110). When <110> analysis

has been required, the <110> axis could be found by measuring ∿35° from the <111> axis along one of the (110) planes as plotted on the stereogram.

As a practical consideration, the backscattered yield is susceptible to random fluctuations in the beam current. During the alignment process, the problem can be eliminated by observing the ratio of the backscatter yield and beam current. This function is performed by a software ratiometer (see Sec. 5.4). Its operation involves setting a "window" on the backscatter spectrum, usually just below the surface. Whenever a preset charge is accummulated, the yield into the window is converted to an analog signal which is output to a meter. The window sampling frequency is set high enough that the pulsing of the meter is adequately smoothed by its response time.

The absolute measurement of the lattice damage by the channeling-backscattering technique requires a precise knowledge of the beam energy. The Van de Graaff energy has been calibrated using the $Al(p,\gamma)Si$[108] nuclear reaction. Such calibration techniques are well described in the literature,[109] and will not be repeated here. In practice, it is convenient to have a more easily preformed calibration procedure. Therefore, a Tennelec model 812 pulser that is connected to the detector pre-amplifier has been calibrated so that a known pulse height corresponds to a given particle energy. Once the beam energy has been determined by the nuclear reaction technique, the pulser can be calibrated with a knowledge of the backscattering angle and certain detector energy corrections.[110] These corrections account for the energy loss the particle undergoes in crossing the thin gold film on the detector surface and for the ionization efficiency of the particle in the detector. Typical correction values for 0.4-1 MeV

He are 20-30 keV.[110]

5.6 Target Materials

The single crystal semiconductors that have been investigated are: Si (N- and P-type), Ge (P-type), GaP (N-type) and GaAs (N-type). All materials are cut within a few degrees of a {111} surface. For GaP and GaAs, the channeling-backscattering analysis has been made on the B-face. Listed in Table 5.2 are the materials specifications, i.e.: dopant and resistivity. All materials have been subjected to a degreasing procedure, chemical etch and de-ionized water rinse immediately before being placed in the target chamber. The etching solutions are:

Si: dilute (~8%) HF,

Ge: 1:20 $HF:HNO_3$,

GaP: dilute (~50%) aqua regia,

GaAs: 50:10:13 $H_2SO_4:H_2O:H_2O_2$ (cold solution).

Table 5.2: Materials specifications.

Material	Dopant	Resistivity (Ω-cm)
N-Si	P	5-10
P-Si	B	7-14
P-Ge	B	0.13-0.23
N-GaP	S	7-13
N-GaAs	Te	~1

The crystal quality before implantation is commonly inferred directly from the channeling-backscattering technique by considering the ratio of

the backscattered yield immediately below the surface for channeled and non-channeled conditions. Under ideal conditions, this ratio, χ_{min}, is defined by Eq. (4.10). The presence of lattice strain, defects, surface contamination (e.g. oxide), and non-zero beam divergence will all contribute to an increase in χ_{min}. Given in Table 5.3 is a comparison between the measured and best-value χ_{min}'s (from Eq. (4.10)) for 1.0 MeV He^+. In all instances, the crystal quality is considered satisfactory.

Table 5.3: Measured and predicted χ_{min} values (1.0 MeV He^+).

Material	Temperature	Direction	Measured χ_{min}	Predicted χ_{min}
Si	35K	<111> <110>	0.015 0.012	0.011 0.009
	300K	<111>	0.034	0.035
Ge	35K	<111>	0.013	0.007
	300K	<111>	0.034	0.035
GaP (Ga only)	50K	<111> <110>	0.024 0.011	0.009 0.007
GaAs	50K	<111> <110>	0.021 0.014	0.007 0.006

CHAPTER VI

DAMAGE FROM LOW-Z_1 BOMBARDMENT OF Si, GaP AND GaAs AT 50K

6.1 Introduction

This chapter reports on the investigation of the damage induced in three semiconductors, namely Si, GaP and GaAs, by ion implantation of low-Z_1 ions ($2 \leq Z_1 \leq 30$) at 50K as measured "in-situ" using the channeling-backscattering technique. Ion energies ranged from ~10 to 100 keV. Implantation beam currents were ~10-50 nA/cm^2 for the lowest-Z_1 implants (e.g. He^+,N^+) and 0.5-10 nA /cm^2 for the heavier ions (e.g. Zn^+). No dose rate effects were evident over these current ranges. The analyzing beam was 1.5 MeV He^+ for the He bombardments, and 1.0 MeV He^+ for all others.

For most of the ion-target systems studied, the damage depth was significantly greater than the detector depth resolution, and the damage profiles could be extracted. In Sec. 6.2, a detailed comparison is made of these profiles with the theoretical distribution of energy deposited into atomic collisions. It was shown in Chapter III that this distribution will be directly proportional to the damage distribution, provided the theory used to describe the energy loss processes is strictly correct. It is also assumed that the measured damage distribution is directly related to the damage resulting from the collision cascade, i.e.: effects such as annealing are minimal. In Sec. 6.3, the radial distribution of displaced atoms across the channel is studied by introducing a small misalignment ($\psi \leq 0.36\ \psi_1$) of the crystal axis to the analysing beam. Such misalignment

will increase the mean transverse energy of the channeled particles and thereby vary the area of the channel accessible to the beam. This "Off-Axis" effect is examined as a function of ion mass and dose. Finally, the damage versus dose behaviour for various Z_1 is discussed in Sec. 6.4. A quantitative model is presented to explain the observations.

6.2 The Damage Profiles

In this section, the general characteristics of the ion-induced damage profiles in Si, GaP and GaAs at 50K are examined.[37,38] The target temperature of 50K is assumed low enough that minimal defect annealing can occur either during bombardment or the following analysis. For Si, no defect annealing has been observed in this temperature region, except for the inferred exchange, during electron irradiation at 4.2K, between silicon interstitials and Group III substitutional impurities.[111] Annealing studies[112] in GaP and GaAs also suggest the absence of major recovery stages in these materials for this temperature range.

For GaAs, where the mass resolution of Ga and As in the backscatter spectra is less than the detector resolution, the substrate has been treated as a monatomic target in the extraction procedure. For GaP, significant energy separation exists in the surface yields for each component. However, only the Ga damage profiles have been extracted since the large Ga dechanneling rate under the P damage peak made accurate extraction of the latter difficult. The Ga profile has been assumed characteristic of that for the compound. Irradiation energies have been chosen such that the Ga damage peak does not extend into the P yield.

It has been previously observed[113] that, following 300 keV Kr^+

bombardment at 25K, the damage measured in GaAs and GaP by the channeling-backscattering technique showed a distinct anisotropy. In fact, in GaAs, damage levels measured along the <111> direction exceeded by as much as 100% the damage levels obtained by channeling along the <110> direction; furthermore, the difference actually increased with ion dose. Such discrepancies are inexplicable in terms of known channeling-related effects, such as flux peaking or shadowing of preferential defect sites. Consequently, we have made damage measurements for 20-80 keV He^+, N^+ and Zn^+ irradiations of the three semiconductors, with the analysis performed along the <111> and <110> directions of each target. No anisotropy of the magnitude previously reported[113] was found. However, in the case of the lowest dose irradiations ($\lesssim$10% damage) of He^+ and N^+, a small but consistent anisotropy (at the level of the experimental error) was observed in GaP and Si, with the damage measured along the <111> axis being the larger. No anisotropy was observed in GaAs (Fig. 6.1). This is in marked contrast to results for GaAs reported in Ref. 113. For the higher dose cases, any possible anisotropy decreased (as the statistical accuracy increased) and eventually could not be observed, even though the maximum damage level was below the saturation level. From these results it is concluded that damage anisotropy does not exceed 10-15% in the ion-target systems investigated.

In Figs. 6.2, 6.3 and 6.4, the normalized damage profiles are shown for 30 keV He^+ (24 keV He^+ in GaP) and 40 keV N^+ irradiations of Si, GaP and GaAs and for 80 keV Zn^+ irradiation of Si. Peak damage levels range from 40-50%. Both <111> and <110> directions have been analyzed. Also given are the theoretical deposited energy profiles generated by the Edgeworth series expansion (see Eq. (2.28)) of the first four moments

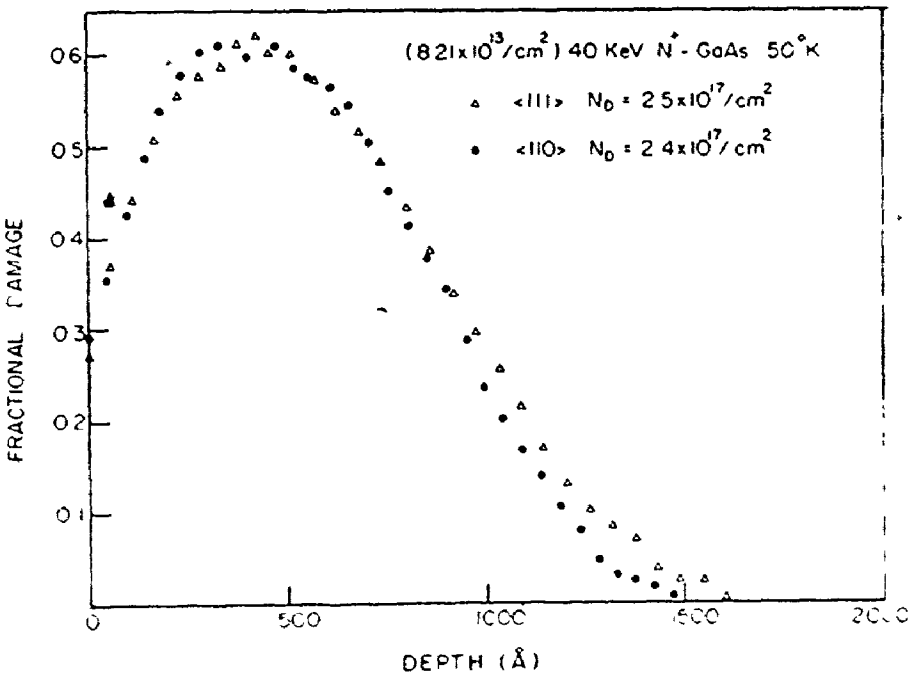

Fig. 6.1: Comparison of damage profiles obtained <111> and <110> for GaAs irradiated at 50K with 8.21×10^{13} cm^{-2} 40 keV N^+.

interpolated from the tables of Winterbon.[2] For He^+ and N^+ irradiations of Si (Fig. 6.2a, 6.3a) the calculated damage range is significantly greater than the measured damage range. Since for these light ions, ~60-80% of the incident ion energy goes into electronic stopping,[2] this suggests that the standard Lindhard electronic stopping cross-section used in the theoretical development is low. The profile shape will be quite sensitive to the absolute value of the electronic cross-section; for example, in the

(a)

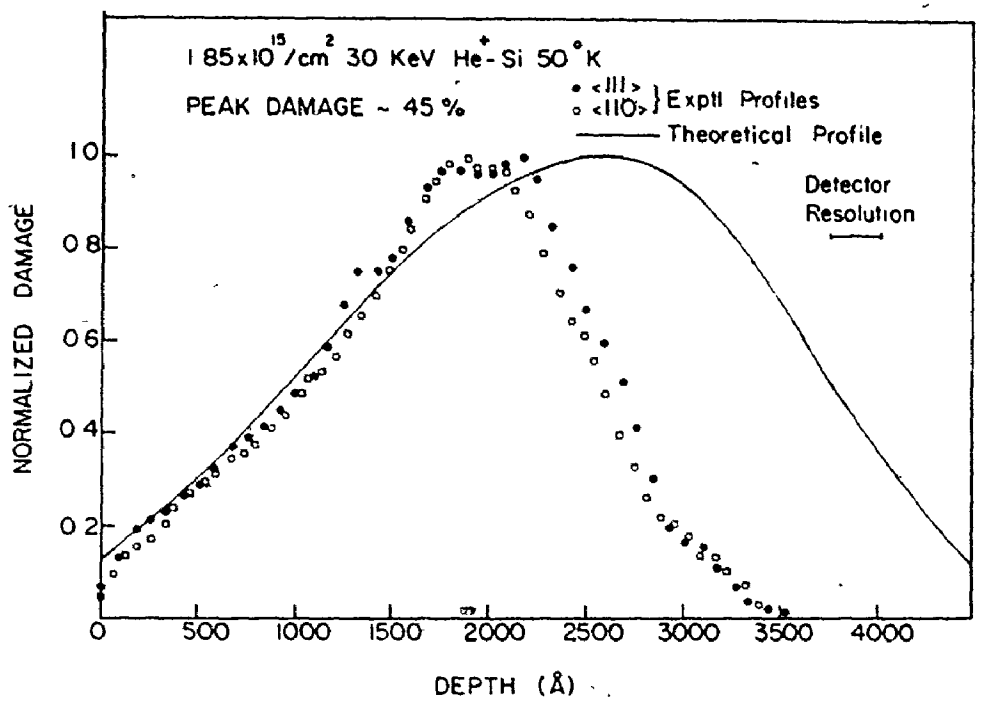

(b)

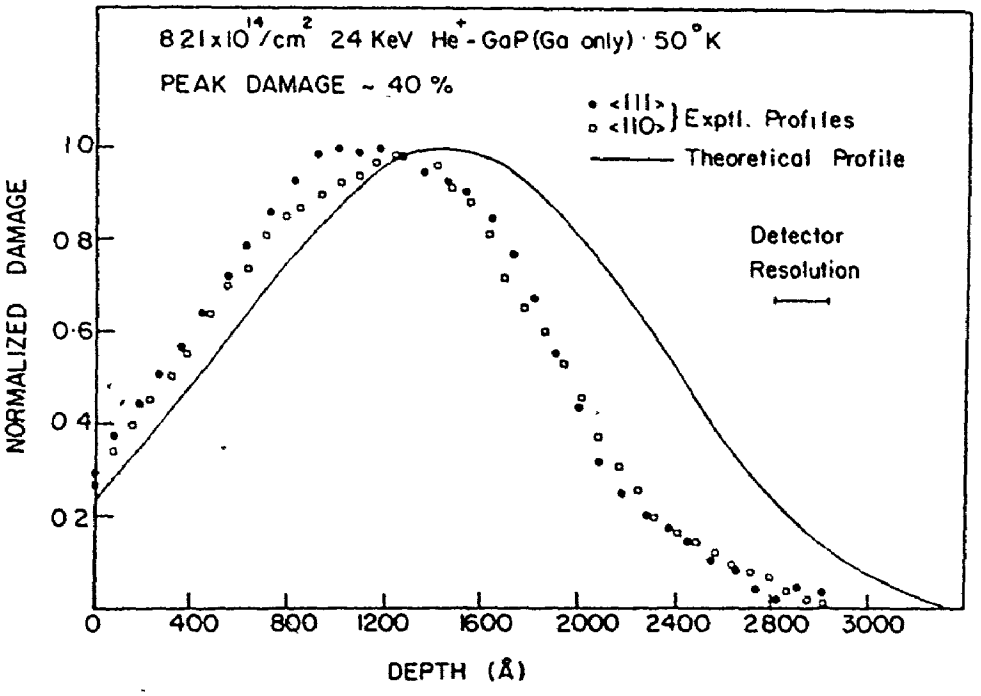

Fig. 6.2: Normalized damage profiles for He^+ bombardment at 50K of: (a) Si, (b) GaP (Ga only), and (c) GaAs. Profiles are given for <111> and <110> channeling analysis. Theoretical profiles have

(c)

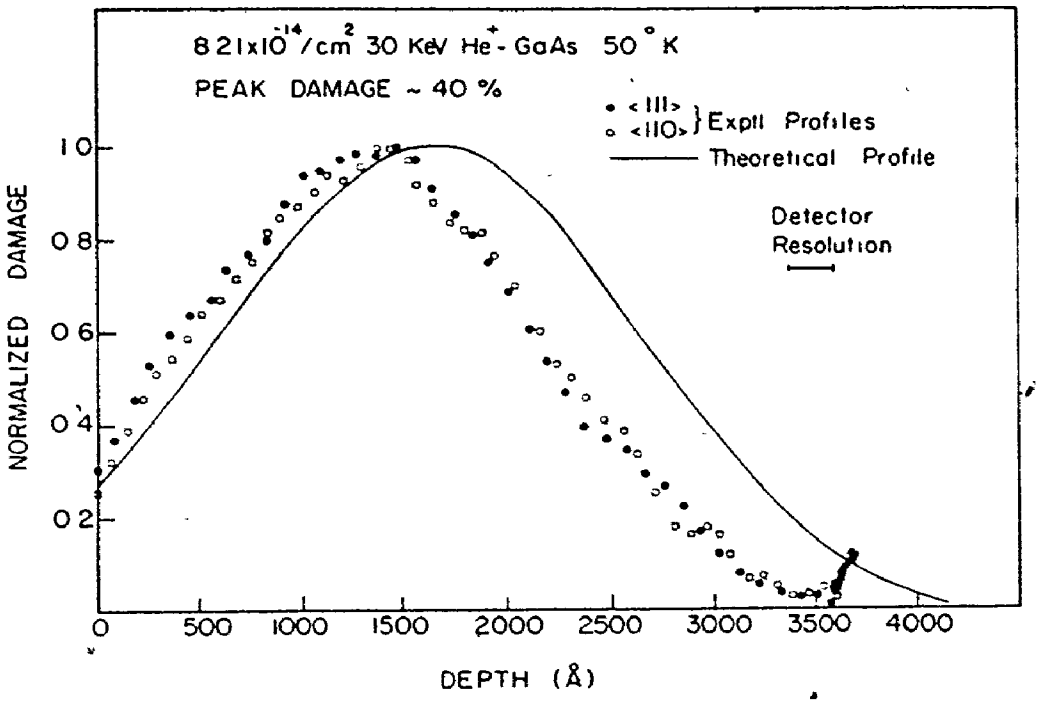

(a)

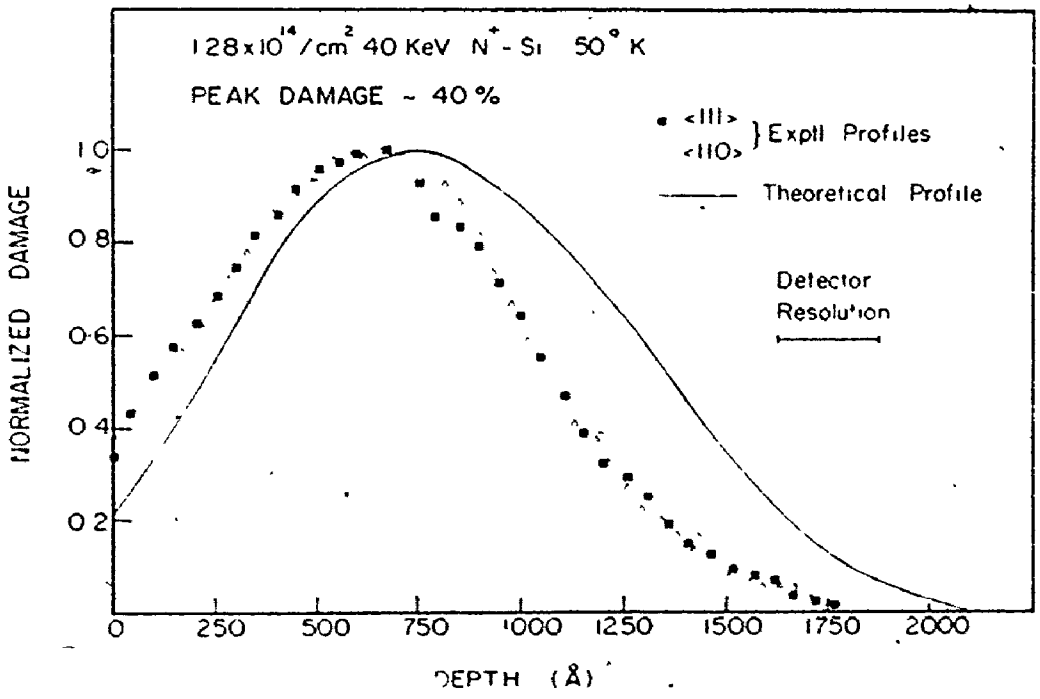

Fig. 6.3: Normalized damage profiles for 40 keV N^+ bombardment at 50K of: (a) Si, (b) GaP (Ga only), and (c) GaAs. Profiles are given for both <111> and <110> channeling analysis. Theoretical profiles
been

(b)

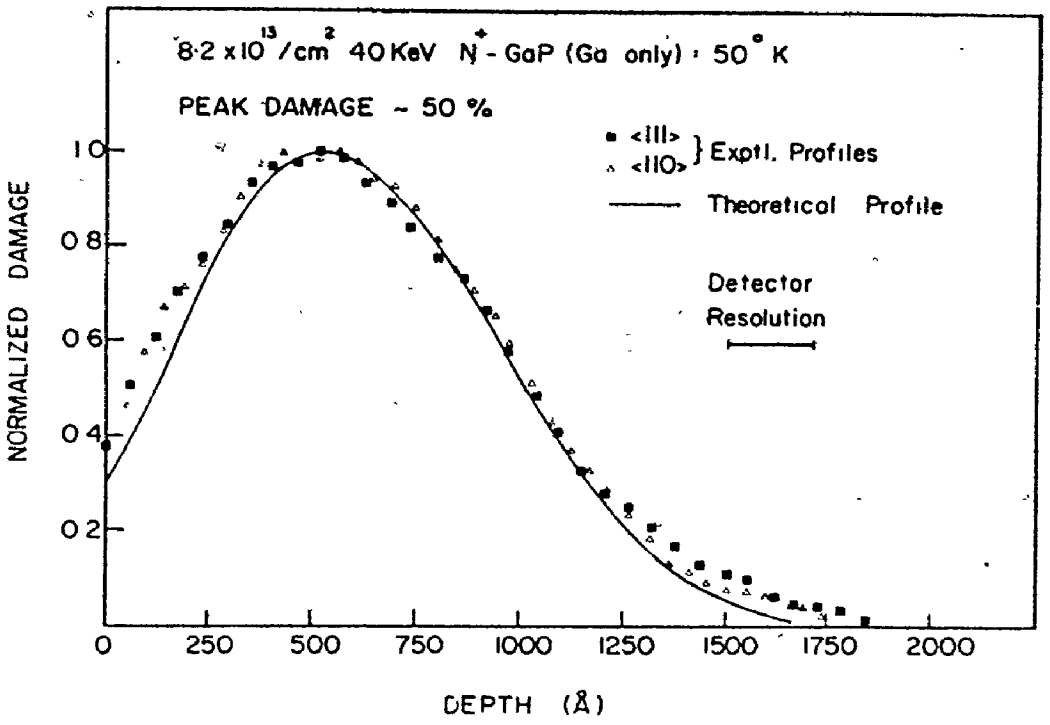
8·2 x 10^13 /cm^2 40 KeV N+ - GaP (Ga only) : 50° K
PEAK DAMAGE ~ 50 %
<111>
<110>
Expt. Profiles
Theoretical Profile
Detector Resolution
NORMALIZED DAMAGE
1·0
0·8
0·6
0·4
0·2
0
250
500
750
1000
1250
1500
1750
2000
DEPTH (Å)

(c)

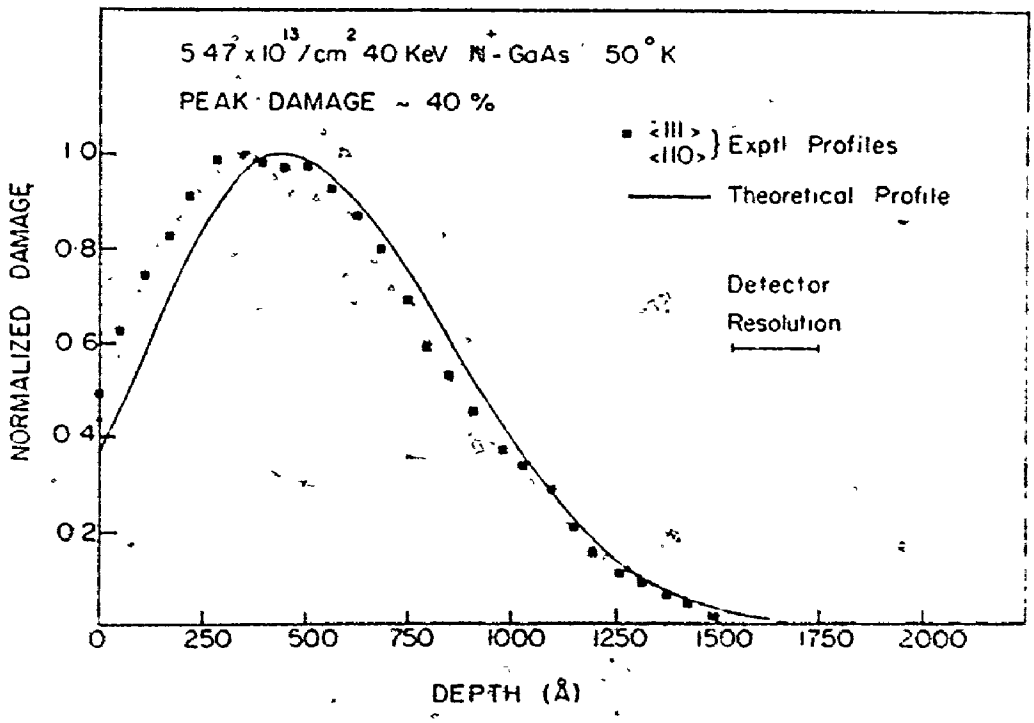
5·47 x 10^13 /cm^2 40 KeV N+ - GaAs 50° K
PEAK DAMAGE ~ 40 %
<111>
<110>
Expt Profiles
Theoretical Profile
Detector Resolution
NORMALIZED DAMAGE
1·0
0·8
0·6
0·4
0·2
0
250
500
750
1000
1250
1500
1750
2000
DEPTH (Å)

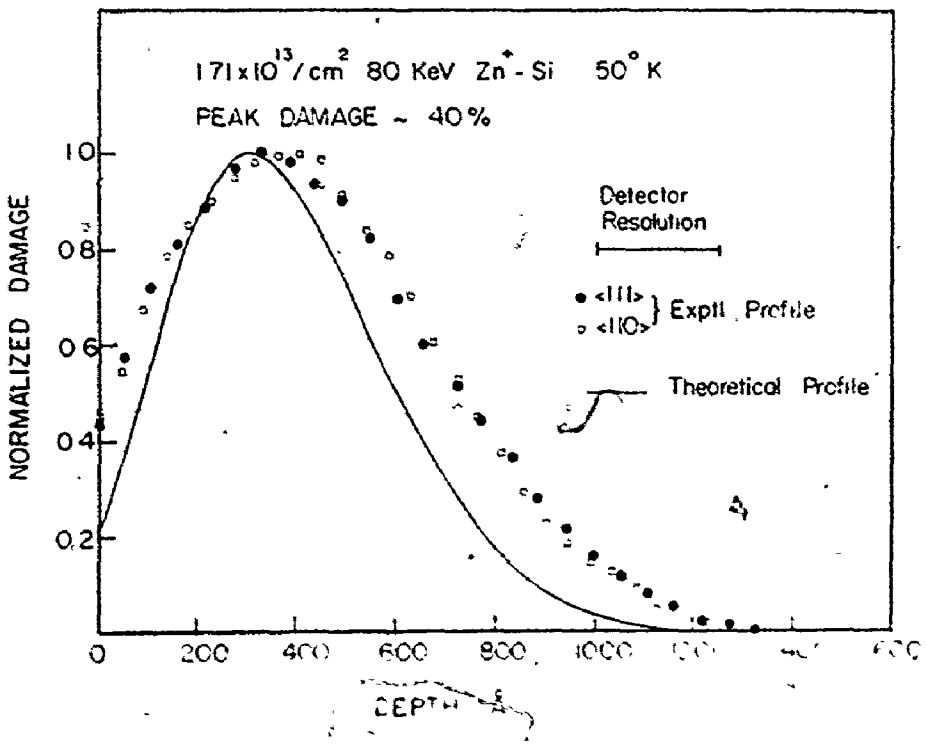

Fig. 6.4: Normalized damage profiles obtained by <111> and <110> channeling analysis of Si bombarded with 80 keV Zn^+. Theoretical profiles have been taken from Winterbon.

case of the He bombardment, ~50% increase in the electronic stopping coefficient, k_L, of Eq. (2.22) will bring the calculated distribution into line with the measured distribution. This should be compared with recent damage measurements[114] of proton bombarded Si, where it was determined that k_L must be scaled by ~60% for the damage profiles to agree. Similarly, Hofker et. al.[33] have observed that in measurements of range distributions

of 70-300 keV B^+ in Si, k_L should be increased by ~50%. For N^+ bombarded Si (Fig. 6.3a), the theoretical value for the electronic stopping appears underestimated by ~40%. In the case of Zn^+ bombardment of Si (Fig. 6.4), theory underestimates the damage range, although the detector resolution, when added in quadrature, accounts for ~25% of the discrepancy. In this instance, it becomes difficult to estimate accurately the correction in k_L necessary to achieve agreement, since the electronic stopping is a smaller part of the energy loss (~40%) and the electronic energy loss by Si recoils can no longer be ignored. However, it is significant that the N^+ and Zn^+ damage depths are consistent with the observed "Z_1-oscillations" of the electronic stopping,[32] since N^+ occurs near a maximum and Zn^+ near a minimum in these oscillations. For He^+ bombardment of GaP and GaAs (Figs. 6.2b and 6.2c), significant deviations between theory and experiment are again noted. However, for the N^+ bombardments (Fig. 6.3b,c), good agreement is found. Discrepancies at shallow depths are, in part, related to the finite detector resolution.

The above discussion suggests it would be of interest to examine the Z_1 dependence of the required adjustment in the electronic stopping necessary to fit the theoretical and measured damage profiles. Therefore, a series of bombardments with $3 \leq Z_1 \leq 10$ in Si have been performed at 50K, namely: 30 keV Li^+, 30 keV B^+, 40 keV C^+, 60 keV O^+, and 80 keV Ne^+. The ion velocities lie in the range 0.34 to 0.64 v_B, where v_B is the Bohr velocity, i.e.: well within the region of predicted velocity-proportionality of the electronic stopping. Peak damage levels were 30-50%. The profiles have been fitted by adjusting the ratio k/k_L until the total damage depths agree.[38] The actual fitting procedure has used a Monte Carlo code[70] to

generate the theoretical profiles. Fig. 6.5 is the ratio, k/k_L, for $1 \leq Z_1 \leq 10$. The values from the He^+ and N^+ data of Figs. 6.2 and 6.3 are included, as well as that from the H^+ data of Ref. 114. These values are averaged over the stopping path lengths encountered as the ion is brought to rest, as distinct from monoenergetic stopping values. The error bars indicate the predicted standard deviation error in the measurements. Included in Fig. 6.5 are monoenergetic foil transmission measurements[115] for He^+ in aluminum. Qualitative agreement in the Z_1-dependent oscillatory behaviour is observed.

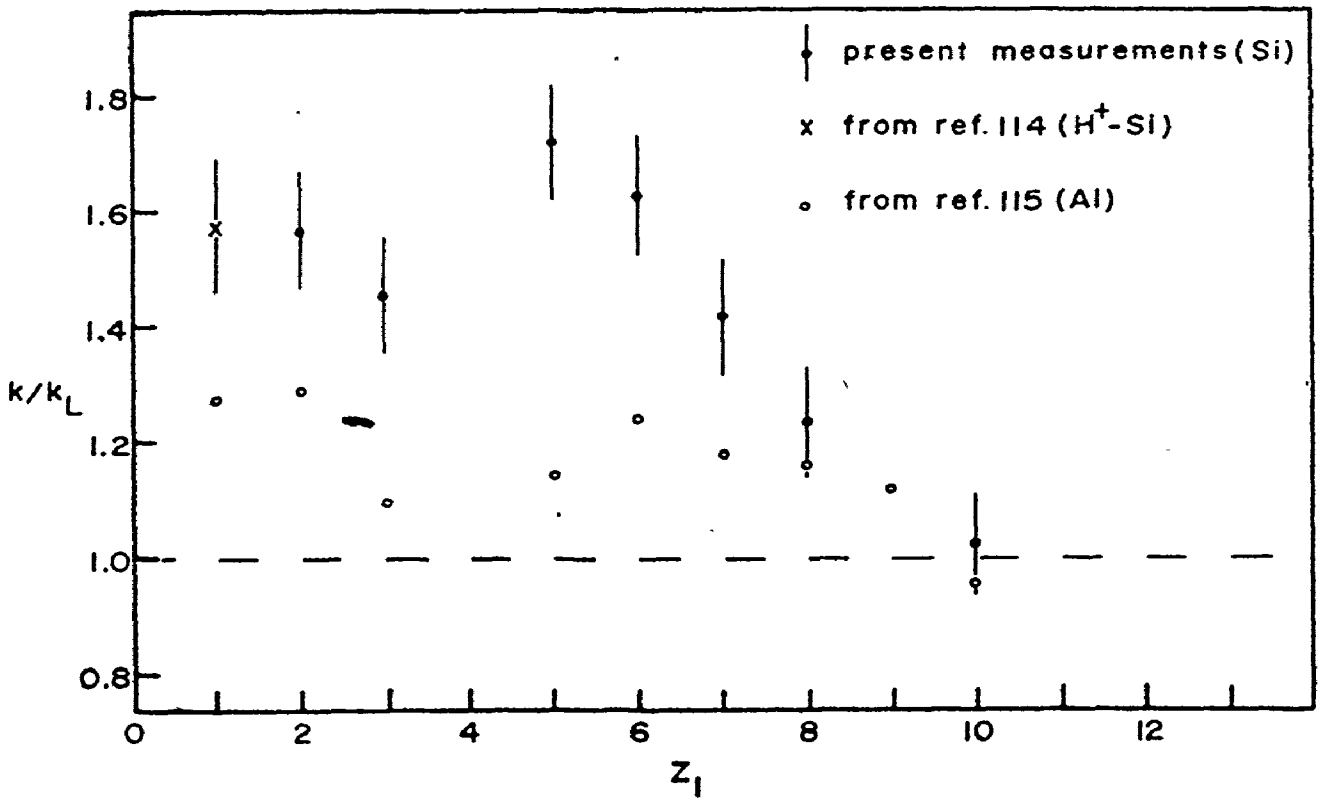

Fig. 6.5: (k/k_L) as a function of Z_1.

In Figs. 6.2-6.5, good agreement is obtained in the shapes of the normalized profiles as measured along the <111> and <110> directions. This result gives confidence in the analysis method since χ_{min}'s for the <111> and <110> spectra differed by as much as 40-50%. Secondly, it tends to justify the use of non-aligned stopping powers in the depth scale conversion, at least at the damage levels reported. Since the stopping powers along <111> and <110> differ for undamaged crystal (see Sec. 4.2.2), the use of non-aligned values would produce a difference ($\sim$10% for He^+ in Si) between the profile depths obtained along both directions if the aligned values were appropriate. There appears to be no such consistent deviation in the data for peak damage levels $\gtrsim$15%.

The profile shapes, however, were found to be weakly dependent on dose. At peak damage levels $\lesssim$15%, the profiles were shallower by $\lesssim$10%. This could well be related to the above arguments concerning the use of non-aligned stopping powers, but the poorer statistics associated with the lower damage levels mean larger inaccuracies. For peak damage levels between $\sim$15% and 70%, the profile shape was unchanged. At higher damage levels, saturation effects were manifested by a broadening of the profiles.

6.3 The "Off-Axis" Effect

In Sec. 4.3.3, it was noted that the number of displaced atoms, $N_d(z)$ measured by the channeling-backscattering technique is the result of weighting the actual radial displaced atom distribution, $G(x,y,z)$ by the channeled beam flux distribution, $F(x,y,z)$, i.e.:

$$\frac{N_d(z)}{N} = \int_A G(x,y,z)F(x,y,z)dA \quad , \tag{4.27}$$

where A is the area of the channel sampled by the beam and N is the atom density. It is possible to obtain information on $G(x,y,z)$ by measuring $N_d(z)$ for different values of area, A. This requires that $F(x,y,z)$ is constant over A, i.e.: flux peaking is not important. Arguments supporting this assumption have been given in Sec. 4.3.3.

One particularly convenient method of varying A in a controlled manner is to vary the mean transverse energy, $E_\perp$, of the channeled beam by tilting the crystal to some small angle, ψ_{in}, relative to the best-alignment condition. The change in transverse energy, $\Delta E_\perp$, becomes:

$$\Delta E_\perp = E\psi_{in}^2 \quad , \tag{6.1}$$

where E is the beam energy. The approach distance, r, of the channeled beam to the lattice row, and hence the area sampled, may be determined by equating the total transverse energy to the string potential, $U(r)$, i.e.:

$$U(r) - U_{min} = E\psi_{in}^2 + \Delta E_\perp' \quad , \tag{6.2}$$

where U_{min} adjusts the potential so that it is zero at the potential minimum. The factor, $\Delta E_\perp'$, accounts for the additional increase in transverse energy due to multiple scattering from the radiation damage, inelastic scattering, finite beam collimation, etc.

Recently, the angular dependence of the channeled backscatter yield has been obtained in Si irradiated at room temperature with 300 keV N^+.[116] The analysis did not consider the additional multiple scattering components listed above. The observed increase in the extracted damage profiles for increasing ψ_{in} was correlated to a non-uniform distribution of defects across

the channel. The distribution was strongly peaked towards the lattice row, indicative of the atom relaxations resulting from the lattice strains necessary to accommodate the damage. Similar effects have been observed[117] following 300 keV D^+ bombardments of Si and Ge. The above suggest that the result is characteristic of at least light ion damage, and that lattice strains may contribute to $N_d(z)$. Discussed in this section, is the investigation[118] of this "Off-Axis" effect, i.e.: the dependence of $N_d(z)$ on ψ_{in}, as measured at 50K in Si, GaP and GaAs bombarded with low-mass ions (He^+, N^+ and Zn^+) in the 20-40 keV region.

Channeled backscatter spectra have been taken for misalignments of 0.18 ψ_1 and 0.36 ψ_1, where ψ_1 is defined in Eq. (4.4). These misalignments range from 0.11° to 0.44°. Measurements have been taken for peak damage levels ~10% and ~50% for the He^+ and N^+ induced disorder and at somewhat higher levels in the Zn^+ bombardments. The goniometer precision is estimated at ±0.025°.

Since as noted in the previous section, damage levels measured along the <111> and <110> directions agreed within $\lesssim$10%, the reported data are the average of both directions, unless otherwise stated. Fig. 6.6a,b give the aligned and 0.4° misaligned spectra obtained from 40 keV N^+ bombarded GaP for doses of 3.4×10^{13} N/cm^2 and 8.2×10^{13} N/cm^2 respectively, together with the corresponding unirradiated spectra. The calculated dechanneling lines generated using the semi-empirical single-scattering dechanneling technique described in Sec. 4.3.2 are included. To examine the possibility that the "Off-Axis" effect is an artifact of an incorrect dechanneling calculation, a dechanneling line has been determined for which the "Off-Axis" profile could be forced to fit the profile found under best

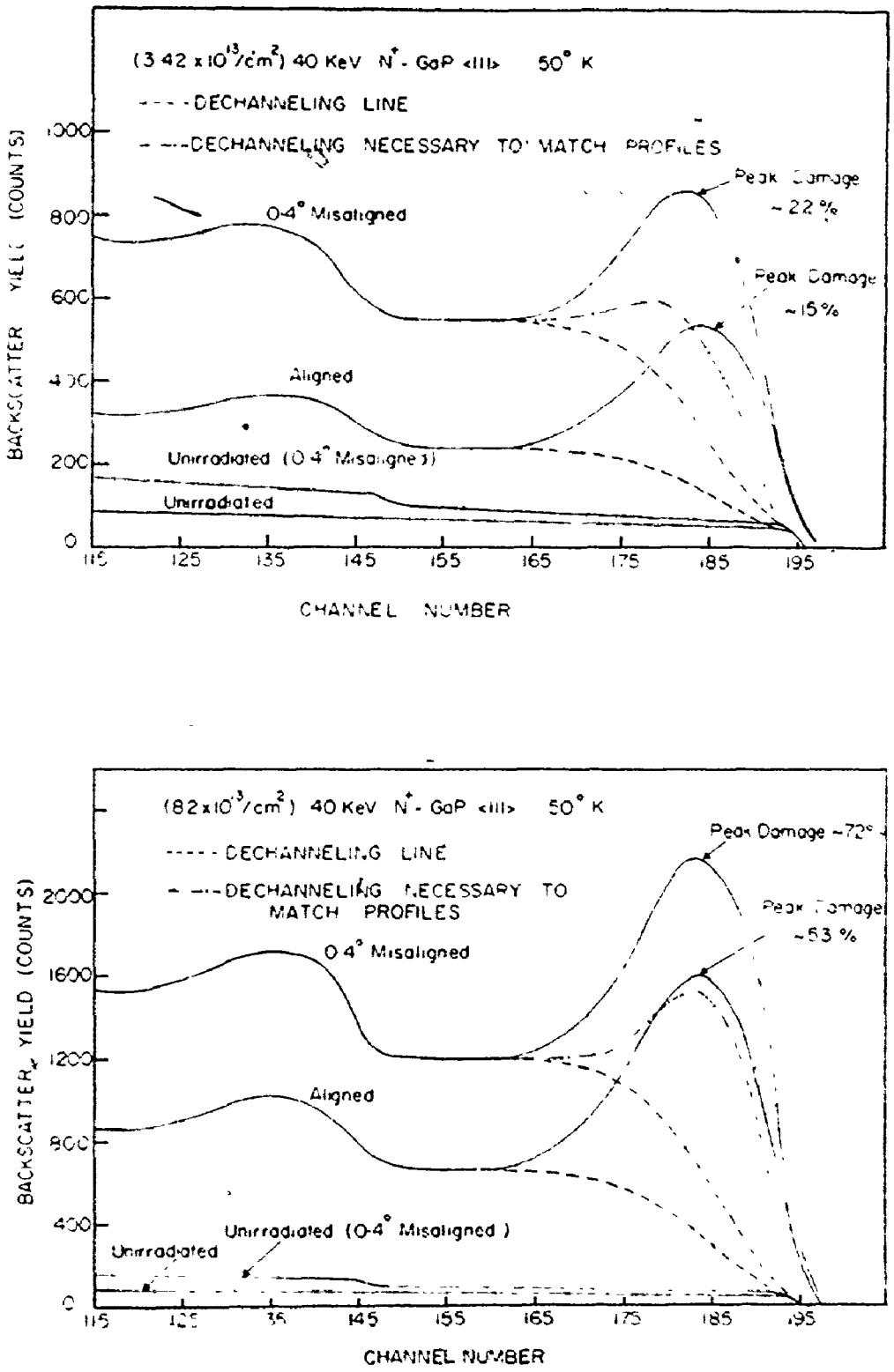

Fig. 6.6: He backscatter spectra from GaP for best alignment <111> and for 0.4° misalignment before and after 40 keV N^+ bombardment (a) N^+ dose 3.42×10^{13} cm^{-2}, and (b) 8.2×10^{13} cm^{-2}.

alignment conditions. These modified dechanneling lines are included in Fig. 6.6a,b. Clearly, such a dechanneling line is physically meaningless since it is required to exceed χ_{min}.

Spectra similar to those of Fig. 6.6 have been measured for all other ion-target systems and the damage profiles extracted where the detector resolution allowed. For the Zn^+ bombardments, only the total disorder, N_D, has been obtained. Fig. 6.7 shows typical damage profiles for best alignment ($\psi_{in} = 0$) and both "Off-Axis" tilts for a GaAs sample bombarded with $4.1 \times 10^{14}/cm^2$ of 30 keV He^+. A dramatic increase in the damage can be seen for the "Off-Axis" analyses. The results of the cases investigated are given in Tables 6.1a,b. The data from the Zn^+ bombardments are separated (Table 6.1b) since the detector resolution did not enable the peak damage to be measured; therefore, a mean damage is given as the percent damage referenced to the extrapolated saturation level. In both tables, the magnitude of the total "Off-Axis" effect, $\Delta N_D/N_D$, integrated over the damage depth, is given. Several features of the data are noteworthy:

(a) $\Delta N_D/N_D$ increases with misalignment and the rate of increase is non-linear, i.e.:

$$\frac{\Delta N_D/N_D(\psi_{in} = 0.36\ \psi_1)}{\Delta N_D/N_D(\psi_{in} = 0.18\ \psi_1)} > 2 \quad .$$

(b) In the cases where the "Off-Axis" effect is greater than the estimated relative experimental error of ~0.05-0.1, the magnitude and the non-linearity of the effect generally decreases at the higher damage levels. However, even with peak damage levels of 50-60%, the "Off-Axis" effect still exists. For still higher damage levels (i.e. ≳80% peak damage), no effect was observed.

Table 6.1: Magnitude of the "Off-Axis" damage increase.

(a) For He^+ and N^+ irradiations.

Target	Peak Damage %	Bombarding particle			
		He^+		N^+	
		$\frac{\Delta N_D}{N_D}\left[\frac{\psi_{in}}{\psi_1} = 0.18\right]$	$\frac{\Delta N_D}{N_D}\left[\frac{\psi_{in}}{\psi_1} = 0.36\right]$	$\frac{\Delta N_D}{N_D}\left[\frac{\psi_{in}}{\psi_1} = 0.18\right]$	$\frac{\Delta N_D}{N_D}\left[\frac{\psi_{in}}{\psi_1} = 0.36\right]$
Si	8-12	0.03	0.29	0.01	0.18
	50-60	0.08	0.26	0.10	0.30
GaP	8-12	0.28	1.00	0.13	0.48
	50-60	0.12	0.30	0.14	0.35
GaAs	8-12	0.22	0.86	0.21	0.65
	50-60	0.17	0.36	0.16	0.30

(b) For Zn^+ irradiations.

Target	Mean Damage %	$\frac{\Delta N_D}{N_D}\left[\frac{\psi_{in}}{\psi_1} = 0.18\right]$	$\frac{\Delta N_D}{N_D}\left[\frac{\psi_{in}}{\psi_1} = 0.36\right]$
Si	15-20	0.08	0.26
	60-70	0.11	0.19
GaP	15-20	0.09	0.48
	60-70	0.07	0.23
GaAs	15-20	0.08	0.29
	60-70	0.03	0.14

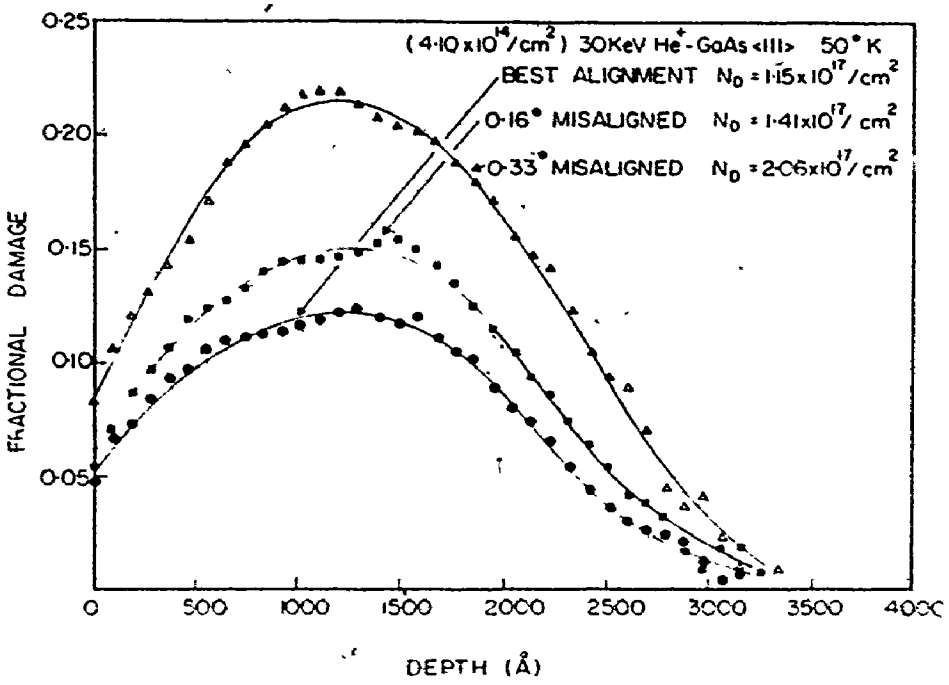

Fig. 6.7: Damage profiles for GaAs bombarded at 50K with 30 keV He^+ extracted from best alignment conditions and for various degrees of misalignment.

(c) In the case of GaP and GaAs, the "Off-Axis" effect decreases as the mass of the bombarding ion increases.

(d) $\Delta N_D/N_D$ is a factor ~3 greater in GaP and GaAs than in Si under low dose He^+ and N^+ irradiations.

Figure 6.6a,b also reveal that χ_{min}, as measured immediately behind the damage peak, increases significantly as the misalignment is increased.

In general, it was found that $\Delta\chi_{min}/\chi_{min} \sim 2\Delta N_D/N_D$. Such a strong dependence of the dechanneling on N_D is not apparent in any of the amorphous scattering models considered in Sec. 4.3.2. This supports the concept proposed in that section that an additional dechanneling component results from correlated scattering from the lattice strain. The effect influences the dechanneling much more strongly than direct backscatter, and therefore accounts for the more rapid increase in χ_{min} as ψ_{in} is increased.

For the He^+ and N^+ damage profiles, the "Off-Axis" effect has also been investigated as a function of damage depth. Shown in Table 6.2 is the fractional increase in $N_d(z,\psi_{in})$, for $\psi_{in} = 0.36\ \psi_1$, relative to $N_d(z,0)$ as measured at three points on the profile - the peak and 50% maximum damage levels on either side of the peak. At low damage levels (~10% peak damage) the trend is an increase in $\Delta N_d/N_d$ with depth. At high dose the increases at the half-maxima are comparable, while that at the peak is slightly less.

The above observations can be discussed quantitatively if certain simplifying assumptions are made. Firstly, a cylindrical symmetry of the <111> and <110> channels is assumed, so that Eq. (6.1) becomes:

$$\frac{N_d(z)}{N} = \int_o^{r_o} G(r,z)F(r,z)2\pi r dr \ , \qquad (6.3)$$

with r being the perpendicular distance from the channel row and r_o the channel radius, e.g.:

$$r^2_{o<111>} = 1/(Nd_{<111>}) \ . \qquad (6.4)$$

Secondly, the flux distribution, $F(r,z)$ is approximated by a rectangular distribution, i.e.: F_r is a constant in the radial interval r_o to r, with

Table 6.2: Damage profile dependence of "Off-Axis" effect for $\psi_{in} = 0.36\ \psi_1$

Target	Peak Damage %	$\frac{\Delta N_d(z)}{N_d(z)}$ (He^+ irradiation)				$\frac{\Delta N_d(z)}{N_d(z)}$ (N^+ irradiation)			
		Shallow 1/2 max	Peak	Deep 1/2 max	Profile Mean	Shallow 1/2 max	Peak	Deep 1/2 max	Profile Mean
Si	∿10	0.22	0.24	0.34	0.28	0.11	0.18	0.26	0.18
	∿50	0.26	0.22	0.32	0.26	0.32	0.28	0.35	0.30
GaP	∿10	0.56	0.97	1.48	0.99	0.10	0.49	0.75	0.45
	∿50	0.48	0.18	0.32	0.29	0.37	0.40	0.35	0.35
GaAs	∿10	0.62	0.79	1.04	0.84	0.30	0.61	0.87	0.69
	∿50	0.45	0.25	0.37	0.34	0.34	0.27	0.31	0.31

r given by Eq. (6.2), and zero elsewhere. This implicitly assumes that the flux has reached a statistical equilibrium and that flux peaking is not important. For unirradiated crystal, the former condition is satisfied at a distance of ~1000Å.[16] However, multiple scattering of the channeled particles due to the presence of defects will cause a more rapid approach to equilibrium as well as causing a smearing[119] of any flux peaking. The rapid decrease in flux at radii < r justifies the rectangular approximation.[116] Normalization of the flux requires:

$$F_r \pi (r_o^2 - r^2) = 1 \quad . \tag{6.5}$$

The solution of Eq. (6.2) for r requires an estimate of the additional increase in transverse energy due to the finite beam collimation, inelastic multiple scattering, and elastic multiple scattering from any amorphous surface layer, thermal vibrations and radiation damage. Since the experiments have been performed at 50K, the thermal vibration contribution to $E_\perp$ is ignored. The other components are calculated in the following manner:

(i) Beam collimation. For a half-angular beam divergence, ψ_{coll}, the increase in transverse energy $\delta E_\perp$ is $\delta E_\perp = E\psi_{coll}^2/3$.[119] For the experimental $\psi_{coll} = 0.038°$, and E = 1.0 MeV, $\delta E_\perp = 0.14$ eV.

(ii) Inelastic multiple scattering. The increase in transverse energy is assumed directly proportional to the energy lost via inelastic collisions,[119] i.e.:

$$\delta E_\perp = \frac{m_e}{M_1} \left(-\frac{\partial E}{\partial z}\right)_{inel} \cdot z \quad , \tag{6.6}$$

where m_e and M_1 are the electron and ion masses respectively. $(-\partial E/\partial z)_{inel}$ is the experimentally measured inelastic stopping power. The random stopping powers of Ziegler and Chu[86] have been used. The appropriate values for Si and GaAs are included in Table 6.3.

(iii) Scattering from amorphous surface layers and radiation damage. In both these cases, a single scattering model[92] has been employed, with the increase, $\delta E_\perp$, in transverse energy for N' scattering centers per unit area, becoming:

$$\delta E_\perp = E\langle\theta^2\rangle N' \quad , \tag{6.7}$$

where

$$\langle\theta^2\rangle = \int_0^{\psi_1} \theta^2 d\sigma \quad , \tag{6.8}$$

and $d\sigma$ is the nuclear scattering cross-section for the channeled particle single scattering. The upper limit has been chosen to include only scattering within ψ_1, that is, only those particles which remain channeled are considered. Table 6.3 gives $\langle\theta^2\rangle$ for 1.0 MeV and 1.5 MeV He^+ in Si and GaAs as calculated using the piece-wise power cross-section approximation to the Thomas-Fermi cross-section (see Sec. 2.2.2). The values are within ~10% of those obtained from the complete numerical integration[92] of the Thomas-Fermi

cross-section. The increase, $\delta E_{\perp}$ (surface), in transverse energy due to the estimated surface scattering in Si and GaAs appears in Table 6.3.

Table 6.3: Parameters used in determination of the defect and inelastic multiple scattering in Si and GaAs.

Substrate	He^+ Energy (MeV)	$(-\frac{\partial E}{\partial z})_{inel}$ eVÅ^{-1}	Direction	$10^{22}\langle\theta^2\rangle$ (rad^{2}cm^2)	$\delta E_{\perp}$ (surface) (eV)
Si	1.0	33.2	<111>	1.56	0.94
			<110>	1.67	1.00
	1.5	28:7	<111>	0.79	0.71
			<110>	0.83	0.75
GaAs	1.0	36.4	<111>	4.84	1.45
			<110>	5.33	1.60
	1.5	33.9	<111>	2.65	1.19
			<110>	2.93	1.32

For the He^+ and N^+ induced damage profiles, r may be calculated from Eq. (6.2) using the above estimates of $\Delta E_{\perp}'$ and for each tilt angle, ψ_{in}. The Lindhard continuum potential,[16] defined by Eq. (4.3), has been chosen to define U(r). For cylindrical symmetry of the channel, U_{min} occurs at $r = r_o$. Three values of r, i.e.: r_1, r_2, r_3, can be generated at ψ_{in} = 0, 0.18 ψ_1, 0.36 ψ_1, respectively. The average radial defect distribution, $G((r_i+r_{i-1})/2, z)$, over each radial interval can be obtained using Eqs.

(6.3)-(6.5), i.e.:

$$G\left(\frac{r_o + r_1}{2}, z\right) = \frac{N_d(z,0)}{N} \quad , \tag{6.9}$$

$$G\left(\frac{r_1 + r_2}{2}, z\right) = \frac{\frac{N_d(z,\ 0.18\ \psi_1)}{N}\pi(r_o^2 - r_2^2) - \frac{N_d(z,\ 0)}{N}\pi(r_o^2 - r_1^2)}{\pi(r_1^2 - r_2^2)} \quad , \tag{6.10}$$

$$G\left(\frac{r_2 + r_3}{2}, z\right) = \frac{\frac{N_d(z,\ 0.36\ \psi_1)}{N}\pi(r_o^2 - r_3^2) - \frac{N_d(z,\ 0.18\ \psi_1)}{N}\pi(r_o^2 - r_2^2)}{\pi(r_2^2 - r_3^2)} \quad . \tag{6.11}$$

Shown in Fig. 6.8 are the calculated G(r,z), with z equal to the most probable damage range, for the He^+ and N^+ low-damage distributions in Si and GaAs. The GaP results are comparable to those for GaAs. Both <111> and <110> analyses are included, and the values are plotted with respect to the fractional distance to the channel center. The Thomas-Fermi screening radius, a, relative to the <111> direction, is indicated for comparison. The Zn^+ damage data correspond to the average G(r) integrated over z, with $N_d(z)/N$ of Eqs. (6.9)-(6.11) replaced by N_D/N_{sat}, N_{sat} being the extrapolated saturation damage level. The extension of G(r,z) to values greater than unity at small r in GaAs indicates the limitations of the approach. The horizontal error bars correspond to the error introduced in r by an error in ψ_{in} of ±0.025°, combined with the estimated ±5% error in both N_D and z. The latter parameters enter into the defect and inelastic multiple scattering calculations. The vertical error bars represent a ±5% error in $N_d(z)/N$. The relevant observations are:

(1) As suggested by the previous observations,[116,117]

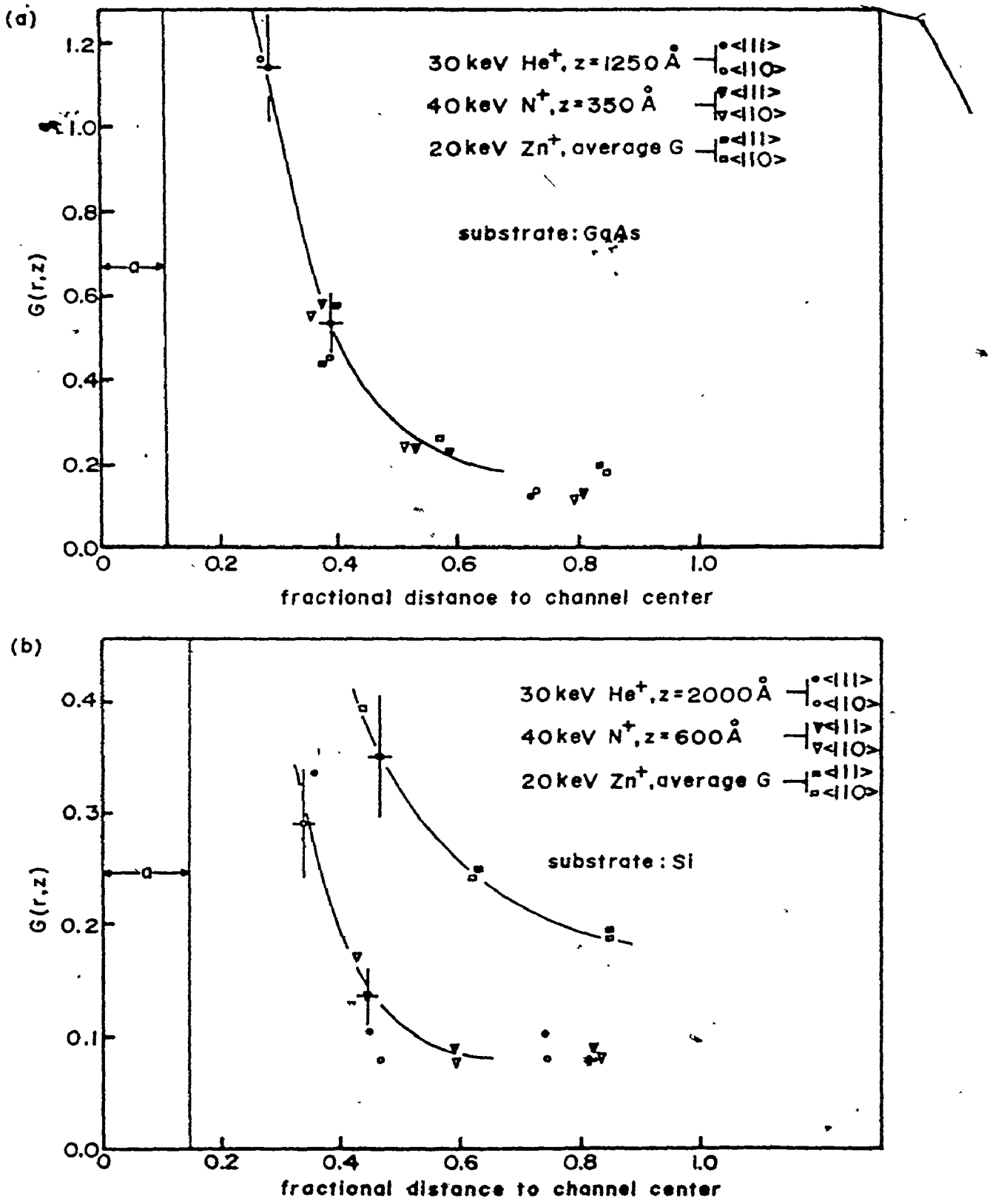

Fig. 6.8: Radial distribution of displaced atoms, G(r,z) in (a) GaAs, (b) Si. Both <111> and <110> analyses are included.

$G(r,z)$ increases as the lattice row is approached. This is apparently due to the atom relaxations resulting from the lattice strains necessary to accommodate the damage.

(ii) The relaxations extend inward in both Si and GaAs by up to $\sim 0.4\ r_o$, at least at the $\sim$10% peak damage level. There appears to be no significant directional dependence of the strains. However, the amount of strain is somewhat greater in GaAs than in Si, although the difference is much less than that suggested by the data of Table 6.1, once the corrections are applied for the multiple scattering processes. It is suggested that the additional ionic nature of the crystal bonds in the III-V compounds could result in the greater observed atom relaxations.

(iii) At low damage levels, and for $\psi = 0$, the strains will contribute in only a small way to the direct backscatter yield. This is because the beam is effectively confined to the central region of the channel ($0.5\ r_o \lesssim r \lesssim r_o$), into which the strains do not extend.

(iv) The shape of $G(r,z)$ is essentially independent of M_1, within the error limits, for the three ions studied. Thus the apparent M_1 dependence of the "Off-Axis" effect in the data of Table 6.1 is largely a consequence of the fact that a greater area is sampled by the beam for the lighter ion bombardments, due to the increased

defect and inelastic multiple scattering. The lack of mass dependence is interesting since one would have expected more strains to be associated with the simpler and more isolated defects that are produced in the lighter ion cascades. However, at 10% damage levels, and in the absence of defect annealing, the features of the individual cascades for these light ions will be smeared, since cascades are required to overlap in order to achieve the measured damage level. This is evident if we examine the fractional damage, F_D, contained within these individual cascades; F_D is defined in Eq. (7.5). For example, for 40 keV N^+-Si, $F_D \sim 0.002$, while for 20 keV Zn^+-Si, it is increased to $\sim$0.03. Thus, in order to measure a damage level of $\sim$0.10, cascade overlap is required, with the result that a fairly homogeneous defect distribution will exist over the bombardment area. Once the features of the individual cascades are smeared, the mass independence of the strains is reasonable. For heavier ion implants, where the damage consists more of highly-damaged, or amorphous, zones a mass dependence would be expected to develop, at least at low damage levels, since the individual cascades will remain fairly isolated. Then since less strain would be associated, per defect, with the defects of an amorphous cluster, the average amount of strain should diminish. This point will be discussed further in the following section. It is emphasized that

the lack of a mass dependence in $G(r,z)$ is not attributed to a similarity of the damage structures for the ions studied, but rather results from the gross averaging behaviour of the channeling technique itself.

It was observed that at low damage levels, the "Off-Axis" effect increases with depth (see Table 6.2). Plotted in Figs. 6.9 and 6.10 is the relative increase in the radial distribution of displaced atoms, $\Delta G/G$, with respect to $G((r_0+r_1)/2, z)$, for He^+ and N^+ bombardment of Si and GaAs respectively. In each instance, $\Delta G/G$ has been obtained at the three depths for which the data of Table 6.2 has been generated, i.e.: the depth at maximum damage, and the 50% maximum damage levels. The error bars indicate the same errors as in Fig. 6.8. Both <111> and <110> directions have been analyzed. No significant depth dependence of $\Delta G/G$ is apparent in the data. Therefore, the depth dependence of the "Off-Axis" effect exhibited in the damage profiles is mainly the result of the increasing area sampled by the beam as it penetrates the damage layer, because of defect and inelastic scattering. In both Si and GaAs, $\Delta G/G$ is essentially identical for He^+ and N^+ bombardment, again showing the insensitivity of the channeling technique to the features of the defect structures.

It was noted with regard to Tables 6.1 and 6.2 that the "Off-Axis" effect persists to peak damage levels of 50-60%. One can attempt to explain this observation in two ways:

(i) Assume that the damage is heterogeneously distributed as heavily-damaged regions surrounded by lightly damaged crystal. Channeling remains defined only

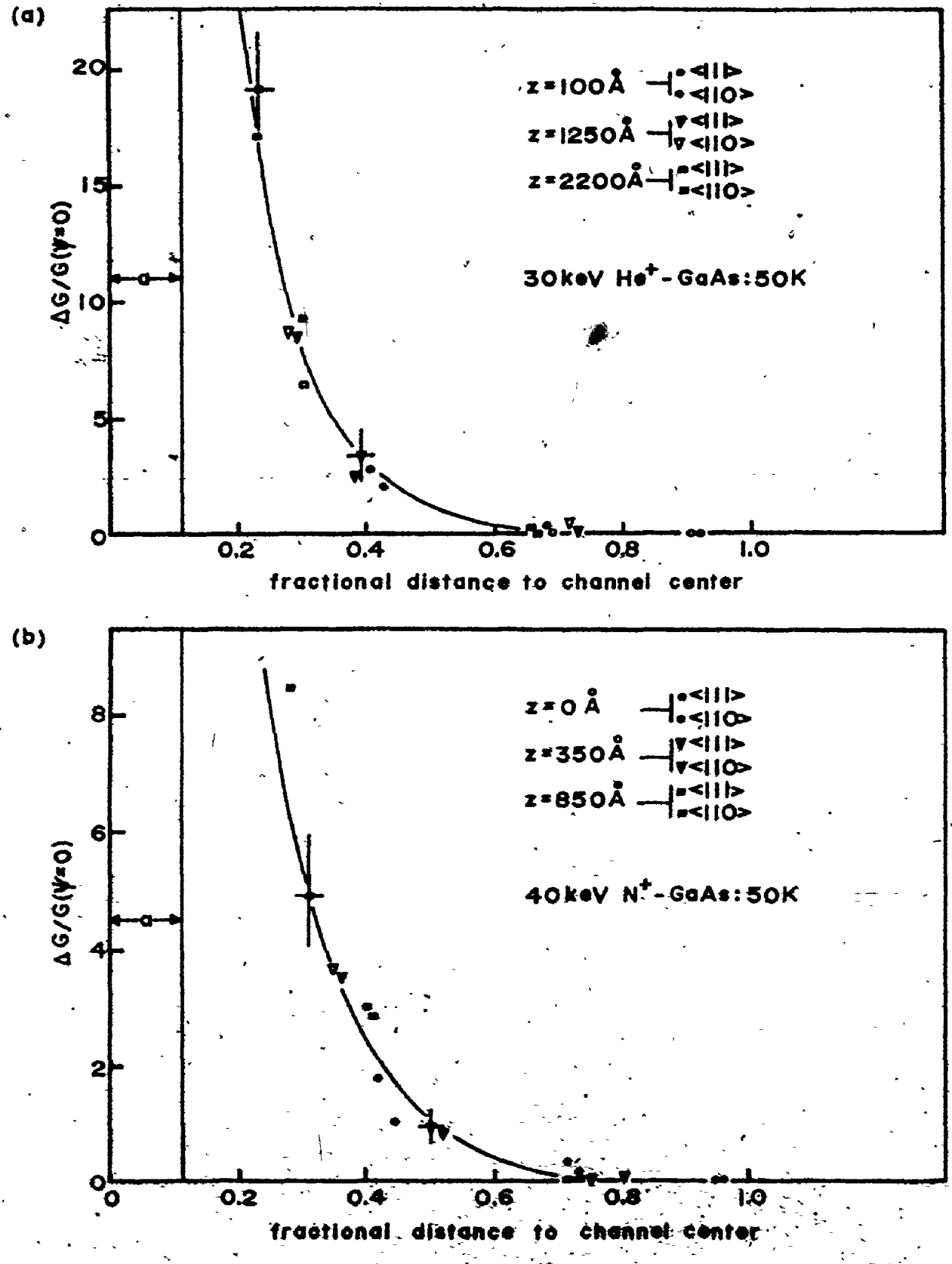

Fig. 6.9: Relative increase in the radial distribution of displaced atoms at various depths in GaAs at 50K for (a) 30 keV He^+ irradiation, (b) 40 keV N^+ irradiation.

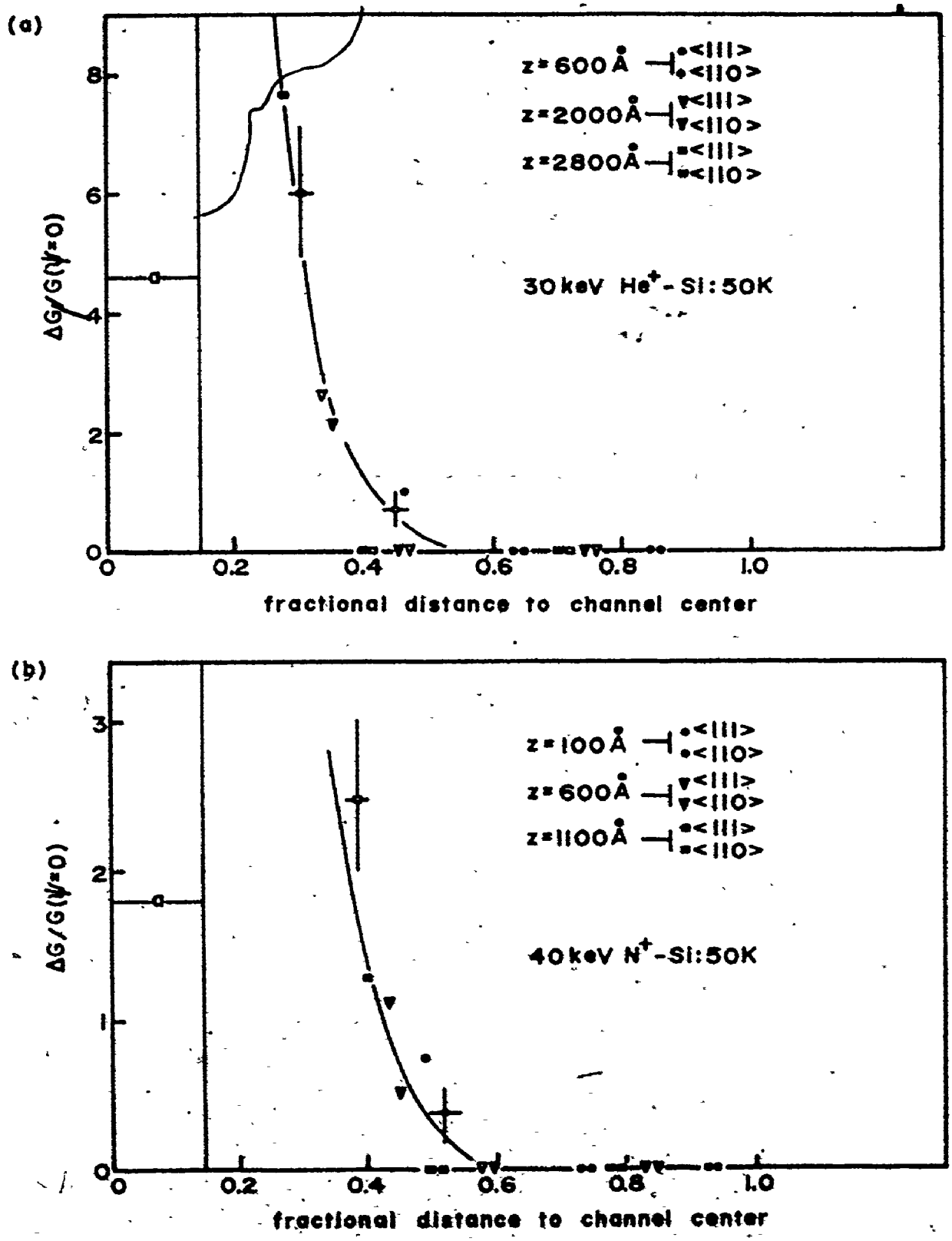

Fig. 6.10: Relative increase in the radial distribution of displaced atoms of various depths in Si at 50K for (a) 30 keV He^+ irradiation, and (b) 40 keV N^+ irradiation.

in the latter volume and the "Off-Axis" effect results from lattice strains in this region alone. The magnitude of the effect reflects the relative amount of heavily to lightly damaged material.

(ii) Assume the damage is relatively homogeneously distributed across the bombardment volume. Then lattice strains account for the "Off-Axis" effect in the same manner as at lower damage levels. Its decrease in magnitude can result from increasing atom relaxations so that G(r,z) is less steep, as well as to the weakening of the channeling mechanism itself as the critical angle decreases at the high damage levels.

The latter model is considered more correct for the lighter ion irradiations, e.g.: He^+, N^+ (although a certain amount of heterogeneous amorphous structure has been observed by electron microscopy[45,46] even for such light ions). A combination of both models may be relevant for heavier ion bombardment.

Since channeling is defined at 50-60% peak damage levels (i.e.: the "Off-Axis" effect is still present), the measured $N_d(z)$ at the high damage levels cannot correspond to only those atoms displaced by the collision cascade. For instance, at 50% measured peak damage, if one atom in two was actually significantly displaced, channeling would be expected to be completely destroyed and a backscatter yield characteristic of an amorphous target should be approached. Since channeling does exist, $N_d(z)$ must consist of the actual damage created as a result of the ion irradiation,

plus an additional component; the most obvious explanation for the additional component is backscatter from the atom relaxations due to the lattice strains, since they are attributed to the "Off-Axis" effect. However, at sufficiently low damage levels ($\lesssim$10% peak damage) the observations related to Figs. 6.8-6.10, indicate the atom relaxation contribution is minimal under best-alignment conditions. These suggestions are consistent with the observed damage-dose behaviour given in the next section.

6.4 Damage Versus Ion Dose

After prolonged ion bombardment of the semiconductors at temperatures $\lesssim$ a few hundred °C, it is possible to convert the entire implant volume into the amorphous state. The build-up of damage in the ion-bombarded semiconductors as a function of the ion dose has received considerable attention in the literature.[47,120,121] This has been stimulated by the technological necessity of understanding the amorphization process, since it is known that an ion-implanted semiconductor device will have a lower defect concentration after the anneal (by epitaxial regrowth) of an amorphous layer than after anneal of a more lightly damaged layer.

The understanding of the solid-state phenomena which control the damage rate is not complete. Conflicting models of the processes have been proposed; for example, models calling for the heterogeneous[120] or homogeneous[121] nucleation of local amorphous zones, or for combinations of both[47] have been used to analyze damage-dose behaviour. As well, the determination of the amorphous transition appears to be sensitive to the measurement technique itself.[122]

The majority of the damage-dose measurements have been performed

at or above room temperature, mainly for technological reasons. However, this will significantly complicate the damage-dose behaviour, since defect annealing and nucleation can occur. In this section, the damage-dose relationship is studied in Si, GaP and GaAs at 50K[118] as measured using the channeling-backscattering technique. Defect migration is assumed minimal at this temperature. Ions used in the analysis are the same species employed in the "Off-Axis" measurements of the previous section. Damage data supplied by A. Golanski[123] for 23.5 keV As^+, 15 keV Te^+ and 15 keV Tl^+ bombardments of Si is also examined. It will be shown that an analytical description of the data is possible, provided the contribution from atom relaxations to the measured damage at high dose is included.

Figures 6.11-6.13 show the variation in the measured total number, N_D, of displaced atoms/cm^2 as a function of irradiated dose, ϕ, for the He^+, N^+, and Zn^+ irradiations respectively of the three semiconductors. The solid curves through the data points shall be discussed shortly. For the GaP samples irradiated with He^+ and N^+ it was only possible to accurately determine the Ga damage. Following the Zn^+ bombardments the P damage peak was well resolved and a reasonably accurate (~15%) estimate of the number of displaced phosphorus atoms could be obtained. It was found that $N_D(P)$ agreed with $N_D(Ga)$ within 10% although the P damage was consistently higher (see Fig. 6.13). This equality of the Ga and P damage agrees with measurements[124] of 40 keV Te^+ induced damage in GaP at room temperature.

The significant feature of the He^+ and N^+ damage-dose curves is the non-linear increase in damage in the low-dose region. The high-dose non-linearities are the result of the onset of saturation effects. The

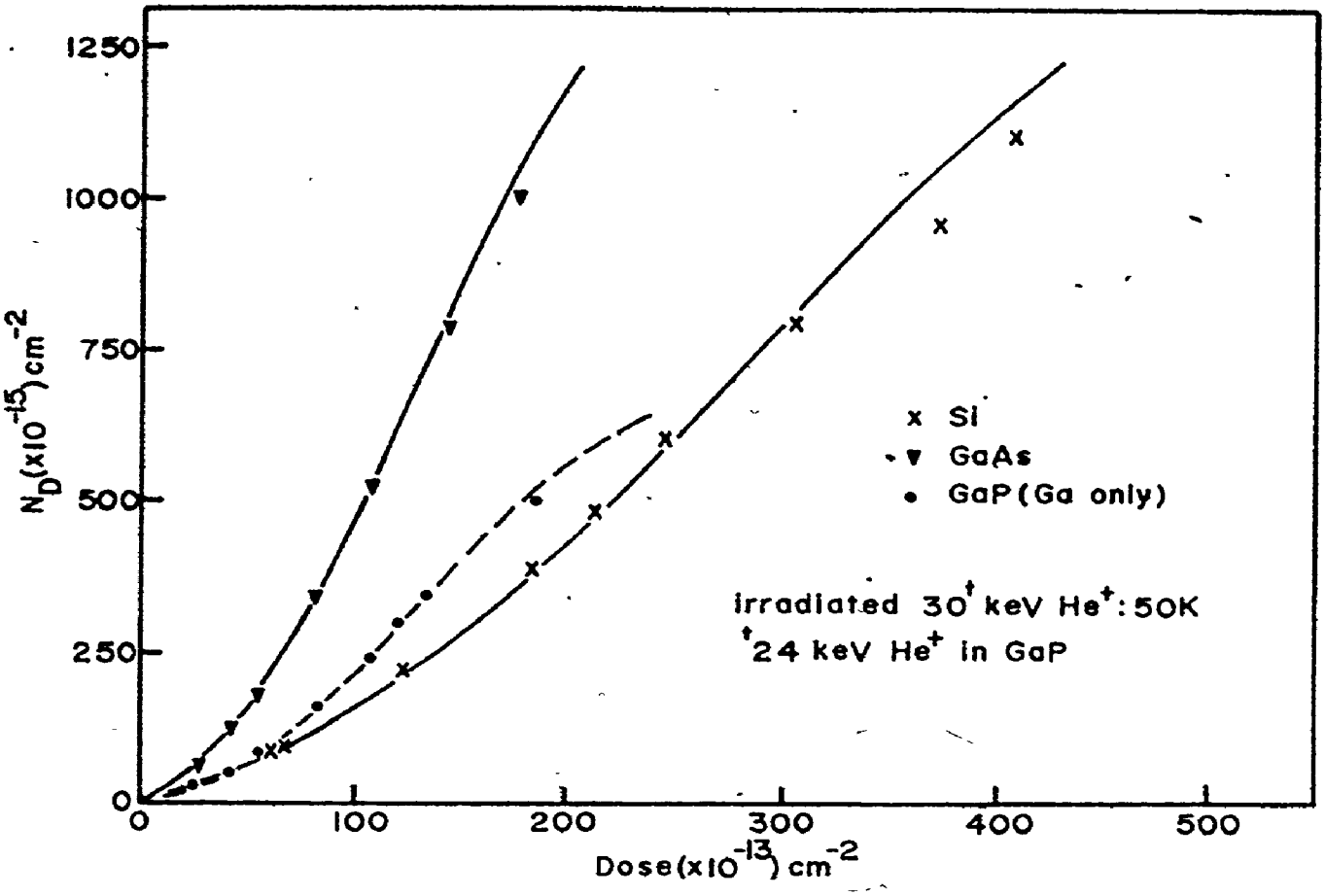

Fig. 6.11: Damage versus He^+ bombardment dose.

former non-linear behaviour has often been observed in room temperature low-Z damage measurements (cf. ref. 47). It is generally attributed to the nucleation of stable defect complexes as the damage increases. At 50K, this cannot account for the non-linearity. In fact, if defect annealing and nucleation cannot occur, the actual number of atoms displaced by the ion-bombardment should be expected to follow the relationship:

$$\frac{dN_D}{d\phi} = N_D^*\left(1 - \frac{N_D}{N_{sat}}\right) , \qquad (6.12)$$

where N_D^* is the number of displacements/ion at the onset of bombardment,

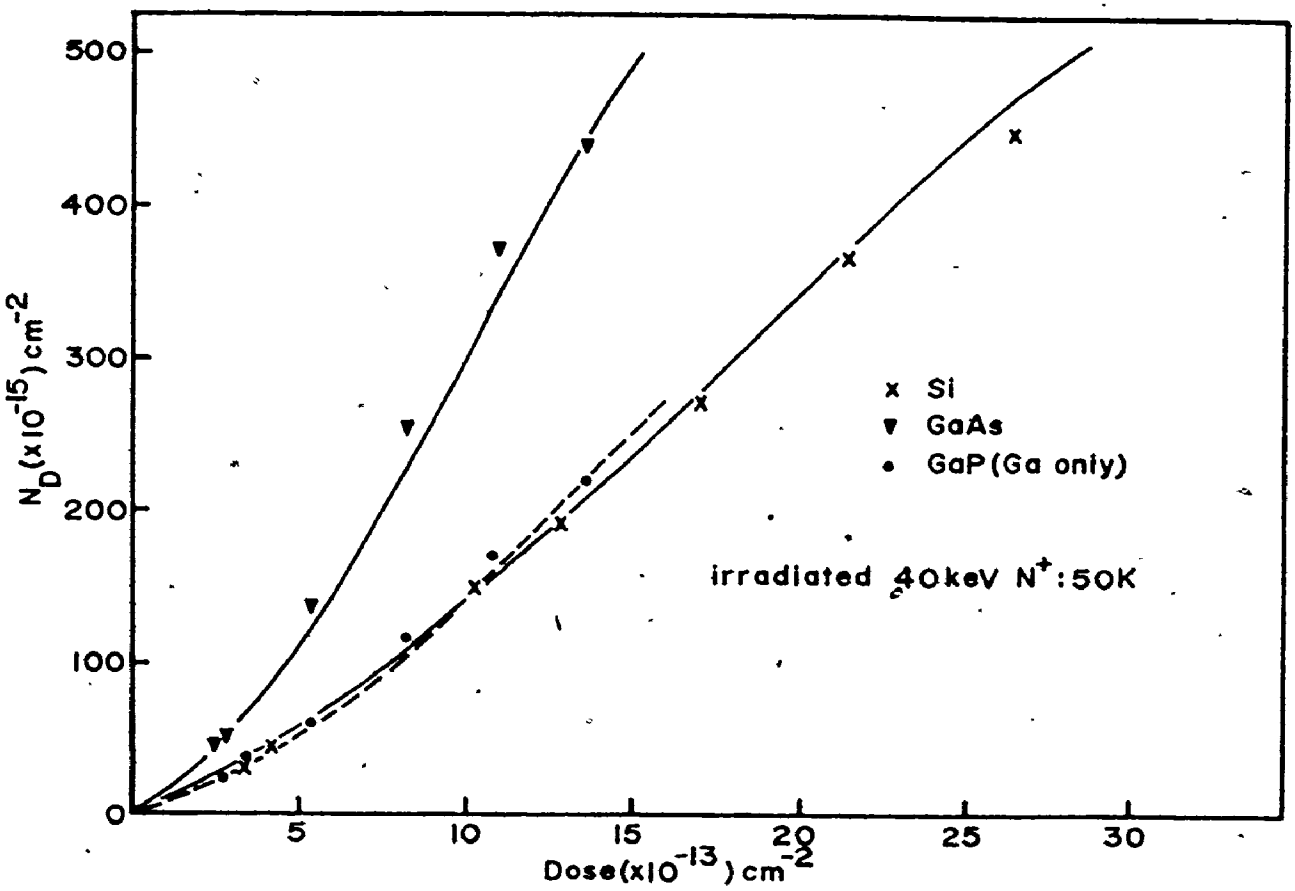

Fig. 6.12: Damage versus 40 keV N^+ bombardment dose.

and N_{sat} is the saturation damage level. The term $(1 - N_D/N_{sat})$ imposes the boundary condition that $dN_D/d\phi \to 0$ as $\phi \to \infty$. The solution of Eq. (6.12) is:

$$N_D = N_{sat}(1 - \exp(-\frac{N_D^* \phi}{N_{sat}}) \quad . \tag{6.13}$$

The development assumes a uniform defect distribution over the implant depth, i.e.: $N_d(z)$ is a constant. If the depth dependence is incorporated, Eq. (6.14) becomes:

$$N_D = N_{sat} - \int_0^R \frac{N_{sat}}{R} \exp(-\frac{N_d^*(z)\phi}{RN_{sat}})dz \quad , \tag{6.14}$$

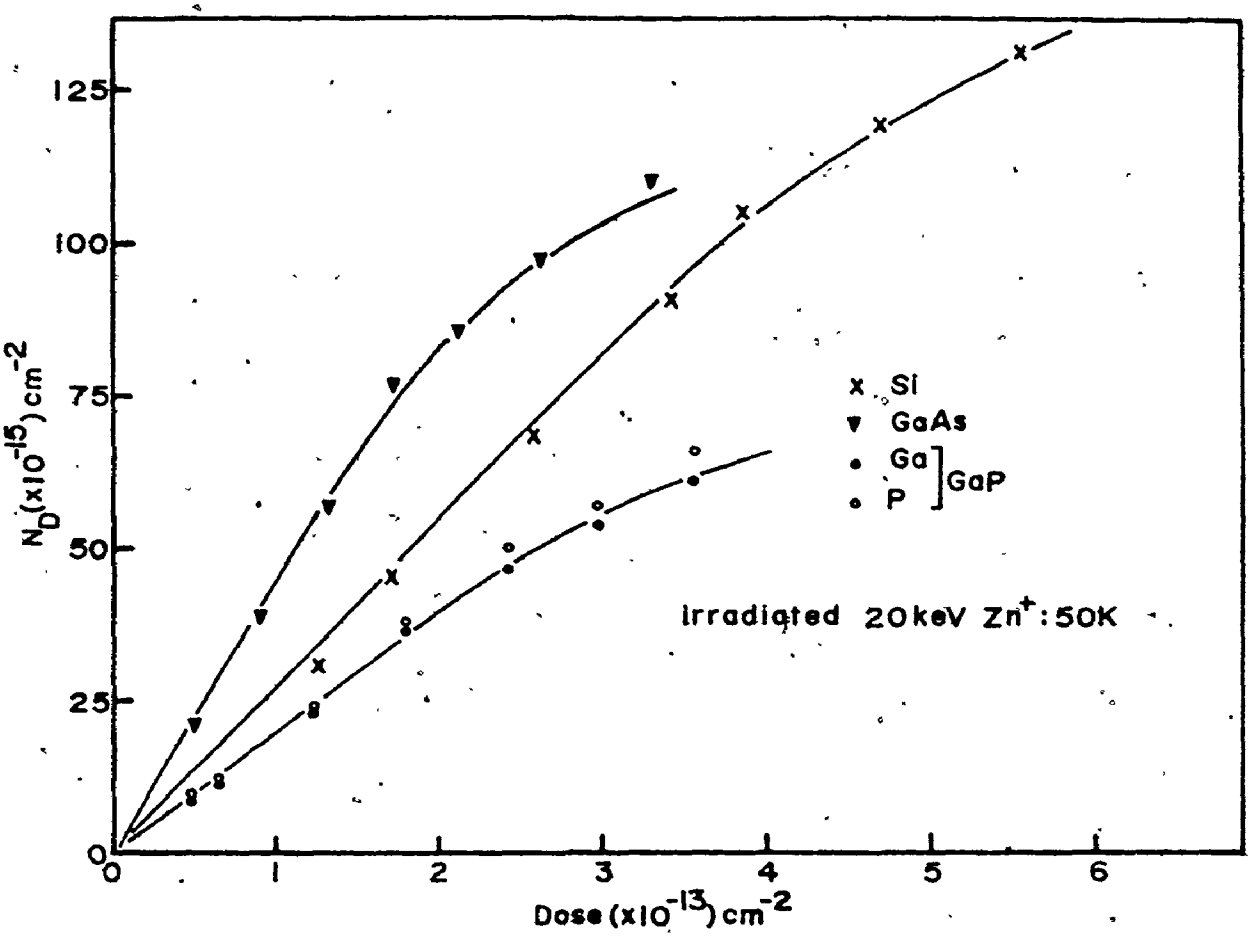

Fig. 6.13: Damage versus 20 keV Zn^+ bombardment dose.

where R is the total damage range. This equation has been examined numerically for a Gaussian distribution of $N_d^*(z)$. The resultant damage-dose curve differs little from the curve obtained for a uniform distribution, provided the integration limit, R, does not extend too far relative to the Gaussian. For example, for $R = 1.5\ \sigma$, where σ is the Gaussian standard deviation, Eq. (6.13) exceeds Eq. (6.14) by at most ~3%; for $R = 2\ \sigma$, the maximum difference increases to ~7%. The depth dependence of the damage has therefore been neglected in the following discussion.

It is obvious that $dN_D/d\phi$ of Eq. (6.12) decreases monotonically

for increasing ϕ, and the observed increase in $dN_D/d\phi$ for low-Z_1 bombardments is not predicted. Even for higher Z_1 bombardments, where $dN_D/d\phi$ does decrease monotonically, the absolute damage-dose behaviour is not satisfied by Eq. (6.13). For example, shown in Fig. 6.14 is the measured damage versus dose for 23.5 keV As^+ in Si,[123] together with the curve defined by Eq. (6.13). The parameters N_D^* and N_{sat} have been taken from the experimental curve. The measured data increase more rapidly than the prediction of Eq. (6.13).

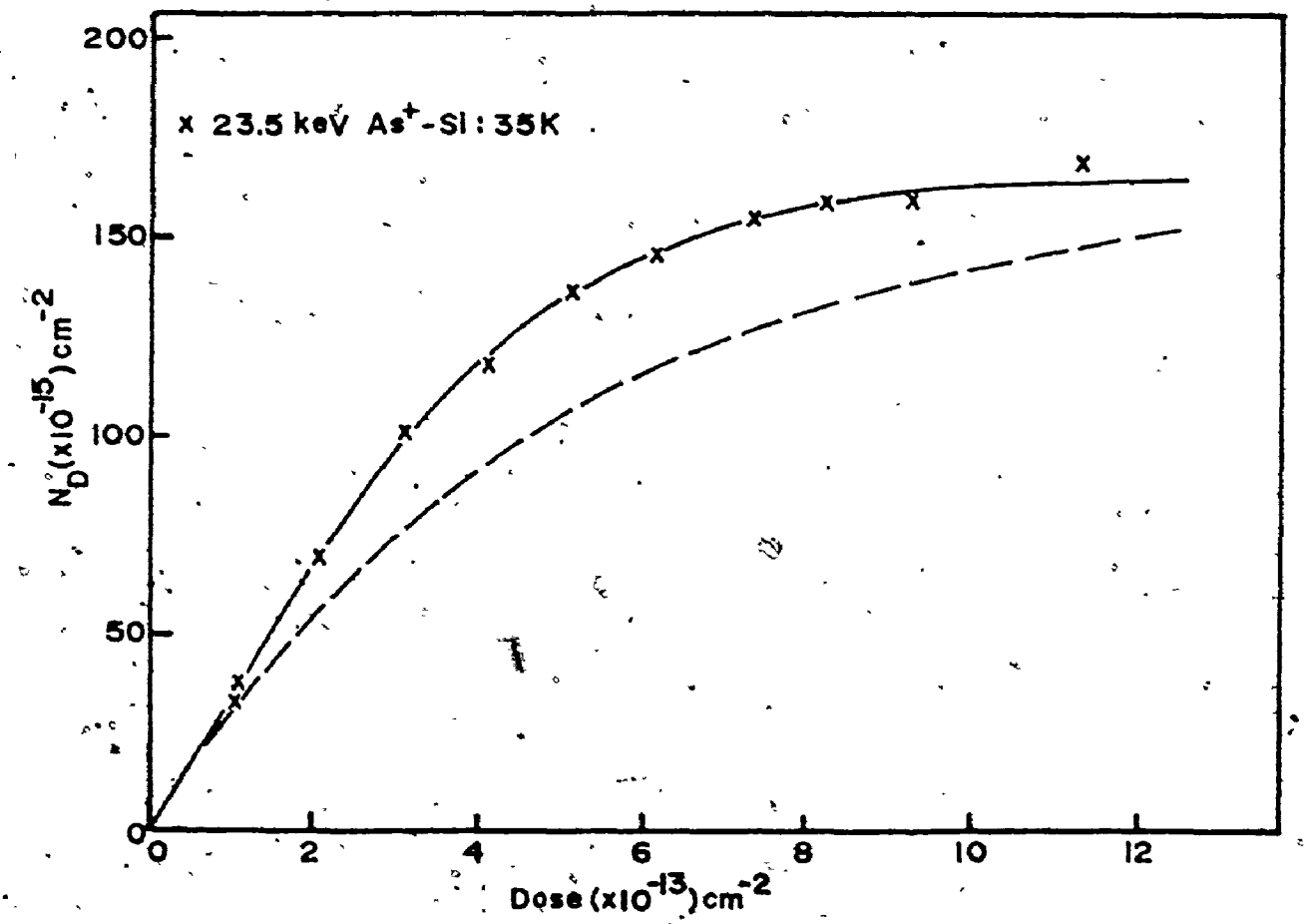

Fig. 6.14: Damage versus 23.5 keV As^+ bombardment dose in Si at 50K. Dashed line, Eq. (6.13). Solid line, Eq. (6.16) with $c = 9 \times 10^{-18}$ cm^2. Data from ref. 123.

The "Off-Axis" effect discussed in the previous section suggests that at high doses, the measured N_D combines the actual displaced atom concentration with a contribution due to direct backscatter from the lattice strains resulting from the damage. The latter contribution is negligible at low damage levels, but progressively increases with the damage. The simplest and most obvious method of incorporating the strain component into the damage-dose model is to assume it is directly proportional to N_D, i.e.:

$$\frac{dN_D}{d\phi} = N_D^*(1 - \frac{N_D}{N_{sat}})(1 + cN_D) \quad , \tag{6.15}$$

with c being the constant of proportionality. The expression $(1 + cN_D)$ satisfies the boundary condition that $dN_D/d\phi \to N_D^*$ as $N_D \to 0$. This proportionality is also suggested from the profile comparisons in Sec. 6.2. Any other proportionality would produce a distortion in the shape of the measured profiles that should be evident in comparison to the theoretical profiles.

The solution of Eq. (6.15) is:

$$N_D = \frac{1}{2}(N_{sat} - \frac{1}{c}) + \frac{1}{2}(N_{sat} + \frac{1}{c})\tanh(\frac{\phi N_D^*}{2}(\frac{1}{N_{sat}} + c) + K) \quad , \tag{6.16}$$

where

$$K = \tanh^{-1}(-\frac{N_{sat} - \frac{1}{c}}{N_{sat} + \frac{1}{c}}) \quad .$$

Eq. (6.16) has an inflection point at:

$$N_D = \frac{1}{2}(N_{sat} - \frac{1}{c}) \tag{6.17}$$

Provided $N_{sat} > 1/c$, $dN_D/d\phi$ will increase at low dose. Once $N_{sat} \leq 1/c$, the low-dose non-linearity will disappear and $dN_D/d\phi$ will decrease monotonically. Thus Eq. (6.16) will describe at least qualitatively the damage-dose behaviour for progressively higher-Z_1 ion bombardments.

Table 6.4 gives the results of the quantitative examination of the various damage-dose data in the three semiconductors. The parameter c has been obtained by a linearly-weighted least-squares fit of Eq. (6.16) to the experimental points of Figs. 6.11-6.13. Additional Si data provided by Golanski[123] has also been analyzed. N_D^* and N_{sat} have been estimated from the damage curves. Where the damage was not taken to saturation, e.g. He^+ and N^+ bombardments, N_{sat} has been determined from the measured depth of the damage profiles (see Figs. 6.2-6.4). For the He^+ and N^+ irradiations, the error limits on c represent the effect of the estimated worst-case error of ±10% in both N_D^* and N_{sat}. For the higher-Z_1 bombardments, this error is reduced to ±5%. However, since the shape of the damage-dose curve becomes less sensitive to c, the error limit on c increases. The solid lines of Figs. 6.11-6.13 correspond to Eq. (6.16), with the appropriate value of c given in Table 6.4. In all cases, a satisfactory fit is obtained.

The important feature of the tabulated values of c is that it is a constant in each semiconductor, within the rather large error limits, over the various ion bombardments. Note in particular the Si results, where ions spanning essentially the entire periodic table have been used. For Si, $c = 8.8 \pm 1.4 \times 10^{-18}$ cm^2; for GaAs, $c = 12 \pm 1.1 \times 10^{-18}$ cm^2; and for GaP, $c = 13.5 \pm 1.1 \times 10^{-18}$ cm^2. This observation agrees well with the lack of a significant dependence on the ion mass of the radial defect

Table 6.4: Fitting parameters for damage-dose data of Figs. 6.11-6.13. Included is a comparison between the measured (N_D^*) and calculated (N_{kp}) displaced atoms/ion. N_{kp} was obtained using the threshold energies, E_d(Si) = 12.9 eV,[125] E_d(GaP) = 10 eV (estimated), and E_d(GaAs) = 9.5 eV.[126]

Substrate	Ion	Energy (keV)	N_{sat} ($\times 10^{-17}$) (cm^{-2})	$C(\times 10^{18})$ (cm^2)	N_D^*	N_{kp}	N_D^*/N_{kp}
Si	He^+	30	16.7	7 ± 2.5	110	160	0.69
	N^+	40	7.7	8.5 ± 2.5	1000	590	1.7
	Zn^+	20	1.65	11.5 ± 3.5	2590	460	5.6
	As^{+*}	23.5	1.65	9 ± 3.0	3300	530	6.2
	Te^{+*}	15	0.88	9 ± 4.0	3320	360	9.2
	Tl^{+*}	15	1.00	8 ± 4.0	4700	370	12.7
GaAs	He^+	30	14.8	10.5 ± 2.5	190	220	0.86
	N^+	40	7.25	12.5 ± 2.5	1500	730	2.1
	Zn^+	20	1.17	13.0 ± 3	4500	640	7.0
GaP (Ga only)	He^+	24	7.05	12 ± 2.5	85	95	0.89
	N^+	40	4.0	14.5 ± 3	650	380	1.7
	Zn^+	20	0.78	14 ± 3	1800	300	6.0

* Data provided by Golanski[123].

distribution, as measured by the channeling technique. Again, it is expected to be mainly due to the fact that channeling displays only the gross average features of the damage. Although it is within the error limits, the downward trend in c for the heaviest ions in Si may well be significant. Such a trend is expected since strains must certainly be of less importance in the more heavily damaged regions resulting from the higher-Z_1 bombardments. In this regard, the dose dependence of 30 keV Te_2^+ in Si[123] has been analyzed; it will be shown in the following chapter that more damage is created per atom of the molecular ion than for the monatomic ion bombardment. In this instance, $c \sim 5 \times 10^{-18}$ cm^2, and is consistent with the predicted downward trend. Also, in agreement with the relative amount of strains observed in the previous section, c is comparable in GaAs and GaP, both of which are greater than c for Si.

Shown in Fig. 6.15 is the experimental damage-dose data for 30 keV He^+ in Si fitted by Eq. (6.16), together with the prediction of the dose dependence of the actual number of displacements produced directly in the ion bombardment (Eq. (6.13)). Only at the lowest dose does one actually measure this quantity by the channeling technique. It is interesting to observe that when ~50% of the atoms in the bombarded layer are predicted to have been displaced, the backscatter measurements correspond to total damage saturation. In this instance, the damage is fairly uniformly distributed across the implant area. Then when one atom in two has been displaced, the lattice is essentially destroyed in terms of channeling. As the ion mass increases, saturation is measured at a progressively higher percentage atom displacement (see Fig. 6.14). This is indicative of the increasingly heterogeneous distribution of the heavier ion damage over the

implant area.[47] When 50% of the atoms have been displaced, crystalline material can still exist between the highly damaged zones, and channeling can still occur. For He^+ and N^+ bombardment of GaAs and GaP, saturation is measured when only ~30% of the atoms are displaced. This is again attributed to the larger strains in the III-V semiconductors.

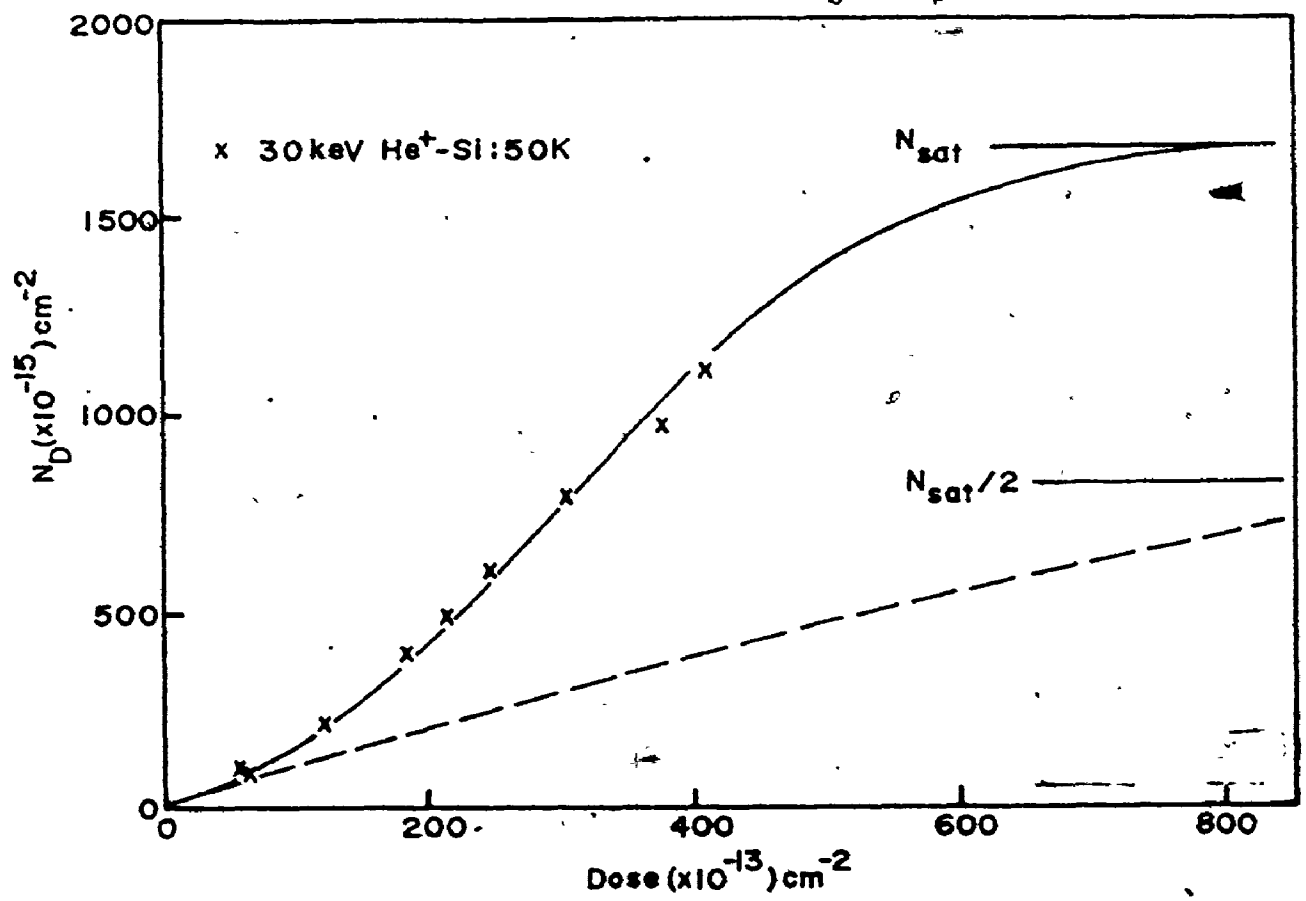

Fig. 6.15: Damage versus 30 keV He^+ bombardment dose in Si at 50K. Dashed line, Eq. (6.13). Solid line, Eq. (6.16) with $c = 7 \times 10^{-18}$ cm^2.

Therefore, except for low damage levels (typically <10%), channeling measurements of radiation damage must be interpreted with care. Atom

relaxations may contribute by up to ~50% of the backscatter yield at high damage levels. In agreement with the above arguments, Chadderton and Eisen[122] have observed by electron microscopy that when the peak in the damage profile obtained from channeling measurements for B implanted at 80K in Si reaches saturation, a uniform amorphous layer at the peak damage depth was not present. The damage behaviour is expected to become more complex at temperatures where defect migration may result. Then not only must strains be considered, but the different backscatter probabilities of the particular defect structures must be taken into account.

Predictions of the local defect density necessary to induce the amorphous phase in the semiconductors have ranged from 2%[48]-50%.[49] The data presented above, and the model used to describe the damage-dose behaviour support the view that the lattice remains stable to the higher defect densities.

Included in Table 6.4 is the number of displaced atoms/ion, N_{kp}, as predicted by the modified Kinchin-Pease Eq. (2.34). Also given is the ratio, N_D^*/N_{kp}. For the He^+ bombardments, the binary collision theory reasonably predicts N_D^*. This gives confidence that the channeling technique is a reliable measure of the ion-induced damage, provided the measurements are performed at sufficiently low dose (≲5-10% total damage), and sufficiently low temperatures. However, as the ion mass increases, a significant discrepancy develops between the measured and predicted damage, with the former being greater. The discussions of this Chapter suggest the difference is not an artifact of the channeling-backscattering technique when it is used under the above conditions. Rather, it appears that a real solid-state phenomenon must account for the discrepancy. A detailed investigation of this phenomenon is the subject of the next chapter.

CHAPTER VII

DAMAGE FROM HIGH-Z_1 BOMBARDMENT OF Si AND Ge AT 35K

7.1 Introduction

It was seen in Table 6.4 that for ion bombardment of the semiconductors at low temperature, the number, N_D^*, of displaced atoms produced by each ion is not predicted by collision theory except for the case of very light mass ions (i.e.: He^+). As the ion mass is increased, N_D^* becomes significantly greater than the predicted value. For example, for 15 keV Tl^+ in Si at 50K, the discrepancy is more than an order of magnitude. The discussions of the previous chapter indicate these large differences are not an artifact of the channeling-backscattering technique used to obtain N_D^*. It will be shown that for heavy ions, the collision cascade can no longer be completely described by a linear transport equation. Instead, the concept of "energy-spike" serves to better describe the energy deposition process within a significant fraction of the cascade volume. It appears that the energy-spike initiates a local highly-disordered, or amorphous, region within the semiconductor, thereby accounting for the large N_D^*.

In this chapter, a detailed investigation of N_D^* is presented for ~10-250 keV high-Z_1 ($Z_1 \lesssim 81$) irradiation of Si and Ge at 35K. N_D^* has been measured "in-situ" using the channeling-backscattering technique. In Sec. 7.2, the breakdown of the linear transport theory is examined and possible influence of the breakdown on the semiconductor lattice structure

is outlined. The concepts of energy density and spike lifetime are introduced as being relevant to the energy-spike model. These parameters are used to predict the relative importance of the energy spike at both high and low energies. Published data are discussed which suggest the significance of energy density in controlling the damage remaining after ion bombardment of both metals and semiconductors. Of particular interest are the results of polyatomic (or molecular) ion bombardment; such irradiations provide a convenient method of varying the instantaneous energy density within the individual cascade volume, without significantly affecting the cascade dimensions. The mass (M_1) and energy dependence of N_D^* is studied in Sec. 7.3. Presented is a semi-empirical model to predict N_D^* which separates the damage into collisional and energy-spike components. Also examined is the damage enhancement that is observed when equal atom-dose and equal energy/atom implants of atomic and molecular ions are compared. It is found that for the heavier ions, the enhancement in damage can be predicted from the semi-empirical model. For the lighter ions, the decrease in the effect is accounted for on consideration of the more prevalent subcascade structure. Finally, the observations allow for the estimation of a critical energy density and critical spike volume which limit the spike at high and low energies respectively. These estimations give some insight into the mechanisms by which the energy-spike produces the local crystalline to non-crystalline transition.

7.2 Energy-Spike Concepts

7.2.1 Breakdown of Linear Collision Theory

A basic assumption of the linear transport theory used to describe

the collision cascade is that the ion-atom and atom-atom collisions remain binary, with the struck atom being stationary before collision, in all collisions necessary for the complete dissipation of the incident ion energy. Obviously, this assumption becomes invalid as the moving particle reaches thermal energies. For light ion (e.g. H^+, He^+) bombardment, the consequences of the breakdown are not expected to be severe in terms of the effect on the solid state, since collisions are well enough separated that the thermal energy is readily dissipated. However, for heavier ion bombardment, a large number of atoms will be in motion with low energies at approximately the same time within the limited cascade volume. The close proximity of these low-energy moving atoms will prevent the rapid outward dissipation of the energy and a local "heating" of the lattice may persist for times significantly longer than the time required to generate the cascade. This discussion is supported by Fig. 7.1, which shows the energy, E*, below which a moving particle will transfer at least a minimum energy, T_{min}, at every lattice spacing. E* has been calculated by equating the mean free path, λ, between collisions of energy transfer greater than T_{min} to the interatomic spacing, d. The power cross-section approximation to the Thomas-Fermi nuclear cross-section has been used. Two values of T_{min} have been chosen:

(i) $T_{min} = E_d$ (E_d = 13 eV in Si [125]), where E_d is the threshold displacement energy. E* defines the onset of the so-called "displacement-spike"[53] (see Sec. 2.3.2). Clearly, as a keV heavy ion comes to rest, a significant fraction of its total range will fall within this region.

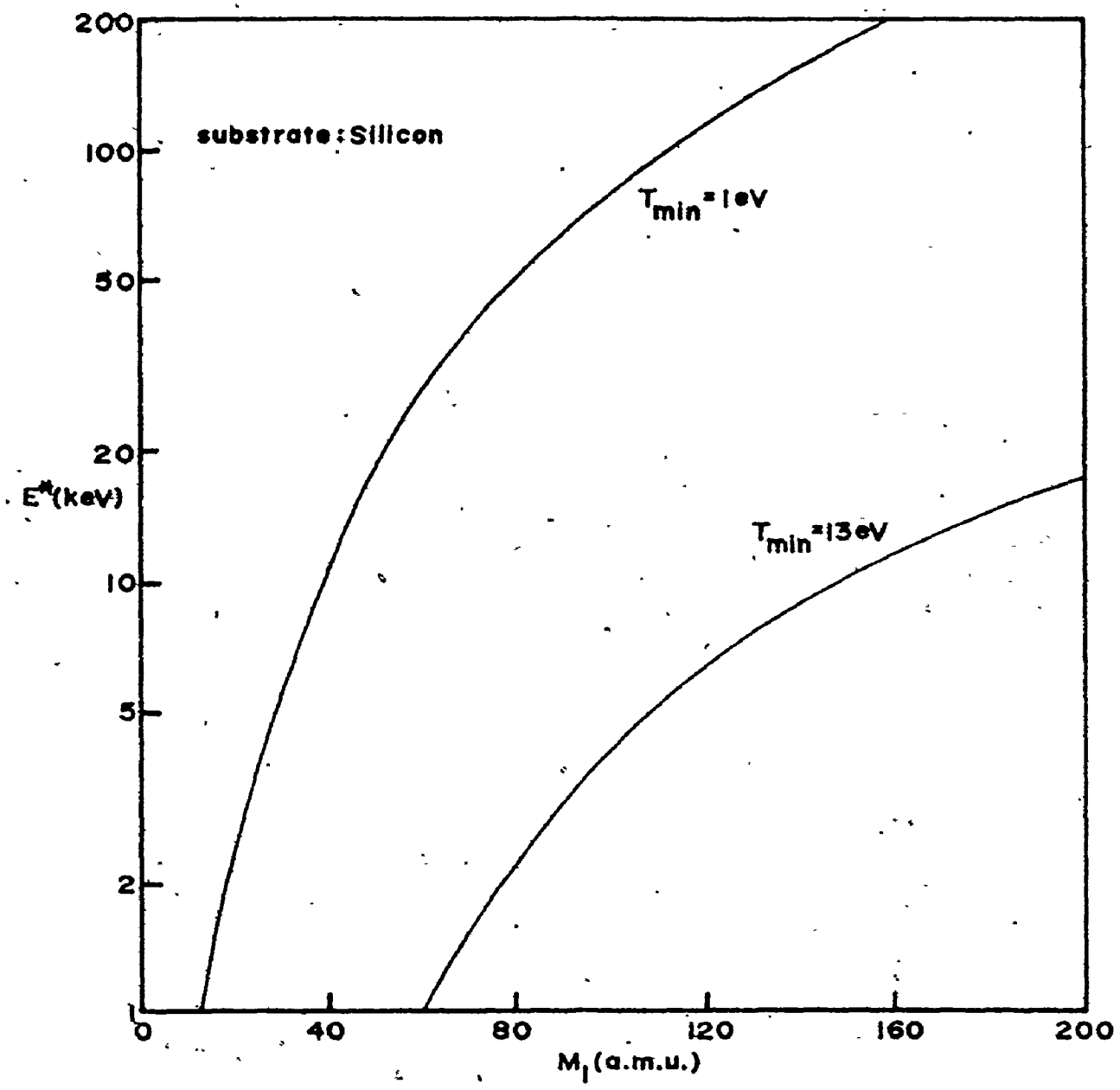

Fig. 7.1: The energy, E*, below which an energy transfer of at least T_{min} occurs at every lattice spacing. The substrate is Si.

(ii) T_{min} = 1 eV. This energy is near the energy each lattice atom has at the melting point (~0.8 eV/atom in Si). The condition is met over virtually the entire path of any keV heavy ion. E* for Si-Si is ~5 keV; since this energy is greater than typical recoil energies (e.g.: the average recoil energy produced by a 100 keV ion in Si is $\lesssim$1 keV) all recoiling atoms will fall within the region as well.

The above suggests that for the heavier ion bombardments it becomes more meaningful at some point to speak not of individual collisions, but of a limited volume in which the majority of atoms are in motion. This volume will be referred to as an "energy-spike".[51]

7.2.2 The Energy Spike and Semiconductor Lattice

It has been noted that the measured N_D^* exceeds the predictions of collision theory for most ion bombardments. As well, electron microscopy observations[45-47] of ion bombardment damage in the semiconductors have found the presence of small ($\lesssim$100Å) damage clusters with the same microscopic structure as the amorphous layer that results from prolonged ion bombardment. It will be inferred from the observations of Sec. 7.3.3 that it is the presence of these small amorphous zones which accounts for the enhanced damage; the important question becomes what initiates their formation. It is suggested that the local transformation results from the presence of an energy-spike. The spike may initiate the process by at least two mechanisms:

(i) Theoretical calculations[52] have shown that the brief local heating of the lattice that is associated with the energy-spike can be

sufficient to destroy the long-range order within the heated region. This concept is consistent with the "thermal-spike" model that was presented in Chapter II to account for the observed non-linear effects in heavy ion sputtering. For such a mechanism to be important, the energy contained within the spike volume would be expected to be of the order of the heat of melting (the heat of melting in Si is ~0.8 eV per atom, and for Ge ~0.5 eV).

(ii) Accompanying the thermal activation of the lattice atoms due to the energy-spike is an increased lattice instability. This is caused by the high local concentration of broken lattice bonds and increased potential energy associated with the displaced atoms. The unstable lattice may then collapse athermally into the energetically-favourable metastable amorphous structure. The increase in energy in the amorphous state has been estimated[48] at ~0.11 eV/atom for Ge. The value is expected to be somewhat higher in Si. Swanson et.al.[48] have concluded on this basis that the semiconductor lattice will be unstable to defect concentrations of 2-4 at .%. The damage-dose data of Sec. 6.4 does not support the model that a local amorphous structure is created in regions where repeated cascade overlap has produced a defect concentration in excess of this critical limit. However, during the cascade propagation, the lattice instability due to the combined effects of thermal activation, broken bonds and increased potential energy may be sufficient to initiate the transformation. The energy density necessary to initiate the mechanism would be expected to be somewhat less than that required for the "thermal-spike" process.

The exact definition of what fraction of the incident ion energy is involved in the energy-spike requires some clarification. In terms

of a "thermal-spike" mechanism, the energy that influences the spike will mainly be the energy, $\nu(E)$, deposited into elastic scattering. The energy component, $\eta(E)$, into inelastic scattering was shown in Sec. 2.3.3 to be relatively inefficient in contributing to the thermal motion. However, it was noted in Chapter III that if an energy, U, is considered lost to the lattice at every atom displacement the total ΣU can be a sizeable portion of the total energy. U is deposited in breaking the atom bonds and overcoming the potential minimum in which the lattice atom is located. For $U = E_d$, Fig. 3.3 reveals that ΣU will account for up to $\sim$45% of the incident ion energy. It is unlikely that a significant part of ΣU will contribute to the thermal motion. However, when considering the final damage state of the lattice, ΣU is expected to be closely involved in the second of the above mechanisms, since it will influence the local lattice stability. As far as damage is concerned, it is then likely that at least a portion of ΣU should be considered in the energy-spike. The results of the Monte-Carlo code in Sec. 3.3 have shown that if ΣU is summed with $\nu(E)$, the resultant energy agrees within 10% of the $\nu(E)$ value obtained for $U = 0$. In the following analysis, for simplicity, the spike energy has been designated as the latter.

Basically, two parameters will determine the relative significance of the energy-spike in establishing the damage for a given ion-target system. These are the energy contained within the spike volume, i.e.: the local energy density, and the time required to dissipate the spike energy, i.e.: the spike lifetime. These parameters are defined below.

7.2.3 Energy Density

We shall define the energy density, $\bar{\theta}_v$, in units of energy per

atom. as:

$$\bar{\theta}_\nu = \frac{\int_V \nu(E) F(x,y,z) dV}{N \int_V dV} \quad , \tag{7.1}$$

where $F(x,y,z)$ is the spatial distribution of energy deposition into $\nu(E)$ (from Winterbon[2]), and N is the atom density. The subscript, ν, on $\bar{\theta}_\nu$ indicates that the inelastic energy component, $\eta(E)$, is not included. The definition requires the assignment of a realistic volume, V, over which the energy of the spike is averaged. For $M_1 \gtrsim M_2$, it is adequate to define V as a spheroid having longitudinal and transverse axes given by the longitudinal and transverse straggling components, $\langle \Delta z^2 \rangle^{1/2}$ and $\langle x^2 \rangle^{1/2}$ respectively, of the distribution $F(x,y,z)$, i.e.:

$$V = \frac{4\pi}{3} \langle \Delta z^2 \rangle^{1/2} \langle x^2 \rangle V_R \quad . \tag{7.2}$$

V_R is the ratio between the individual and statistical cascade volumes; it has been computed in Sec. 3.4 using a Monte Carlo computer code. For the heavy ions, the distribution, $F(x,y,z)$, can be reasonably approximated by a three-dimensional Gaussian distribution, so that the numerator of Eq. (7.1) becomes:

$$\int_V F(x,y,z) dV = \left(\frac{2}{\pi}\right)^{1/2} \int_0^1 e^{-r^2/2} r^2 dr = 0.2 \quad , \tag{7.3}$$

where

$$r^2 = \frac{x^2}{\langle x^2 \rangle} + \frac{y^2}{\langle x^2 \rangle} + \frac{(z - \langle z \rangle)^2}{\langle \Delta z^2 \rangle}$$

The skewness of the distribution has been neglected. These definitions (Eqs. (7.2), (7.3)) have implicitly assumed that the energy deposition is

reasonably homogeneous throughout the cascade volume. However, as M_1 becomes less than M_2 an isolated subcascade structure becomes more apparent,[25] and the definitions become less valid. The consequences of this observation are discussed in Sec. 7.2.5.

The energy, $\bar{\theta}_\nu$, per atom, within the volume defined by Eq. (7.2) is:

$$\bar{\theta}_\nu = 0.2\nu(E)/N_V \quad , \tag{7.4}$$

with $N_V = N \cdot V$. $\bar{\theta}_\nu$ is plotted in Fig. 7.2 for various mass ions ($M_1 \geq M_2$) in both Si and Ge as a function of the incident ion energy, E. For comparison, the total heat of melting is indicated for the two semiconductors. For the higher-Z_1 bombardments and at low energies, $\bar{\theta}_\nu$ exceeds the heat of melting. Two features of $\bar{\theta}_\nu$ are important:

(i) The absolute value of $\bar{\theta}_\nu$ depends critically on the definition of volume. For example, the maximum energy density, $\bar{\theta}_\nu^{max}$, is ~30% greater than $\bar{\theta}_\nu$ as defined by Eq. (7.4). If the volume is extended out to two standard deviations, $\bar{\theta}_\nu$ decreases by a factor of ~3. However, in each case the general features of $\bar{\theta}_\nu$ are retained.

(ii) $\bar{\theta}_\nu$ represents the gross average density within a volume determined by the initial ion energy. Since N_V increases with energy more rapidly than linearly, $\bar{\theta}_\nu$ decreases with energy (see Fig. 7.2). This does not mean that the energy-spike will not exist in the higher energy ion cascades. For example, if an energy-spike is present in, say, a 20 keV ion cascade, it will also be present to at least the same magnitude at all greater ion energies, since the ion eventually slows down through 20 keV. Sigmund[51] has ignored this fact in his model for predicting the significance of the energy-spike. Since his arguments were aimed in

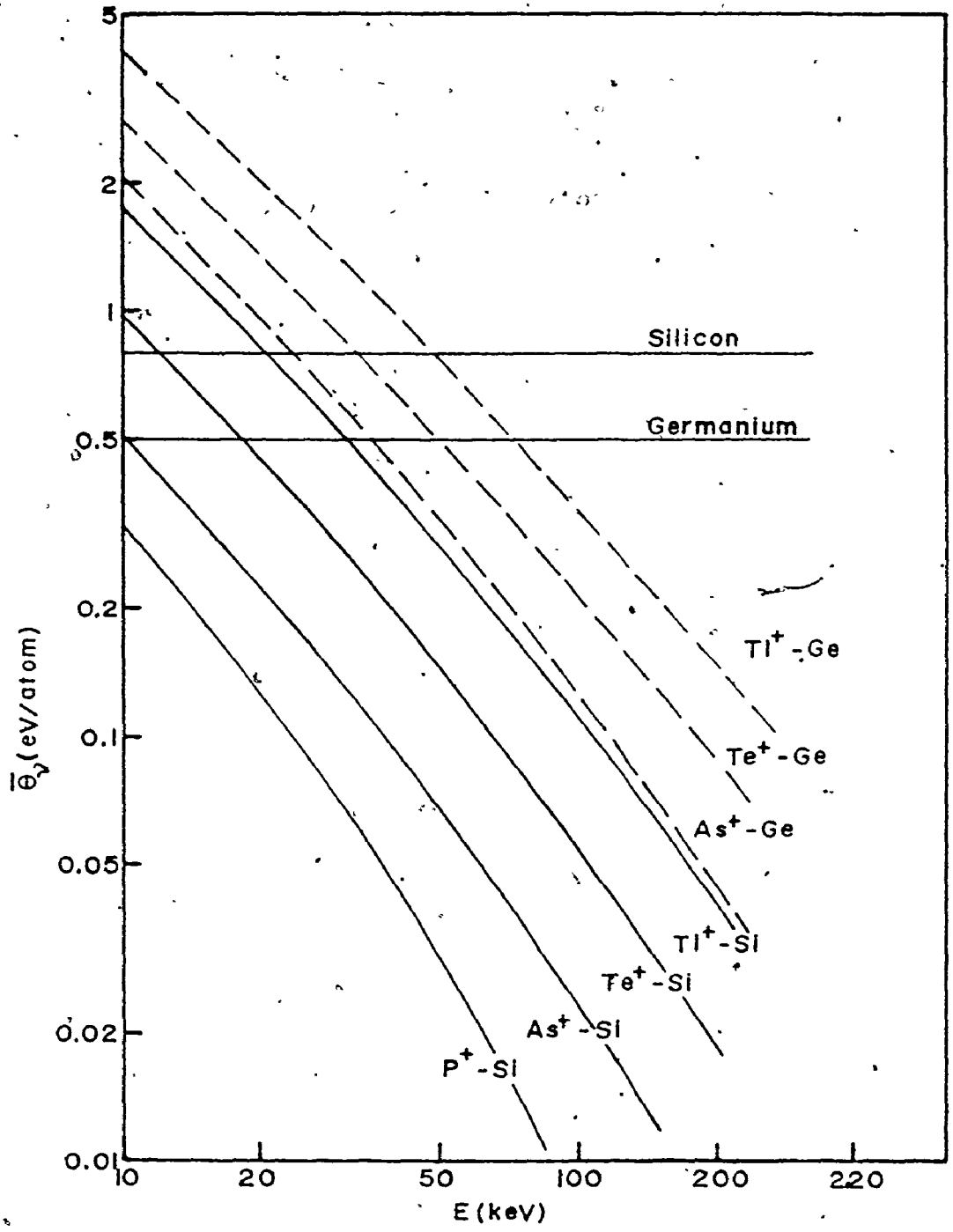

Fig. 7.2: The energy density, $\bar{\theta}_v$, from Eq. (7,4), for various ions in Si (solid lines) and Ge (dashed lines). The horizontal lines indicate the heat of melting for each semiconductor.

particular at explaining anomolous sputtering data, this is reasonably valid; the spike will occur at the end of the higher energy ion trajectory and will be buried beneath the surface. In terms of the damage, the effect cannot be ignored.

In a manner analogous to the definition of energy density given by Eq. (7.4), we can define the fractional damage, F_D, within the cascade as:

$$F_D = 0.2N_D^*/N_V \quad . \tag{7.5}$$

This definition has been used previously in Chapter VI in connection with the damage for the lower-Z_1 bombardments.

7.2.4 Spike Lifetime

Sigmund[51] has attempted to define the spike lifetime, τ, in terms of the initial rate of conduction of the maximum energy density, under the assumption of a local equilibrium. For a heat transport cross-section determined using the power cross-section with m = 0, τ becomes:

$$\begin{aligned} \tau &= H_2 E^3/N^2 \quad \text{for } m = 1/2 \\ &= H_3 E^{11/6}/N^2 \quad \text{for } m = 1/3 \quad . \end{aligned} \tag{7.6}$$

H_2 and H_3 are parameters tabulated in ref. 57, and E is the ion energy. In view of the previous discussion of spike energy, it appears that E in Eq. (7.6) should be replaced by $\nu(E)$. There are several weaknesses inherent in the approach. For example, Eq. (7.6) only defines the spike half-life[51]; in terms of the energy-spike model, the time necessary to reach a minimum energy per atom near the heat of melting would be more appropriate. Thus, Eq. (7.6) may significantly underestimate the realistic lifetime. However, it gives at least an order of magnitude estimate of the

time involved; typical lifetimes range from 10^{-14}-10^{-11} sec. Comparative values are given in the next section.

7.2.5 The Energy Dependence of the Spike

(a) The spike at low energies:

Figure 7.2 shows that as the ion energy decreases, the energy density reaches extremely high values. This results from the rapid decrease in the cascade volume. In close connection to the decrease in cascade volume at low energies, Eq.(7.6) predicts that the spike lifetime becomes extremely short. It has been suggested[51] that the spike will not have sufficient time to influence the lattice unless its lifetime is at least comparable to the time necessary to generate the cascade. The latter time will be of the order of the slowing-down time, τ_o, of the ion, i.e.:

$$\tau_o = \int_o^E \frac{dE}{vNS_n(E)} \quad , \qquad (7.7)$$

where $S_n(E)$ is the nuclear stopping cross-section and v is the ion velocity. The ratio, τ/τ_o, is plotted in Fig. 7.3 for various ions in Si and Ge. E has been replaced by $\nu(E)$ in Eq. (7.6). τ_o has been calculated using the power cross-section approximation for $S_n(E)$ (see Fig. 2.3). It is evident that for energies greater than ~10 keV, the spike will be expected to influence the damage behaviour. In fact, since it was noted that Eq. (7.6) will underestimate the spike lifetime, the energy limit of ~10 keV is likely high. Below a critical lifetime, τ_c, the energy will be dissipated too quickly. The concept of a critical spike lifetime is comparable to defining a critical spike volume, V_c, which must be exceeded for the

spike to influence the damage. The concept of spike lifetime is particularly relevant to the "thermal-spike" mechanism. With regard to lattice stability considerations, a critical volume may likewise exist in order for the metastable amorphous state to be induced.[127] Evidence for the existence of a critical volume will be given in Sec. 7.3.4.

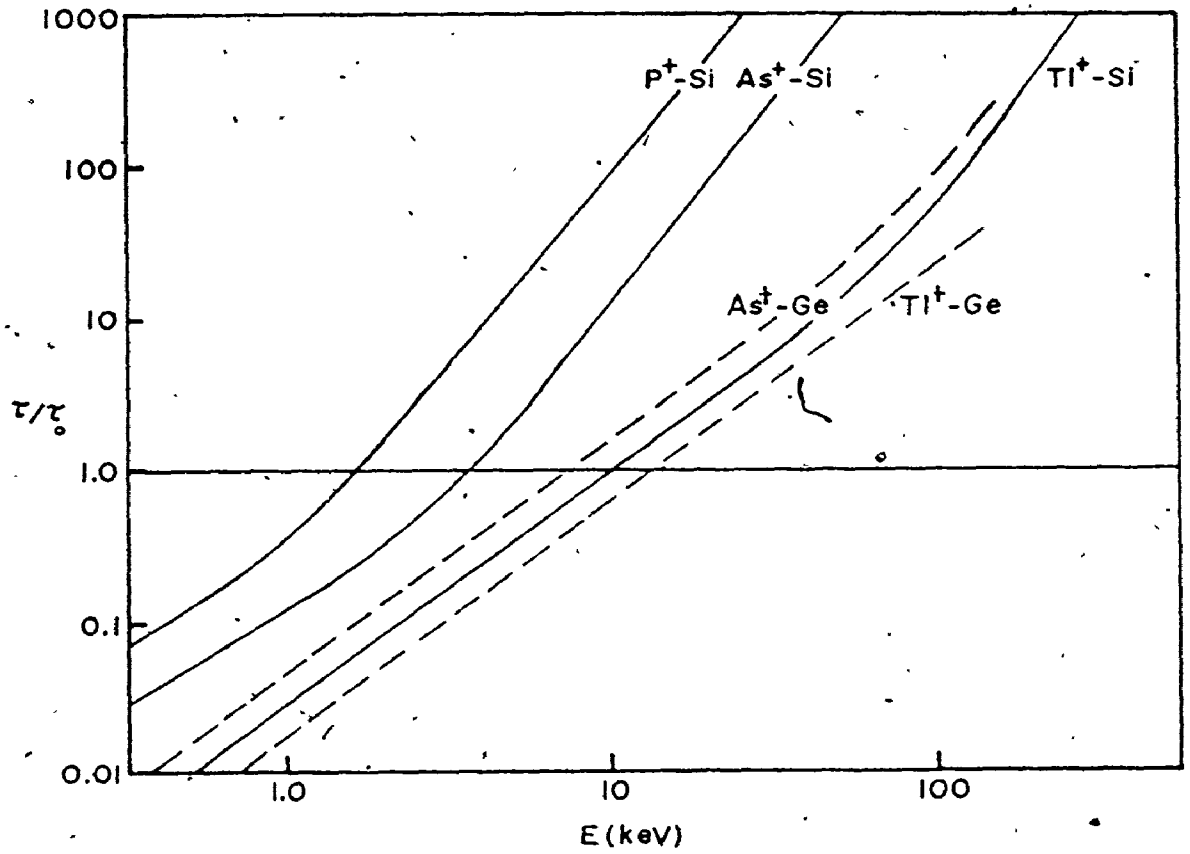

Fig. 7.3: Ratio of spike lifetime, τ, Eq. (7.6) to slowing-down time, τ_0, Eq. (7.7) as a function of ion energy. Solid lines, Si. Dashed lines, Ge.

(b) The spike at high energies:

Although the spike lifetime continues to increase at higher

energies, the energy density eventually drops below the heat of melting and continues down to insignificant values (see Fig. 7.2). Therefore, over the initial portion of the ion trajectory, the rate of energy deposition will be dispersed enough that the spike is of little consequence. The mass and energy dependence of the rate of energy deposition has been discussed with reference to Fig. 7.1. As the ion loses energy, the frequency of collisions will increase and a significant energy-spike may eventually be initiated. The measured damage results from the integral of this effect over all energies $\leq$ the incident ion energy. The decreasing importance of the spike at higher energies would therefore be expected to be better reflected in the rate of change of damage with increasing energy.

(c) Subcascade structure:

The definitions of energy density and spike lifetime have assumed that the energy is deposited relatively homogeneously within the cascade volume. However, for $M_1 \lesssim M_2$ the energy deposition becomes more heterogeneous, as an isolated subcascade structure develops with the ion trajectory undergoing large fluctuations. This feature is indicated in Fig. 7.4 for the Monte Carlo simulated cascades of 20 keV N^+ in Si and 20 keV P^+ in Ge. E_d has been arbitrarily chosen at 25 eV, and the cut-off energy, E_F = 150 eV, in order to facilitate the plotting. It is obvious that the Gaussian approximation to the energy deposition within an individual cascade is invalid for these ion-target systems. As well, the subcascades are sufficiently isolated that the energy dissipation in each subcascade should be treated independently. No provision was made for this behaviour in the earlier definitions of energy density and spike lifetime. From Fig.

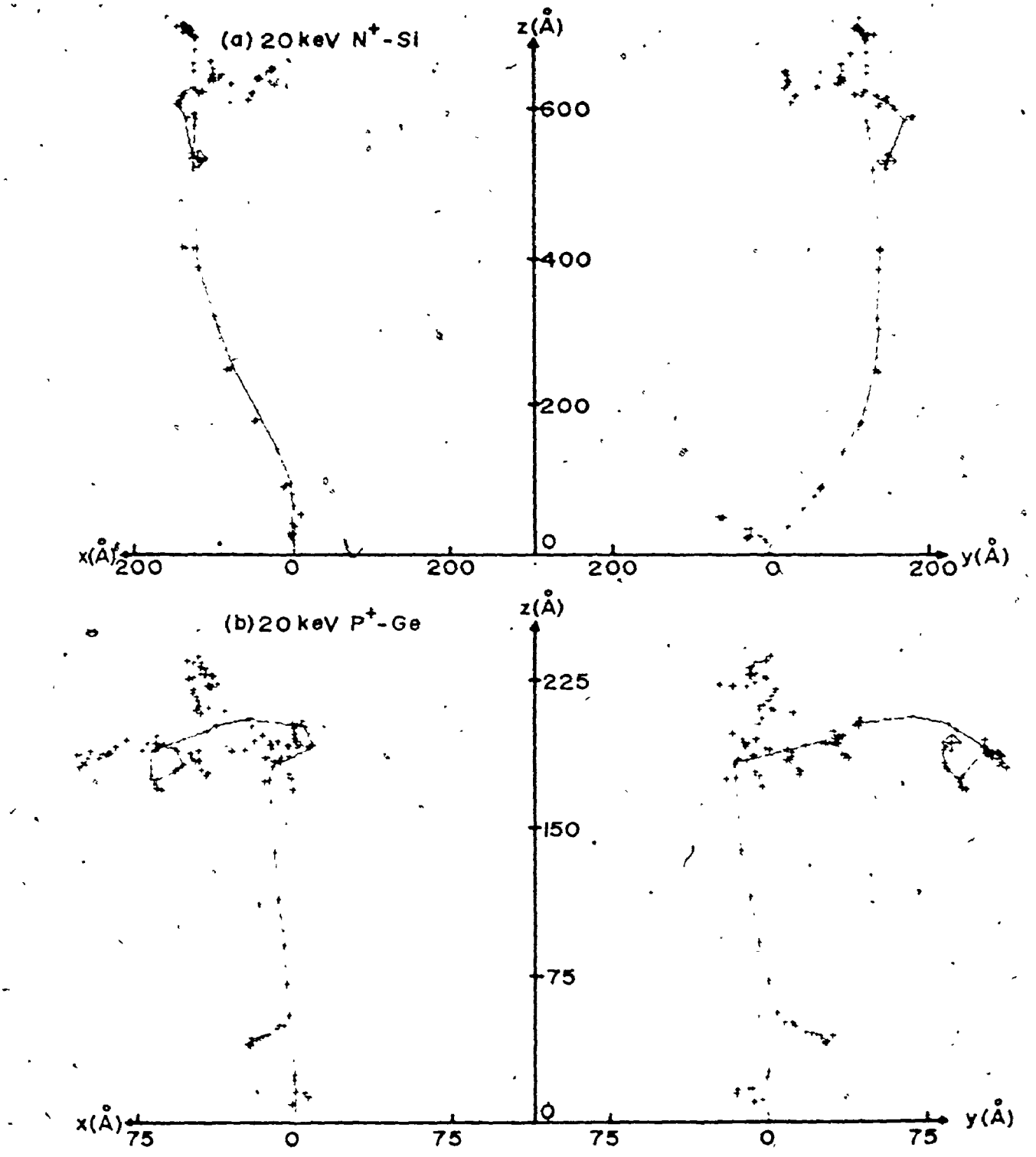

Fig. 7.4: Monte Carlo cascades for (a) 20 keV N^+-Si, (b) 20 keV P-Ge. Displaced atom final location (+). E_d = 25 eV, E_F = 150 eV.

7.4, it is also evident that if two low-Z_1 ions were to strike the surface simultaneously, the individual subcascades of each ion would have only a small probability of overlapping, and thereby altering the local energy density and lifetime associated with the particular subcascade. In Sec. 7.3.2, it will be seen that the above has important consequences when molecular ion bombardments are considered.

7.2.6 Evidence for Energy Spike Effects in Damage

From the previous discussion, it becomes apparent that an analysis of ion-induced damage should also consider the energy density of the individual ion cascades. This was first suggested in an experimental study of implantation damage in Si by Picraux and Vook.[105] They attempted to correlate their damage data for different ion bombardments in terms of the energy accumulated within the total implant volume. Their results indicated that at low temperatures (87K), the damage induced by light ion (O^+) and heavy ion (Sb^+) bombardments is similar, in that equal damage was observed for equal energy per unit implant volume at a given rate of energy deposition. For room temperature bombardment, where significant annealing can occur, the damage for equal energy deposition was smaller for the lighter ions. This was interpreted as due to the difference in energy density of the individual ion cascades for O^+ and Sb^+ - the higher the cascade energy density, the more extensive the damage, and consequently the less the annealing.

In ion bombarded metals, TEM observations have shown that the amount and nature of the damage is correlated to the cascade energy density. For 50-keV ion bombardments of Au at room temperature, vacancy

clusters have been noted[128] to form preferentially, at the expense of interstitial clusters, as the ion mass (and energy density) is increased. The number of defect clusters also increases with mass. Similar behaviour has been reported in ion-irradiated Cu[129] and Fe.[130]

One way of demonstrating that the cascade energy density influences crystal behaviour under ion bombardment is by comparison of polyatomic (or molecular) versus monatomic ion irradiations. For example, when a diatomic ion having atoms of the same mass strikes the target surface, it will almost immediately dissociate into atomic ions having equal energy. The individual cascades will overlap within the cascade propagation time ($\sim 10^{-13}$ sec). The extent of overlap is indicated by the ratio, V_R, of the individual to statistical cascade volumes (as discussed in Sec. 3.4). For large V_R, the overlap will be essentially complete. Then the molecular ion (of equal energy per atom as the corresponding monatomic ion) provides a simple way of approximately doubling the cascade energy density without altering the cascade dimensions. For lighter ions, where V_R is small, Fig. 7.4 has revealed that there is a greatly reduced probability of overlap of the subcascades. In this case, although the molecular bombardment may double the energy density contained within the cascade envelope, the energy density at the microscopic level is not doubled.

The use of molecular ions to study the damage behaviour in the semiconductors was first reported by Moore et.al.[131] They found that in GaAs, for room temperature bombardments for the same atom doses of 40 keV As_2^+ and 20 keV As^+, about 50% more damage occurred in the diatomic case. Similar damage enhancement has been reported[42] for various molecular ion bombardments of Si and Ge at room temperature. The enhancement is even greater for polyatomic ions. For example, the damage resulting

from room temperature polyatomic-carbon-ion bombardment of Si has been observed[132] to increase approximately with n^2, where n is the number of atoms comprising the ion. However, the damage created by much lighter ions (300 keV D^+ and 600 keV D_2^+) does not exhibit the damage enhancement under molecular bombardment.[133] The lack of enhancement is suggested to be due to both the greatly reduced energy density and the insignificant overlap that the subcascades generated by these light ions would have.

Molecular ions have also been used to study the preferential formation of vacancy clusters in metals for higher-Z_1 ion bombardments. In agreement with the behaviour expected in terms of energy density, more vacancy clusters are formed in As_2^+ irradiated Au, than for As^+ irradiation.[134]

It was noted in Sec. 2.3.3 that sputtering yields exhibit a similar enhancement for heavy molecular ion bombardment of both metals and semiconductors. Such non-linear sputtering effects must be related to events during, or immediately following, cascade propagation, such as the energy-spike.

While the energy-spike may initiate the damage enhancement observed for the room temperature molecular ion irradiations of the semiconductors, the overall magnitude of the non-linearity in damage production will be affected by processes such as annealing which will be dependent on the defect density remaining after the energy-spike has subsided. Apparently, a larger defect density results for the higher energy density cascades of the molecular ions; this damage is more stable and the amount of annealing is reduced. To isolate these competing effects it is necessary to measure the damage at temperatures sufficiently low that defect annealing or nucleation cannot occur. Such experiments are discussed in the

remainder of the chapter. Preliminary reports of the findings have been published.[43,44]

7.3 Experimental Characteristics of High-Z_1 Induced Damage

7.3.1 Mass (M_1) and Energy Dependence of N_D^*

In this section, a systematic investigation of the damage due to high-Z_1 (up to Z_1 = 81) bombardment of Si and Ge at 35K is reported. The parameter measured is N_D^*, the number of displaced atoms per incident ion. Implantation doses were $\sim 10^{11}$-$10^{13}/cm^2$, and have been chosen for each ion-target system so that the average measured damage level was ~5%. It was noted in Chapter VI that at these damage levels, the channeling-backscattering technique can be used to obtain an accurate measure of N_D^*. Implantation beam currents were 0.5-5 nA/cm^2. No dose rate effects have been observed. In all cases, the analysis beam was 1.0 MeV He^+. Implantation beam energies were 10-250 keV. Energies greater than 150 keV were achieved by using doubly-charged ions. In general, each reported value of N_D^* is the average of four measurements, so that the relative error is considered to be better than ±5%. The systematic error, due to errors in the He^+ stopping powers, He^+ beam energy, implantation dose, etc., will make the total error somewhat higher.

Shown in Fig. 7.5 (Si) and Fig. 7.6 (Ge) is N_D^* at 35K as a function of $\nu(E)$ for various ions - Tl^+, Te^+, As^+, P^+ in Si, and Tl^+, Te^+, As^+ in Ge. The nature of the solid lines will be discussed shortly. The parameter, $\nu(E)$, is the component of energy into elastic collisions (from Winterbon[2]). It has been chosen for the abscissa scale, since collision

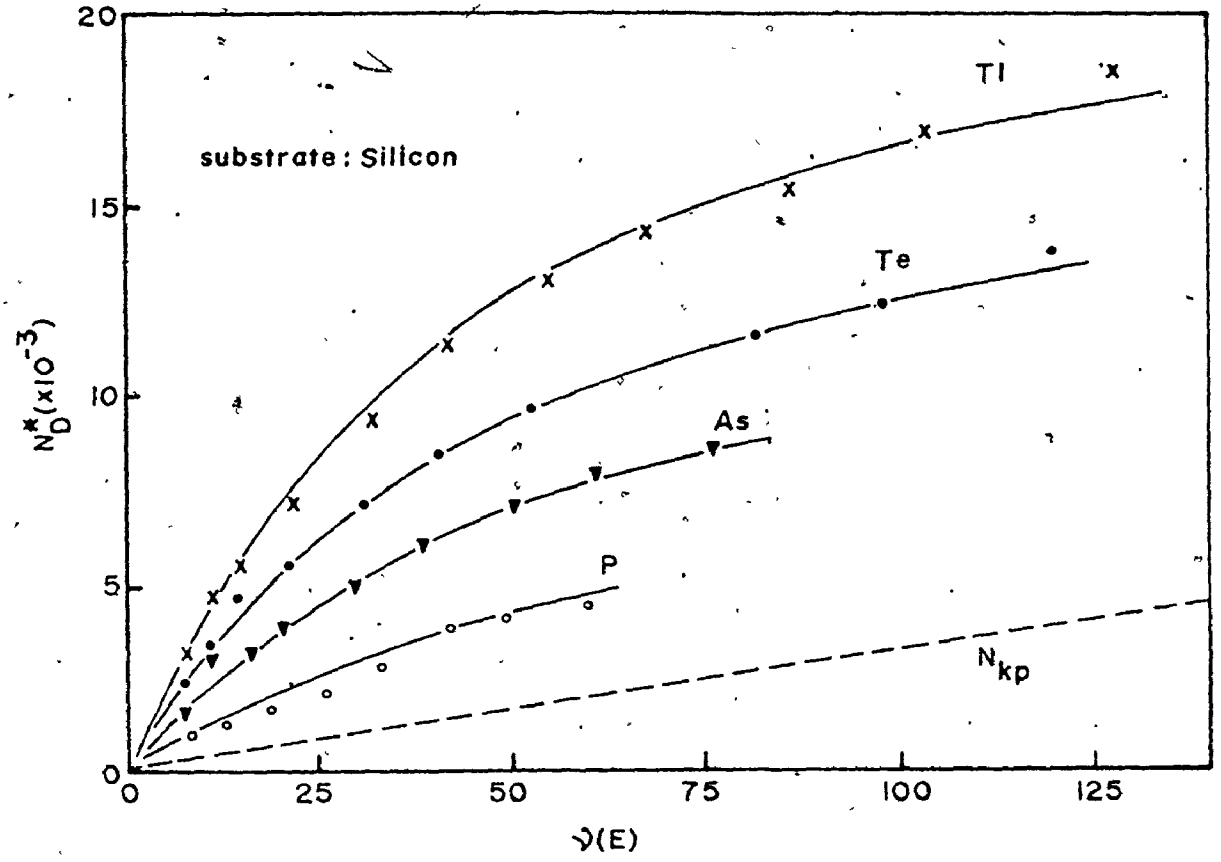

Fig. 7.5: The number, N_D^*, of displaced atoms per ion versus $\nu(E)$ in Si at 35K. The number, N_{kp}, of defects predicted by collision theory is indicated.

theory predicts that N_D^* will be directly proportional to $\nu(E)$. The results of the Monte Carlo code of Chapter III have indicated there is some question as to the absolute magnitude of the proportionality. The modified Kinchin-Pease estimate (Eq. (2.34)) of the number, N_{kp}, of defects will be used for comparison to N_D^* with the reservation that there may be as much as ~30% variation in the former value, depending upon the choice of

$\xi(m)$ (see Eq. (2.33)). The comparison will be seen to be quite insensitive to this variation.

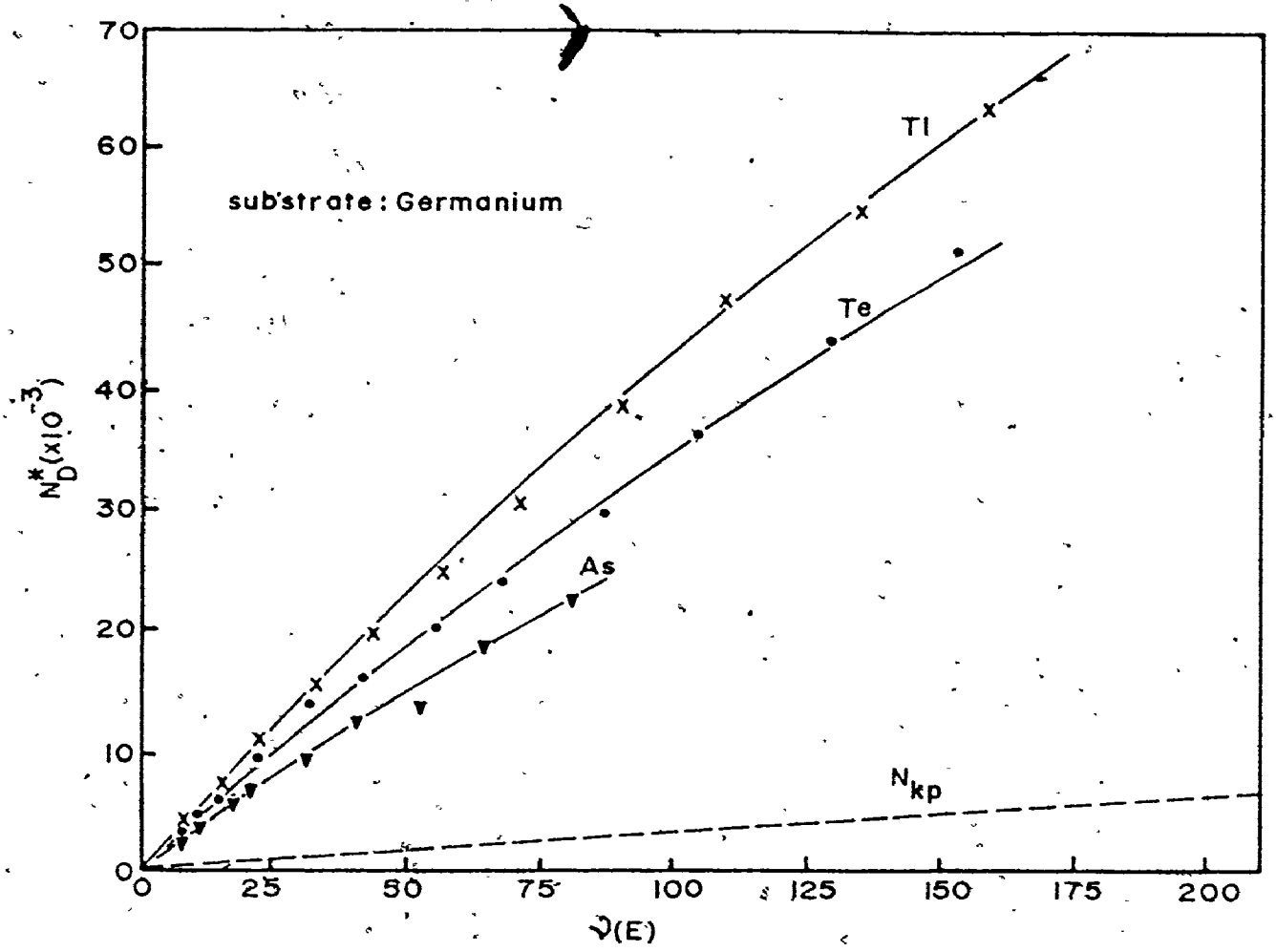

Fig. 7.6: The number, N_D^*, of displaced atoms per ion versus $\nu(E)$ in Ge at 35K. The number, N_{kp}, of defects predicted by collision theory is indicated.

The dashed lines in Figs. 7.5 and 7.6 show N_{kp} as $\nu(E)$ is increased. In all cases, N_D^* significantly exceeds N_{kp}, with the deviation for the high-Z_1 ion bombardments being greater than an order of magnitude. A

systematic variation of N_D^* with both M_1 (or Z_1) and $\nu(E)$ is evident. For constant $\nu(E)$, N_D^* consistently increases as M_1 increases. For constant M_1, the gradient of N_D^* versus $\nu(E)$ decreases as $\nu(E)$ increases; the dependence is more pronounced in Si. In fact in Si, for $\nu(E) \gtrsim 60$ keV, $dN_D^*/d\nu(E)$ appears to approach $dN_{kp}/d\nu(E)$, although this observation is insensitive to the possible 30% variation in the latter gradient. Such behaviour is expected in view of the model of the energy-spike at high energies (see Sec. 7.2.5). Therefore, it is proposed that the measured damage be considered as comprised of two components: N_{kp}, due to the collision cascade, and N_s, due to the energy-spike. At sufficiently high energies (and low energy densities), the recoiling atoms generated over the initial part of the ion trajectory are well enough separated and the energy deposition dilute enough that an energy-spike of sufficient magnitude to influence the damage is not generated. The disappearance of N_s at high ion energies is apparent in the energy gradient of N_D^*, not in the total N_D^*, since the latter includes the cumulative effects of the energy-spike integrated over all energies $\leq$ the initial ion energy.

In the above framework, N_D^* becomes:

$$N_D^* = N_s + N_{kp} \quad . \tag{7.8}$$

It can be shown that in Si, $dN_D^*/d\nu(E)$ is reasonably approximated by an exponential function of $\nu(E)$, i.e.:

$$\frac{dN_D^*}{d\nu(E)} = K_1 e^{-\nu(E)/\nu_1} + K_{kp} \quad , \tag{7.9}$$

where ν_1 is found to be a constant; $\nu_1 = 30 \pm 4$ keV, for the four different

mass ions considered in Fig. 7.5. The Kinchin-Pease value of $d\bar{N}_{kp}/d\nu(E)$ has been assigned to K_{kp}, i.e.:

$$K_{kp} = 0.42/E_d \simeq 3.2 \times 10^{-2}\ eV^{-1} \quad ,$$

with E_d taken as ~13 eV in both Si and Ge.

Although the variation in $dN_D^*/d\nu(E)$ with $\nu(E)$ is less in Ge over the range of $\nu(E)$ for which it has been measured, the Ge data may nevertheless be placed in the form of Eq. (7.9). For Ge, ν_1 is found to be 270 ± 40 keV. The much larger value of ν_1 in Ge is indicative of the weaker gradient variation.

Equation (7.9) can be integrated to obtain:

$$N_D^* = K_s(1 - e^{-\nu(E)/\nu_1}) + \frac{0.42\nu(E)}{E_d} \quad . \qquad (7.10)$$

Shown in Fig. 7.7 is the dependence of the constant, K_s, of Eq. (7.10) on the mass (M_1) of the incident ion for both Si and Ge. K_s has been obtained for each ion mass by a linear-weighted least-squares fit of Eq. (7.10) to the data of Figs. 7.5 and 7.6. Over the range of M_1 considered, K_s has an $\sim M_1^{0.75}$ dependence in Si and $\sim M_1^{0.5}$ dependence in Ge. Since the energy-spike will be related to the nuclear stopping power, it is expected that the weaker mass dependence of K_s in Ge is reflected in part by the weaker mass dependence of the nuclear stopping power in that material in the energy interval considered. The latter fact is apparent in Fig. 7.2 where $\bar{\varepsilon}_\nu$ is seen to be less sensitive to ion mass in Ge than in Si.

Equation (7.8) may be placed in the following semi-empirical formulation for N_D^*, i.e.:

$$N_D^* = N_s + N_{kp} \ ,$$

$$N_D^* = 251 \cdot M_1^{0.75} \cdot \left(1 - \exp\left(\frac{-\nu(E)}{30(\text{keV})}\right)\right) + 0.032\nu(E) \quad \text{in Si} \ , \qquad (7.11a)$$

$$N_D^* = 9.10 \times 10^3 \cdot M_1^{0.5} \cdot \left(1 - \exp\left(\frac{-\nu(E)}{270(\text{keV})}\right)\right) + 0.032\nu(E) \quad \text{in Ge,} \qquad (7.11b)$$

where M_1 is the ion mass in atomic mass units. The normalization constants on N_s are equal to $K_s(M_1 = 1)$.

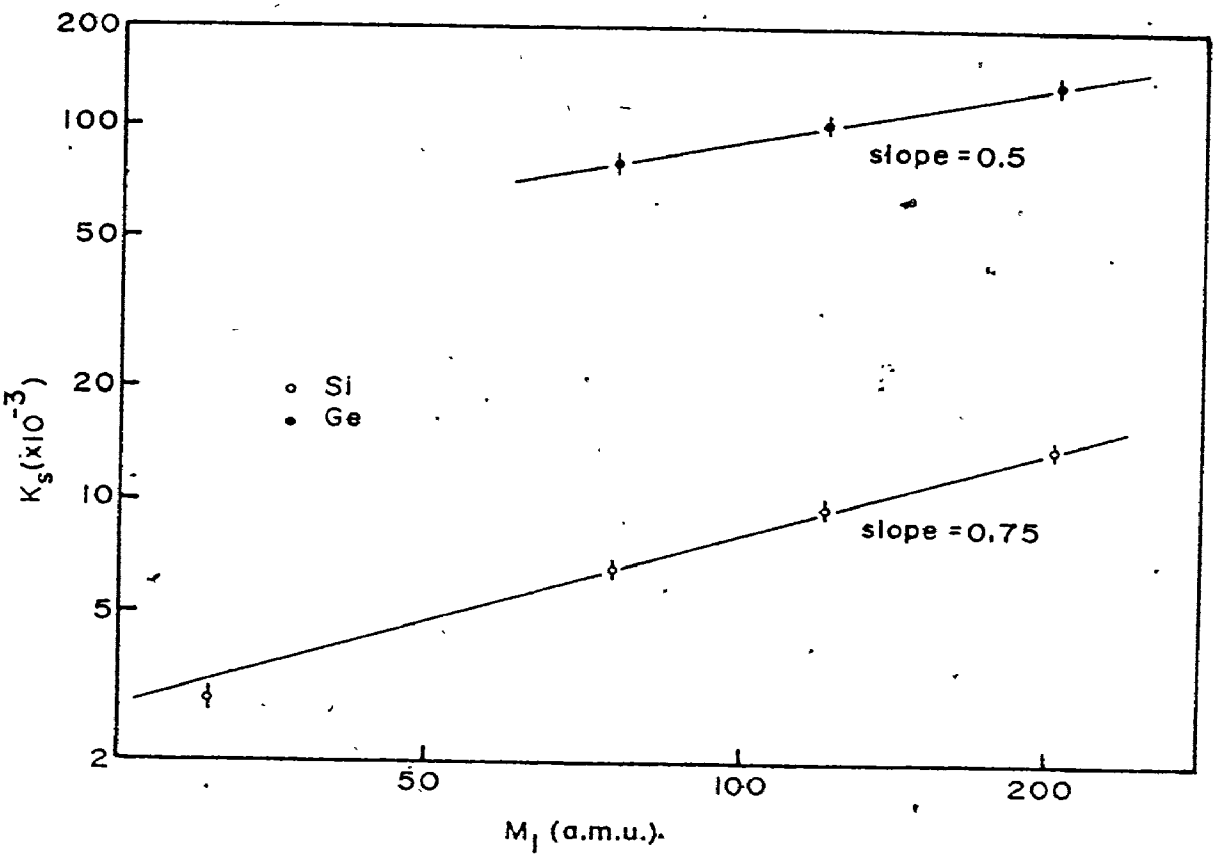

Fig. 7.7: The constant, K_s, of Eq. (7.10) versus ion atomic mass.

The solid lines of Figs. 7.5 and 7.6 are the plots of Eq. (7.11) for Si and Ge respectively. In most cases, agreement with the measured

N_D^* values is within the estimated relative error of ±5%. The formulation has been tested for a few additional ions in both semiconductors, and the measured and predicted N_D^* are compared in Table 7.1. The agreement is satisfactory.

Table 7.1: Comparison of measured N_D^* and N_D^* interpolated from Eq.(7.11) in Si and Ge at 35K.

Ion	Energy (keV)	ν(E) (keV)	N_D^* (Measured)	N_D^* (Interpolated)	$\frac{N_D^*(\text{Measured})}{N_D^*(\text{Interpolated})}$
(a) Silicon					
N^+	20	10.8	1000	894	1.11
Ar^+	30	18.6	2490	2500	1.00
Zn^+	20	14.0	2600	2590	1.00
Zn^+	40	26.4	4650	4210	1.10
Cd^+	15	11.0	3110	3000	1.04
W^+	15	11.2	4260	4260	1.00
W^+	30	21.6	6430	7120	0.90
(b) Germanium					
N^+	20	10.4	1530	1620	0.95
W^+	15	11.6	6105	5560	1.09

Equation (7.11) provides an adequate prediction of N_D^* for ~10-250 keV ion ($14 \lesssim M_1 \lesssim 204$) bombardment of Si and Ge at low temperatures. However, the semi-empirical nature of the equation is stressed; the mathematical formulation of N_s is not the result of the application of a particular theory, but is merely a form found to satisfactorily fit the observations. Two features should be kept in mind:

(i) The equation is not expected to remain valid at energies much below 10 keV. The semi-empirical model predicts that at low energies, $dN_s/d\nu(E)$ becomes a constant, and the energy-spike will continue to contribute to the damage to effectively zero ion energy. However, in the discussion of Sec. 7.2.5 concerning the behaviour of the energy-spike at low energies, it was suggested that a critical spike lifetime or critical spike volume would exist below which the spike could not influence the damage. Once the ion energy is sufficiently small (<< 10 keV) that this limit is no longer exceeded, the semi-empirical model must break down. Unfortunately, experimental limitations discussed in Sec. 7.3.4 prevent extension of the damage measurements much below 10 keV.

(ii) Implicit in the semi-empirical formulation is that the collisional and spike components of the damage are independent and separable. For high energies, where $dN_D^*/d\nu(E) \rightarrow dN_{kp}/d\nu(E)$, this approximation is reasonable. At lower energies, the separation becomes less distinct, since virtually the entire N_{kp} will be contained in the energy-spike. As the energy is increased, more of N_{kp} will be outside the spike volume and the damage components may be treated as being independent. Also, the collisional damage component may be closely involved in determining the local lattice stability within the cascade volume. Then N_{kp} will at least

partly control N_s.

7.3.2 Molecular Versus Atomic Ion Bombardment

In the semi-empirical description of N_D^* developed in the previous section, it has been presupposed that the additional damage component is due to an energy-spike. It has been discussed in Sec. 7.2.6 that one method of testing whether the energy-spike indeed accounts for the additional damage is by comparison of equal atom-dose and energy/atom molecular and monatomic ion bombardments. This comparison is the topic of the present section. The measurements are all made at 35K so that the complication resulting from defect annealing is removed. The comparisons will concentrate on Si.

Shown in Fig. 7.8a,b,c is the ratio, $N_D^*(\text{molecular})/2 \cdot N_D^*(\text{atomic})$ plotted as a function of the atomic ion energy for Te, As and P bombardment of Si at 35K. The error bars represent the estimated ±5% error in the ratio. It is observed that a significant damage enhancement results at the lower energy bombardments, i.e.: at the higher energy densities. The energy dependence and magnitude of the ratio is due to two factors:

(i) As the ion energy increases, the energy-spike becomes of decreasing significance, i.e.: $dN_s/d\nu(E) \to 0$ as $E \to \infty$.

(ii) As the ion mass is reduced, a discrete and isolated subcascade structure develops within the cascade envelope (see Sec. 7.2.5). This will reduce the probability of overlap of the branches of the cascades for the individual atoms of the molecular ion. The local energy density associated with these subcascades will no longer be doubled. The effect will produce a reduction in the damage enhancement as the ion mass decreases, and as the ion energy increases.

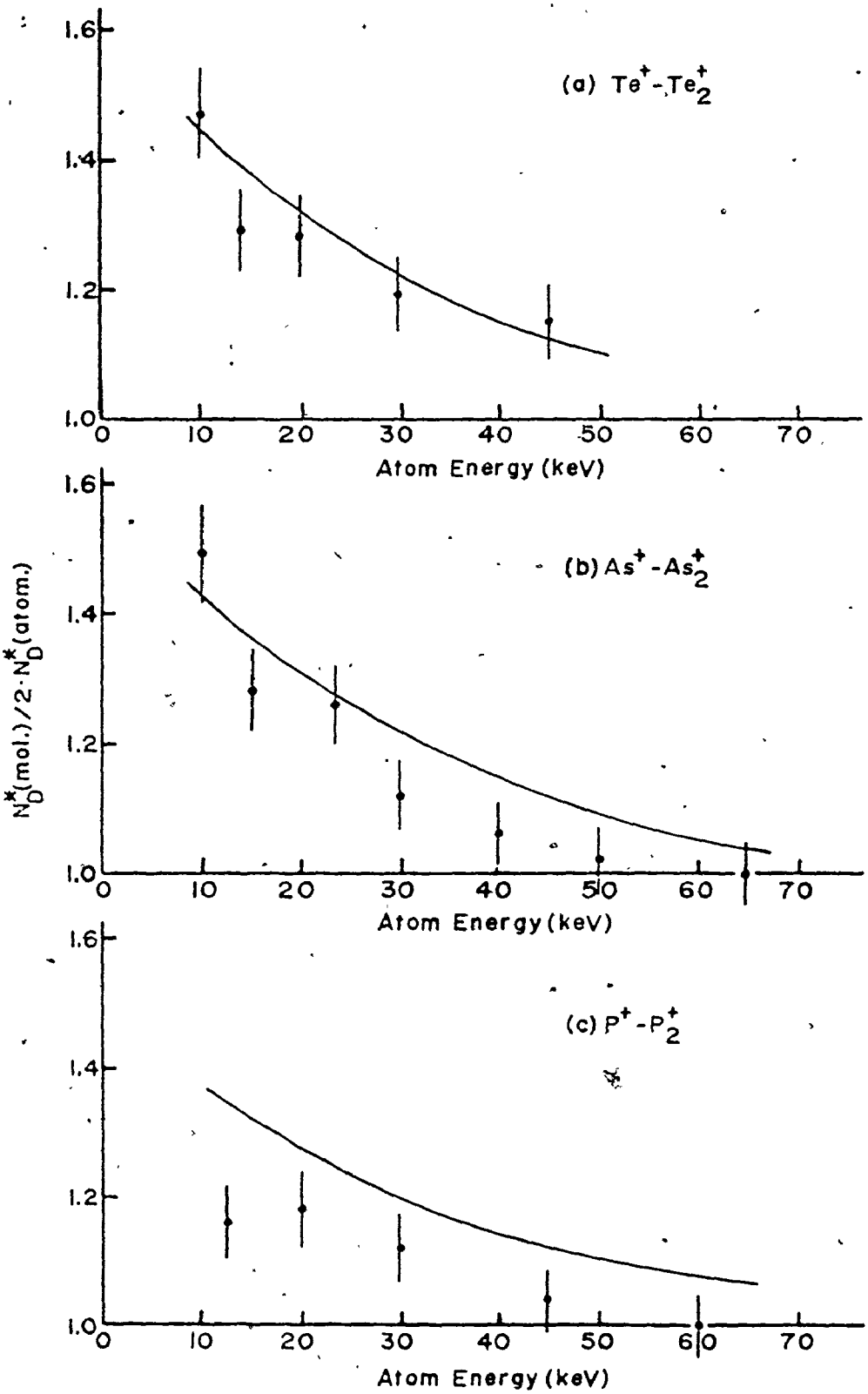

Fig. 7.8: The ratio, N_D^*(molecular)/2N_D^*(atomic), versus ion energy/atom for various ions in Si at 35K. The solid lines result from the semi-empirical model, Eq. (7.11).

It would be expected that the first factor is accounted for in the semi-empirical model, whereas no provision has been made for the second factor. The significance of the latter is largely determined by the magnitude of the ratio, V_R, of the individual to statistical cascade volumes. For large V_R, the overlap of the individual atom cascades of the molecular ion is complete enough that the energy density is effectively doubled. As V_R decreases, the second factor will become more important, and in the limit of very small V_R, the damage enhancement should completely disappear. Such behaviour has been reported in Sec. 7.2.6 for room temperature molecular and atomic deuteron bombardment of Si.[133]

The above predictions agree with the observations of Fig. 7.8. The solid lines represent the damage enhancement interpolated from the semi-empirical model, Eq. (7.11), for N_D^*. The molecular ion damage has been obtained from the equation by simulating the molecule (as far as the damage is concerned) as an ion of twice the atom mass and twice the atom energy. For Te in Si, the method reasonably predicts the damage enhancement at all energies for which it has been measured, and the second of the above factors cannot play an important role. This agrees with the large value of V_R (for Te-Si, $V_R \sim 0.52$).

However, the energy independence of V_R that is found for the heavier ions (see Fig. 3.8) does not necessarily imply that the second factor can always be ignored at higher energies. V_R represents the average correlation of the individual and statistical volumes; near the surface the correlation will always be essentially unity. Near the end of the ion trajectories, the correlation could well be much less than the average V_R. Since it is the latter region which is mainly involved in the energy-spike, the second

factor must eventually be considered. This effect will account for the As-As_2 damage behaviour where at energies $\gtrsim$20 keV, Eq. (7.11) overestimates the damage enhancement. For P bombardment, the Monte Carlo cascades of Fig. 7.4 and 3.7 reveal the presence of increasingly heterogeneous energy deposition (for P-Si, $V_R \sim 0.15$); Fig. 7.8c shows that for P in Si, the second factor influences the molecular ion damage at all energies considered, since Eq. (7.11) consistently overestimates the enhancement.

Figure 7.9 gives the variation of the damage enhancement for constant energy per atom (20 keV) as a function of ion mass (M_1) in Si at 35K. The solid line again results from Eq. (7.11) by treating the molecule as an ion of twice the atom mass and twice the atom energy. Also included is the volume ratio, V_R, for 20 keV ions in Si, as generated from the Monte Carlo code of Chapter III. For $M_1 \gtrsim 75$, the semi-empirical model adequately predicts the measured damage enhancement. For lower M_1, the rapid decrease in the measured enhancement is consistent with the rapid decrease in V_R. It is seen that for 20 keV N^+-40 keV N_2^+ in Si, the damage enhancement has entirely disappeared (for N-Si, $V_R \sim 0.02$). The particularly strong subcascade structure for 20 keV N^+ in Si is evident in Fig. 7.4. The disappearance of the damage enhancement does not suggest that the energy-spike is no longer of importance to the damage. In fact, for 20 keV N^+ in Si, N_D^* is still a factor of $\sim$3 greater than N_{kp}. Subscascade formation within the total cascade of sufficient energy density to influence the observed damage remains possible, and the damage continues to exceed the predictions of collision theory.

7.3.3 Evidence for Local Amorphization on Ion Bombardment

It has been noted that small amorphous zones ($\lesssim$100Å diameter) are

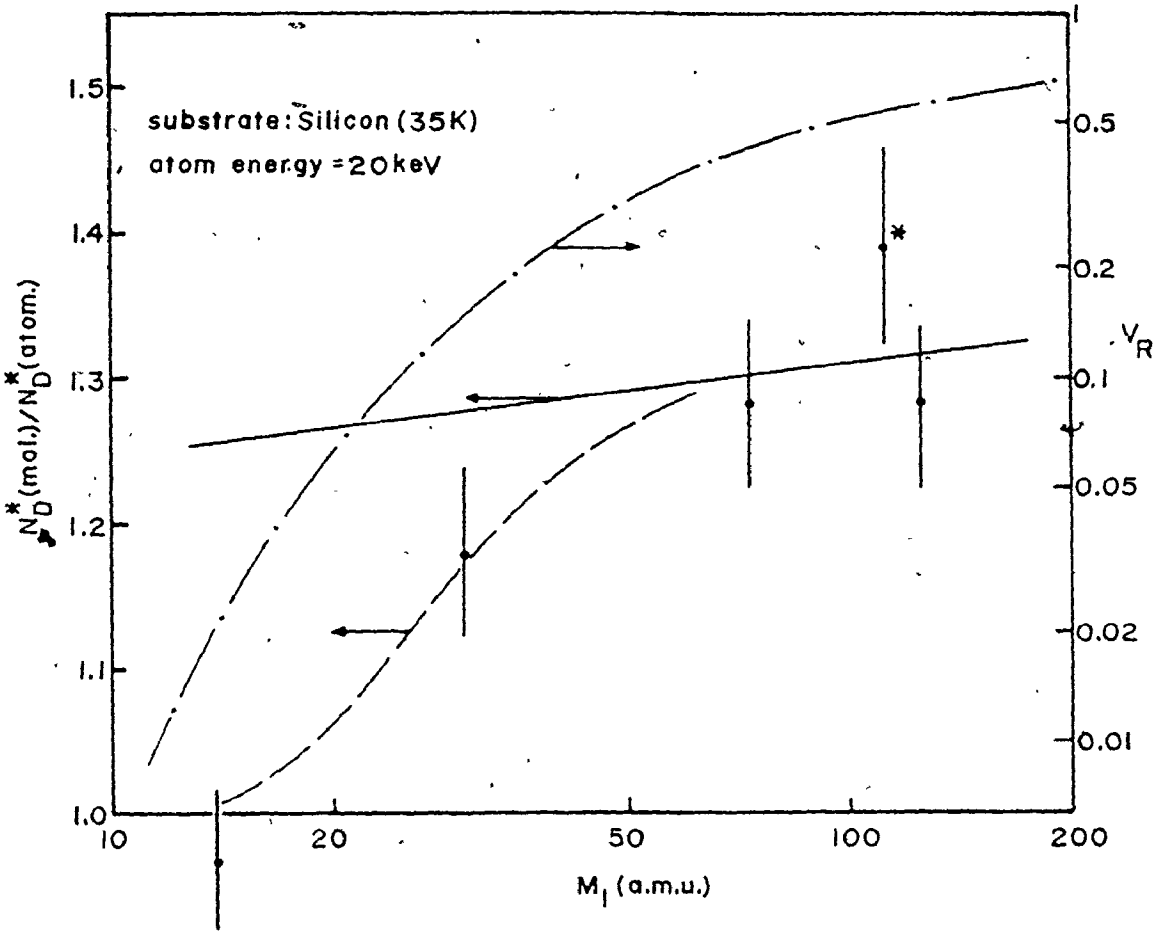

Fig. 7.9: The ratio, N_D^*(molecular)/2·N_D^*(atomic), at constant ion energy/atom (20 keV) versus ion atomic mass. (* 15 keV Cd^+-30 keV Cd_2^+). Solid line, from Eq. (7.11). Dot-dash line, volume ratio at 20 keV (from Sec. 3.4).

observed[45-47] by electron microscopy in ion bombarded semiconductors. We suggest that the presence of these amorphous regions accounts for the enhanced damage measurements, and furthermore that the energy-spike is instrumental in initiating the local amorphous transition. However, there

has been some controversy as to whether these amorphous zones can result from the individual ion collision cascade, or if they are due to collapse of the lattice in regions of repeated cascade overlap. In this section, observations related to the measurement of N_D^* are discussed, from which it is inferred that amorphous zones are indeed created by single ions. In the following section, the actual amorphization process will be discussed.

Two features of the measurements are of relevance to this discussion:

(i) The measurements of N_D^* have been made at dose levels such that the damage level is ~5%. At these doses cascade overlap, at least for the heavier ions, is virtually non-existent;

(ii) The model used to explain the low temperature damage-dose behaviour in Chapter VI, does not support the concept of spontaneous local amorphization once repeated cascade overlap produces a critical defect concentration of 2-4 at .%.[48]

The following observations support local amorphization by single ions:

(a) Damage stability

The damage enhancement for molecular versus atomic ion bombardment is generally greater at room temperature than at low temperature. This results since at room temperature, defects are mobile, and annealing can occur. The amount of annealing depends on the defect density; the higher defect density associated with the molecular ion bombardment is more stable at room temperature than is the lower defect density of the atomic ion bombardment. The magnitude of the damage enhancement therefore reflects the

competition between damage creation (viz. atom collisions and energy-spike) and damage removal (viz. annealing).

The ability of the damage to anneal is expected to be closely related to the energy density, since it is the latter which controls the defect density via the energy-spike. This dependence is examined in Table 7.2, where the damage for various ion bombardments in Si and Ge at 35K and 300K are compared. The values of N_D^* (300K) marked with an asterisk were acquired at Chalk River Nuclear Laboratories. The experimental facilities have been described elsewhere.(73) The values of N_D^{**} (35K) marked with a double asterisk were interpolated from the semi-empirical fit, Eq. (7.11), to the experimental data. Included are various diatomic as well as monatomic ion bombardments at both 35K and 300K. The ratio, N_D^*(molecular)/ $2 \cdot N_D^*$(atomic) is given at each temperature. The damage enhancement is greater at 300K than at 35K, because of the dual processes of energy-spike and annealing effects present in the former case. In Sec. 7.3.2 it was seen that the damage enhancement has disappeared at low temperatures for N^+-N_2^+ bombardments; at room temperature the enhancement continues to even lower ion masses. For example, a large enhancement has been reported for room temperature polyatomic-carbon-ion irradiations of Si.(132) Apparently, the extent of defect annealing remains sensitive to the local defect density to extremely low values of the latter.

Also given in Table 7.2 are the corresponding energy densities, $\bar{\theta}_\nu$, as taken from Fig. 7.2. It is observed that for increasing $\bar{\theta}_\nu$, the ratio $N_D^*(300K)/N_D^*(35K)$ increases towards unity. The variation of this ratio with $\bar{\theta}_\nu$ is plotted in Fig. 7.10 for both Si and Ge. In Si, for $\bar{\theta}_\nu \gtrsim 1$ eV/atom, the annealing has been almost entirely inhibited. Somewhat higher energy

Table 7.2

(a) Silicon data (35K, 300K).

Ion	Energy	ν(E)	N_D^*(35K)	$\frac{N_D^*(\text{Molecular})}{2 \cdot N_D^*(\text{Atomic})}$	N_D^*(300K)	$\frac{N_D^*(\text{Molecular})}{2 \cdot N_D^*(\text{Atomic})}$	$\frac{N_D^*(300K)}{N_D^*(35K)}$	$\bar{E}_D$ (eV/atom)
Ga	57	36.6	**5450		*1440		0.26	0.05
Ga	20	14.0	**2710		*1150		0.42	0.20
As	25	17.3	**3470	1.26	*1690	1.78	0.49	0.17
As_2	50	34.7	**8730		*6010		0.69	0.34
As	23.5	16.4	3210	1.26	1400	1.77	0.44	0.19
As_2	47	32.7	8100		4960		0.82	0.37
Sb	25	17.9	**4760	1.27	*3290	1.52	0.69	0.32
Sb_2	50	35.8	**12100		*10000		0.83	0.64
Te	14	10.4	3340	1.29	2470	1.60	0.74	0.70
Te_2	28	20.8	8600		7920		0.92	1.40
Te	10	7.59	2350	1.47	2040	1.60	0.87	1.00
Te_2	20	15.2	6920		6510		0.94	2.00

... continued ...

Table 7.2, continued

(b) Germanium Data (35K, 300K)

Ion	Energy	$\nu(E)$	$N_D^*(35K)$	$\frac{N_D^*(\text{Molecular})}{2 \cdot N_D^*(\text{Atomic})}$	$N_D^*(300K)$	$\frac{N_D^*(\text{Molecular})}{2 \cdot N_D^*(\text{Atomic})}$	$\frac{N_D^*(300K)}{N_D^*(35K)}$	$\bar{\epsilon}_D$ (eV/atom)
As	25	18.0	**5630	1.31	*3050	1.66	0.54	0.75
As_2	50	36.0	**14800		*10100		0.68	1.50
As	23.5	16.9	*5450	1.32	3300	1.65	0.61	0.80
As_2	47	33.8	14400		10880		0.76	1.60
Te	14	10.7	4820	1.17	3610	1.38	0.75	2.00
Te_2	28	21.4	11300		9970		0.86	4.00

* Indicates CRNL data.

** Interpolated from Eq. (7.11).

densities are required in Ge for total stability of the damage. This is perhaps indicative of the lower-temperature anneal stages exhibited in Ge. The stability of the damage at high energy densities suggests that essentially the entire cascade volume must be in the form of a highly-disordered or amorphous zone.

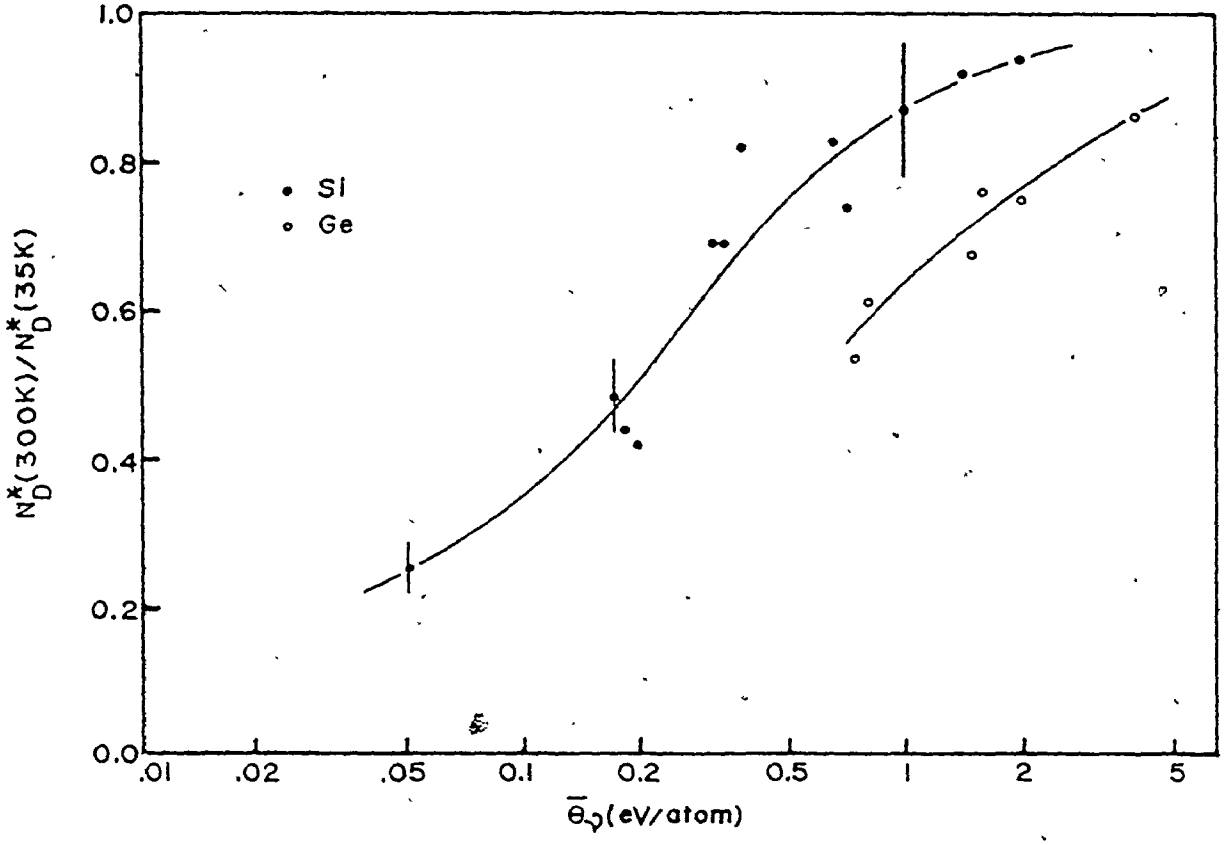

Fig. 7.10: Ratio of $N_D^*(300K)$ to $N_D^*(35K)$ versus energy density, $\bar{\theta}_\nu$, in both Si and Ge.

(b) Fractional damage, F_D, versus energy density

Plotted in Figs. 7.11 and 7.12 is the fractional damage, F_D, as defined by Eq. (7.5), versus $\bar{\theta}_\nu$ for Tl^+, Te^+, and As^+ bombardment of Si and

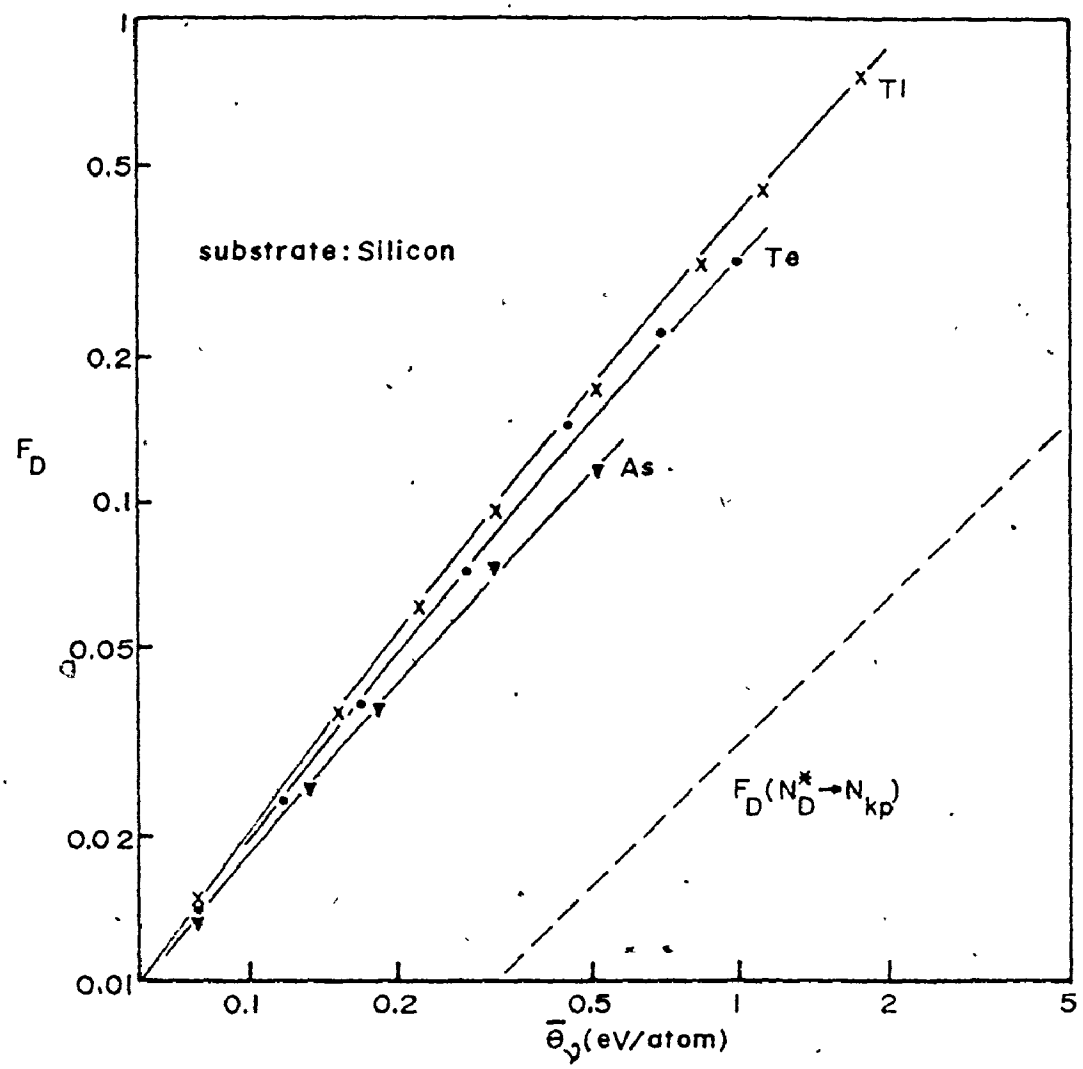

Fig. 7.11: Fractional damage, F_D, versus energy density, $\bar{\theta}_\nu$, for various ions in Si at 35K. Values of N_D^* taken from Fig. 7.5. Included is the collisional F_D, with N_D^* replaced by N_{kp}.

Ge respectively at 35K. (The values of N_D^* have been taken from Figs. 7.5 and 7.6.) Included for comparison is the collisional fractional damage, obtained by replacing N_D^* with N_{kp} in Eq. (7.5). For the highest energy densities obtained, F_D approaches unity in Si and actually exceeds unity

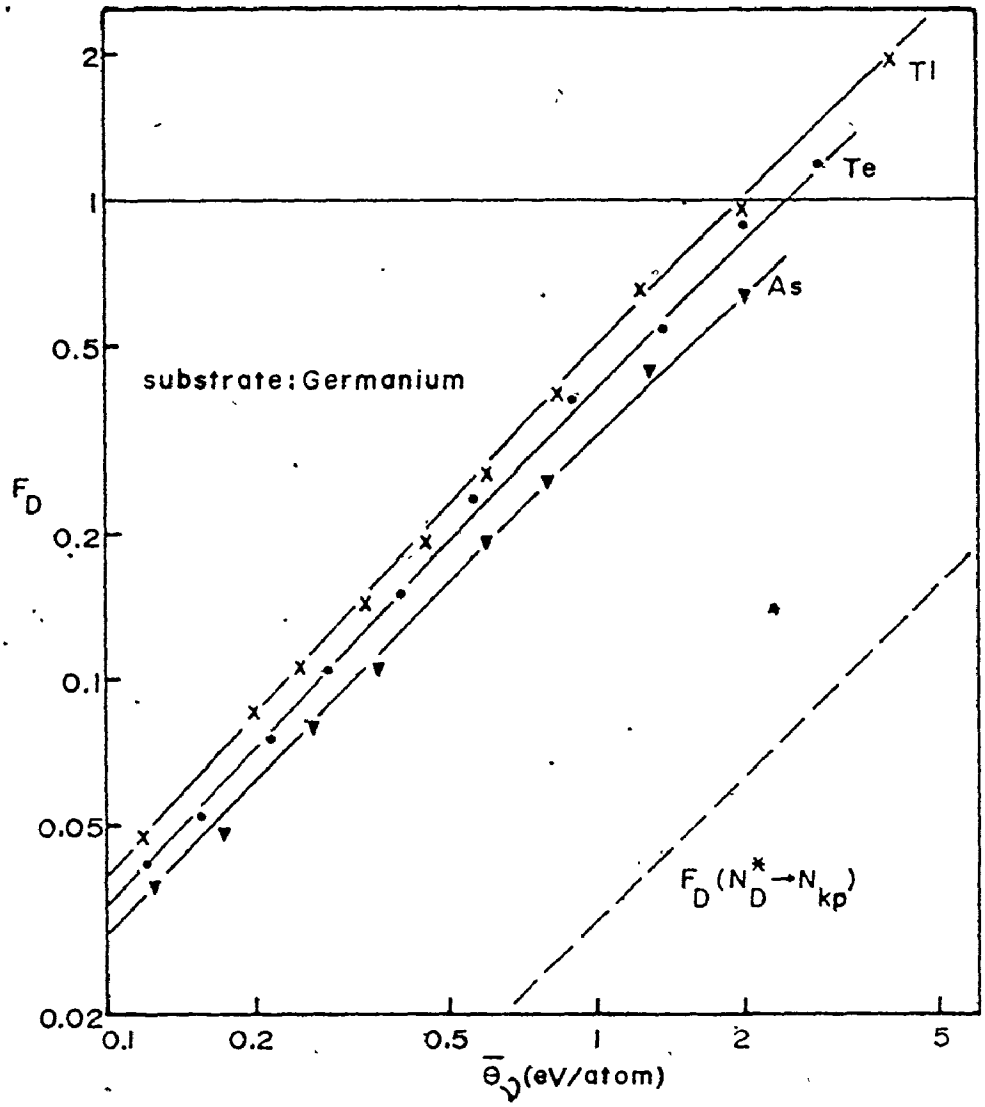

Fig. 7.12: Fractional damage, F_D, versus energy density, $\bar{\theta}_\nu$, for various ions in Ge at 35K. Values of N_D^* taken from Fig. 7.6. Included is the fractional F_D, with N_D^* replaced by N_{kp}.

in Ge. No saturation of F_D is evident at $F_D \sim 1$. These observations indicate that an amorphous region must extend as far as, and even beyond, the perimeter of the collision cascade. The propagation of the damage zone beyond the

dimensions of the cascade has been noted in measurements[123] of the saturation damage level resulting from low temperature ion bombardment. From these measurements it is inferred that:

(i) the damage depth begins to significantly exceed the predictions of collision theory for very heavy ions. For example, Table 6.4 shows that the damage depth in Si due to 15 keV Tl^+ exceeds that for the lighter 15 keV Te^+;

(ii) the damage depth for molecular ion bombardment becomes greater than that for equal energy/atom monatomic ion bombardment as the ion mass increases. For example, the damage depth due to 30 keV Te_2^+ in Si is ~10% greater than that for 15 keV Te^+.

(c) The spike damage volume

The semi-empirical model of N_D^* has separated the damage into collisional and spike components. On the assumption that the spike component, N_s, of the damage is in the form of a spherical amorphous zone, a spike diameter, D_s, can be assigned to N_s. Shown in Fig. 7.13a,b is D_s in Si and Ge respectively at 35K for the same ions as in Fig. 7.5 and 7.6. N_s has been derived using the semi-empirical fit, Eq. (7.11), to the data. While the separation of the collisional and spike damage components at low energies is less valid, the spike diameter, D_s, is relatively insensitive to whether only N_s or the total N_D^* is used.

The dimensions of the damage regions implied by Fig. 7.13 are in agreement with the size of the amorphous zones that have been observed by electron microscopy. For example, Baranova et.al.[47] report the presence

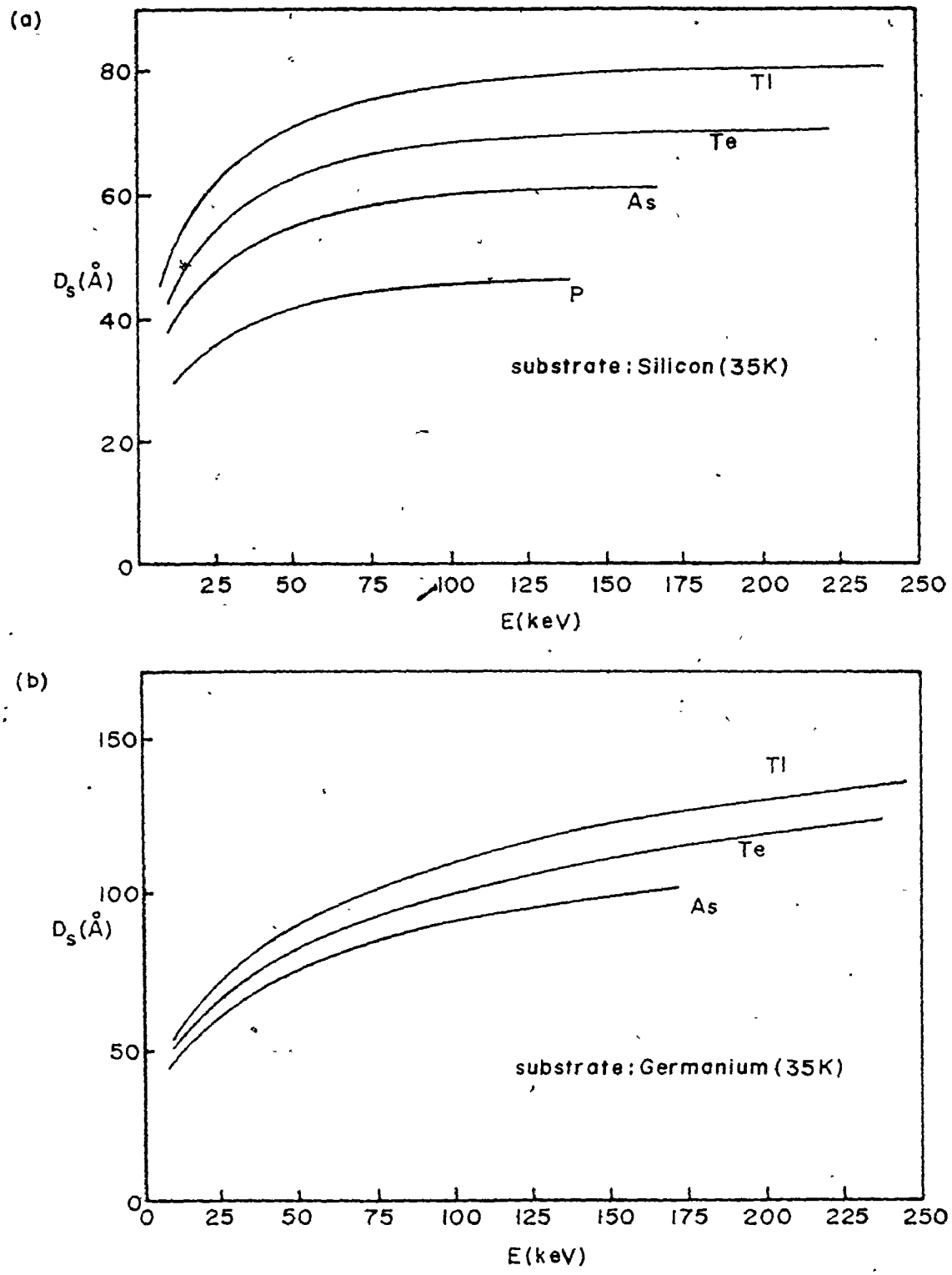

Fig. 7.13: The spike diameter, D_s, that results from assuming the energy-spike damage component, N_s, is in the form of a spherical amorphous zone. N_s interpolated via Eq. (7.11) for the data of Figs. 7.5 and 7.6.

of ~50-100Å diameter amorphous zones after room temperature bombardment of Si with 80 keV Sb^+, Ar^+, Ne^+, C^+, and B^+. Mazey et.al.[46] have similarly found ~50Å diameter zones in Si for room temperature bombardment with 20-90 keV Ne^+, P^+, and Si^+. Parsons[45] has observed ~89Å average diameter amorphous zones in Ge at 30K following 100 keV O^- bombardment. In fact, a distribution of zones were evident, with the minimum diameter being ~40Å. These observations are a good indication that it is indeed the amorphous zones which account for the increased measured damage over the predictions of collision theory.

7.3.4 The Amorphization Process

(a) The critical volume

It is interesting that the amorphous zones observed by electron microscopy are of roughly the same dimensions for high-Z_1 to low-Z_1 bombardment. As well, there appears to be a minimum diameter below which the zones are not evident, where the critical diameter is ~40-50Å. This would support the previously discussed concept that a minimum spike volume may exist below which the spike could not influence the lattice structure. In Fig. 7.13b, for the lowest energy ions considered in Ge, D_s always exceeds 40Å; this is the minimum zone diameter reported by Parsons[45] for 100 keV O^- irradiation of Ge. In Si, Fig. 7.13a shows that for ions heavier than As, a minimum D_s of 40Å could be accommodated. However, for P in Si, D_s falls below 40Å for $E \lesssim 40$ keV. For lighter ion damage, e.g. N^+, D_s would be even less. This would imply that as the ion mass decreases, the probability of formation of an amorphous zone for each incoming ion falls below unity, so that the average D_s is less than the critical diameter.

Such behaviour has been reported by Parsons[45] for 100 keV O^- bombardment of Ge; he found that there was only one amorphous zone created for about every three incoming ions.

(b) Damage versus energy density

The correlation between damage and energy density for low temperature ion bombardment of the semiconductors is examined in Fig. 7.14, where $dN_D^*/d\nu(E)$ has been plotted against $\bar{\varepsilon}_\nu$ for both Si and Ge at 35K. The ordinate scale has been obtained by differentiating the semi-empirical fit, Eq. (7.11), to the measurements presented in Figs. 7.5 and 7.6. The gradient of N_D^* has been chosen, rather than the total N_D^*, since the separation of the damage into a collisional and energy-spike related component will be more readily apparent in such an analysis. $\bar{\varepsilon}_\nu$ only extends over these values corresponding to the energy interval for which N_D^* was measured. In accordance with the formulation of Eq. (7.11), $dN_D^*/d\nu(E)$ for Si approaches asymptotically the prediction of collision theory as the energy density decreases. Much lower energy densities (an order of magnitude lower) are required in Ge for the energy-spike effect to disappear. For increasing energy density, $dN_D^*/d\nu(E)$ eventually saturates for each ion species at a level determined by the constant K_s, of Eq. (7.10). Saturation is expected since the high energy densities of Fig. 7.14 have been attained by the concentration of the ion energy into smaller and smaller volumes. Eventually the volume will reach a critical volume (~40Å) and the spike contribution to the damage will diminish. The energy at which this occurs is evidently << 10 keV. Unfortunately, this behaviour cannot be further examined with the present experimental methods, since a minimum bombardment energy of ~10 keV is imposed. As well, for the high-Z_1 implants, the presence of the surface

oxide, which the ion must penetrate, and the enhanced sputtering yields[61] interfere with the damage measurement at low energies.

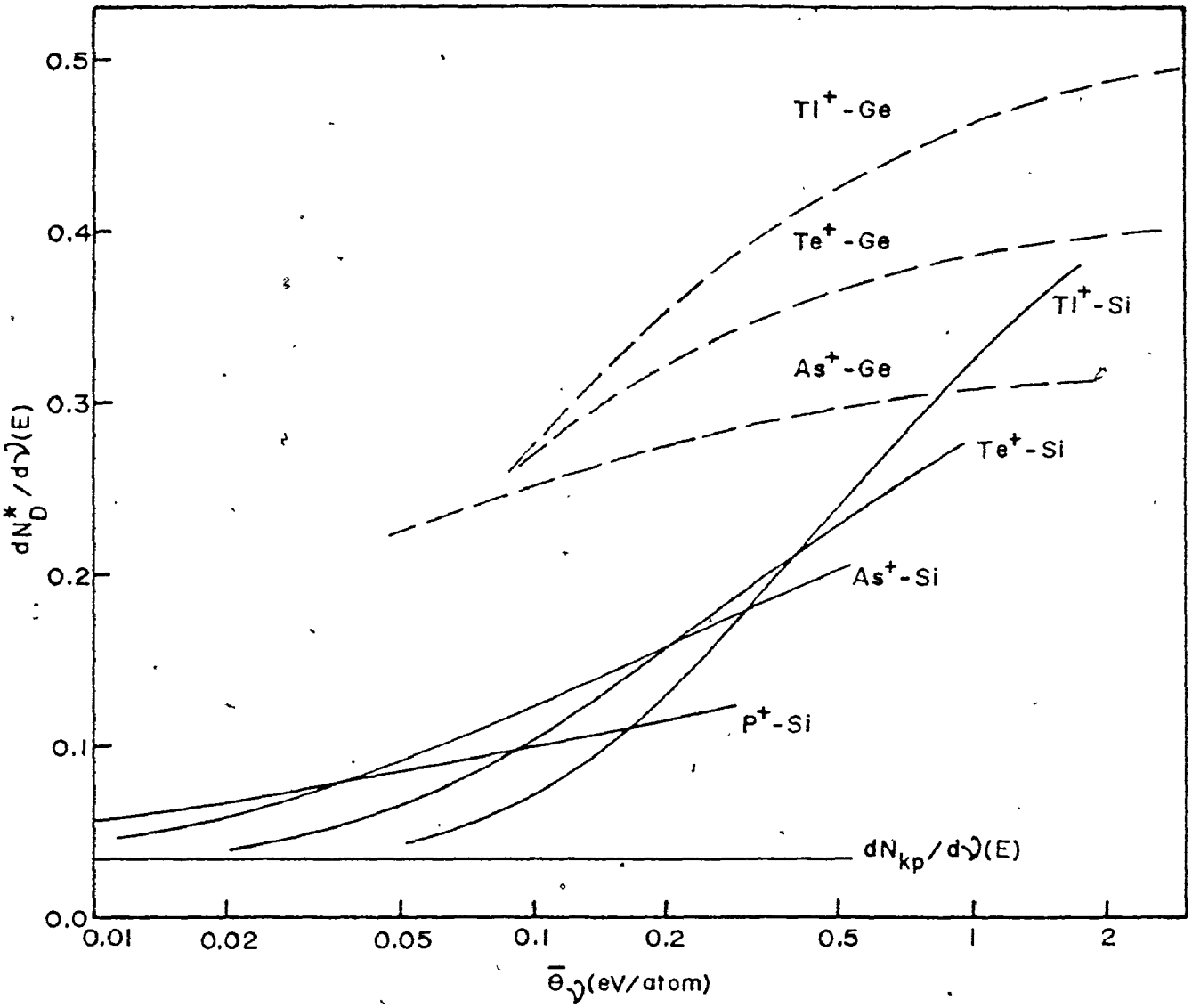

Fig. 7.14: $dN_D^*/d\nu(E)$ versus $\bar{\theta}_\nu$ for various ions in Si and Ge at 35K. The ordinate has been interpolated via Eq. (7.9) for the data of Figs. 7.5 and 7.6.

(c) The critical energy density

Figure 7.14 has shown that in Si, the damage begins to exceed collision theory for energy densities between ~0.1-1 eV/atom. In Ge, the damage increases for energy densities about an order of magnitude lower. It is suggested that there may be fundamentally different mechanisms responsible for the local amorphous transition in each semiconductor. In particular, the Si data suggest a "thermal-spike" process as initiating the transformation (the heat of melting in Si ~ 0.8 eV/atom). The Ge data support the model that a local lattice collapse occurs due to the excess of defects, broken bonds, and potential energy (the increase in energy of Ge in the amorphous state has been estimated at ~0.11 eV/atom). It is relevant to note that in Fig. 7.13b, the collisional fractional damage in Ge is only ~5-10 at .% when F_D reaches unity; it does not differ greatly from the estimated critical defect concentration of 2-4 at .%.[48]

Thus, it is concluded that the energy-spike initiates a local amorphous region within the semiconductor, which accounts for the larger measured damage than collision theory predicts. A minimum critical volume exists of ~40Å diameter. For heavy ions, the probability is essentially unity that one amorphous zone of diameter ≥ the critical diameter forms on each ion bombardment. For lighter ions, this probability falls below unity. The energy density at which the damage begins to deviate from collision theory indicates that the amorphization process in Si may be via a "thermal-spike" mechanism. For Ge, it appears more relevant to speak of the local athermal collapse of the unstable lattice. The high-energy limit of spike-effects in the damage corresponds to an energy density of ~0.1 eV/atom in Si and about an order of magnitude lower in Ge. The low-energy limit is evidently << 10 keV.

CHAPTER VIII

SUMMARY

This chapter summarizes the observations made in the work and the conclusions that have been drawn.

1) Analysis Techniques

The dechanneling of channeled particles due to defect scattering in a radiation damaged semiconductor at low temperatures is generally not adequately described by scattering models for amorphous targets. This results since channeled particles can undergo additional correlated scattering from the atom relaxations due to the lattice strains that accompany the damage; the amorphous models cannot account for such scattering. Rather than attempt to predict this component, it is adequate to impose certain intuitive boundary conditions on the calculated dechanneling. The damage profile is relatively insensitive to the exact shape of the resultant semi-empirically derived dechanneling line.

2) Monte Carlo Results

(i) If an amount of energy, U, is considered expended at every atom displacement, ΣU can be a significant portion of the incident ion energy. For $U = E_d$, $\Sigma U = 1.30\ \nu(E)$, where $\nu(E)$ is the total energy into elastic scattering.

(ii) The Monte Carlo estimate of the number of displaced atoms

resulting from the collision cascade exceeds by ~50 the value predicted by the modified Kinchin-Pease equation (Eq. (2.34)).

(iii) For U = 0, the Monte Carlo code shows that replacement collisions account for 0.28 of the total number of displacement collisions. This agrees with Sigmund,[3] who has used collision theory to estimate the replacement fraction at ~0.30. However, for the more realistic situation of $U = E_d$, the fraction obtained from the Monte Carlo code decreases to 0.19.

(iv) The individual cascade volume can be up to three orders of magnitude smaller than the statistical cascade volume for low-Z_1 ion bombardment of Si and Ge. For a volume ratio, $V_R \geq 0.05$ (corresponding to $M_2/M_1 \lesssim 1$-2), the ratio is independent of ion energy in the energy interval 10-100 keV. For lower V_R, the ratio decreases with increasing energy.

(v) V_R obtained from the Monte Carlo code is consistently lower than the value that results from correlation theory.[25] For large M_2/M_1, the saturation of V_R predicted by correlation theory is not observed in the Monte Carlo values. In fact, we predict that even lower values of V_R are realistic, since the Monte Carlo definition of V_R does not take into account possible subcascade structure within the cascade volume.

3) Damage Profiles

(i) Directional (<111>,<110>) damage dependence does not exceed 10-15% in Si, GaAs and GaP at 50K, in contradiction to the results of Bottiger and Whitton.[113]

(ii) For damage levels ≳15%, the use of non-aligned stopping powers in energy-to-depth scale conversion appears appropriate, in agreement with

the observations of Böttiger and Eisen.[84b]

(iii) Deviations between the measured and theoretical damage profiles in Si, GaP and GaAs at 50K suggest that the standard value of the electronic stopping power, as given by Lindhard, is often an underestimate. The adjustment in the electronic stopping in Si necessary to match the theoretical profiles to those measured is in qualitative agreement with the Z_1-oscillatory behaviour of the electronic stopping reported in foil transmission measurements.[115]

4) Radial Defect Distribution

(i) The measured damage increases by up to ~100% for small misalignment of the channeled beam direction relative to the crystal axis ($\psi_{in} \leq 0.36\ \psi_1$).

(ii) This "Off-Axis" effect is due to direct backscatter from the atom relaxations that result from the lattice strains which accompany the radiation damage. At low damage levels (~10%), the relaxations extend perpendicular to the channel row by up to ~40% of the channel radius. The extent of the relaxations is comparable in GaP and GaAs, and slightly less in Si. It is suggested that the ionic nature of the III-V compounds may account for their greater relaxations.

(iii) At low damage levels ($\lesssim$10%) and under best-alignment conditions, the channeling backscattering technique gives a reliable estimate at low temperatures of the grossly displaced atoms, with contributions from atom relaxations being negligible. However, since the "Off-Axis" effect persists to peak damage levels $\gtrsim$50%, atom relaxations must begin to contribute to the measured damage at high damage levels. The maximum contribution under

best-alignment conditions is estimated at ~50% of the measured damage.

(iv) The magnitude of the "Off-Axis" effect increases both for decreasing ion mass and increasing damage depth. This does not result from differences in the damage structures; it results mainly from the increasing area of the channel (and hence more atom relaxations) sampled by the analysing beam. The area increases because of the greater inelastic and defect scattering of the channeled He^+ particles in the deeper damage layers for the lower-Z_1 bombardments. The apparent insensitivity of the radial displaced atom distribution to the ion mass reflects the gross averaging nature of the channeling-backscattering technique.

5) The Ion Dose Dependence of the Damage

(i) For low-Z_1 ion damage in the semiconductors at low temperatures, the damage exhibits a greater than linear increase at low ion doses. As Z_1 increases, the non-linearity disappears.

(ii) The damage-dose behaviour at low temperatures is adequately described if the contribution to the measured damage due to direct back-scatter from atom relaxations is included. We have incorporated the component as being directly proportional to N_D. The proportionality factor, c, is found to be essentially constant over a wide range of ion bombardments. This again shows the gross-averaging behaviour of the channeling technique, although certain trends may be significant. For example, for the heaviest ions in Si, the observed decrease in c, although within experimental error, is expected; as the damage is concentrated into heavily-damaged regions for the high-Z_1 bombardments, the relative contribution due to lattice strains should diminish.

(iii) The proportionality factor, c, is larger in GaP and GaAs than in Si. This agrees with the relative amount of atom relaxations inferred in the materials from the "Off-Axis" effect.

(iv) The damage-dose data, and the proposed model, do not support the concept[48] that a local collapse of the lattice will occur when a critical defect concentration of 2-4 at .% is achieved by repeated cascade overlap.

6) Damage and the Energy-Spike

(i) Linear collision theory reasonably predicts the number of displaced atoms per ion at low temperature only for very low-Z_1 ions (e.g. He^+). For higher-Z_1 bombardments, the measured damage exceeds by as much as an order of magnitude the predicted value. Observations indicate this effect is not an artifact of the channeling-backscattering technique. We propose that an energy-spike generated by the ion can initiate a stable amorphous zone in the semiconductor, thereby accounting for the enhanced damage.

(ii) $dN_D^*/dv(E)$ in Si at 35K approaches the prediction of collision theory at high ion energies ($\gtrsim$100 keV). This suggests that the damage consists of a collisional component and an additional energy-spike component which disappears at sufficiently high energy. A semi-empirical model has been developed around this assumption to fit the damage data in Si and Ge at ion energies of 10-250 keV and ion atomic masses of $\sim$14-200.

(iii) More damage is created per atom at low temperatures for molecular ion bombardment of the same energy/atom as for monatomic ion bombardment. For high-Z_1 irradiations, the magnitude of the enhancement is

consistent with the semi-empirical model. For lower-Z_1 irradiations, the disappearance of the enhancement is expected because of the rapid decrease in the volume ratio, V_R, of the individual to statistical cascades.

(iv) It is inferred that the energy-spike can initiate a local amorphous zone since:

(a) The damage becomes completely stable up to room temperature bombardment at energy densities $\gtrsim$1 eV/atom.

(b) The fractional damage approaches and actually exceeds unity for energy densities $\gtrsim$1 eV/atom, with no indication of saturation.

(c) If the damage component resulting from the energy-spike is assumed in the form of a spherical amorphous zone, the inferred dimensions agree with the size of the amorphous zones observed by electron microscopy[45-47] of ion bombarded semiconductors.

(v) The high energy limit for energy-spike effects in the damage corresponds to an energy density of $\sim$0.1 eV/atom in Si, and $\sim$0.01 eV/atom in Ge. The low energy limit for spike effects is evidently $\ll$ 10 keV.

(vi) Associated with the low energy limit for spike effects, is a critical volume necessary for the amorphous zone to remain stable. The critical diameter is inferred to be $\sim$40Å in both Si and Ge. For $Z_1 \gtrsim 30$ and $E \gtrsim 10$ keV, the probability is unity that one stable amorphous zone is induced per ion. As Z_1 decreases, the probability falls below unity.

(vii) A thermal-spike mechanism appears to control the local amorphization process in Si; in Ge, an athermal lattice collapse better explains the observations.

ADDENDUM

The addendum contains documentation and listings of the various computer codes that have been developed in the course of the work of the thesis, namely:

(1) MONTY - The Monte Carlo collision cascade simulation code presented in Chapter III;

(2) data analysis via the methods of Sec. 4.3:

(i) DCULD - determination of N_D using linear dechanneling,

(ii) DCUSS - determination of N_D and profile extraction (with plot) using semi-empirical single scattering dechanneling,

(iii) SPEDS - spectra plot, including energy and depth scale generation;

(3) PHA11 - data acquisition code for pulse-height analysis and data manipulation (see Sec. 5.4).

The codes listed under (1) and (2) are FORTRAN -IV language routines written for a PDP-15 minicomputer under the ADSS operating system. The operating environment includes:

32K-18 bit word code memory;

additional 20K word common storage;

four 256K word fixed-head disks;

dual DEC-TAPE units;

DEC VT05 video terminal;

Centronics 306 Printer;

Calcomp 565 plotter;

dot-matrix display;

optical paper tape reader and punch.

The programs exist as EXECUTE files, which use a link structure via the disk, so that virtual memory space is available.

The data acquisition code is a machine language routine written for a PDP-11/05 minicomputer under the RT-11 operating system. Fig. 5.3 shows schematically the operating environment. The memory is 20K-16 bit word core memory.

A.1 MONTY - Monte Carlo Collision Cascade Simulation Routine

(a) Routines:

FORTRAN-IV - MONTY, INCON, SIGEN, FCT, GUTS , PLTSET, CASPLT, FOLLOW, SEARCH, TRANS, ANGLE, STORE, RESTOR, OUTGO, EVALS, RANDOM.

MACRO - SHIFT.

Chain structure:

Resident = MONTY
L1 = INCON
L2 = SIGEN, FCT
L3 = GUTS/FOLLOW, SEARCH, RANDOM, SHIFT
L4 = OUTGO/EVALS
LL0 = TRANS, STORE, RESTOR, ANGLE
LL1 = PLTSET/CASPLT
L1:L2:L4:L3,LL0
LL0:LL1

(b) Listings:

Listings are included for all routines.

(c) Program operation:

Program operation may be commenced by typing:

E MONTY

The code is interactive, i.e.: it requires run-time user response to programmed questions regarding the input parameters. However, it is possible to pre-program the replies on paper tape and have operation proceed in BATCH mode by typing:

B PR

The paper tape must commence with:

```
JOB name
A PRA 2
E MONTY
$DATA
```

followed by appropriate replies to the questions.

The questions are self-explanatory and need not be elaborated upon here. Chapter III contains a detailed discussion of the features of the code.

A.2 Data Analysis Routines

(a) Spectra input

All data analysis routines require that the spectra to be analyzed exist as ASCII files on disk no. 1 (DK1). Only 256-channel spectra are accepted. The file structure must consist of:

one title line in format 8A5,

one line containing analysis beam dose (in units of 10^{-10} Coulombs) in free format;

26 lines of channel data (10/line, except for last line) in free format. Each data line may optionally begin with (PDP-11 format) or without (ND1100 format) the channel number of the first channel of the line.

(b) Listings:

Listings are given here for all FORTRAN routines necessary. The routines ESCAL, LINREG, ELOSS and SP are common to all analysis codes and appear at the end of the listings. MACRO programs DSPGF, TTIN, IDSP, AIPA, ERRPRT are user-library routines available on the PDP-15 and are not included here. The first three control spectra display on the dot-matrix display unit. AIPA assigns the Calcomp plotter to logical unit 3. It calls ERRPRT. AIPA can be deleted from wherever it appears provided the following assignment is made immediately prior to execution:

A IPA 3.

(c) Program execution:

All analysis routines exist as EXECUTE files, operation of which may be commenced by typing:

E (name)

Note that the ASCII file COEFF must be present on DK1 during program operation. It contains information related to the electronic stopping powers. A listing of COEFF appears at the end of the analysis-routine listings.

All programs are interactive, with the required user-supplied information being self-explanatory. Individual program features are described below.

A.2.1 DCULD - Linear Dechanneling Routine

(a) Routines:

FORTRAN-IV - DCULD, LD1, LD2, ESCAL, ELOSS, LINREG, SP.

MACRO - DSPGF, TTIN, IDSP.

(b) Chain structure:

Resident = DCULD, ESCAL, ELOSS, LINREG, LD1, SP, LD2, DSPGF, TTIN, IDSP.

(c) Program features:

DCULD will calculate N_D via Eq. (4.23). The aligned spectrum after bombardment must exist on DK1. It is displayed to allow for user choice of the damage end-channel, b'. The user inputs: the non-aligned yield, y_N, counts in the surface peak, and χ_{min} for the aligned spectrum before bombardment. Appropriate data are output on the printer.

A.2.2 DCUSS - Semi-empirical Single Scattering Dechanneling Routine

(a) Routines:

FORTRAN-IV - DCUSS, DECHO, PRINT, DPLOT, DECH1, DTCAL, SCALE, LAX, ESCAL, LINREG, ELOSS, SP.

MACRO - DSPGF, TTIN, IDSP, AIPA, ERRPRT.

(b) Chain structure:

Resident = DCUSS, #PLOT, AIPA, ERRPRT.

L1 = DECHO/DECH1, DSPGF, TTIN, IDSP, ESCAL, LINREG, ELOSS, DTCAL, SP.

L2 = PRINT

L3 = DPLOT/SCALE, LAX.

L1:L2:L3

(c) Program features:

DCUSS will calculate N_D as well as the damage profile via the methods of Sec. 4.3.2. Three spectra must exist on DK1: the non-aligned spectrum and the aligned spectra before and after bombardment. The spectra are displayed at various locations in the analysis to allow certain user decisions to be made. The order of analysis is:

1) subtract the surface peak on the aligned spectrum before bombardment from the aligned spectrum after bombardment,
2) perform the Rutherford correction, normalized to the surface yield,
3) optionally perform a three-point weighted smooth of the data,
4) calculate the semi-empirical single scattering dechanneling line,
5) optionally print out the data,
6) optionally plot the damage profile.

A.2.3 SPEDS - Spectra Plot with Energy and Depth Scale Generation

(a) Routines:

FORTRAN-IV - SPEDS, SPL1, SPL2, SCALE, AXIS, DSCAL, HESP, ESCAL, ELOSS, LINREG, SP.

MACRO - AIPA, ERRPRT.

(b) Chain structure:

Resident = SPEDS, #PLOT, AIPA, ERRPRT.

L1 = SPL1/ESCAL, LINREG, ELOSS.

```
L2 = SPL2/SCALE. AXIS, DSCAL, HESP, SP.
L1:L2
```

(c) Program features:

SPEDS will plot up to five 256-channel spectra on the Calcomp plotter. The spectra to be plotted must exist on DK1. User scaling may be performed; the vertical axis is chosen automatically. Energy and depth scales may optionally be generated. The depth scale is found by numerical integration of Eq. (4.13).

Following are the appropriate listings for the routines.

```
C       FILE MONTY ON DECTAPE SWPP5U
C       BY P S WALKER  S S U  FUEHLMAN  JAN  1ST
C       MAINLINE TO GENERATE AN ION-SOLID INTERACTION
C         SIMULATION VIA THE MONTE CARLO TECHNIQUE
C       PRODUCING 1 = RANGE DATA ONLY
C                 2 = DAMAGE PRIMARY RECOILS = DATA ONLY
C                 3 = DAMAGE ALL RECOILS = DATA ONLY
C                 4 = INDIVIDUAL CASCADE DETAILS AND PLOT
C       SUBROUTINES REQUIRED SPC-INCON,FCT,SIGEN,GETS,CHARLI,OUTGT,
C                  SEARCH,FOLLOW,ANGLE,TPHAS,RESTOR,STOPE,EVALS,
C                  RANDOM,SHIFT
C                            BIN-HIPH,EPPPPT,PHIDY
C       USE
C                 # E MONTY
C                 ACC BITS  00-TURN ON TO EXTEND # OF PROCESSED PARTICLES
C                           ABOVE THE PRESET VALUE AND THEN OFF TO STOP
C                           PROCESSING AT THE CURRENT PARTICLE # + 1
C                           01-DISPLAYS ON TTY THE CURRENT PARTICLE #
C                           AT THE START OF PROCESSING
C
        DIMENSION T(600),SIGVAL(600)
        COMMON /BLK1/TITLE(16,4),NOP,NOINT,NOINT,NOPT,MODE,ITYPE
        COMMON /BLK2/Z1,Z2,AM1,AM2,E1,ECUT(2),HTDEN,EL,ELD,UDD
        COMMON /BLK3/GAMMA(2),EPS0(2),SCR(2),ELI(2),AMP(2),EST(2,2)
        COMMON /BLK4/TK,ELOSS,ELEC,PATH,TH1,PH1,TH2,PH2
        COMMON /BLK5/STO(100,6),X0,Y0,Z0,TH0,PH0,EV
        COMMON /BLK6/DEP(50),STOP(50),NSPUT(2)
        COMMON /BLK7/JTOP,RANGE,PROJP,AVI,AVII,AVIII,VOL
        COMMON /BLK8/UM(4,2),TERM(2,2)
        COMMON /BLK9/IND,IPNT(2000,2),NDEF,DEF,IPPM(400,2),NPPM
C
C       LIST OF VARIABLES--NOT EXHAUSTIVE
C
C       ECUT(1,2)=INCIDENT & RECOIL CUT OFF ENERGIES (EV)
C       EL=DISPLACEMENT ENERGY (EV)
C       EPS0=EPSILON (REDUCED ENERGY) FOR 1 KEV
C       E1=PROJECTILE ENERGY IN KEV
C       ITYPE=COLLISION TYPE:1.)IF INCIDENT ON SUBSTRATE
C                            2.)IF SUBSTRATE-SUBSTRATE
C       MODE=MODE OF OPERATION:1.)IF RANGE
C                              2.)IF DAMAGE FOLLOWING PRIMARY RECOILS
C                              3.)IF DAMAGE FOLLOWING ALL RECOILS
C                              4.)IF CASCADE REQUIRED
C       MOPT = M OPTION;       0.)M=1/3
C                              1.)M=0.055
C                              2.)M=0
C       NOINT=NUMBER OF HISTOGRAM INTERVALS
C       NOP=NUMBER OF PARTICLES TO BE PROCESSED
C       RANDY = RANDOM NUMBER GENERATER FUNCTION
C       SCR=SCREENING RADIUS (ANGS)
C       WOINT=WIDTH OF HISTOGRAM INTERVALS
C
999     WRITE(4,2)
2       FORMAT(1H1,25X,"MONTY",/,26X,5("="),//)
        WRITE(1,2)
C
C       GET INPUT DATA AND CALCULATE CONSTANTS
```

```
C
      WRITE(1,15)
15    FORMAT(" ENTER INCON")
      CALL INCON(ISEED,LINE,NOPT)
C
C     GENERATE STOPPING POWER INTEGRATION TABLES OF SIGMA
C          FOR VALUES OF T BETWEEN E-4 AND 1E+6
C
      WRITE(1,37)
37    FORMAT(" ENTER SIGEN")
      TM=(EPS0(1)*E1)**2
      TM1=(EPS0(2)*E1)**2
      IF(TM1 GT TM)TM=TM1
      IF(TM LT  .0001)GO TO 41
      CALL SIGEN(T,SIGVAL,TM)
41    WRITE(1,35)
35    FORMAT(" ENTER GUTS")
C
C     DO MODE OPERATION FOR NOP PARTICLES
C
      CALL GUTS(T,SIGVAL,ISEED,LINE,NOPT)
C
C     FINISHED.  SO OUTPUT RESULTS
C
      CALL OUTGO
      GO TO 999
      STOP
      END



      SUBROUTINE INCON(ISEED,LINE,NOPT)
C     ROUTINE TO INPUT DATA AND OPTIONS, WHICH THEN CALCULATES
C      CONSTANTS
C
      DIMENSION TLE(2)
      COMMON /BLK1/TITLE(16,4),NOP,NOINT,NOINT,MOPT,MODE,ITYPE
      COMMON /BLK2/Z1,Z2,XM1,XM2,E1,ECUT(2),ATDEN,ED,EDD,UDD
      COMMON /BLK3/GAMMA(2),EPS0(2),SCR(2),ELE(2),XMR(2),EST(2,2)
      COMMON /BLK9/IN5,IPNT(2000,2),NDEF,DEF,IPRM(400,3),NPRM
C
C     INPUT DATA SECTION
C
99    WRITE(1,2)
2     FORMAT(" SELECT PROGRAM MODE OF OPERATION",/,2X,
     1 "RANGE(1),DAMAGE-PRIMARY RECOILS(2),DAMAGE-ALL RECOILS(3),"
     2 ",CASCADES(4)")
      READ(2,) MODE
      IF(MODE.LE.0.OR.MODE.GE.5) GO TO 99
      WRITE(1,4)
4     FORMAT(" INPUT PROJECTILE ELEMENT(5 CHARS MAX )<CR>,
     1 ATOMIC NUMBER<CR>",/,5X,"MASS NUMBER<CR> AND ENERGY(KEV)<CR>"
      READ(2,1) EL1
1     FORMAT(A5)
      READ(2,) Z1
```

```
      READ(2,) TM1
      READ(2,) E1
      WRITE(1,6)
6     FORMAT(" INPUT TARGET ELEMENT(OR -1 FOR MIX) AND
     1 SPECIFIC GRAVITY")
      READ(2,1) EL2
      READ(2,) Z1
      READ(2,) AM2
      READ(2,) ATDEN
      WRITE(1,5)
5     FORMAT(" INPUT DISPLACEMENT ENERGY (EV)")
      READ(2,) ED
      WRITE(1,105)
105   FORMAT(" INPUT ENERGY LOSS PER COLLISION (EV)")
      READ(2,) EDD
      UDD = EDD
      IF(EDD.EQ.0) GO TO 109
      WRITE(1,107)
107   FORMAT(" IS U TO BE ADDED INTO DEP. ENERGY DISTR (0 OR 1)")
      READ(2,) ISU
      IF(ISU.EQ.0) UDD = 0.0
109   WRITE(1,26)
26    FORMAT(" DO YOU WISH MINIMUM CUTOFF ENERGY(Y=1)?")
      READ(2,) ILOW
      IF(ILOW.EQ.1) GO TO 55
      WRITE(1,28)
28    FORMAT(" INPUT CUTOFF ENERGY(EV) FOR INC-SUB, SUB-SUB")
      READ(2,) ECT1
      READ(2,) ECT2
      ECUT(1)=ECT1
      ECUT(2)=ECT2
      GO TO 30
55    ECUT(1) = 2.0 * ED
      ECUT(2) = 2.0 * ED
30    WRITE(1,8)
8     FORMAT(" ALL INPUT DATA OK  SO FAR(Y=1)?")
      READ(2,) NOK
      IF(NOK.NE.1) GO TO 99
C
C     SECTION TO SET UP TITLES AND FINISH INPUT OF DATA
C
      ENCODE(5,TLE,3) E1
3     FORMAT(F5.1)
9     TITLE(3,MODE)=TLE(1)
      TITLE(4,MODE)=5H KEV
      TITLE(5,MODE)=EL1
      TITLE(6,MODE)=5H ON
      TITLE(7,MODE)=EL2
      TITLE(8,MODE)=5H WITH
      TITLE(10,MODE)=5H PART
      TITLE(11,MODE)=5HICLES
      TITLE(12,MODE)=5H  AND
      TITLE(13,MODE)=5H M =
      GO TO (11,12,12,13),MODE
11    TITLE(1,1)=5HRANGE
      TITLE(2,1)=5H FOR
```

```
      GO TO 15
12    TITLE(1,MODE)=5HGAMMA
      TITLE(2,MODE)=5HE DF
      GO TO 15
11    TITLE(1,4)=5HCASCA
      TITLE(2,4)=5HLE DF
      TITLE(10,4)=5H CHSG
      TITLE(11,4)=5HADES
      WRITE(1,16)
16    FORMAT(" INPUT THE NUMBER OF CASCADES TO BE PLOTTED")
      READ(2,) NOP
      WRITE(1,101)
101   FORMAT(" INPUT #ANGSTROMS/INCH FOR PLOT(MAX=10 INCHES)")
      READ(2,)INC
      GO TO 10
15    WRITE(1,14)
14    FORMAT(" INPUT # PROJECTILES TO BE USED")
      READ(2,)NOP
10    WRITE(1,17)
17    FORMAT(" INPUT NUMBER OF HISTOGRAM INTERVALS(DEF. AND",/,"
     1 THE WIDTH OF EACH(DEF")
      READ(2,)NOINT
      READ(2,)WOINT
      ISEED = 0
      LINE = 1
60    WRITE(1,62)
62    FORMAT(" DO YOU WISH NORMAL SEED,LINE 1 OPTION FOR RANDOM # S
     1EED=1")
      NOPT = 1
      READ(2,) NOK
      IF(NOK.EQ.1) GO TO 70
      WRITE(1,64)
64    FORMAT(" INPUT  SEED & LINE ,THEN OPTION(1-2)")
      READ(2,) ISEED,LINE,NOPT
      IF(NOPT.GT.2 OR NOPT.LT.1) GO TO 60
      IF(ISEED.EQ.0) GOTO 60
70    WRITE(1,18)
18    FORMAT(" SELECT M=1/2(0) OR M=0.055(1) OR M=0(2) CALCULATION")
      READ(2,) MOPT
      IF(MOPT.LT.0.OR.MOPT.GT.2) GO TO 10
      IF(MOPT.EQ.0) TIT=5H1/2
      IF(MOPT.EQ.1) TIT=5H0.055
      IF(MOPT.EQ.2) TIT=5H0
      WRITE(1,8)
      READ(2,) NOK
      IF(NOK.NE.1) GO TO 9
C
C     SECTION TO CALCULATE THE CONSTANTS
C
      E1 = 1.0E+03 * E1
      ATDEN = 6.023E-1 * ATDEN/XM2
      XMR(1) = XM2/XM1
      XMR(2) = 1.00
      XM12 = XM1 + XM2
      GAMMA(1) = 4.0*XM1*XM2 / XM12**2
      IF(ILOW.EQ.1) ECUT(1) = ECUT(1) / GAMMA(1)
      GAMMA(2) = 1.00
      XM22 = 2.0*XM2
```

```
      Z12 = Z1**(2.0/3.0) + Z2**(2.0/3.0)
      SCR(1) = 0.468346 / SQRT(Z12)
      Z22 = 2.0*Z2**(2.0/3.0)
      SCR(2) = 0.468346 / SQRT(Z22)
      EST(1,2) = Z2 0819*(SCR(1))**2*XM12/XM2*L14*Z2
      EST(2,2) = 64.1638*(SCR(2))**2*Z2*Z2
      EST(1,1) = 1.214579*XM12*Z1*Z2/(SCR(1)*XM2)
      EST(2,1) = 2.429159*Z2*Z2/SCR(2)
      EPS0(1) = XM2 * SCR(1) / (XM12*Z1*Z2*14.4)
      EPS0(2) = SCR(2) / (28.8*Z2*Z2)
      ELI(1) = 1.0/(Z12**(2/3.0/4.0) * XM1 * SQRT(XM1) + SQRT(XM2))
      ELK(1) = (Z1*Z2)**(0.5) * ELK(1) * XM12 * SQRT(XM12)
      ELK(1) = 0.0793 * Z1**(1.0/6.0) * ELK(1)
      ELK(1)=ELK(1)*2.1415926*ATDEN*SCR(1)**2*GAMMA(1)*SQRT(EPS0(1))
      ELI(2) = 1.0 / (Z22**(2/3.0/4.0) * XM2 * XM2)
      ELK(2) = Z2 * ELI(2) * XM2** * SQRT(XM22)
      ELI(2) = 0.0793 * Z2**(1.0/6.0) * ELI(2)
      ELK(2)=ELK(2)*2.1415926*ATDEN*SCR(2)**2/SQRT(EPS0(2))
C
C     HARDCOPY INPUT DATA AND CALCULATED CONSTANTS
C
      ENCODE(5,TLE,22)NOP
22    FORMAT(I5)
      TITLE(9,MODE) = TLE(1)
      TITLE(14,MODE) = TIT
      WRITE(4,25) (TITLE(I,MODE),I=1,16)
25    FORMAT(5X,16A5,/)
      IF(MODE.EQ.2)WRITE(4,125)
      IF(MODE.EQ.3)WRITE(4,126)
125   FORMAT(" ONLY PRIMARY RECOILS WILL BE FOLLOWED",/)
126   FORMAT(" ALL RECOILS WILL BE FOLLOWED",/)
      WRITE(4,31) EL1,EL2
31    FORMAT(5X,"PARTICLE",11X,"INCIDENT",7X,"SUBSTRATE",/,
     1 5X,"PARAMETER",12X,A5,11X,A5,/)
      WRITE(4,32) Z1,Z2
32    FORMAT(6X,"ATOMIC NO.",10X,F4.0,12X,F4.0)
      WRITE(4,33) XM1,XM2
33    FORMAT(6X,"ATOMIC MASS",8X,F6.1,8X,F8.3)
      WRITE(4,34) ECUT
34    FORMAT(6X,"CUTOFF ENERGY",6X,F6.1,9X,F6.1)
      WRITE(4,35) ED
35    FORMAT(6X,"DSPLCMNT EN",23X,F6.1)
      WRITE(4,81)EDD
81    FORMAT(6X,"ENERGY LOSS/COLLISION",13X,F6.1)
      WRITE(4,36) ATDEN
36    FORMAT(6X,"ATOMIC DENSITY(ANGS**-3)",5X,G16.8,/)
      WRITE(4,41)
41    FORMAT(5X,"INTERACTION",7X,"INCIDENT",12X,"SUBSTRATE",/,
     1 5X,"PARAMETER",9X,"-SUBSTRATE",10X,"-SUBSTRATE",/)
      WRITE(4,42)
42    FORMAT(6X,"ITYPE",16X,"1",19X,"2")
      WRITE(4,43) GAMMA
43    FORMAT(6X,"GAMMA",9X,G16.8,4X,G16.8)
      WRITE(4,44) EPS0
44    FORMAT(6X,"EPS(1EV)",6X,G16.8,4X,G16.8)
      WRITE(4,45) SCR
```

```
45      FORMAT(6X,"SCRNG RAD",5X,G16.8,4X,G16.8)
        WRITE(4,46) ELI
46      FORMAT(6X,"EL LOSS I ",5X,G16.8,4X,G16.8)
        WRITE(4,48) ((EST(I,J),I=1,2),J=1,2)
48      FORMAT(6X,"E STAR(0,0S5)",1X,G16.8,4X,G16.8,/,16X,"(0)",1X,
     1  G16.8,4X,G16.8)
        WRITE(4,68) ISEED,LINE,NOPT
68      FORMAT(/," INITIAL RANDOM # SEED IS",I7," AND LINE IS",
     1I7,/," WITH OPTION OF",I5,/)
        RETURN
        END



        SUBROUTINE SIGEN(T,SIGVAL,TM)
C       ROUTINE TO CALCULATE STOPPING POWEER INTEGRATION TABLE
C       T IS INDEPENDENT VARIBLE FROM .0001 TO 1300
C        IN 100 STEPS PER DECADE TO 1 AND 200 STEPS TO 1300
C
        DIMENSION T(1),SIGVAL(1)
        COMMON /BLKT/JTOP,RANGE,PROJR/AVI,AVII,AVX(3),VOL
C
        T(1) = 0.0001
        SIGVAL(1) = 0.0
        DO 10 I=2,400
        T(I) = 1.0/(10.0**((408-I)*4.0/299.0))
        SIGVAL(I)=(T(I)-T(I-1))*(FCT(T(I))+FCT(T(I-1)))/2.0+SIGVAL(I-1)
        IF(T(I).GT.TM) GO TO 30
10      CONTINUE
        DO 20 I=1,200
        J=I+400
        T(J) = 1300.0+((I/199.0)
        SIGVAL(J)=SIGVAL(J-1)+(T(J)-T(J-1))*(FCT(T(J))+FCT(T(J-1)))/2.0
        IF(T(J).GT.TM) GO TO 40
20      CONTINUE
30      J=I
40      JTOP = J
        RETURN
        END



        FUNCTION FCT(X)
C       STOPPING POWER APPROXIMATION POLYNOMIAL
        FCT = 1.0 / ((1.0+1.9*X**(4.0/9.0))**1.5*X**1.3333)
        RETURN
        END
```

```
      SUBROUTINE GUTS(T,SIGVAL,ISEED,LINK,NOPT)
C MAIN WORKINGS OF MONTE-CARLO CODE.
C FOLLOWS COLLISION THROUGH SUBROUTINE FOLLOW
C IF MODE=1 ONLY FOLLOW INCIDENT PARTICLE FOR RANGE DISTRIBUTION
C IF MODE=2 FOLLOW INCIDENT+PRIMARY RECOILS FOR DAMAGE DIST
C IF MODE=3 GENERATE ENTIRE CASCADE AND PLOT ON PLOTTER
C
      LOGICAL ISENSW
      DIMENSION B(3,3),AQ(3,3),A2(3,3),T(1),SIGVAL(1),TLE(2)
      COMMON /BLK1/TITLE(16,4),NOP,NOINT,NOPT,MODE,ITYPE
      COMMON /BLK2/E1,E2,XM1,XM2,E1,ECUT(2),ATMEN,ED,EDD,UDD
      COMMON /BLK3/GAMMA(2),EPSM(2),SCP(2),ELI(2),XMP(2),ES(2,2)
      COMMON /BLK4/T1,ELOSS,ELEC,PATH,TH1,PH1,TH2,PH2
      COMMON /BLK5/STO(100,6),X0,Y0,Z0,TH0,PH0,EV
      COMMON /BLK6/DEP(50),STOP(50),NSPUT(2)
      COMMON /BLK7/JTOP,RANGE,PROJP,AV1,AV2,AV1D,VOL
      COMMON /BLK8/IN1,IPNT(2000,2),NDEF,DEF,IPRM(400,3),NPRM
C
10    WRITE(4,2)
2     FORMAT(10X,"REFLECTED PARTICLE STATISTICS",//,5X,
     1 "SPECIES",4X,"PRTCLE #",2X,"COLLN #",6X,"POSITION",10X,
     2 "ENERGY")
C     ZERO SUMMING ARRAYS
C
      DO 10 J=1,NOINT
      DEP(J) = 0.0
10    STOP(J) = 0.0
      RANGE = 0.0
      PROJP = 0.0
      AV1 = 0.0
      AV2 = 0.0
      AV1D = 0.0
      NSPUT(1) = 0
      NSPUT(2) = 0
      DEF=0
      XJ1 = 0.0
      XJ2 = 0.0
      VOL=0.0
      IF(MODE EQ 4)XNX=100./INX
C MAIN DO-LOOP FOR EACH INCIDENT PARTICLE: IJ=PRESENT PARTICLE
      DO 100 IJ=1,NOP
C INITIALIZE COLLISION PARAMETERS
      IF(ISENSW(0)) NOP = IJ + 1
      IF(ISENSW(1)) WRITE(1,4) IJ
4     FORMAT(I5)
      X0=0.
      Y0=0.
      Z0=0.
      PH0=0.
      TH0=0.
      ITYPE=1
      LL=1
      EV=E1
      NCOLL=0
      NDEF = 0
      NPRM = 0
C     WRITE(4,406)IJ,ISEED,LINK
```

```
40E       FORMAT(1X,3I7)
          IF(MODE LT 3)GO TO 5
          XXS = 0.0
          YYS = 0.0
          ZZS = 0.0
          ZZ = 0.0
C FOLLOW A COLLISION
5         CALL FOLLOW(ISEED,LINK,NOPT,T,SIGVAL)
          XJ1 = XJ1 + 1.0
          IF(XJ1/NOPT LT 87381.)GO TO 152
          ISEED = 0
          LINK = 1
          NOPT = NOPT +1
          IF(NOPT.NE.4)GO TO 152
          NOP = IJ - 1
          GO TO 100
152       NCOLL=NCOLL+1
C DETERMINE NEW COLLISION LOCATION
          X0=X0+SIN(TH0)*SIN(PH0)*PATH
          Y0=Y0+SIN(TH0)*COS(PH0)*PATH
          Z0=Z0+COS(TH0)*PATH
C CHECK IF PARTICLE REFLECTED OR OUT OF RANGE
C IF IT IS STOP FOLLOWING IT
          ID=Z0/WOINT+1
          IF(ID.GT.NOINT)GO TO 200
          IF(ID.GE.1)GO TO 245
          NSPUT(ITYPE)=NSPUT(ITYPE)+1
          WRITE(4,8) ITYPE,IJ,NCOLL,Z0,EV
8         FORMAT(3I10.6X,2G1E.8)
C  RESTORE PREVIOUS COLLISION PARAMETERS
200       GO TO 113
C READY TRANSFORMATION TO ORIGIN COORDINATES
245       CALL TRANS(B,TH0,PH0)
          CALL TRANS(A0,TH1,PH1)
C GENERATE NEW TH0,PH0 FOR RECOIL "1" IN ORIGIN COORDINATES
          CALL ANGLE(A0,B)
C IF DOING RANGE ONLY, FORGET RECOIL "2"
          IF(MODE.EQ.1) GOTO 120
C IF DAMAGE WANTED FOR PRIMARIES ONLY ,FORGET PRIMARY RECOIL RECOILS
          IF(MODE.EQ.2.AND.ITYPE.EQ.2)GO TO 110
C OTHERWISE GENERATE TH0,PH0 FOR RECOIL "2" IN ORIGIN COORDINATES
C FIRST STORE RECOIL "1" PARAMETERS
          CALL STORE(LL)
C IF PLOTTING CASCADE,KEEP TRACK OF INCIDENT PATICLE PATH
          IF(ITYPE.EQ.2.OR.MODE.EQ.2)GO TO 210
          XTEMP = X0
          YTEMP = Y0
          ZTEMP = Z0
          IF(MODE.EQ.3) GO TO 210
          NPRM=NPRM+1
          IPRM(NPRM,1)=X0*XNX+400
          IPRM(NPRM,2)=Y0*XNX+1250
          IPRM(NPRM,3)=Z0*XNX
C READY TRANSFORMATION MATRIX
210       CALL TRANS(A2,TH2,PH2)
C GENERATE NEW TH0,PH0 FOR RECOIL "2" IN ORIGIN COORDINATES
          CALL ANGLE(A2,B)
```

```
          ITYPE=2
          LL = LL + 1
          EV =TI
          IF(TI EQ 0.0) GO TO 119
          GO TO 111
C
C ROUTINE TO HANDLE RANGE,STRAGGLING,DEPOSITED ENERGY INFO
C
C ENTRY IF MODE =.1
120       RANGE=RANGE + PATH
C ENTRY IF MODE = 2
110       DEP(ID) = DEP(ID) +TI
          AVXD =  AVXD + TI*X0**2
C ENTRY IF MODE = 3,4
111       DEP(ID)= DEP(ID) + UDO
          AVXD = AVXD + UDO*X0**2
          XJ2 = XJ2 + 1
C IS PARTICLE STOPPED?
114       IF(EV GT ECUT(ITYPE)) GO TO 5
C YES SO UPDATE PARAMETERS
119       STOP(ID)=STOP(ID)+1.0
          PROJR=PROJR + Z0
          AVX= AVX + X0
          AVXX = AVXX + X0**2
          DEF=DEF+1
          NDEF=NDEF+1
          IF(MODE LT. 3)GO TO 112
          XXS=XXS+(X0-XTEMP)**2
          YYS=YYS+(Y0-YTEMP)**2
          ZZS=ZZS+Z0**2
          ZZ=ZZ+Z0
C IF PLOTTING CASCADES,KEEP TRACK OF DEFECT LOCATION
          IF(MODE. EQ. 3)GO TO 112
          IPNT(NDEF,1)=X0*XNX+400
          IPNT(NDEF,2)=Y0*XNX+1250
          IPNT(NDEF,3)=Z0*XNX
112       DEP(ID)=DEP(ID)+EV
          AVXXD=AVXXD + EV*X0**2
C IF MODE =1 WE'RE FINISHED WITH PARTICLE
          IF(MODE. EQ. 1)GO TO 100
C RESTORE PREVIOUS COLLISION PARAMETERS
117       IF(ITYPE EQ. 1)GO TO 116
          LL = LL - 1
          CALL RESTOR(LL)
          ID = Z0/WOINT + 1
          IF(LL. EQ. 1) ITYPE = 1
C IF EV LESS THAN ED IT'S A REPLACEMENT COLLISION
          IF(EV. LE. ED) GO TO 112
          GO TO 114
C IF CASCADE TO BE PLOTTED,DO IT NOW
116       IF(MODE. LT. 3)GO TO 100
          XXS=XXS*ZTEMP/(NDEF*SQRT(ZTEMP**2+XTEMP**2))
          YYS=YYS*ZTEMP/(NDEF*SQRT(ZTEMP**2+YTEMP**2))
          ZZS=ABS(ZZS-ZZ**2./NDEF)
          ZZS=ZZS*SQRT(ZTEMP**2+XTEMP**2+YTEMP**2)/(ZTEMP*NDEF)
          VOL0=4.19*SQRT(XXS*YYS*ZZS)
          VOL=VOL+VOL0
```

```
      IF(MODE EQ 4)CALL PLTSET
100   CONTINUE
C
C WE'RE OUT OF THE COLLISION CASCADE LOOP NOW
C
      ENCODE(5,11,21) NOP
21    FORMAT(I5)
      TITLE(9,MODE) = TLE(1)
      WRITE(4,24) NOP
24    FORMAT(/," LAST PARTICLE ACTUALLY PROCESSED IS",I5,/)
      LTOT = NOP
      IF(LTOT.EQ.0) LTOT = 1
      ELOSS = ELOSS / LTOT
      NDEF=DEF/LTOT
      IF(MODE.NE.1)WRITE(4,121)NDEF
121   FORMAT(/," AVERAGE # DEFECTS PER INCIDENT PARTICLE IS",I10)
      WRITE(4,38) ISEED,NOPT,LINK
38    FORMAT(/," FINAL RANDOM # SEED IS",I6,/," WITH OPTION",I5,/
     1," AND LINK AS",I5,/)
      XJ1=XJ1/LTOT
      XJ2=XJ2/LTOT
      WRITE(4,36)XJ1
36    FORMAT(/," AV.  # CALLS TO 'FOLLOW' PER PARTICLE IS",F8.0)
      WRITE(4,37)XJ2
37    FORMAT(/," AV  # DISPLACEMENT COLLISIONS PER PARTICLE IS",F8.0)
      RANGE = RANGE / DEF
      PROJP = PROJP / DEF
      AVX = AVX / DEF
      AVXX = AVXX / DEF
      AVXD=AVXD/LTOT
      VOL=VOL/LTOT
      UDD=XJ2+EDD
      RETURN
      END



      SUBROUTINE PLTSET
CROUTINE TO PLOT AXES AND SCALES FOR CASCADE PLOT
C
      COMMON /BLK1/TITLE(16,4),NOP,NOINT,NO1NT,MOPT,MODE,ITYPE
      COMMON /BLK9/INX,IPNT(2000,3),NDEF,DEF,IPRM(400,3),NPRM
      CALL AIPA(3)
C READY PLOTTER
      CALL PLOT(-1.0,0)
      CALL PLOT(0.0,0)
      CALL CONTRO(3,0,2,0)
C DRAW X-AXES
      NXX=0
      DO 20 I=1,2
      INT=NXX
      INR=-4*INX
      CALL PLOT(5,NXX,0)
```

```
      DO 25 I1=1,9
      CALL PLOT(4,INT,-10)
      DO 35 I=1,5
      NUMB=IWP/10**I
      IF(NUMB EQ 0)GO TO 40
35    CONTINUE
40    J1=6*(I-1)
      CALL CONTRO(3,2,INT-J1,-25)
      WRITE(3,100)IWP
100   FORMAT(1X,I6)
      IF(I1 EQ 9)GO TO 20
      DO 30 I2=1,4
      INT=INT+25
      CALL PLOT(5,INT,0)
30    CALL PLOT(4,INT,-5)
25    IWP=IWP+INC
20    NXX=850
      CALL PLOT(5,INT,0)
      CALL PLOT(4,0,0)
C DRAW Y-AXES
      NXX=0
      DO 65 I=1,2
      INT=0
      IWP=0
      CALL PLOT(5,NXX,0)
      DO 55 I1=1,10
      CALL PLOT(4,NXX-10,INT)
      CALL CONTRO(3,2,NXX-80,INT-6)
      WRITE(3,100)IWP
      IWP=IWP+INC
      DO 55 I2=1,4
      INT=INT+25
      CALL PLOT(5,NXX,INT)
55    CALL PLOT(4,NXX-5,INT)
      CALL PLOT(5,NXX,INT)
      CALL PLOT(4,NXX,0)
65    NXX=850
      NXX=0
      DO 80 I=1,2
      CALL CONTRO(3,2,NXX+50,950)
      WRITE(3,102) (TITLE(JJ,4),JJ=3,7)
102   FORMAT(1X,5A5)
      CALL PPLOT(11,1,NXX+50,928)
      CALL CONTRO(3,2,NXX+75,925)
      WRITE(3,103)TITLE(7,4)
103   FORMAT(1X,A5,13H INTERSTITIAL)
      CALL PPLOT(4,3,NXX+50,905)
      CALL CONTRO(3,2,NXX+75,900)
      WRITE(3,104)TITLE(5,4)
104   FORMAT(1X,A5,15H FINAL POSITION)
      CALL CONTRO(3,2,NXX+75,875)
      WRITE(3,105)NDEF
105   FORMAT(I6,14H DISPLACEMENTS)
      CALL CONTRO(3,2,NXX-40,475)
      WRITE(3,151)
      WRITE(3,152)
```

```
      WRITE(3,153)
      WRITE(3,154)
      WRITE(3,155)
151   FORMAT(2H D)
152   FORMAT(2H E)
153   FORMAT(2H P)
154   FORMAT(2H T)
155   FORMAT(2H H)
      CALL CONTPO(3,2.,NXX+225,-40)
      IF(I EQ 1)WRITE(3,156)
      IF(I EQ.2)WRITE(3,157)
156   FORMAT(15H X DIMENSION(A))
157   FORMAT(15H Y DIMENSION(A))
80    NXX=850
      CALL PLOT(5,1650.0)
      CALL PLOT(4,1650.1000)
      CALL PLOT(5,800.1000)
      CALL PLOT(4,800,0)
      CALL PLOT(5,-50,0)
      CALL PLOT(4,-50,1000)
      CALL CASPLT
      CALL PLOT(5,1750,0)
      RETURN
      END
```

```
      SUBROUTINE CASPLT
C
C ROUTINE TO PLOT LOCATION OF INTERSTITIAL
C
      COMMON /BLK5/STO(100,6),X0,Y0,Z0,TH0,PH0,EV
      COMMON /BLK9/IN5,IPNT(2000,3),NDEF,DEF,IPRM(400,3),NPRM
      CALL PLOT(5,400,0)
      DO 5 I=1,NPRM
5     CALL PLOT(4,IPRM(I,1),IPRM(I,3))
      NN=NDEF-1
      DO 10 I=1,NN
      IF(IPNT(I,3).GT.1000) IPNT(I,3)=1000
10    CALL PPLOT(11,1,IPNT(I,1),IPNT(I,3))
      CALL PPLOT(4,3,IPNT(NDEF,1),IPNT(NDEF,3))
      CALL PLOT(5,1250,0)
      DO 25 I=1,NPRM
25    CALL PLOT(4,IPRM(I,2),IPRM(I,3))
      DO 20 I=1,NN
20    CALL PPLOT(11,1,IPNT(I,2),IPNT(I,3))
      CALL PPLOT(4,3,IPNT(NDEF,2),IPNT(NDEF,3))
      RETURN
      END
```

```
      SUBROUTINE FOLLOW(ISEED,LINE,NOPT,T,SIGVAL,
C SUBROUTINE TO FOLLOW THE COLLISION
C CALCULATES THE SCATTERING ANGLES,PATH LENGTH,ELECTRONIC LOSS
C
      DIMENSION T(1),SIGVAL(1)
      COMMON /BLK1/TITLE(16,4),NOP,NOINT,NOINT,MOPT,MODE,ITYPE
      COMMON /BLK2/C1,C2,CM1,CM2,E1,ELOST,A,HIDEN,ED,EDD,UDD
      COMMON /BLK3/GAMMA(2),EPS0(2),SCR(2),ELI(2),IMF(2),EST(2,2)
      COMMON /BLK4/T1,ELOSS,ELEC,PATH,TH1,PH1,TH2,PH2
      COMMON /BLK5/STO(100,6),XO,YO,ZO,THO,PHO,EV
      COMMON /BLK7/ITOP,RANGE,PROJR,AVX,AVXX,AVXXD,VOL
      COMMON /BLK9/INC,IPNT(2000,2),NDEF,DEF,IPPM(400,2),NPPM
      STMAX=(EPS0(ITYPE)*EV)**2
      STMIN=(EPS0(ITYPE)*EV*EV+EV*EV*GAMMA(ITYPE)
      GO TO (1,2,3),NOPT
1     Q1 = RANDOM(ISEED,LINE)
      Q2 = RANDOM(ISEED,LINE)
      Q3 = RANDOM(ISEED,LINE)
      GO TO 5
2     Q2 = RANDOM(ISEED,LINE)
      Q3 = RANDOM(ISEED,LINE)
      Q1 = RANDOM(ISEED,LINE)
      GO TO 5
3     Q3 = RANDOM(ISEED,LINE)
      Q1 = RANDOM(ISEED,LINE)
      Q2 = RANDOM(ISEED,LINE)
5     TMAX=GAMMA(ITYPE)*EV
C     WRITE(4,404) Q1,Q2,Q3
404   FORMAT(/,3G18.8)
C IF M=.055 TO BE USED , DECIDE NOW
      IF(EV.GT.EST(ITYPE,NOPT).OR.NOPT.EQ.0)GO TO 100
      GO TO (50,150),NOPT
50    TK =(1.-Q1)/(ED**.055)+Q1/(TMAX**.055)
      TK=(1./TK)**18.18
      RA=TK/TMAX
      SIGTOT=102.1*(1./(STMIN**.055)-1./(STMAX**.055))
      GO TO 201
C IF M=0. CHECK E STAR(EST) IF IN CORRECT RANGE
150   TK = (1.0-Q1)*ALOG(ED) + Q1*ALOG(TMAX)
      TK = EXP(TK)
      RA = TK / TMAX
      SIGTOT =18.335*(ALOG(STMAX)-ALOG(STMIN))
      SIGTOT = SIGTOT*(.219**2)/(SCR(ITYPE)**2)
      GO TO 201
C IF STMAX < 10**-4, USE M=1/3
100   IF(STMAX.GT..0001)GO TO 250
      TK=(1.-Q1)/(ED**.3333)+Q1/(TMAX**.3333)
      TK=(1./TK)**3
      RA=TK/TMAX
      SIGTOT=3.0*(1./(STMIN**.3333)-1./(STMAX**.3333))
      GO TO 201
C IF STMAX > 10**-4 USE EXACT INTEGRATION
C FIRST SEARCH T FOR STMAX
250   CALL SEARCH (T,STMAX,JJ)
      SIGMAX=(STMAX-T(JJ-1))/(T(JJ)-T(JJ-1))
      SIGMAX=(1.-SIGMAX)*SIGVAL(JJ-1)+SIGMAX*SIGVAL(JJ)
C IF STMIN < 10**-4 USE M=1/3 RATHER THAN TABLE
```

```
C FIRST SEARCH T FOR STMAX
250       CALL SEARCH (T,STMAX,JJ)
          SIGMAX=(STMAX-T(JJ-1))/(T(JJ)-T(JJ-1))
          SIGMAX=(1 -SIGMAX)*SIGVAL(JJ-1)+SIGMAX*SIGVAL(JJ)
C IF STMIN < 10**-4 USE M=1/2 RATHER THAN TABLE
          IF(STMIN.LT. 0001)GO TO 300
C SEARCH FOR STMIN
          CALL SEARCH(T,STMIN,JJ)
          SIGMIN=(STMIN-T(JJ-1))/(T(JJ)-T(JJ-1))
          SIGMIN=(1 -SIGMIN)*SIGVAL(JJ-1)+SIGMIN*SIGVAL(JJ)
          SIG=(SIGMAX-SIGMIN)*01+SIGMIN
          SIGTOT=SIGMAX-SIGMIN
C SEARCH SIGVAL FOR SIG
340       CALL SEARCH(SIGVAL,SIG,JJ)
          ST=(SIG-SIGVAL(JJ-1))/(SIGVAL(JJ)-SIGVAL(JJ-1))
          ST=(1 -ST)*T(JJ-1)+ST*T(JJ)
          GO TO 200
C NOW CONSIDER CASE FOR STMIN < 10**-4
300       SIGMIN=2.0*(1./STMIN)** 2232-21 54)
          SIGTOT=SIGMAX+SIGMIN
          SIG=01*SIGTOT
          IF(SIG GT.SIGMIN)GO TO 330
          ST=1./(1./STMIN)** 2232-SIG/2 )**2
          GO TO 200
330       SIG=01*SIGTOT-SIGMIN
          GO TO 340
200       PA=ST/STMAX
          TH=ST*GAMMA(ITYPE)/(EPS0(ITYPE)**2)*EV)
C
C FIND SCATTERING AND AZIMUTHAL ANGLES
201       ARG = 1.0 - PA
          ARG = SQRT(PA/ARG)
          TH = 2.0 * ATAN(ARG)
          THX=1 +XMR(ITYPE)*COS(TH)
          IF(TH.LT. 0)GO TO 505
          TH1=-XMR(ITYPE)*SIN(TH)/THX
          TH1=3.1415926-ATAN(TH1)
          GO TO 506
505       TH1=XMR(ITYPE)*SIN(TH)/THX
          TH1=ATAN(TH1)
506       TH2=SIN(TH)/(1 -COS(TH))
          TH2=ATAN(TH2)
          PH1=6.28318*02
          PH2=3 1415926-PH1
C
C FIND THE PATH LENGTH
C
          PATH =-ALOG(03)/(SIGTOT*ATDEN*2 0562*SCR(ITYPE)**2)
C
C FIND THE ELECTRONIC LOSS ALONG THE PATH LENGTH
C
          DELTA=PATH*ELK(ITYPE)/2.
          ELEC=EV-(SQRT(EV)-DELTA)**2
          PMAX=2.*SQRT(EV)/ELK(ITYPE)
          IF(PATH.LT.PMAX)GO TO 507
          ELEC=EV
```

```
          TI  = 0.0
          PATH=PMAC.
          GO TO 508
507       IF(ELEC .LE. EV-TI) GO TO 508
          TI  = EV-ELEC
          IF(TI .LT. ED) TI  = 0.0
508       ELOSS=ELOSS+ELEC
          EV=EV-TI-ELEC
          IF(TI .NE. 0.0) TI=TI-EDD
          RETURN
          END


          SUBROUTINE SEARCH(X,Y,JJ)
C SUBROUTINE TO SEARCH ARRAY X FOR ELEMENT IMMEDIATELY < Y
C  JJ IS RETURNED AS THAT ELEMENT
C
          DIMENSION X(1)
          COMMON /BLK1/TITLE(16,4),NOP,NOINT,NOINT,MOPT,MODE,ITYPE
          COMMON /BLK2/JTOP,RANGE,PROJP,AVX,AVXX,AVXXX,VOL
          JHI=JTOP
          JLO=1
          JJ=JHI/2
5         IF((JLO+1) .EQ. JHI)GO TO 20
          IF(X(JJ) .LE. Y)GO TO 10
          JJ=(JJ+JLO)/2
          GO TO 15
10        JJ=(JJ+JHI)/2
15        IF(X(JJ) .LE. Y)JLO=JJ
          IF(X(JJ) .GT. Y)JHI=JJ
          GO TO 5
20        JJ=JHI
          RETURN
          END


          SUBROUTINE TRANS(X,ANG1,ANG2)
C SUBROUTINE TO READY CARTESIAN COORDINATE TRANSFORMATION MATRIX
C
          DIMENSION X(1,1),TRIG(4)
          TRIG(1)=COS(ANG1)
          TRIG(2)=SIN(ANG1)
          TRIG(3)=COS(ANG2)
          TRIG(4)=SIN(ANG2)
          X(1,1)=TRIG(3)
          X(2,1)=-TRIG(4)
          X(3,1)=0.
          X(1,2)=TRIG(1)*TRIG(4)
```

```
      X(2,2)=TRIG(1)*TRIG(3)
      X(3,2)=-TRIG(3)
      X(1,3)=TRIG(2)*TRIG(4)
      X(2,3)=TRIG(2)*TRIG(3)
      X(3,3)=TRIG(1)
      RETURN
      END



      SUBROUTINE ANGLE(X,Y)
C SUBROUTINE TO GENERATE TH0,PH0 IN ORIGIN COORDINATES
      DIMENSION X(1,1),Y(1,1),S(3)
      COMMON /BLK5/STO(100,6),X0,Y0,Z0,TH0,PH0,EV
C DETERMINE NECESSARY MATRIX PRODUCT ELEMENTS
      DO 10 I=1,3
      S(I)=0
      DO 10 J=1,3
10    S(I)=S(I)+X(J,I)*Y(I,J)
      AD=SQRT(S(1)**2+S(2)**2)
C DETERMINE TH0,PH0 IN ORIGIN COORDINATE SYSTEM
      SI=S(1)/S(2)
      TANG=ATAN(ABS(SI))
      TANG=SIGN(TANG,SI)
      PI=0
      IF(S(2) LT 0 )PI=3.1415926
      PH0=PI+TANG
      IF(S(3) GT 0 )GO TO 110
      TH0=3.1415926-ATAN(-AD/S(3))
      GO TO 120
110   TH0=ATAN(AD/S(3))
120   RETURN
      END



      SUBROUTINE RESTOR(I)
C SUBROUTINE TO RESTORE COLLISION PARAMETERS FROM
C "I" ROW OF ARRAY STO
C
      COMMON /BLK5/STO(100,6),X0,Y0,Z0,TH0,PH0,EV
      X0=STO(I,1)
      Y0=STO(I,2)
      Z0=STO(I,3)
      TH0=STO(I,4)
      PH0=STO(I,5)
      EV=STO(I,6)
      RETURN
      END
```

```
      SUBROUTINE STORE(I)
C SUBROUTINE TO STORE PARAMETERS FOR GIVEN COLLISION
C AT POS "I" OF ARRAY STO
C
      COMMON /BLK5/STO(100,6),X0,Y0,Z0,TH0,PH0,EV
      STO(I,1)=X0
      STO(I,2)=Y0
      STO(I,3)=Z0
      STO(I,4)=TH0
      STO(I,5)=PH0
      STO(I,6)=EV
      RETURN
      END



      SUBROUTINE OUTGO
C
C     ROUTINE TO OUTPUT RESULTS AND TO CALCULATE THE EDGWORTH EXP
C
      DIMENSION TOT(2),CMOM(4,2),EDGE(50,2),EMAX(2),CMX(2)
      COMMON /BLK1/TITLE(16,4),NOP,NOINT,NUINT,MOPT,MODE,ITYPE
      COMMON /BLK2/Z1,Z2,AM1,AM2,E1,ECUT,Z,ATDEN,ED,EPS,UPS
      COMMON /BLK4/TH,ELOSS,ELEC,PATH,TH1,PH1,TH2,PH2
      COMMON /BLK6/DEP(50),STOP(50),NSPUT(2)
      COMMON /BLK7/JTOP,RANGE,PROJR,AVX,AVXX,AVXXX,VOL
      COMMON /BLK8/UM(4,2),TERM(3,2)
      COMMON /BLK9/INX,IPNT(2000,2),NDEF,DEF,IPRM(400,2),NPRM
C
      DEMAX=0.0
      DETOT=0.0
      TOTN = 0.0
      DE = NOINT
C NORMALIZE HISTOGRAMS
      DO 10 J=1,NOINT
      DEP(J) = DEP(J) / NOP
      DETOT=DETOT+DEP(J)
      IF(DEMAX.LT.DEP(J)) DEMAX=DEP(J)
      IF(MODE.NE.1) STOP(J) = STOP(J)/NOP
      TOTN = TOTN + STOP(J)
10    CONTINUE
C SET PARTICLE OR DEFECT DISTRIBUTION FIRST MOMENT
      UM(1,1) = PROJR
      TOT(1) = NOP
      IF(MODE.NE.1)TOT(1)=NDEF
      SUM1 = 0.0
      CO = DE / 2.0
C DETERMINE DEPOSITED ENERGY DISTRIBUTION FIRST MOMENT
      DO 15 I=1,NOINT
      SUM1 = SUM1+DEP(I)*CO
15    CO = CO + DE
      UM(1,2) = SUM1 / DETOT
      TOT(2) = DETOT
C CALCULATE SECOND, THIRD AND FOURTH MOMENTS
```

```
      DO 25 J=1,2
      SUM2 = 0.0
      SUM3 = 0.0
      SUM4 = 0.0
      CO = DE/2.0
      DO 20 I=1,NOINT
      IF(J EQ 1)PART=STOP(I)
      IF(J EQ 2)PART=DEP(I)
      SUM2 = SUM2 + PART*(CO-UM(1,J))**2
      SUM3 = SUM3 + PART*(CO-UM(1,J))**3
      SUM4 = SUM4 + PART*(CO-UM(1,J))**4
20    CO = CO + DE
      UM(2,J) = SUM2/TOT(J)
      UM(3,J) = SUM3/TOT(J)
25    UM(4,J) = SUM4/TOT(J)
C CALCULATE LONGITUDINAL AND TRANSVERSE STRAGGLING
      STRAGX = SQRT(ABS(AVXD-AVX**2))
      STRAGZ = SQRT(UM(2,1))
      STRDZ=SQRT(UM(2,2))
      AVXD = AVXD/DETOT
      STRDX=SQRT(AVXD)
55    WRITE(4,12) (TITLE(I),MODE),I=1,16)
12    FORMAT(1H1,16A5,/)
      DO 11 J=1,2
      TERM(1,J)=UM(3,J)/6.0+UM(2,J)*SQRT(UM(2,J))
      TERM(2,J)=1./24.*(UM(4,J)/UM(2,J)**2-3.0)
11    TERM(3,J)=UM(3,J)**2/(72.*UM(2,J)**3)
      DO 22 J=1,2
      ZMOM(1,J)=UM(1,J)
      ZMOM(2,J)=UM(2,J)/(UM(1,J)**2)
      ZMOM(3,J)=UM(3,J)/(UM(2,J)*SQRT(UM(2,J)))
22    ZMOM(4,J)=UM(4,J)/(UM(2,J)**2)
      TMOM=STRAGX**2/UM(2,1)
      TMOMD=AVXD/UM(2,2)
      IF(MODE EQ 1)WRITE(4,14)
      IF(MODE.NE.1)WRITE(4,17)
14    FORMAT("   INTERVAL",2X,"DEPTH",5X,"PARTICLE",6X,
     1 "EDGEWORTH",7X,"DEPOSITED",5X,"EDGEWORTH")
17    FORMAT("   INTERVAL",2X,"DEPTH",5X,"DEFECT   ",6X,
     1 "EDGEWORTH",7X,"DEPOSITED",5X,"EDGEWORTH")
      WRITE(4,16)
16    FORMAT("    NUMBER",3X,"CENTER",2X,"DISTRIBUTION",
     1 4X,"EXPANSION",8X,"ENERGY",7X,"EXPANSION",/)
18    FORMAT(I5,2X,F10.1,1X,F8.1,2X,G20.6,G16.6,1X,G14.6)
C DETERMINE EDGEWORTH DISTRIBUTIONS
      DO 155 J=1,2
      EMAX(J)=0.
      CMAX(J)=0.
      CO=DE/2.0
      SUM=0.
      DO 157 I=1,NOINT
      EDGE(I,J)=EVALS(J,CO)
      SUM=SUM+EDGE(I,J)
      IF(EMAX(J).GT.EDGE(I,J))GO TO 157
      EMAX(J)=EDGE(I,J)
      CMAX(J)=CO
```

```
157       CO=CO+DE
          DO 155 I=1,NOINT
155       EDGE(I,J)=EDGE(I,J)*TOT(J)/(DE*SUM)
C PRINT OUT DISTRIBUTIONS
          CO=DE/2.0
          DO 30  I=1,NOINT
          WRITE(4,18) I,CO,STOP(I),EDGE(I,1),DEF(I),EDGE(I,2)
30        CO=CO+DE
          WRITE(4,64)
64        FORMAT(23X,6("="),24X,6("="))
          WRITE(4,66) TOTN,DETOT
66        FORMAT(21X,F6.1,24X,G16.8,/)
C
C         SECTION TO GET EDGE MAXIMUM TO SNGL PCSN ACCURACY
C
          DO 40 K=1,2
          DO 40  J=1,10
          EMAX(K) = 0.0
          CO = CMAX(K) - DE
          DE = DE / 10.0
          DO 40  I = 1,20
          EDG=EVALS(K,CO)
          CO = CO + DE
          IF(EDG.LE.EMAX(K))GO TO 45
          EMAX(K)=EDG
          CMAX(K) = CO - DE
          GO TO 40
45        IF(EDG.NE.EMAX(K)) GO TO 40
          CMAX(K) = CO - DE/2.0
          CO = CMAX(K)
          EMAX(K)=EVALS(K,CO)
          GO TO 161
40        CONTINUE
C OUTPUT EDGEWORTH TERMS
161       I=1
          IF(MODE.EQ.2)I=2
          DO 199 J=I,2
          IF(I.EQ.1.AND.MODE.EQ.1)WRITE(4,203)
          IF(I.EQ.1.AND.MODE.NE.1)WRITE(4,205)
          IF(I.EQ.2)WRITE(4,207)
203       FORMAT(" PARTICLE EDGEWORTH DISTRIBUTION TERMS:")
205       FORMAT(" DEFECT EDGEWORTH DISTRIBUTION TERMS:")
207       FORMAT(" DEPOSITED ENERGY EDGEWORTH DISTRIBUTION TERMS:")
          WRITE(4,209) (TERM(K,J),K=1,3)
209       FORMAT(" TERM1 =",G20.6,/," TERM2 =",G20.6,/," TERM3 =",G20.6,/)
          WRITE(4,211)EMAX(J),CMAX(J)
211       FORMAT(" EDGEWORTH MAXIMUM =",G16.6," AT,",G16.6,"ANGS",/)
199       CONTINUE
          WRITE(4,22) (TITLE(I,MODE),I=1,16)
22        FORMAT(1H1,10X,"EDGEWORTH EXPANSION PARAMETERS",//,1X,16A5,//)
          WRITE(4,58)DETOT
58        FORMAT(" TOTAL DEPOSITED ENERGY=",G16.8,/)
          WRITE(4,59)ELOSS
59        FORMAT(" ELECTRONIC LOSS PER PARTICLE (EV) =",G16.8,/)
          IF(UDD.NE.0.0)WRITE(4,61)UDD
61        FORMAT(" SUM OF U (EV) =",G16.8,/)
```

```
      IF(MODE EQ 2)GO TO 120
      IF(MODE NE 1)GO TO 122
      WRITE(4,62)
62    FORMAT(" PARTICLE PARAMETERS ")
      WRITE(4,84)RANGE
84    FORMAT(" AVERAGE RANGE (ANGS) =",G16.8)
      RAT=UM(1,1)/RANGE
      GO TO 125
122   WRITE(4,63)
63    FORMAT(" DEFECT PARAMETERS")
125   WRITE(4,67)UM(1,1)
67    FORMAT(" AVERAGE PROJECTED RANGE (ANGS) =",G16.8,
      IF(MODE EQ.1)WRITE(4,221)RAT
221   FORMAT(" PROJECTED RANGE / RANGE =",G20.6)
      WRITE(4,68)STRAGZ
68    FORMAT(" AVERAGE LOGITUDINAL STRAGGLING (ANGS) =",G16.8)
      WRITE(4,70)AVX
70    FORMAT(" AVERAGE TRANSVERSE RANGE (ANGS) =",G16.8)
      WRITE(4,72)STRAGX
72    FORMAT(" AVERAGE TRANSVERSE STRAGGLING (ANGS) =",G16.8,/)
      WRITE(4,74)
74    FORMAT(" LONGITUDINAL MOMENTS",16X,"TRANSVERSE MOMENTS")
      WRITE(4,24)ZMOM(1,1),ZMOM(2,1),TMOM,ZMOM(3,1),ZMOM(4,1)
24    FORMAT(" MOMENT 1 =",G20.6,/," MOMENT 2 =",G20.6,
     1 5X,"MOMENT 2 =",G20.6,/," MOMENT 3 =",G20.6,/," MOMENT 4 =",
     2 G20.6,/)
      TUM = STRAGX**2
      WRITE(4,26)UM(1,1),UM(2,1),TUM,UM(3,1),UM(4,1)
26    FORMAT(" MU1 =",G20.6,/," MU2 =",G20.6,10X,"MU2 =",G20.6,
     1 /," MU3 =",G20.6,/," MU4 =",G20.6,/)
120   WRITE(4,77)
77    FORMAT(" DEPOSITED ENERGY PARAMETERS:")
      WRITE(4,67)UM(1,2)
      WRITE(4,68)STRDZ
      WRITE(4,72)STRDX
      WRITE(4,74)
      WRITE(4,24)ZMOM(1,2),ZMOM(2,2),TMOMD,ZMOM(3,2),ZMOM(4,2)
      WRITE(4,26)UM(1,2),UM(2,2),AVXXD,UM(3,2),UM(4,2)
      RCOEF=FLOAT(NSPUT(1))/NOP
      SCOEF=FLOAT(NSPUT(2))/NOP
      WRITE(4,361)RCOEF
361   FORMAT(" REFLECTION COEFFICIENT =",G16.6,/)
      WRITE(4,363)SCOEF
363   FORMAT(" SPUTTERING COEFFICIENT =",G16.6,/)
      IF(MODE LT.3)RETURN
      VOL1=4.19*STRAGZ*STRAGX**2
      WRITE(4,365)VOL1
365   FORMAT(" AVERAGE CASCADE VOLUME (ANGS**3) =",G16.6)
      WRITE(4,367)VOL
367   FORMAT(" INDIVIDUAL CASCADE VOLUME (ANGS**3) =",G16.6)
      RAT=VOL/VOL1
      WRITE(4,369)RAT
369   FORMAT(" VOLUME RATIO =",G16.6)
      RETURN
      END
```

```
C       FUNCTION EVALS TO EVALUATE EDGEWORTH EXPANSION
C        FROM THE PARAMETERS IN COMMON
C
        FUNCTION EVALS(I,CO)
C
        COMMON /BLK8/UM(4,2),TERM(3,2)
C
        ZEE = (CO-UM(1,I)) / SQRT(UM(2,I))
        FCTN = 1.0 - TERM(1,I) * (3.0*ZEE - ZEE**3
        1 + TERM(2,I)* (3.0-6.0*ZEE**2+ZEE**4)
        2 - TERM(3,I) * (15.0-45.0*ZEE**2+15.0*ZEE**4-ZEE**6)
        EVALS = 1.0 / (SQRT(2.0*3.141592)) * EXP(-ZEE**2/2.0) * FCTN
        RETURN
        END



        FUNCTION RANDOM(ISEED,LINK)
        CALL SHIFT(ISEED,LINK)
        RANDOM = ISEED*2.0 + LINK
        RANDOM = RANDOM / 262143.0
        RETURN
        END



        .TITLE SHIFT
        .GLOBL SHIFT,.DA
SHIFT   0
        JMS* .DA
        JMP  .+2+1
ISEED   0
LINK    0

        LAW  -21
        DAC  CTR
        LAC* LINK
        RAR
        LAC* ISEED
        RAL
        DAC  TEMP1
LOOP    RTL
        DAC  TEMP
        SWHA
        RTL
        XOR  TEMP
        RAR
        LAC  TEMP1
        RAL
        DAC  TEMP1
```

```
            ISZ   CTR
            JMP   LOOP
            RCR
            DAC*  ISEED
            GLK
            DAC*  LINK
            JMP*  SHIFT
CTR         0
TEMP        0
TEMP1       0
            .END
```

```
C DCULD
C       ROUTINE TO CALCLATE DAMAGE USING LINEAR DECHANNELING
        DIMENSION FARRAY(2)
        COMMON IARRAY(256)
        DATA FARRAY(2)/4H SRC/
        IT=0
        WRITE(1,150)
150     FORMAT(" IS DATA IN PDP11(0) OR ND1100(1) STRUCTURE?")
        READ(2,)IGNO
1       WRITE(1,10)
10      FORMAT(" TAG OF ALIGNED IMPLANTED SPECTRUM=")
        READ(2,11)FARRAY(1)
11      FORMAT(A5)
        CALL FSTAT(5,FARRAY,I)
        IF(I.NE.0)GO TO 5
        WRITE(1,15)FARRAY
15      FORMAT(" FILE ",2A5," DOES NOT EXIST ON DISC")
        GO TO 1
5       CALL SEEK(5,FARRAY)
        READ(5,)
        READ(5,)
        I1=10
        DO 20 I2=1,26
        IF(I2.EQ.26)I1=6
        I3=(I2-1)*10+1
        I4=I3+I1-1
        IF(IGNO.EQ.0)READ(5,,ERR=25)IGNOR,(IARRAY(J),J=I3,I4)
        IF(IGNO.EQ.1)READ(5,,ERR=25)(IARRAY(J),J=I3,I4)
20      CONTINUE
        GO TO 30
25      WRITE(1,35)FARRAY,I2
35      FORMAT(" READ ERROR IN FILE ",2A5," LINE",I3)
        PAUSE
30      IF(IT.EQ.0)GO TO 40
        WRITE(1,45)
45      FORMAT(" SAME ENERGY CALIBRATION?(0 OR 1)")
        READ(2,)K
        IF (K.EQ.1)GO TO 50
40      CALL ESCAL(SLOPE,YINT)
50      WRITE(1,55)
55      FORMAT(" SURFACE CHANNEL=")
        READ(2,)AN2
        N2=AN2
        E1=AN2*SLOPE+YINT
        E1=E1+ELOSS(E1)
        IF(IT.EQ.0)GO TO 58
        WRITE(1,59)
59      FORMAT(" SAME PARAMETERS?(0 OR 1)")
        READ(2,)K
        IF (K.EQ.1)GO TO 75
58      WRITE(1,60)
60      FORMAT(" INPUT CHI(MIN)")
        READ(2,)CHI
        WRITE(1,65)
65      FORMAT(" INPUT RANDOM YIELD(NORM. TO IMPLANTED SPECTRUM")
        READ(2,)IYN
        WRITE(1,70)
70      FORMAT(" INPUT COUNTS IN SURFACE PEAK(NORM. AS ABOVE)")
```

```
      READ(2,)ISP
75    CALL LD1(IT,E1,E0,SLOPE,SAVR,TILT,TT)
      WRITE(1,80)
80    FORMAT(" CHOOSE CHANNEL BEHIND DAMAGE")
      CALL LD2
      WRITE(1,85)
85    FORMAT(" WHAT IS IT?")
      READ(2,)N1
      C1=0
      DO 90 I=1,4
90    C1=C1+IARRAY(N1+I-1)
      C1=C1/4
      SUM=0
      NN2=N2+10
      NN1=N1+1
      DO 95,I=NN1,NN2
95    SUM=SUM+IARRAY(I)
      C2=CHI*IYN
      XX=(C1+C2)/2
      DECH=(AN2-N1)*XX
      CHNL=AN2-N1
      YP=SUM-DECH-ISR
      AND=YP*TILT/((IYN-XX)*SAVR/SLOPE)
      WRITE(1,100)AND
100   FORMAT(" DAMAGE=",F6.1,"X10**15/CM**2")
      IT=1
      WRITE(1,105)
105   FORMAT(" PRINTOUT?(0 OR 1)")
      READ(2,)K
      IF(K.EQ.0)GO TO 1
      WRITE(4,200)FAPRAY(1)
200   FORMAT(//," TAG:",A5)
      WRITE(4,205)
205   FORMAT(2X,"YN",6X,"C1",6X,"N1",6X,"C2",6X,"N2",3X,"CHNLS",
     1  4X,"Y'",6X,"DECH",5X,"SP",4X,"TILT")
      WRITE(4,206)IYN,C1,N1,C2,AN2,CHNL,SUM,DECH,ISP,TT
206   FORMAT(I5,F8.2,I8,F8.2,F8.1,F6.1,F9.1,F9.1,I7,F8.2)
      WRITE(4,210)SLOPE,SAVR
210   FORMAT(" KEV/CHNL=",F6.2,5X,"STP. PWR. =",F8.4,"KEV/10**15/CM**2")
      WRITE(4,211)E0
211   FORMAT(" BEAM ENERGY=",F7.0," KEV")
      WRITE(4,215)AND
215   FORMAT(" DAMAGE=",F6.1,"X10**15DISP./CM**2")
      GO TO 1
      STOP
      END



C     LD1
      SUBROUTINE LD1(IT,E1,E0,SLOPE,SAVR,TILT,TT)
C ROUTINE TO CALCULATE DEPTH(A)/CHANNEL
      DIMENSION FILE(2),XM(2,2),PTEMP(6),P(6),MM(2)
```

```
      DATA FILE/5HCOEFF,4H SRC/
C SET UP STOPPING POWER COEFF  (ACCORDING TO BRAGG ADDITIVITY LAW)
1     WRITE(1,100)
100   FORMAT(" TILT(DEGREES)=")
      READ(2,)TT
      TILT=COS(TT*.01745)
      IF(IT EQ 0)GO TO 501
      WRITE(1,204)
204   FORMAT(" SAME SUBSTRATE?(0 OR 1)")
      READ(2,)IK
      IF(IK.EQ.1)GO TO 500
501   WRITE(1,107)
107   FORMAT(" NO  OF ELEMENTS COMPRISING SUBSTRATE (MAX 2)")
      READ(2,)NEL
      WRITE(1,120)
120   FORMAT(" DO YOU KNOW THE SUBSTRATE MOLECULAR DENSITY?(0 OR 1)")
      READ(2,)IATOM
      IF(IATOM EQ 0)GO TO 130
      WRITE(1,121)
121   FORMAT(" MOLECULAR DENSITY OF SUBSTRATE(10**22 ATOMS/CM**3) ")
      READ(2,)ATMOL
      GO TO 135
130   WRITE(1,101)
101   FORMAT(" DENSITY OF SUBSTRATE(G/CM**3).")
      READ(2,)DEN
135   DO 5 I=1,NEL
      K=1
      WRITE(1,102)I
102   FORMAT(" ATOMIC NUMBER AND MASS OF M2(",I1,")")
5     READ(2,)XM(I,1),XM(I,2)
      IF(NEL EQ.1)GO TO 10
15    WRITE(1,103)
103   FORMAT(" RATIO OF M2(1) M2(2)? (E.G. 1,2)")
      READ(2,)MM(1),MM(2)
      ATWT=XM(1,2)*MM(1)+XM(2,2)*MM(2)
      GO TO 25
10    MM(1)=1
      MM(2)=0
      ATWT=XM(1,2)
25    IF(IATOM.EQ.0)ATMOL=6.023*DEN/ATWT
C READ IN PROPER COEFFICIENTS FROM DISK FILE COEFF SRC
      CALL FSTAT(5,FILE,L)
      IF(L.NE.0)GO TO 30
      WRITE(1,105)
105   FORMAT(" FILE COEFF SRC MUST BE PUT ON DISK")
      STOP
30    DO 27 I=1,6
27    P(I)=0.
      DO 35 I=1,NEL
      CALL SEEK(5,FILE)
      MX=XM(I,1)
      DO 40 J=1,MX
40    READ(5,106,ERR=98,END=99)X,(PTEMP(K),K=1,6)
106   FORMAT(A5,3X,6E10.3)
      CALL CLOSE(5,FILE)
      DO 35 K=1,6
```

```
35        P(K)=P(K)+PTEMP(I)*MM(I)
C CALCULATE K**2
202       B=1.95
          C=3.494
          BIG=XM(1,2)
          IF(NEL.EQ.1)GO TO 45
          IF(XM(2,2).GT.BIG)BIG=XM(2,2)
45        RK=((SQRT(BIG**2-B**2)-C)/(4.0026+BIG))**2
500       E0=E1/RK
C CALCULATE AVERAGE STOPPING POWER AND ANGSTROMS/CHANNEL
201       SAVR=(RK*SP(P,E0)+SP(P,E1))*.873)/1000
          RETURN
C ERROR IN READ STATEMENTS
98        WRITE(1,110)
110       FORMAT(" WE'VE HAD AN ERROR WHEN READING THE COEFFICIENTS")
          CALL CLOSE(5,FILE)
          GO TO 112
99        WRITE(1,111)
111       FORMAT(" END OF COEFF FILE REACHED BEFORE PROPER VALUES FOUND")
112       WRITE(1,113)
113       FORMAT(" TRY AGAIN")
          GO TO 1
          END
```

```
C         LD2
C ROUTINE TO DISPLAY 1 SPECTRUM
          SUBROUTINE LD2
          DIMENSION AC(10),MKA(3),MKB(5)
          COMMON IARRAY(256)
          EQUIVALENCE (MKB(1),MB),(MKA(1),MA)
          DATA NP,IPCN,NYSC,NXSC/256,128,0,0/
          DATA MKA/-1,-1,-1/
          DATA MKB/-1,-1,-1,-1,-1/
          CALL TTIN(AC(1))
10        CALL DSPGF(IARRAY(1),NP,MB,MA,IPCN,NXSC,NYSC)
          CALL IDSP(IPCN+1,1)
          CALL IDSP(IARRAY(IPCN+1),2)
          CALL WAIT(IN)
          IF(.NOT.IN)GO TO 10
          RETURN
          END
```

```
C         DCUSS
C ROUTINE TO GENERATE DAMAGE PROFILES USING SEMI-EMPIRICAL
C SINGLE SCATTERING DECHANNELING
C
          COMMON IARRAY(256,3),DAM(100),IDAT1(256),IDAT2(256),IDAT3(256)
          COMMON SLOPE,YINT,P(6),MM(2),RK,ATMOL,E0,INX,INY,DECH(100),TL(8)
          COMMON COUNT(3),IGNO
          IT=0
          KK=1
          ITIME=-1
          WRITE(1,150)
150       FORMAT(" IS DATA IN PDP11(0) OR ND1100(1) STRUCTURE?")
          READ(2,)IGNO
1         CALL DECH0(IT,NN,DT,ATDEN,DN,N2,ALPHA,SE0,SE1)
          IT=1
          WRITE(1,120)
120       FORMAT(" PRINTOUT?(0 OR 1)")
          READ(2,)K
          IF(K EQ.1)CALL PPINT(NN,N2,DT,ATDEN,ALPHA,SE0,SE1)
          WRITE(1,100)
100       FORMAT(" PLOT PROFILE(0 OR 1)")
          READ(2,)K
          IF(K EQ.0)GO TO 1
          IF(ITIME.EQ.-1)GO TO 20
          WRITE(1,110)
110       FORMAT(" SAME GRAPH(0 OR 1)?")
          READ(2,)ITIME
20        CALL DPLOT(ITIME,KK,NN,DT,ATDEN,DN)
          GO TO 1
          STOP
          END



C         DECH0
C ROUTINE TO CALCULATE DAMAGE PROFILES AND TOTAL DAMAGE
C FROM BACKSCATTERING SPECTRA
C
          SUBROUTINE DECH0(IT,NN,DT,ATDEN,DN,N2,ALPHA,SE0,SE1)
          DIMENSION FTEMP(2),FARRAY(3),ITEMP(10)
          DIMENSION AXIS(10,2)
          COMMON IARRAY(256,3),DAM(100),IDAT1(256),IDAT2(256),IDAT3(256)
          COMMON SLOPE,YINT,P(6),MM(2),RK,ATMOL,E0,INX,INY,DECH(100),TL(8)
          COMMON COUNT(3),IGNO
          DATA FTEMP(2)/4H SRC/
C SET UP SPECTRA TO BE ANALYZED
1         WRITE(1,100)
100       FORMAT(" TAG OF ALIGNED IMPLANTED SPECTRUM=")
          READ(1,101)FARRAY(1)
101       FORMAT(A5)
          WRITE(1,102)
102       FORMAT(" TAG OF VIRGIN SPECTRUM=")
          READ(1,101)FARRAY(2)
```

```
          WRITE(1,103)
103       FORMAT(" TAG OF RANDOM SPECTRUM=")
          READ(1,101)FARRAY(3)
C READ IN SPECTRA
          DO 7 I=1,3
          FTEMP(1)=FARRAY(I)
          CALL FSTAT(5,FTEMP,K)
          IF(K.NE.0)GO TO 6
          WRITE(1,104)FTEMP
104       FORMAT(" FILE ",2A5,"DOES NOT EXIST ON DISK")
          PAUSE
          GO TO 1
C SET UP SCALING
6         CALL SEEK(5,FTEMP)
          IF(I.NE.1)GO TO 603
          READ(5,602)TL
602       FORMAT(8A5)
          GO TO 604
603       READ(5,)
604       READ(5,,ERR=10)COUNT(I)
          I1=10
          DO 7 I2=1,26
          IF(I2.EQ.26)I1=6
          IF(IGNO.EQ.0)READ(5,,ERR=10)IGNOR,(ITEMP(J),J=1,I1)
          IF(IGNO.EQ.1)READ(5,,ERR=10)(ITEMP(J),J=1,I1)
          I3=(I2-1)*10
          DO 7 I4=1,I1
7         IARRAY((I3+I4),I)=ITEMP(I4)
          GO TO 11
10        WRITE(1,105)FTEMP
105       FORMAT(" READ ERROR IN FILE ",2A5)
          PAUSE
11        COUNT(2)=COUNT(1)/COUNT(2)
          COUNT(3)=COUNT(1)/COUNT(3)
          COUNT(1)=1
          DO 330 I=1,256
          IDAT1(I)=IARRAY(I,1)
          IDAT2(I)=IARRAY(I,2)
330       IDAT3(I)=IARRAY(I,3)
          CALL DECH1
          IF(IT.EQ.0)GO TO 50
          WRITE(1,110)
110       FORMAT(" SAME ENERGY CALIBRATION?(0 OR 1)")
          READ(2,)K
          IF(K.EQ.1)GO TO 51
C FIND KEV/CHANNEL
50        CALL ESCAL(SLOPE,YINT)
51        WRITE(1,106)
106       FORMAT(" SURFACE CHANNEL OF HEAVIEST ELEMENT IN SUBSTRATE?")
          READ(2,)AN2
          E1=AN2*SLOPE+YINT
          E1=E1+ELOSS(E1)
          N2=AN2
          IF(AN2-N2.GT..5)N2=N2+1
C SUBTRACT SURFACE PEAK IF NECESSARY
          WRITE(1,107)
```

```
107       FORMAT(" IS THERE A SURFACE PEAK TO BE SUBTRACTED?(0 OR 1)")
          READ(2,)K
          IF(K EQ.0)GO TO 20
          DO 22 I=1,10
          AXIS(I,1)=N2-20+I
22        AXIS(I,2)=IARRAY(N2-20+I,2)
          CALL LINREG(AXIS,10,A,B)
          NN1=N2-10
          NN2=N2+3
          DO 24 I=NN1,NN2
          NN=I*A+B
          IARRAY(I,1)=IARRAY(I,1)+(NN-IARRAY(I,2))*COUNT(2)
24        IARRAY(I,2)=NN
C PERFORM 3-POINT SMOOTH TO ALIGNED IMPLANTED SPECTRUM
20        WRITE(1,403)
403       FORMAT(" SMOOTH IMPLANTED ALIGNED SPECTRUM?")
          READ(2,)K
          IF(K EQ.0)GO TO 31
29        IDAT3(1)=0
          IDAT3(256)=0
          DO 28 I=2,255
28        IDAT3(I)=.25*IARRAY(I-1,1)+.5*IARRAY(I,1)+.25*IARRAY(I+1,1)
          CALL DECH1
          WRITE(1,305)
305       FORMAT(" USE SMOOTHED SPECTRUM?")
          READ(2,)K
          IF(K.EQ.0)GO TO 31
          DO 32 I=1,256
32        IARRAY(I,1)=IDAT3(I)
C FIND DEPTH(A)/CHANNEL
31        CALL DTCAL(IT,E1,DT,N2,ATDEN,CORR,ALPHA,SE0,SE1)
C FIND YN, RUTHERFORD CORRECTION MADE IN DTCAL
          YN=0.
          NN3=N2-30
          NN4=N2-10
          DO 33 I=NN3,NN4
33        YN=YN+IARRAY(I,3)
          YN=YN/21.*COUNT(3)
          WRITE(1,302)YN
302       FORMAT(" YN=",E12.4)
C FIND C1
          WRITE(1,109)
109       FORMAT(" INPUT C1 CHANNEL")
          READ(2,)N1
          C1=0.
          DO 30 I=1,3
30        C1=C1+IARRAY(N1+I-2,1)
          C1=C1/3.
C MAKE LINEAR FIT TO VIRGIN
          N2N=40
524       NN1=N2-N2N
          DO 25 I=1,10
          AXIS(I,1)=NN1
          AXIS(I,2)=IARRAY(NN1,2)
25        NN1=NN1+3
          CALL LINREG(AXIS,10,A,B)
```

```
            IF(A LT.0)GO TO 527
            N2N=N2N+1
            GO TO 524
527         DO 26 I=N1,N2
26          IARRAY(I,2)=A+I+B
C PERFORM DECHANNELING
            SUM=0
            NN=N2-N1+1
            DO 210 II=1,NN
            I=N2+1-II
210         SUM=SUM+IARRAY(I,1)
            COR=(C1+IARRAY(N2,2)*COUNT(2))*(N2-N1)**2
            C=(C1-IARRAY(N1,2)+COUNT(2))/(SUM-COR)
230         SUM=0
            K=0
            DO 215 II=1,NN
            J=N2+1-II
            K=K+1
            DAM(K)=(IARRAY(J,1)-SUM+C-IARRAY(J,2)+COUNT(2))*(1 +C**2 )
            DECH(K)=IARRAY(J,1)-DAM(K)
215         SUM=SUM+DAM(K)
            C5=(C1-IARRAY(N1,2)+COUNT(2))/SUM
            CHECK=ABS(C-C5)
            IF(CHECK/C.LE .00001)GO TO 250
            C=C5
            GO TO 230
C CALCULATE FRACTIONAL DAMAGE PER CHANNEL
250         WRITE(1,301)C
301         FORMAT(" C=",F10 6)
            DO 40 J=1,NN
40          DAM(J)=DAM(J)/(YN*CORR-DECH(J))
            DO 370 I=1,256
            IDAT1(I)=IARRAY(I,1)
            IDAT2(I)=IARRAY(I,2)
370         IDAT3(I)=0
            K=0
            DO 380 I=1,NN
            K=K+1
380         IDAT3(N2+1-I)=DECH(K)
            CALL DECH1
            DN=0
            DO 60 I=1,NN
60          DN=DN+DAM(I)
            DN=DN*DT*ATDEN
            WRITE(1,601)DN
601         FORMAT(" TOTAL DAMAGE=",E12.4)
            RETURN
            END




C           DECH1
C ROUTINE TO DISPLAY 3 SPECTRA
```

```
      SUBROUTINE DECH1
      DIMENSION AC(10),MKA(5),MKB(5)
      COMMON IARRAY(256,3),DAM(100),IDAT1(256),IDAT2(256),IDAT3(256)
      EQUIVALENCE (MKB(1),MB),(MKA(1),MA)
      DATA NP,IPCN,NYSC,NXSC/256,128,0,0/
      DATA MKA/-1,-1,-1/
      DATA MKB/-1,-1,-1,-1,-1/
      CALL TTIN(AC(1))
10    IF(ISENSW(17))CALL DSPGF(IDAT1(1),NP,MB,MA,IPCN,NXSC,NYSC)
      IF(ISENSW(16))CALL DSPGF(IDAT2(1),NP,MB,MA,IPCN,NXSC,NYSC)
      IF(ISENSW(15))CALL DSPGF(IDAT3(1),NP,MB,MA,IPCN,NXSC,NYSC)
      CALL IDSP(IPCN+1,1)
      CALL IDSP(IDAT1(IPCN+1),2)
      CALL IDSP(IDAT2(IPCN+1),3)
      CALL IDSP(IDAT3(IPCN+1),4)
      CALL WAIT(IN)
      IF(.NOT.IN)GO TO 10
      RETURN
      END



C     DTCAL
      SUBROUTINE DTCAL(IT,E1,DT,N2,ATDEN,CORR,ALPHA,SE0,SE1)
C ROUTINE TO CALCULATE DEPTH(A)/CHANNEL
      DIMENSION FILE(2),XM(2,2),PTEMP(6)
      COMMON IARRAY(256,3),DAM(100),IDAT1(256),IDAT2(256),IDAT3(256)
      COMMON SLOPE,YINT,P(6),MM(2),RK,ATMOL,E0,INX,INY,DECH(100),TL(8)
      DATA FILE/5HCOEFF,4H SRC/
C SET UP STOPPING POWER COEFF  (ACCORDING TO BRAGG ADDITIVITY LAW)
1     WRITE(1,100)
100   FORMAT(" TILT(DEGREES)=")
      READ(2,)TILT
      TILT=COS(TILT*.01745)
      IF(IT.EQ.0)GO TO 501
      WRITE(1,204)
204   FORMAT(" SAME SUBSTRATE?(0 OR 1)")
      READ(2,)KK
      IF(KK.EQ.1)GO TO 500
501   WRITE(1,107)
107   FORMAT(" NO. OF ELEMENTS COMPRISING SUBSTRATE:(MAX.2)")
      READ(2,)NEL
      WRITE(1,120)
120   FORMAT(" DO YOU KNOW THE SUBSTRATE MOLECULAR DENSITY?(0 OR 1)")
      READ(2,)IATOM
      IF(IATOM.EQ.0)GO TO 130
      WRITE(1,121)
121   FORMAT(" MOLECULAR DENSITY OF SUBSTRATE(10**23 ATOMS/CM**3):")
      READ(2,)ATMOL
      GO TO 135
130   WRITE(1,101)
101   FORMAT(" DENSITY OF SUBSTRATE(G/CM**3):")
      READ(2,)DEN
```

```
135       DO 5 I=1,NEL
          K=1
          WRITE(1,102)I
102       FORMAT(" ATOMIC NUMBER AND MASS OF M2(",I1,")")
5         READ(2,)XM(I,1),XM(I,2)
          IF(NEL EQ 1)GO TO 10
15        WRITE(1,103)
103       FORMAT(" RATIO OF M2(1)/M2(2)? (E G  1,2)")
          READ(2,)MM(1),MM(2)
          ATWT=XM(1,2)+MM(1)+XM(2,2)*MM(2)
          GO TO 25
10        MM(1)=1
          MM(2)=0
          ATWT=XM(1,2)
25        IF(IATOM EQ 0)ATMOL=6 023+DEN*ATWT
C READ IN PROPER COEFFICIENTS FROM DISK FILE COEFF SRC
          CALL FSTAT(5,FILE,L)
          IF(L NE. 0)GO TO 30
          WRITE(1,105)
105       FORMAT(" FILE COEFF SRC MUST BE PUT ON DISK")
          STOP
30        DO 27 I=1,6
27        P(I)=0
          DO 35 I=1,NEL
          CALL SEEK(5,FILE)
          MX=XM(I,1)
          DO 40 J=1,MX
40        READ(5,106,ERR=98,END=99)N,(PTEMP(I),I=1,6)
106       FORMAT(A5,3X,6E10 3)
          CALL CLOSE(5,FILE)
          DO 35 K=1,6
35        P(K)=P(K)+PTEMP(K)*MM(I)
C CALCULATE K**2
202       B=1 953
          C=3 494
          BIG=XM(1,2)
          IF(NEL. EQ. 1)GO TO 45
          IF(XM(2,2). GT. BIG)BIG=XM(2,2)
45        RK=((SQRT(BIG**2-B**2)-C)/(4. 0026+BIG))**2
500       E0=E1/RK
C CALCULATE AVERAGE STOPPING POWER AND ANGSTROMS/CHANNEL
201       WRITE(1,221)
221       FORMAT(" WHAT IS ALPHA?")
          READ(2,)ALPHA
          SP0=SP(P,E0)
          SP1=SP(P,E1)
          SE0=SP0/((MM(1)+MM(2))*1000.)
          SE1=SP1/((MM(1)+MM(2))*1000. )
          SAV=(RK*SP0*ALPHA+SP1/. 873)*ATMOL
          SAVR=(RK*SP0+SP1/. 873)*ATMOL
          CORR=SAV/SAVR
          DT=SLOPE*1000. *TILT/SAV
          IBIG=MM(1)
          IF(NEL. GT. 1. AND. XM(1,2). LT. XM(2,2))IBIG=MM(2)
          ATDEN=ATMOL*IBIG
C MAKE RUTHERFORD CORRECTION TO RANDOM & ALIGNED IMPLANTED SPECTRA
```

```
      NN2=N2-100
      DO 115 I=NN2,N2
      E2=SLOPE*I+YINT
      E2=E2+ELOSS(E2)
      TERM0=(E1-E2)/(PK+SP1/(SP0+.873))
      TERM1=(E1-E2)/(RK*SP1/(SP0*ALPHA*.873))
      EE=E0-TERM1
      EEE=E0-TERM0
      IARRAY(I,1)=IARRAY(I,1)*EE**2/E0**2
      IARRAY(I,2)=IARRAY(I,2)*EEE**2/E0**2
115   IARRAY(I,3)=IARRAY(I,3)*EEE**2/E0**2
      RETURN
C ERROR IN READ STATEMENTS
98    WRITE(1,110)
110   FORMAT(" WE'VE HAD AN ERROR WHEN READING THE COEFFICIENTS")
      CALL CLOSE(5,FILE)
      GO TO 112
99    WRITE(1,111)
111   FORMAT(" END OF COEFF FILE REACHED BEFORE PROPER VALUES FOUND")
112   WRITE(1,113)
113   FORMAT(" TRY AGAIN")
      GO TO 1
      END




C     PRINT
      SUBROUTINE PRINT(NN,N2,DT,ATDEN,ALPHA,SE0,SE1)
C ROUTINE TO OUTPUT VARIOUS DATA ON CP
      COMMON IARRAY(256,3),DAM(100),IDAT1(256),IDAT2(256),IDAT3(256)
      COMMON SLOPE,YINT,P(6),MM(2),RK,ATMOL,E0,INX,INY,DECH(100),TL(8)
      COMMON COUNT(3)
      BIG=DAM(1)
      DO 10 I=2,NN
      IF(BIG.LT.DAM(I))BIG=DAM(I)
10    CONTINUE
      WRITE(1,150)
150   FORMAT(" NO. OF CHNLS.?")
      READ(2,)IN
      IN=IN+5
      WRITE(4,100)TL
100   FORMAT(*1*,8A5)
      WRITE(4,140)SE0,SE1,ALPHA
140   FORMAT(" S(E0)=",F8.5,"  S(E1)=",F8.5,"KEV/10**15/CM**2 "
     1 ,"  ALPHA=",F6.3)
      WRITE(4,110)
110   FORMAT(" CHNL IMPLANT. VIRGIN  RANDOM  DECHNL   DEPTH %DAMAGE",
     1  " NORMALIZE  ND(X10**15)")
      AND=0.
      DO 20 I=1,IN
      ICHNL=N2+6-I
      I1=IARRAY(ICHNL,1)
      I2=IARRAY(ICHNL,2)*COUNT(2)
```

```
          I3=IARRAY(ICHNL,3)*COUNT(I)
          I4=0
          AI5=DT*(N2-ICHNL)
          IF(AI5 LT 0 )AI5=0.
          FDAM=0
          ANDAM=0
          IF(ICHNL LT. N2-NN. OR. ICHNL GT N2)GO TO 20
          I4=DECH(N2-ICHNL+1)
          FDAM=DAM(N2-ICHNL+1)
          ANDAM=FDAM/BIG
          AND=AND+FDAM*DT*ATDEN
20        WRITE(4,130)ICHNL, I1, I2, I3, I4, AI5, FDAM, ANDAM, AND
130       FORMAT(I5,4I8,F8.1,2F8.3,F10.1)
          RETURN
          END




C         DPLOT
C
C ROUTINE TO PLOT DAMAGE PROFILES
          SUBROUTINE DPLOT(ITIME,KK,NN,DT,ATDEN,DN)
C ITIME=ENTRY" COUNT
C NN=NO OF CHANNELS OVER WHICH DAMAGE EXISTS
C DT=DEPTH(ANGSTROMS)/CHANNEL
C ATDEN=SUBSTRATE MOLECULAR DENSITY
C DN=TOTAL DAMAGE
          DIMENSION IP(11),TITLE(8)
          COMMON IARRAY(256,3),DAM(100),IDAT1(256),IDAT2(256),IDAT3(256)
          COMMON SLOPE,YINT,P(6),MM(2),RK,ATMOL,E0,INX,INY,DECH(100),TL(8)
          DATA IP/11,4,1,3,7,2,5,6,8,9,10/
C READY PLOTTER
          CALL AIPA(3)
          CALL PLOT(-1,0,0)
          CALL PLOT(0,0,0)
          IF(ITIME.NE.1)GO TO 14
          KK=KK+1
          GO TO 10
14        IF(ITIME.NE.0)GO TO 15
          CALL PLOT(5,1200,0)
          CALL PLOT(0,0,0)
15        KK=1
          ITIME=0
          XX=NN/5.
          IX=XX
          IF((XX-IX).GT..5)IX=IX+1
          IF(XX.GT.8.)IX=8
          MAX=NN*DT
          CALL SCALE(IX,5.,0,MAX,INX)
          CALL LAX(1,0,IX+2,0,INX)
```

```
      WRITE(1,20)
20    FORMAT(" MAX  PERCENT DAMAGE PER INCH(MIN=1)  (6 INCH SCALE)")
      READ(2,)INY
      CALL LAX(2.0,6.0,INY)
C PLOT PROFILE
10    XSTEP=100.*DT/INX
      YSTEP=100./INY
      NX=0
      DO 30 I=1,NN
      NY=DAM(I)*100.*YSTEP
      CALL PPLOT(IP(KK),1,NX,NY)
30    NX=I*XSTEP
      CALL CONTRO(3,0,2,0)
      IF(ITIME.EQ.1)GO TO 122
      CALL CONTRO(3,2,300,-45)
      WRITE(3,100)
100   FORMAT(1X,16HDEPTH(ANGSTROMS))
      CALL CONTRO(3,2,-100,350)
      WRITE(3,101)
101   FORMAT(1X,7HPERCENT)
      CALL CONTRO(3,2,-100,330)
      WRITE(3,102)
102   FORMAT(1X,6HDAMAGE)
      CALL CONTRO(3,2,50,625)
      WRITE(3,103)ATDEN
103   FORMAT(1X,2HN=,F5.3,13HX10  ATOMS/CM)
      CALL CONTRO(3,2,170,635)
      WRITE(3,104)
104   FORMAT(1X,11H23          3)
122   WRITE(1,105)
105   FORMAT(" TITLE?")
      READ(2,106)(TITLE(I),I=1,8)
106   FORMAT(8A5)
      NN1Y=675-(KK-1)*20
      CALL PPLOT(IP(KK),1,400,NN1Y+5)
      CALL CONTRO(3,2,410,NN1Y)
      WRITE(3,107)(TITLE(I),I=1,8)
107   FORMAT(1X,8A5)
      NN2Y=300-(KK-1)*20
      CALL PPLOT(IP(KK),1,600,NN2Y+5)
      CALL CONTRO(3,2,610,NN2Y)
      WRITE(3,108)DN
108   FORMAT(1X,3HND=,F6.1,13HX10  ATOMS/CM)
      CALL CONTRO(3,2,750,NN2Y+10)
      WRITE(3,109)
109   FORMAT(1X,11H15          2)
      IF(ITIME.EQ.1)GO TO 120
      CALL PLOT(5,920,-100)
      CALL PLOT(4,-120,-100)
      CALL PLOT(4,-120,750)
      CALL PLOT(4,920,750)
      CALL PLOT(4,920,-100)
120   CALL PLOT(5,0,0)
      RETURN
      END
```

```
C         SCALE
          SUBROUTINE SCALE(INCH,XMULT,MIN,MAX,INC)
C ROUTINE TO SET AXIS SCALING FOR PLOTTER
C INCH=NO  OF INCHES ALONG AXIS
C XMULT=SCALE MULTIPLE PER 5TH OF AN INCH
C MIN=MIN AXIS VALUE - WILL BE RETURNED AS MOST CONVENIENT MIN FOR SCALE
C MAX=MAX AXIS VALUE - AGAIN MAY BE CHANGED ON RETURN
C INC=SCALE UNITS PER INCH OF PLOT AXIS
C
          IDIFF=MAX-MIN
          XX=IDIFF/(INCH*XMULT)
          DO 10 I=1,10
          K=I-1
          X1=XX*10.**K
          IF(X1 LE 10)GO TO 15
10        CONTINUE
15        IX1=X1
          IF((X1-IX1) GE  .5)IX1=IX1+1
          INC=IX1*XMULT*10.**K
          IY=0
          IF((MIN/(1.*INC)-MIN/INC) GT  .5)IY=1
          MIN=(MIN/INC+IY)*INC
          MAX=MIN+INC*INCH
          RETURN
          END
```

```
C         LAX
          SUBROUTINE LAX(IAXIS,NXY,INCH,MIN,INC)
C ROUTINE TO PLOT AXES AND LABEL THEM
C IAXIS=1 IF X-AXIS
C       =2 IF Y AXIS
C NXY=AXIS START POINT
C INCH=NO  OF INCHES ALONG AXIS
C MIN=LABEL ON FIRST MARKER
C INC=LABEL STEP
C THIS ROUTINE ASSUMES LINEAR SCALES
C
C SET CHARACTER SIZE AT 2
          CALL CONTRO(3,0,2.0)
          IWR=MIN
          DO 10 I=1,INCH
          DO 10 J=1,5
          JJ=(J-1)*20+(I-1)*100
          IF(IAXIS.EQ 1)CALL PLOT(5,JJ,NXY)
          IF(IAXIS EQ 2)CALL PLOT(5,NXY,JJ)
          IF(J EQ 1)GO TO 14
          IF(IAXIS EQ 1)CALL PLOT(4,JJ,NXY-5)
          IF(IAXIS.EQ 2)CALL PLOT(4,NXY-5,JJ)
          GO TO 10
14        IF(IAXIS EQ 1)CALL PLOT(4,JJ,NXY-10)
          IF(IAXIS.EQ 2)GO TO 20
          DO 22 K=1,5
```

```
      NUMB=IWP/10 **I
      IF(NUMB EQ 0)GO TO 25
20    CONTINUE
25    J1=6*(12-I)
      CALL CONTRO(3,2,JJ-J1,NEW-25)
      WRITE(3,100)IWP
100   FORMAT(1X,I6)
      GO TO 9
20    CALL PLOT(4,NEW-10,JJ)
      CALL CONTRO(3,2,NEW-80,JJ-6)
      WRITE(3,100)IWP
9     IWP=IWP+INC
10    CONTINUE
C NOW DRAW AXIS
      IF(IAXIS EQ 1)GO TO 30
      CALL PLOT(5,NEW,JJ)
      CALL PLOT(4,NEW,0)
      RETURN
30    CALL PLOT(5,JJ,NEW)
      CALL PLOT(4,0,NEW)
      RETURN
      END
```

```
C         SPECS
C CHAIN FILE TO PLOT UP TO 5*256 CHANNEL* SPECTRA PLUS ENERGY
C AND DEPTH SCALES
          COMMON IAPPAY(260,5),EOUT(101,2),NVAL(50)
          COMMON ASCAL(5),TITLE(5,8),COUNT(5)
          COMMON ISPEC,ITIME,IENG,IDEPTH,SUPF,E1,SLOPE,YINT
          COMMON P(6),NEL,NM(2,2),ATOEN,ANAME(2),IGNO
          ITIME=0
          WRITE(1,150)
150       FORMAT(" IS DATA IN FOF11.0 OR NO(100.1) STRUCTURE?")
          READ(2,)IGNO
1         CALL SPL1
          CALL SPL2
          ITIME=1
          GO TO 1
          STOP
          END
```

```
C         SPL1
          SUBROUTINE SPL1
C FIRST LINE-SET UP SPECTRA FOR PLOT
          DIMENSION ITEMP(10),FTEMP(2),FAPPAY(5)
          COMMON IAPPAY(260,5),EOUT(101,2),NVAL(50)
          COMMON ASCAL(5),TITLE(5,8),COUNT(5)
          COMMON ISPEC,ITIME,IENG,IDEPTH,SUPF,E1,SLOPE,YINT
          COMMON P(6),NEL,NM(2,2),ATOEN,ANAME(2),IGNO
          DATA FILN/4H SRC/
C         READ IN NO  OF SPECTRA TO BE PLOTTED
C BUT MAKE SURE THEY EXIST ON DISK
1         WRITE(1,100)
100       FORMAT(1X,"NO  OF SPECTRA TO BE PLOTTED(MAX=5)")
          READ(2,)ISPEC
          WRITE(1,101)ISPEC
101       FORMAT(1X,"READ IN",I2," TAG(S) (END EACH WITH CR)")
          DO 5 I=1,ISPEC
5         READ(2,102)FARRAY(I)
102       FORMAT(A5)
C LOOP TO READ IN SPECTRA
C FIRST GET A FILENAME
          DO 6 I=1,ISPEC
          FTEMP(1)=FARRAY(I)
          FTEMP(2)=FILN
C CHECK IF FILE EXISTS AND PAUSE IF NO
          CALL FSTAT(5,FTEMP,K)
          IF(K NE 0)GO TO 7
          WRITE(1,103)FTEMP
103       FORMAT(1X,"FILE ",2A5,"DOES NOT EXIST ON DISK")
          GO TO 1
C OPEN FILE
7         CALL SEEK(5,FTEMP)
C STORE TITLE
```

```
      READ(5,104,ERR=12)(TITLE(I,J),J=1,8)
104   FORMAT(8A5)
C  STORE COUNTS
      READ(5,,ERR=12)COUNT(I)
C  STORE SPECTRUM
      III=10
      DO 6 I1=1,26
      IF(I1 EQ 26)III=6
      IF(IGNO EQ 0)READ(5,,ERR=12)IGNOR,(ITEMP(J),J=1,III)
      IF(IGNO EQ 1)READ(5,,ERR=12)(ITEMP(J),J=1,III)
      I2=(I1-1)*10
      DO 209 I2=1,III
209   IARRAY(I2+I2,I)=ITEMP(I2)
6     IARRAY(1,I)=0
      GO TO 15
C  IF READ ERROR,PAUSE
12    WRITE(1,105)ITEMP,I1
105   FORMAT(1X,"READ ERROR IN FILE ",2A5,"  LINE",I2)
      PAUSE
C  ASK  IF ENERGY OR DEPTH SCALES WANTED
15    WRITE(1,200)
200   FORMAT(" DO YOU WANT AN ENERGY SCALE?(0 OR 1)")
      READ(2,)IENG
      WRITE(1,201)
201   FORMAT(" DO YOU WANT A DEPTH SCALE?(0 OR 1)")
      READ(2,)IDEPTH
      IF(IENG EQ 0 AND IDEPTH EQ 0)GO TO 205
      IF(ITIME EQ 0)GO TO 214
      WRITE(1,215)
215   FORMAT(" DO YOU WANT THE SAME ENERGY CALIBRATION(0 OR 1)")
      READ(2,)ITT
      IF(ITT EQ 1)GO TO 216
214   CALL ESCAL(SLOPE,YINT)
216   IF(IDEPTH EQ 0)GO TO 205
      WRITE(1,203)
203   FORMAT(" SURFACE CHANNEL OF HEAVIEST ELEMENT IN SUBSTRATE?")
      READ(2,)SURF
      E1=SURF*SLOPE+YINT
      E1=E1+ELOSS(E1)
C NOW ASK IF SCALING REQUIRED
C  INITIALIZE SCALING MATRIX
205   DO 9 I5=1,5
9     ASCAL(I5)=1
      WRITE(1,106)
106   FORMAT(1X,"ANY SCALING?(0 OR 1)")
      READ(2,)I4
      IF(I4 EQ 0)GO TO 20
      DO 21 I=1,ISPEC
      SCA=0
25    WRITE(2,107)
107   FORMAT(1X,"TAG?(PRESS CR IF FINISHED)")
      READ(2,102)SCA
      IF(SCA EQ 5H     )GO TO 20
      DO 22 I1=1,ISPEC
      IF(FARRAY(I1) EQ SCA)GO TO 23
22    CONTINUE
```

```
      WRITE(1,108)SCA
108   FORMAT(" NO SUCH TAG AS ",A5,"-TRY AGAIN")
      GO TO 25
27    WRITE(1,109)
109   FORMAT(" SCALE FACTOR?")
      READ(2,)XSCAL
C PERFORM SCALING
      ASCAL(I1)=XSCAL
      DO 21 I6=1,256
21    IARRAY(I6,I1)=IARRAY(I6,I1)*XSCAL
20    RETURN
      END




C     SPL2
      SUBROUTINE SPL2
C SECOND LINK-PLOT SPECTRA+ENERGY AND DEPTH SCALES
      DIMENSION IP(5)
      COMMON IARRAY(260,5),EOUT(101,2),NVAL(50)
      COMMON ASCAL(5),TITLE(5,8),COUNT(5)
      COMMON ISPEC,ITIME,IENG,IDEPTH,SUPF,E1,SLOPE,YINT
      COMMON P(6),NEL(2),M(2,2),ATDEN,ANAME(2)
      DATA IP/11,4,1,2,7/
C NOW WE ARE READY FOR PLOTTING
      CALL AIPA(2)
C CHOOSE MAX AND MIN CHANNELS FOR PLOTTING
      WRITE(1,110)
110   FORMAT(1X,"MIN AND MAX CHANNELS FOR PLOT?")
      READ(2,)MIN,MAX
C INITIALIZE PLOT
      CALL PLOT(-1.0,0)
      CALL PLOT(0.0,0)
C SET NO. OF CHANNELS/INCH(MULTIPLE OF 5)
      CALL SCALE(10.5.,MIN,MAX,INX)
      IF(MAX GT 256)MAX=256
      IWP=MIN
      IF(MIN EQ 0)MIN=1
C DRAW IN X-AXIS MARKERS EVERY .2 IN
C AND LABEL EVERY INCH
      NVAL(1)=0
      DO 45 I=2,50
45    NVAL(I)=NVAL(I-1)+20
      CALL AXIS(1,0,50,5,INR,INX)
C CHOOSE MAX DATUM BETWEEN MIN AND MAX CHANNELS
      IDAT=IARRAY(MIN,1)
      DO 55 I=1,ISPEC
      DO 55 J=MIN,MAX
      IF(IARRAY(J,I).LE.IDAT)GO TO 55
      IDAT=IARRAY(J,I)
55    CONTINUE
C NOW DETERMINE Y COUNTS/INCH(MULTIPLE OF 2 5)
      CALL SCALE(7,2.5,0,IDAT,INY)
C NOW PUT Y-AXIS MARKERS AND LABEL EVERY INCH
```

```
      CALL AXIS(3.0.25,5.0,INY)
C NOW DRAW IN DATA POINTS
      XSTEP=100./INX
      YSTEP=100./INY
      DO 80 I=1,ISPEC
      NNN=0
      IF(MIN EQ 1)NNN=YSTEP
      K=0
      DO 80 J=MIN,MAX
      NY=IARRAY(J,I)*YSTEP
      NX=NNN+0.+XSTEP
      K=K+1
      IF(NY EQ 0)GO TO 80
      CALL PPLOT(IP(I),1,NX,NY)
80    CONTINUE
C NOW PUT IN TITLES
      NY=680
      DO 85 I=1,ISPEC
      CALL PPLOT(IP(I),1,320,NY+4)
      CALL CONTRO(3,2,310,NY)
      WRITE(3,121)
121   FORMAT(2H /)
      CALL CONTRO(3,2,340,NY)
      WRITE(3,112)(TITLE(I,J),J=1,8)
112   FORMAT(1X,8A5)
      CALL CONTRO(3,2,818,NY)
      ICC=COUNT(I),'10
      WRITE(3,123)ICC
123   FORMAT(1X,I7)
      CALL CONTRO(3,2,900,NY)
      WRITE(3,124)
124   FORMAT(2H ::)
      CALL CONTRO(3,2,905,NY)
      WRITE(3,125)ASCAL(I)
125   FORMAT(1X,F7.2)
      CALL CONTRO(3,0,1,0)
      CALL CONTRO(3,2,990,NY)
      WRITE(3,122)
122   FORMAT(1X,1HN)
      CALL CONTRO(3,0,2,0)
      CALL CONTRO(3,2,996,NY)
      WRITE(3,126)
126   FORMAT(1X,1HC)
85    NY=NY-20
C NOW PUT IN AXES TITLES
      CALL CONTRO(3,2,400,-40)
      WRITE(3,150)
150   FORMAT(15H CHANNEL NUMBER)
      CALL CONTRO(3,2,-80,400)
      WRITE(3,151)
      WRITE(3,152)
      WRITE(3,153)
      WRITE(3,154)
      WRITE(3,155)
151   FORMAT(2H Y)
152   FORMAT(2H I)
```

```
152       FORMAT(2H E)
154       FORMAT(2H L)
155       FORMAT(2H D)
C NOW DO ENERGY SCALE IF REQUIRED
          IF(MIN EQ 1)MIN=0
          IF(IENG EQ 0)GO TO 300
          MINE=MIN*SLOPE+YINT
          MINEE=MINE
          MAXE=(MIN+10*INE)*SLOPE+YINT
          MAXEE=MAXE
          CALL SCALE(10.2 5,MINE,MAXE,INE)
          IK=50
          IF(MINE LT MINEE)MINE=MINE+INE
          IF((MINE+10*INE) LT MAXEE)MINE=MINE+INE
          IF((MINE+10*INE) LT MAXEE)GO TO 322
          IK=IK-5
322       E=MINE
          DO 301 I=1,IK
          NVAL(I)=(E-ELOSS(E))-YINT)/SLOPE-MIN)+XSTEP
301       E=E+INE.5
          CALL AXIS(1.,-50,IK,5,MINE,INE)
          CALL CONTRO(3,2,150,-90)
          WRITE(3,308)
308       FORMAT(21H BACKSCATTERED ENERGY)
C NOW DO DEPTH SCALE IF REQUIRED
300       IF(IDEPTH EQ 0)GO TO 330
          IENT=0
          IF(ITIME EQ 0)GO TO 507
          WRITE(1,508)
508       FORMAT(" SAME SUBSTRATE?(0 OR 1)")
          READ(2,)K
          IF(K EQ 0)GO TO 507
          IENT=1
507       DO 305 I=1,ISPEC
          WRITE(1,306)
306       FORMAT(" TAG OF SPEC.  FOR DEPTH SCALE(PRESS CR IF END)")
          READ(2,309)SCA
309       FORMAT(A5)
          IF(SCA EQ 5H     )GO TO 330
          CALL DSCAL(IENT,SCA,XSTEP,MIN)
305       IENT=1
C NOW OUTLINE PLOT
330       CALL PLOT(5,-85,-100)
          CALL PLOT(4,-85,750)
          CALL PLOT(4,1015,750)
          CALL PLOT(4,1015,-100)
          CALL PLOT(4,-85,-100)
C FINISHED
          CALL PLOT(5,1200,0)
          RETURN
          END
```

```
C         SCALE
          SUBROUTINE SCALE(INCH,XMULT,MIN,MAX,INX)
C ROUTINE TO SET AXIS SCALING FOR PLOTTER
C INCH=NO  OF INCHES ALONG AXIS
C XMULT=SCALE MULTIPLE PER 5TH OF AN INCH
C MIN=MIN AXIS VALUE - WILL BE RETURNED AS MOST CONVENIENT MIN FOR SCALE
C MAX=MAX AXIS VALUE - AGAIN MAY BE CHANGED ON RETURN
C INX=SCALE UNITS PER INCH OF PLOT AXIS
C
          IDIFF=MAX-MIN
          XX=IDIFF/(INCH*XMULT)
          DO 10 I=1,10
          I=I-1
          X1=XX*10 **I
          IF(X1 LE 10)GO TO 15
10        CONTINUE
15        IX1=X1
          IF((X1-IX1) GE  5)IX1=IX1+1
          INX=IX1*XMULT*10 **I
          IY=0
          IF((MIN/(1 *INX))-MIN/INX) GT  5)IY=1
          MIN=(MIN/INX+IY)*INX
          MAX=MIN+INX*INCH
          RETURN
          END
```

```
C         AXIS
          SUBROUTINE AXIS(IAXIS,NXY,NP,INT,MIN,INX)
C ROUTINE TO PLOT AXES AND LABEL THEM
C IAXIS=1 IF X-AXIS
C       =2 IF Y AXIS
C NXY=AXIS START POINT
C NVAL=ARRAY CONTAINING PEN POSITION FOR EACH AXIS MARKER
C         WE'VE USED AN ARRAY FOR THIS IN CASE OF A NON-LINEAR SCALE
C NP=NO  OF MARKERS TO BE PLOTTED
C INT=NO OF MARKERS BETWEEN LABELS
C MIN=LABEL ON FIRST MARKER
C INX=LABEL STEP
C
          COMMON IARRAY(260,5),EOUT(101,2),NVAL(50)
C SET CHARACTER SIZE AT 2
          CALL CONTRO(3,0,2,0)
          IWR=MIN
          DO 10 I=1,NP
          IF(IAXIS EQ 1)CALL PLOT(5,NVAL(I),NXY)
          IF(IAXIS.EQ 2)CALL PLOT(5,NXY,NVAL(I))
          J=(I/INT)*INT+1
          IF(I.EQ J)GO TO 14
          IF(IAXIS.EQ 1)CALL PLOT(4,NVAL(I),NXY-5)
          IF(IAXIS.EQ 2)CALL PLOT(4,NXY-5,NVAL(I))
```

```
          GO TO 10
14        IF(IAXIS EQ 1)CALL PLOT(4,NVAL(I),N,Y-10)
          IF(IAXIS EQ 2)GO TO 20
          DO 22 I=1,5
          NUMB=INR*10**I
          IF(NUMB EQ 0)GO TO 25
22        CONTINUE
25        J1=6*(12-I)
          CALL CONTRO(I,3,NVAL(I)-J1,N.Y-25)
          WRITE(3,100)INR
100       FORMAT(1X,I6)
          GO TO 9
20        CALL PLOT(4,N.Y-10,NVAL(I))
          CALL CONTRO(I,3,N.Y-80,NVAL(I)-6)
          WRITE(3,100)INR
9         INR=INR+INC
10        CONTINUE
C NOW DRAW AXIS
          IF(IAXIS EQ 1)GO TO 30
          CALL PLOT(5,N.Y,NVAL(NP))
          CALL PLOT(4,N.Y,NVAL(1))
          RETURN
30        CALL PLOT(5,NVAL(NP),N.Y)
          CALL PLOT(4,NVAL(1),N.Y)
          RETURN
          END




C         DSCAL
          SUBROUTINE DSCAL(IENT,SCA,NSTEP,MIN)
C ROUTINE TO CALCULATE AND PLOT DEPTH SCALES
C IENT=0 IF FIRST ENTRY,1 OTHERWISE
C E1=SURFACE ENERGY OF HEAVIEST ELEMENT IN SUBSTRATE
C SLOPE,YINT=EQUATION FOR ENERGY-CHANNEL CONVERSION
C SCA=TAG ON SPECTRUM FOR WHICH THE DEPTH SCALE IS PLOTTED
C MIN=CHANNEL OFFSET
C
          COMMON IARRAY(260,5),EOUT(101,2),NVAL(50)
          COMMON ASCAL(5),TITLE(5,8),COUNT(5)
          COMMON ISPEC,ITIME,IENG,IDEPTH,SURF,E1,SLOPE,YINT
          COMMON P(6),NEL,XM(2,2),ATDEN,ANAME(2)
          WRITE(1,10)SCA
10        FORMAT(" TILT ANGLE(DEGREES) OF SPECTRUM ",A5)
          READ(2,)TILT
45        WRITE(1,11)
11        FORMAT(" MAX  DEPTH WANTED IN A(UP TO 10,000A) ")
          READ(2,)ID
          IF(ID LE 10000)GO TO 46
          WRITE(1,47)
47        FORMAT(" I SAID NOT GREATER THAN 10,000A (!)")
          GO TO 45
46        ID=ID/100+1
```

```
      WRITE(1,10)
10    FORMAT(' INPUT STOPPING POWER MULTIPLICATION FACTOR ')
      READ(2,*)ALIGN
      CALL HESP(IENT,ALIGN,TILT,ID)
      DO 20 I=1,NEL
      WRITE(1,25)(ANAME(I)
25    FORMAT(' Y LOCATION IN INCHES OF SCALE FOR ',A5,A2)
      READ(2,*)YN,Y
      NCHY=(YN-Y)*100
      NCH1=(EOUT(1,I)-ELOSS(EOUT(1,I)))-YINT)/SLOPE)*STEP
      J=2
30    NCH2=(EOUT(J,I)-ELOSS(EOUT(J,I)))-YINT)/SLOPE)*STEP
      IF((NCH1-NCH2).GE.10)GO TO 20
      J=J+1
      GO TO 30
20    J=J-1
      ID2=ID
      DO 50 NN=1,ID
      IF(EOUT(NN,I).NE.0)GO TO 50
      ID2=NN-1
      GO TO 51
50    CONTINUE
51    ID1=(ID2-1)*J+1
      DO 40 K=1,ID1
      KK=J+(K-1)+1
      EE=EOUT(KK,I)-ELOSS(EOUT(KK,I))
40    NVAL(K)=(EE-YINT)/SLOPE-MIN)*STEP
      CALL AXIS(1,NCHY,ID1,10.0,1.+1000)
      K=NVAL(1)+10
      IF(NVAL(1).GT.800)K=NVAL(ID1)-200
      CALL CONTRO(3,2,K,NCHY-6)
      WRITE(3,60)(ANAME(I)
60    FORMAT(1X,'DEPTH',A5,A2)
20    CONTINUE
      RETURN
      END
```

```
C       HESP
        SUBROUTINE HESP(IENT,ALIGN,TILT,ID)
C THIS ROUTINE CONVERTS 100A STEPS TO BACKSCATTERED HE ENERGY
C IENT=0 IF FIRST ENTRY,1 IF NOT
C E1=SURFACE ENERGY OF HEAVIEST ELEMENT IN SUBSTRATE
C ALIGN=MULTIPLICATION FACTOR ON RANDOM STOPPING POWER
C       E G    8 FOR ALIGNED
C TILT =TILT ANGLE(IN DEGREES)
C EOUT=MATRIX HOLDING BACKSCATTERED ENERGIES FOR 100A DEPTH STEPS
C       CAN HOLD UP TO 2 DATA SETS FOR UP TO 2 SUBSTRATE ELEMENTS
C ANAME=ALPHA MATRIX HOLDING NAMES OF ELEMENTS IN SUBSTRATE
C ID=TOTAL NO  OF 100A STEPS TO GO(MAX=100)
C NEL=NO OF ELEMENTS IN SUBSTRATE
        DIMENSION FILE(2),PTEMP(6),MM(2),EIN(101),M(2)
```

```
      COMMON IARRAY(260,5),EOUT(101,2),NVAL(50)
      COMMON RECAL(5),TITLE(5,8),COUNT(5)
      COMMON ISPEC,ITIME,IENG,IDEPTH,SURF,E1,SLOPE,YINT
      COMMON P(6),NEL,XM(2,2),ATDEN,ANAME(2)
      DATA FILE/'SHCOEFF','4H SRC'/
      IF(IENT EQ 1)GO TO 202
C SET UP STOPPING POWER COEFF  (ACCORDING TO BRAGG ADDITIVITY LAW)
      WRITE(1,100)
100   FORMAT(" NO  OF ELEMENTS COMPRISING SUBSTRATE (MAX 2)")
      READ(2,)NEL
      WRITE(1,120)
120   FORMAT(" DO YOU KNOW THE SUBSTRATE MOLECULAR DENSITY? (0 OR 1)")
      READ(2,)IATOM
      IF(IATOM EQ 0)GO TO 110
      WRITE(1,121)
121   FORMAT(" MOLECULAR DENSITY OF SUBSTRATE(10**22 ATOMS/CM**3) ")
      READ(2,)ATDEN
      GO TO 115
110   WRITE(1,101)
101   FORMAT(" DENSITY OF SUBSTRATE(G/CM**3) ")
      READ(2,)DEN
115   DO 5 I=1,NEL
      WRITE(1,102)I
102   FORMAT(" ATOMIC NUMBER AND MASS OF M(",I1,")")
5     READ(2,)XM(I,1),XM(I,2)
      IF(NEL EQ 1)GO TO 10
15    WRITE(1,103)
103   FORMAT(" RATIO OF M(1) M(2)?  (E G  1,2)")
      READ(2,)MM(1),MM(2)
      ATWT=XM(1,2)*MM(1)+XM(2,2)*MM(2)
      GO TO 25
10    MM(1)=1
      ATWT=XM(1,2)
25    IF(IATOM EQ 0)ATDEN=6.022*DEN/ATWT
C READ IN PROPER COEFFICIENTS FROM DISK FILE COEFF SRC
501   CALL FSTAT(5,FILE,L)
      IF(L NE 0)GO TO 30
      WRITE(1,105)
105   FORMAT(" FILE COEFF SRC MUST BE PUT ON DISK")
      STOP
30    DO 27 I=1,6
27    P(I)=0
      DO 35 I=1,NEL
      CALL SEEK(5,FILE)
      MX=XM(I,1)-1
      DO 40 J=1,MX
40    READ(5,)
      READ(5,106,ERR=98,END=99)ANAME(I),(PTEMP(K),K=1,6)
106   FORMAT(A5,2X,6E10.3)
      DO 35 K=1,6
35    P(K)=P(K)+PTEMP(K)*MM(I)
C NOW LET'S CALCULATE THE DEPTH-ENERGY-IN MATRIX FOR 100A DEPTH STEPS
C FIRST DETERMINE K**2 FOR EACH ELEMENT OF SUBSTRATE
202   B=1.953
      C=3.494
      DO 45 I=1,NEL
```

```
45      PI(I)=(SORT(TM(I,2)**2+B**2-C**2)/(4.0D0*TM(I,2)**2
        BIG=PI(1)
        DO 122 I=2,NEL
        IF(PI(I).LE.BIG)GO TO 122
        BIG=PI(I)
122     CONTINUE
        E0=E1.BIG
        E=E0
        SUM=0
        CI=ALIGN*ATOEN.10.**COS(TILT*.01745)
        DO 50 I=1,ID
        DE=SP(P,E)*CI
        EIN(I)=E0-SUM
        SUM=SUM+DE
50      E=E-DE
C NOW CALCULATE ENERGY OUT AT EACH 100A DEPTH STEP
        CI=ATOEN.*2.**COS(TILT*.01745)
        DO 70 L=1,NEL
        DO 70 I=1,ID
        II=I-1
        EE=EIN(I)*PI(L)
        E=EE
        SUM=0
        DO 60 J=1,II
        DE=SP(P,E)*CI
        SUM=SUM+DE
60      E=E-DE
        EOUT(I,L)=EE-SUM
        IF(EOUT(I,L).LT.400.)GO TO 80
70      CONTINUE
        GO TO 85
80      EOUT(I,L)=0
85      RETURN
C ERROR IN READ STATEMENTS
98      WRITE(1,110)J
110     FORMAT(" READ ERROR WHEN READING COEFFICIENTS LINE ",I)
        PAUSE
        GO TO 501
99      WRITE(1,111)
111     FORMAT(" END OF COEFF FILE REACHED BEFORE PROPER VALUES FOUND")
        PAUSE
        STOP
        END
```

```
C          ESCAL
           SUBROUTINE ESCAL(SLOPE,YINT)
C ROUTINE TO DETERMINE ENERGY-CHANNEL EQUATION
C
           DIMENSION A(15,2)
1          WRITE(1,10)
10         FORMAT(" WE NEED A SURFACE ENERGY OF PULSER CALIBRATION")
           WRITE(1,11)
11         FORMAT(" RESPOND 0 FOR FORMER,1 FOR LATTER")
           READ(2,)ICHO
           IF(ICHO EQ 1)GO TO 40
21         WRITE(1,12)
12         FORMAT(" HOW MANY SURFACE ENERGIES DO YOU KNOW?")
           READ(2,)N
           WRITE(1,13)N
13         FORMAT(" INPUT",I2," CHANNEL-ENERGY(KEV) PAIRS,END WITH CR")
           DO 14 I=1,N
14         READ(2,)A(I,1),A(I,2)
           DO 17 I=1,N
17         A(I,2)=A(I,2)-CLOSS(A(I,2))
           WRITE(1,15)
15         FORMAT(" DO YOU KNOW THE CHANNEL INTERCEPT?0 OR 1")
           READ(2,)IC
           IF(IC.EQ.0)GO TO 20
           N=N+1
           A(N,2)=0
           WRITE(1,16)
16         FORMAT(" WHAT IS IT?")
           READ(2,)A(N,1)
20         IF(N GT 1)GO TO 50
           WRITE(1,21)
21         FORMAT(" WHOOPS-WE NEED MORE THAN ONE POINT-TRY AGAIN!")
           GO TO 21
40         WRITE(1,41)
41         FORMAT(" HOW MANY PULSER VALUES DO YOU HAVE(MIN=2,MAX=5)")
           READ(2,)N
           WRITE(1,13)N
           DO 43 I=1,N
43         READ(2,)A(I,1),A(I,2)
50         WRITE(1,55)
55         FORMAT(" O K ?0 OR 1")
           READ(2,)I
           IF(I.EQ.0)GO TO 1
           CALL LINREG(A(1,1),N,SLOPE,YINT)
           RETURN
           END



C          LINREG
C SUBROUTINE TO DETERMINE ENERGY-CHANNEL RELATION
C
           SUBROUTINE LINREG(A(1,1),N,A,B)
```

```
C  A=SLOPE
C  B=Y-INTERCEPT
          DIMENSION A(IS,1,1)
          S=0.
          SY=0
          SXY=0
          SX=0
          SYY=0
          DO 10 I=1,N
          SX=SX+A(IS,I,1)
          SY=SY+A(IS,I,2)
          SXY=SXY+A(IS,I,1)*A(IS,I,2)
          SXX=SXX+(A(IS,I,1)**2
10        SYY=SYY+(A(IS,I,2)**2
          A=(N*SXY-SX*SY)/(N*SXX-SX**2)
          B=(SY-A*SX)/N
          RETURN
          END



C         ELOSS
          FUNCTION ELOSS(E)
C FUNCTION ROUTINE TO CALCULATE DETECTOR ENERGY LOSSES
C
          ELOSS=E-.006*E**.5
          RETURN
          END



C         SP
C FUNCTION ROUTINE FOR CALCULATING STOPPING POWERS
C
         *FUNCTION SP(P,E)
          DIMENSION P(1)
          SP=P(1)+P(2)*E+P(3)*E**2+P(4)*E**3+P(5)*E**4+P(6)*E**5
          RETURN
          END
```

TABLE OF STOPPING POWERS FROM ZIEGLER AND CHU FOR HE
VALID FOR ENERGIES 400 KEV AND 2 MEV
FOLLOWING ARE THE FIRST SIX COEFFICIENTS FOR THE SEMI-EMPIRICAL
POWER SERIES IN E

H	1.060E1	1.662E-2	-2.433E-5	1.196E-8	-2.575E-12	2.054E-16
HE	9.852E0	2.754E-2	-3.072E-5	1.326E-8	-2.818E-12	1.962E-16
LI	2.059E1	8.638E-3	-1.225E-5	5.697E-9	-1.077E-12	7.722E-17
BE	2.609E1	7.082E-3	-1.327E-5	5.857E-9	-1.137E-12	8.396E-17
B	2.608E1	2.934E-2	-5.808E-5	1.719E-8	-3.507E-12	2.709E-16
C	1.595E1	6.905E-2	-7.659E-5	3.379E-8	-6.859E-12	5.291E-16
N	3.101E1	6.400E-2	-7.697E-5	3.476E-8	-7.127E-12	5.523E-16
O	2.590E1	7.330E-2	-8.050E-5	3.517E-8	-7.100E-12	5.462E-16
F	2.113E1	7.024E-2	-6.908E-5	2.829E-8	-5.455E-12	4.052E-16
NE	1.952E1	7.425E-2	-7.210E-5	2.956E-8	-5.694E-12	4.207E-16
NA	3.329E1	3.227E-2	-2.979E-5	1.088E-8	-1.918E-12	1.339E-16
MG	4.742E1	1.715E-2	-4.569E-5	2.013E-8	-4.078E-12	3.154E-16
AL	5.594E1	6.773E-4	-4.752E-6	1.401E-10	2.662E-11	-4.046E-17
SI	5.797E1	5.659E-2	-7.766E-5	3.641E-8	-7.624E-12	5.995E-16
P	4.729E1	7.415E-2	-8.848E-5	4.009E-8	-8.329E-12	6.570E-16
S	3.329E1	1.156E-1	-1.265E-4	5.627E-8	-1.161E-11	9.120E-16
CL	5.734E1	1.140E-1	-1.467E-4	6.963E-8	-1.483E-11	1.183E-15
AR	4.823E1	1.507E-1	-1.866E-4	8.828E-8	-1.881E-11	1.502E-15
K	4.869E1	1.351E-1	-1.454E-4	6.175E-8	-1.208E-11	9.000E-16
CA	6.825E1	9.992E-2	-1.145E-4	4.860E-8	-9.422E-12	6.956E-16
SC	6.901E1	9.547E-2	-1.080E-4	4.570E-8	-8.889E-12	6.607E-16
TI	6.401E1	1.098E-1	-1.255E-4	5.567E-8	-1.137E-11	8.827E-16
V	6.245E1	9.597E-2	-1.083E-4	4.818E-8	-9.853E-12	7.664E-16
CR	5.064E1	1.108E-1	-1.156E-4	4.910E-8	-9.690E-12	7.290E-16
MN	4.919E1	1.084E-1	-1.142E-4	4.940E-8	-9.962E-12	7.562E-16
FE	4.436E1	1.375E-1	-1.421E-4	6.102E-8	-1.201E-11	9.011E-16
CO	4.004E1	1.201E-1	-1.176E-4	4.842E-8	-9.240E-12	6.905E-16
NI	4.159E1	9.779E-2	-9.119E-5	3.732E-8	-7.482E-12	5.893E-16
CU	4.072E1	7.399E-2	-5.666E-5	1.806E-8	-2.656E-12	1.452E-16
ZN	4.560E1	7.190E-2	-6.375E-5	2.368E-8	-4.188E-12	2.886E-16
GA	5.687E1	6.524E-2	-6.322E-5	2.441E-8	-4.429E-12	3.112E-16
GE	5.871E1	7.352E-2	-7.513E-5	3.036E-8	-5.739E-12	4.182E-16
AS	5.716E1	9.444E-2	-9.778E-5	4.073E-8	-7.931E-12	5.938E-16
SE	5.666E1	1.071E-1	-1.178E-4	5.199E-8	-1.064E-11	8.308E-16
BR	6.173E1	1.402E-1	-1.655E-4	7.600E-8	-1.588E-11	1.250E-15
KR	6.545E1	1.537E-1	-1.840E-4	8.561E-8	-1.808E-11	1.437E-15
RB	5.069E1	1.898E-1	-2.082E-4	9.313E-8	-1.922E-11	1.506E-15
SR	6.859E1	1.645E-1	-1.860E-4	8.293E-8	-1.698E-11	1.320E-15
Y	5.626E1	2.201E-1	-2.543E-4	1.191E-7	-2.556E-11	2.068E-15
ZR	6.691E1	1.963E-1	-2.188E-4	9.794E-8	-2.022E-11	1.585E-15
NB	7.185E1	1.881E-1	-2.112E-4	9.492E-8	-1.966E-11	1.546E-15
MO	6.136E1	1.930E-1	-2.102E-4	9.362E-8	-1.933E-11	1.518E-15
TC	6.292E1	2.104E-1	-2.286E-4	1.007E-7	-2.049E-11	1.586E-15
RU	4.661E1	2.220E-1	-2.300E-4	9.979E-8	-2.018E-11	1.557E-15
RH	4.318E1	2.218E-1	-2.285E-4	9.953E-8	-2.025E-11	1.572E-15
PD	1.357E1	2.852E-1	-2.874E-4	1.249E-7	-2.524E-11	1.939E-15
AG	2.660E1	2.289E-1	-2.198E-4	9.050E-8	-1.735E-11	1.261E-15
CD	4.600E1	1.866E-1	-1.803E-4	7.386E-8	-1.416E-11	1.037E-15
IN	7.623E1	9.667E-2	-7.842E-5	2.350E-8	-2.830E-12	8.811E-17
SN	7.020E1	1.442E-1	-1.458E-4	6.037E-8	-1.163E-11	8.555E-16
SB	9.118E1	1.021E-1	-1.137E-4	5.029E-8	-1.036E-11	8.144E-16
TE	9.456E1	1.119E-1	-1.303E-4	5.901E-8	-1.201E-11	9.746E-16

I	8	762E1	1	998E-1	-2	436E-4	1	142E-7	-2	412E-11	1 909E-15
XE	1	081E2	1	581E-1	-1	982E-4	9	319E-8	-1	975E-11	1 571E-15
CS	7	748E1	2	100E-1	-2	310E-4	1	035E-7	-2	142E-11	1 685E-15
BA	9	441E1	1	909E-1	-2	181E-4	9	676E-8	-1	994E-11	1 559E-15
LA	8	909E1	2	270E-1	-2	567E-4	1	156E-7	-2	291E-11	1 874E-15
CE	8	921E1	1	889E-1	-2	876E-4	9	131E-8	-1	857E-11	1 427E-15
PR	8	730E1	1	859E-1	-2	017E-4	8	798E-8	-1	787E-11	1 368E-15
ND	8	598E1	1	814E-1	-1	958E-4	8	451E-8	-1	700E-11	1 307E-15
PM	8	465E1	1	774E-1	-1	888E-4	8	133E-8	-1	629E-11	1 248E-15
SM	8	362E1	1	736E-1	-1	843E-4	7	917E-8	-1	591E-11	1 221E-15
EU	8	262E1	1	693E-1	-1	784E-4	7	648E-8	-1	529E-11	1 171E-15
GD	8	269E1	1	716E-1	-1	807E-4	7	722E-8	-1	539E-11	1 176E-15
TB	8	002E1	1	609E-1	-1	674E-4	7	116E-8	-1	415E-11	1 080E-15
DY	6	025E1	1	943E-1	-1	926E-4	8	111E-8	-1	610E-11	1 229E-15
HO	6	297E1	1	678E-1	-1	636E-4	6	757E-8	-1	522E-11	1 000E-15
ER	6	251E1	1	638E-1	-1	590E-4	6	548E-8	-1	378E-11	9 652E-16
TM	6	199E1	1	606E-1	-1	559E-4	6	411E-8	-1	259E-11	9 533E-16
YB	5	154E1	1	573E-1	-1	622E-4	6	267E-8	-1	226E-11	9 276E-16
LU	6	413E1	1	597E-1	-1	555E-4	6	500E-8	-1	280E-11	9 748E-15
HF	6	511E1	1	676E-1	-1	640E-4	6	888E-1	-1	341E-11	1 021E-15
TA	5	879E1	1	771E-1	-1	724E-4	7	169E-8	-1	411E-11	1 071E-15
W	6	169E1	1	565E-1	-1	509E-4	6	245E-8	-1	213E-11	9 421E-16
RE	6	795E1	1	752E-1	-1	716E-4	7	158E-8	-1	416E-11	1 082E-15
OS	6	424E1	1	810E-1	-1	749E-4	7	258E-8	-1	434E-11	1 096E-15
IR	6	099E1	1	851E-1	-1	764E-4	7	277E-8	-1	433E-11	1 094E-15
PT	4	978E1	1	906E-1	-1	811E-4	7	250E-8	-1	438E-11	1 005E-15
AU	5	709E1	1	932E-1	-1	854E-4	7	798E-8	-1	559E-11	1 194E-15
HG	5	320E1	1	840E-1	-1	708E-4	7	002E-8	-1	382E-11	1 058E-15
TL	6	732E1	1	702E-1	-1	633E-4	6	801E-8	-1	353E-11	1 041E-15
PB	7	964E1	1	777E-1	-1	763E-4	7	469E-8	-1	501E-11	1 160E-15
BI	7	846E1	1	776E-1	-1	806E-4	7	775E-8	-1	578E-11	1 229E-15
PO	7	675E1	1	061E-1	-2	024E-4	8	829E-8	-1	809E-11	1 418E-15
AT	7	031E1	2	251E-1	-2	329E-4	1	023E-7	-2	102E-11	1 658E-15
RN	6	148E1	2	569E-1	-2	648E-4	1	168E-7	-2	412E-11	1 902E-15
FR	8	269E1	2	412E-1	-2	578E-4	1	146E-7	-2	371E-11	1 868E-15
RA	8	873E1	2	264E-1	-2	481E-4	1	107E-7	-2	288E-11	1 800E-15
AC	9	814E1	2	394E-1	-2	608E-4	1	158E-7	-2	383E-11	1 859E-15
TH	9	529E1	2	539E-1	-2	735E-4	1	207E-7	-2	473E-11	1 931E-15
PA	9	187E1	2	397E-1	-2	527E-4	1	101E-7	-2	236E-11	1 796E-15
U	8	972E1	2	367E-1	-2	459E-4	1	061E-7	-2	139E-11	1 651E-15

A.3 PHA11 - Data Acquisition Routine

```
MULTI-CHANNEL ANALYZER (PHA11) --- ENABLES USE OF THE
      PDP11/05 AS A MULTICHANNEL ANALYZER WITH A 4096 CHANNEL
      BUFFER THAT MAY BE SUBDIVIDED IN INTO A MAXIMUM OF 16 GROUPS
      OF FROM 64 TO 4096 CHANNELS,EACH   I/O AND ADC OPERATIONS ARE
      ACCOMPLISHED VIA THE TELETYPE KEYBOARD WITH ONE CHARACTER COM-
      MANDS AND MAY BE CARRIED ON SIMULTANEOUSLY. THAT IS, THE ADC
      CAN BE DIRECTED TO ACCUMULATE A SPECTRUM IN ONE GROUP
      WHILE THE TELEPRINTER IS OUTPUTTING ANOTHER SPECTRUM OR
      PORTION THEREOF WHICH IS CURRENTLY ON DISPLAY
            -- R S WALKER & S  W  POEHLMAN  OCT 24, 1976
LOADING INTO CORE          . R PHA11 <CR>
                             ------------

      IF THE LOAD IS SUCCESSFUL THE TELEPRINTER WILL RESPOND WITH
            PHA11-PGM VSN  NUMBER
            GROUP WIDTH
      AT THIS JUNCTURE SET THE GROUP WIDTH, SAY 256 CHANNELS
      BY TYPING              256 <CR>
                             ---------

      AFTER WHICH IS PRINTED
            MAXIMUM NUMBER OF GROUPS IS 00016
            CLEAR SPECTRA BUFFER?(YES=Y):
      IF ALL POSSIBLE GROUPS ARE TO BE ZEROED THEN TYPE
                                          Y <CR>
                                          ------

      ANY OTHER CHARACTER WILL BE ASSUMED AS A
      NEGATIVE RESPONSE  THIS LATTER CASE, WHEN SPECTRAL BUFFERS
      ARE NOT CLEARED, ALLOWS A RESTART OR RELOAD OF THE PROGRAM
      WHERE SPECTRA ARE RECLAIMED UNDISTURBED.
      NOTE1:  THIS IS TRUE ONLY WHEN NO INTERVENING PROGRAM
              HAS BEEN RUN BY THE MONITOR
      AFTER THE CLEAR BUFFER RESPONSE HAS BEEN SELECTED, THE
      PROGRAM RESPONDS WITH THE GREATER THAN SIGN, WHICH
      SIGNIFIES THAT ANY ONE OR TWO CHARACTER VALID COMMAND
      WILL BE ACCEPTED.  THESE ARE OUTLINED BELOW.
OPERATING PROCEDURES:
      ALL COMMANDS MUST BE PROCEEDED BY THE ESCAPE KEY WHICH
      IS ECHOED ON THE TELEPRINTER AS $. - ANY OTHER TELETYPE
      CHARACTERS FROM THE KEY BOARD ARE IGNORED BUT ECHOED
      SO AS TO ALLOW USER LOGGING OF COMMENTS ON THE TELEPRINTER.
      NOTE THAT THESE COMMENTS WILL BE ECHOED BY PHA11 WITH BELL
      AFTER MORE THAN 80 CHARACTERS ARE INPUT ON THE TELETYPE
      KEYBOARD -- THIS IS EXCLUSIVE OF ANY COMPUTER
      GENERATED OUTPUT ON THE TELEPRINTER WHICH MAY INCLUDE
      CR/LF.  WHEN THIS OCCURS ANY COMMANDS, EVEN IF PREFIXED
      WITH THE ESCAPE KEY (ESC) WILL BE IGNORED.  THEREFORE,
      IF NO COMMANDS ARE BEING EXECUTED, USE,
       ^U TO DELETE THE LINE AND RETYPE WITH
      <CR> BEFORE 80 CHARACTERS.
      THE CHARATER TYPED AFTER THE ESC KEY IS A COMMAND LETTER
      WHOSE FUNCTION IS OUTLINED BELOW.
      IN MOST CASES THE THIRD CHARACTER WILL BE A NUMBER
      WHICH INFORMS THE COMPUTER ON WHICH GROUP THE SPECIFIED
      ACTION IS TO TAKE PLACE
      EG.  TO PRINT THE CONTENTS OF GROUP 0 ON THE TELEPRINTER
      TYPE:                $P0 <CR>
                           ---------

      NOTE THAT THE 16 GROUPS ARE LABELLED FROM 0 TO 15 AND
```

FOR DISPLAY PURPOSES CAN BE VIEWED SIMPLY BY LIFTING THE APPROPRIATE TOGGLE ON THE SWR OF THE PDP11-05 FRONT PANEL. OVERLAP DISPLAYS CAN BE SELECTED BY HAVING MORE THAN ONE TOGGLE IN THE UP POSITION.

1 RESTART PROCEDURE.

AFTER THE GREATER THAN SIGN IS PRESENT, THE PROGRAM CAN BE RESTARTED AT ANY TIME BY TYPING.

$G <CR>.

THE INITIAL DIALOGUE WILL BE REPEATED SO THAT EITHER BUFFER CLEAR OR DIFFERENT GROUP WIDTHS CAN BE SELECTED. THIS COMMAND IS IGNORED IF THE ? APPEARS AFTER THE <CR>. THIS ERROR CONDITION EXISTS IF THE ADC IS ON. TO REMEDY THE PROBLEM TURN OFF THE ADC AND REPEAT THE COMMAND.

2 START AND STOP ACCUMULATION AS DESIRED BY THE ADC CONTROL COMMANDS.

3 OUTPUT THE SPECTRUM DISPLAYED WITH PRINT COMMAND. IF THE PUNCH IS TO BE USED, TURN OFF THE DISPLAY MODE AND ENABLE PUNCH IMMEDIATELY AFTER <CR>. IF THE HARDWARE DISPLAY MODE, AS SELECTED ON THE PDP11 POLL SWR'S MODULE, IS ON, THEN NO BLANK LEADER OR TRAILER WILL BE OUTPUT. NOTE THAT ANY BLANK LEADER PAPER TAPE CAN BE GENERATED DURING THE ABOVE PAUSE BY SETTING THE TELETYPE TO LOCAL MODE AND DEPRESSING THE HERE IS KEY THREE OR FOUR TIMES WITH THE PUNCH ON. RETURN THE TELETYPE TO LINE MODE AND RESUME NORMAL COMPUTER OPERATIONS. FOR PERMANENT STORAGE OF SPECTRA USE THE WRITE ON FLOPPY DISC COMMAND <W>. AT A LATER TIME THE SPECTRA CAN BE TRANSFERRED TO THE PDP-15 FOR DATA ANALYSIS VIA THE PROGRAM PIP15 AND THE HIGH SPEED LINK.

4. PROGRAM ABORT PROCEDURE.

^C
--
^C
--

NORMAL EXIT COMMAND:

$X <CR>
----

5. ERROR CONDITIONS:

THESE ARE NOTED WHEN ? APPEARS ON THE TTY OUTPUT AND INDICATE THAT THE PREVIOUS COMMAND WAS ILLEGAL OR THAT ILLEGAL CONDITIONS EXIST FOR IT TO TAKE PLACE. SPECIFICALLY IF THE LETTER AFTER THE $ IS NOT AN ASSIGNED COMMAND THEN THE ? IS PRINTED. FOR ALL COMMANDS REQUIRING A GROUP NUMBER N, THE ? WILL BE OUTPUT IF N EXCEEDS THE MAXIMUM NUMBER OF GROUPS WHOSE VALUE IS OUTPUT DURING THE INITIAL DIALOGUE. OTHER ERROR CONDITIONS ARE A FUNCTION OF THE COMMAND GIVEN AND ARE EXPLAINED IN THE COMMAND SUMMARY BELOW.

6. COMMAND SUMMARY:

<A> ADC

> $AN <CR> -- STARTS THE ADC, ANALYZING IN GROUP N

IF THE ADC IS ALREADY ON -- USE #S TO TURN IT OFF FIRST

#S <CR> -- STOPS THE ADC

(B) DISPLAY

THE DISPLAY COMMANDS ARE IMPLEMENTED IN PHA11 AT BOTH THE SOFTWARE AND HARDWARE LEVELS. THE HARDWARE OPTIONS ARE SELECTED BY THE LABELLED SWITCHES OF THE PDP11 POLL SWR'S SINGLE WIDTH NIM MODULE LOCATED ABOVE THE DISPLAY SCOPE. OPTING FOR THE DISPLAY MODE ON YIELDS TWO VERTICAL MARKER LINES VISIBLE AT THE ENDS OF THE SPECTRUM THEIR POSITIONS MAY BE SET BY THE LOWER SWITCHES AS INDICATED BY THE FUNCTION LABELS. THE SOFTWARE COMMANDS ARE LISTED BELOW

< #EN <CR> -- ZEROES GROUP N SPECTRUM AND ITS ASSOCIATED TITLE (SEE T COMMAND).

< #D <CR> -- THE PROGRAM NOW DISPLAYS ONLY THOSE CHANNELS BETWEEN THE MARKERS. TO EXPAND THE SCALE, DECREASE THE RANGE SWITCH BELOW THE DISPLAY TO LESS THAN THE GROUP WIDTH. WHILE IN THE DISPLAY MODE, THE PRINT COMMAND OUTPUTS CHANNEL CONTENTS IN THIS RANGE ONLY, AND USE OF THE MARKERS MOTION SWITCHES WILL MOVE THE SPECTRUM THROUGH THIS WINDOW. THE MODE CAN BE TERMINATED BY TURNING OFF THE DISPLAY MARKER MODE SWITCH ON THE PDP11 POLL SWR'S MODULE.

> #M <CR> -- PRINTS OUT THE CURRENT CHANNELS NUMBERS OF THE MARKERS REGARDLESS OF THE DISPLAY MODE

(C) I/O

> #TN<CR> -- PHA11 NOW ENTERS THE TEXT MODE WHERE ALL FOLLOWING CHARACTERS (UP TO 80) ARE STORED INTO A TITLE BUFFER ASSOCIATED WITH GROUP N. ALL RUBOUT AND LINE DELETE COMMANDS ARE OPERATIONAL UNTIL TERMINATION OF THE TITLE MODE VIA ESC CR.

EG. #T0 <CR>
THIS IS A TEST <CR>
$ <CR>

> $PN<CR> -- NORMALLY PRINTS OUT THE FULL CONTENTS
--------- OF GROUP N IN THE FORMAT
TITLE (OF NO GREATER THAN 80 CHARACTERS)
CHANNEL NUMBER AND 10 CHANNEL CONTENTS PER LINE
IF THE DISPLAY MODE IS OPERATIONAL THEN ONLY
THE CONTENTS OF THE CHANNELS BETWEEN THE MARKERS
IS OUTPUT TO ABORT PRINTOUT, PRESS
<CR> WHEREUPON THE PROGRAM WILL COMPLETE
ONLY THE CURRENT LINE IN THE OUTPUT BUFFER

> $WN <CR>

INPUT FILE NAME (MAX. 6 CHAR'S)
(EG.) RSW01<CR> -- WILL WRITE ON THE USER FLOPPY DISK (DX1)
---------- THE CONTENTS OF GROUP N WITH THE FILE NAME
GIVEN. IN THIS CASE IT IS RSW01 IT IS
STORED ON DX1 AS RSW01 DAT AND FOR 256
CHANNEL SPECTRA REQUIRES 4 BLOCKS OF STORAGE

> $PN <CR>

INPUT FILE NAME (MAX 6 CHAR'S)
(EG.) SWP01<CR> -- READS INTO GROUP N OF THE ANALYZER THE
---------- SPECTRUM SWP01.DAT FROM DX1 IF THERE IS
NO SUCH FILE, THE SYSTEM PRINTS THE
APPROPRIATE MESSAGE.

(D) SPECIAL MODES OF OPERATION

(1)RATIOMETER:
-- THE "O" COMMAND, ON FIRST ISSUE, TURNS
ON THE RATIOMETER IN THE FOLLOWING MANNER:
THE NUMBER TO BE INPUT FIRST IS THE PRESET
BEAM CURRENT VALUE TO WHICH THE COMPUTER
WILL COUNT WHILE ACCEPTING ALL PULSES THAT
OCCUR IN A SPECTRAL WINDOW TO BE SET UP NEXT.
UPON REACHING THE PRESET, THE CONTENTS
OF THE WINDOW ARE OPTIONALLY SCALED AND THEN
SENT TO THE RATIOMETER.

> $O INPUT DIGITIZER SAMPLE FREQUENCY: 100<CR> (E G.)
--- -------
SET RATIOMETER WINDOW AND PRESS <CR>

> -- AFTER THE COMMAND INPUT DATA IS GIVEN
THE RATIOMETER MAY BE PEAKED FOR OPERATION
BY THE P.B SET PUSH BUTTONS, LOCATED
BELOW THE CPU ON THE MEIR SPECTROMETER
PANEL NEAR THE LOWER RIGHT HAND CORNER.
PRESSING P.B. 2. WILL MULTIPLY THE
INTEGRATED WINDOW CONTENTS BY 2, WHILE
P.B. 1 WILL PERFORM A DIVISION BY 2.

> $O <CR> -- ON SECOND ISSUE, THE "O" COMMAND
------- WILL TURN OFF THE SPECIAL RATIOMETER
MODE.

(2) WINDOW

> #M <CR> -- PRINTS OUT THE CURRENT LOCATIONS OF THE MARKERS REGARDLESS OF THE DISPLAY MODE

-- UP TO 8 WINDOWS (0-7) MAY BE SET UP ON ANY SPECTRUM AND ANY WINDOWS SO OPERATIONAL WILL HAVE THEIR INTEGRATED COUNTS PRINTED WHENEVER THE TIMER/SCALER (T/S) GATE CHANGES FROM ON TO OFF STATES AT THIS TIME THE DIGITIZER CONTENTS ARE OUTPUT AND WINDOWS ON IN THE CASE BELOW. IF SET OR NONE IF THE ADC IS OFF IN THE FORMAT 0000000 N 0000000 O 0000000 ETC

> #MN<CR> -- WILL PRINT THE CURRENT MARKER CHANNEL POSITIONS FOR WINDOW N IF IT IS OPERATIONAL IF THE WINDOW IS NOT SET THEN THIS IS NOTED.

> #MNS<CR> -- WILL SET THE CURRENT MARKER LOCATIONS AS THE LIMITS FOR WINDOW N THIS OCCURS REGARDLESS OF DISPLAY MODE

> #MNE<CR> -- ERASES THE LIMITS SELECTED FOR WINDOW N.

> #MNM<CR> -- MOVE MARKERS TO THE LIMITS FOR WINDOW N. IF NO WINDOW HAS BEEN SET THE APPROPRIATE MESSAGE IS OUTPUT.

```
          TITLE PHA11 MAC  VSN 21-SEP-76
          PROGRAM FOR PULSE HEIGHT ANALYSIS
          BY SWP & RSW   SEPT.'76

          PS=177776
          SWR=177570
          TPB=177566
          TPS=177564
          TKB=177562
          TKS=177560
          MTREG=164026
          AUXREG=164024
          SCLR=164022
          MPCSR=164020
          ADC2=164014
          ADC1=164012
          ADCSR=164010
          MREG=164006
          YREG=164004
          XREG=164002
          DSPSR=164000
          KYBPRI=5
          PTRPRI=4
          ADCPRI=7
          SLRPRI=5
          GTRPPI=6
          ERRWRD=52

          MEMORY ALLOCATIONS

          .MCALL ..V2.., REGDEF, EXIT., INTEN., SYNCH, TTOUTR
          .MCALL .TTYIN, TTINR, TTYOUT, PRINT, EXIT
          .MCALL .CSIGEN, WRITW, READW, CLOSE
          ..V2..
          .REGDEF
          K2=643                    ; ADCSR ROB MASK
          BUFLEN=20000              ; MAX. LENGTH OF THE DATA BUFFER
          K4=174000                 ; MRCSR ROB MASK
          BUFSA=15000               ; SET BUFFER FOR DATA IN MEMEORY
          BUFEND=BUFSA+BUFLEN       ; END ADDR FOR DATA BUFFER


          INTERRUPT VECTORS
          .ASECT

          .=130             ; ADC
L0:       ADCX              ; LD VTR ADDR FOR ADC
L2:       340               ; LEVEL 6
          .=150             ; SCALE AND INTEGRATERR
M0:       SCALE             ;LD VTR ADDR FOR SCALER
M2:       340               ; LEVEL 5
M4:       INTEG             ; LD VTR ADDR FOR INTEGRATER
M6:       340               ; LEVEL 7

          .CSECT

          START OF MAIN-LINE ROUTINE
```

```
START:  BIC #40,@#MPCSR          ; CLEAR RESET
        BIS #42000,@#MPCSR       ; ENABLE INTEGRATOR INTERRUPT
        MOV #BUFSA,ADCSA         ; INIT ADC S.A
        BIS #100,@#44            ; SET C SO DONT WAIT FOR TT INP
; ROUTINE TO INPUT GRP WIDTH AND SET UP GRPS
        .PRINT  #MSG1            ; PRINT THE TITLE
RSTRT:  .PRINT  #MSG2            ; PRINT GP WIDTH
        JSR  PC,INPT1            ; INPUT GP WIDTH
        MOV  R3,GPWDTH           ; STORE IT
        MOV  R4,DSPLEN           ; STOR # BYTES
        INIT MARKER POSITIONS
        CLR LTMRK                ; ZERO LEFT MARKER
        MOV GPWDTH,RTMRK         ; RIGHT MRK=GRP WIDTH
        DEC RTMRK                ; -1
;       CALC # GPS
        MOV  DSPLEN,R2           ; R2 = # BYTES
        CLR  R4                  ; NO
CONT5:  CMP  #BUFLEN,R2
        BMI  CONT6               ; BEYOND BUF
        INC  R4                  ; SO R4 = GP # MAX
        ADD  DSPLEN,R2           ; CHECK MORE
        BR  CONT5                ; TILL BEYOND BUF
CONT6:  CMP R4,#20               ;GRP #>16?
        BMI GOOD                 ;NO SO O.K.
        MOV #20,R4               ;YES SO SET TO 16
GOOD:   MOV  R4,GRPNUM           ; STOR GP #MAX
        MOV  #1,WRFLG            ; INIT FLG TO PRNT ONLY
        MOV #1,GTEFLG            ; INIT TS-GATE FLG HI
        .PRINT #MSG4             ; PNT MAX GP #
        JSR  PC,PRNTDC           ; OUTPUT THE #
;
;       CLEAR SPECTRA BUFFER AND TITLE BUFFER IF REQ'D
;
        .PRINT #MSG5             ; ASK IF CLEAR WANTED
        .TTYIN                   ; GET RESPONSE
        CMPB #'Y,R0              ; IS RESPONSE "Y"?
        BNE REDO                 ; NO SO EXIT
        MOV #BUFSA,R1            ; POINT TO BUFFERS.A
CLRSPC: CLR (R1)+                ; CLR BUFFER
        CMP R1,#BUFEND           ; END OF BUFFER?
        BNE CLRSPC               ; NO SO CLR MORE
        MOV #TITSA,R1            ; POINT TO TITLE BUFFER
CLRTLE: CLR (R1)+                ; CLR BUFFER
        CMP R1,#IOTMP            ; END OF BUFFER?
        BNE CLRTLE               ; NO SO CLR MORE
; COMMAND RE-ENTRY POINT
REDO:   .PRINT #MSG0             ;PNT ">"
        CLR ERFLG                ;AND CLEAR ERROR FLG
;
;       GO TO BKGD TILL CHAR STRING INPUT
JPBKGD: JSR PC,BKGDI             ;BKGD.BRANCH
;
        CMPB R1,#33              ;IS CHAR ESC?
        BNE JPBKGD               ;NO SO CONTINU BKGD
;
;       ANALYZE INPUT COMND
```

```
RSTRT2   JSR  PC,KBIN          ; INPUT COMND
         MOV #TTBUF+1,TEMP1    ,POINT TO DIGITS
         SUB  #1,DCTR          ,DCTR HAS # DIGITS
         CMP #0,DCTR           ,#DIGITS 0?
         BNE  CONT4            ,NO SO CONT
         CLR P4
         DEC P4
         MOV  P4,GRCOM         , YES SO GRCOM=-1
         BR  CONT3             , JMP OUT OF ANALYSIS
CONT4:   CMPB #'M,TTBUF        , IN MARKER COMMAND MODE?
         BNE CONT44            ; NO SO BRANCH
         MOV #1,DCTR           ; YES SO SET DIGIT CTR TO 1
CONT44:  JSR  PC,INBIN         , CNVT TO BIN #
         CMP  #0,ERFLG         ; LEGAL #?
         BEQ  CONT2            ; YES SO CONT
RSTRT4:   PRINT #MSGG          , NO SO ?
         BR  REDO              ; RESTART
CONT2:   CMPB #'M,TTBUF        , IN MARKER COMMAND?
         BNE CONT22            ; NO SO NORMAL # CHECK
         CMP #7,BINMB          ; COMPARE MARKER # TO 7
         BMI RSTRT4            ; > SO ERROR
         BR CONT23             , JMP OVER NORMAL # CHECK
CONT22:  MOV GRPNUM,R4         ; DEC # GRPS BY 1
         DEC P4
         CMP  P4,BINMB         ; # TOO BIG?
         BMI  RSTRT4           ; YES SO RESTART
CONT23:  MOV  BINMB,GRCOM                ; STOR GP CMND
; SEARCH TABLE FOR WHERE TO BRANCH FOR COMMAND
CONT3:   MOV #JTBLE,JPTR                 ; SET JP TBL PTR
         MOV  #CTBLE,R4        ; R4 PTS TO VALID CMND
         MOV  #14,R5           ; SET UP CTR
LOOP10:  CMPB  TTBUF,(R4)+     ; VALID CMND LETTER
         BNE  NOGO             ; NO SO GET NOTHR
         JMP  @JPTR            ; YES SO TO TBLE JMP
NOGO:    DEC  R5               ; DEC CTR
         BEQ  RSTRT4           ; INVALID CHAR SO EXIT
         ADD  #4,JPTR          ; INC JPTR FOR JP TBL
         BR  LOOP10            ; NO SO CHECK MORE
;
CTBLE:   .ASCII /ASEPTWRGDOM:/
         EVEN
JPTR:    .WORD  0              ; JMP TBLE PTR
JTBLE:   JMP  ADCST            ; ADC START
         JMP  STOP             ; STOP THE ADC
         JMP  ERASE            ; ERASE SPECTRUM
         JMP  PRNT             ; PRINT SPECTRUM
         JMP  TITLE            ; INPUT TITLE
         JMP  WRITE            ; WRITE ON DISK
         JMP  READ             ; READ FROM DISK 1
         JMP  GAIN             ; RESET GRWDTH
         JMP  DSPMRK           ; DISPLAY BETWEEN MARKERS ONLY
         JMP  RATIO            ; RATIOMETER MODE OF OP.
         JMP MARKR             ; MARKER WINDOW SET ROUTINE
         JMP DUMP              ; PROGRAM EXIT
         JMP  RSTRT4           ; ILLEGAL CMND EXIT
;
```

```
GPWDTH:  .WORD  0          ; GP WDTH (CHANNELS)
DSPLEN:  .WORD  0,0        ; DISPLAY LENGTH (BYTES)
GRPNUM:  .WORD  0          ; MAX # OF GPS
GRCOM:   .WORD  0          ; COMMAND LETTER EXTRACTED
SISTN:   .WORD  20         ; # BITS PER WORD
MRKR:    .WORD  0          ; MRKR STORAGE SPACE
DSPLSA:  .WORD  0          ; DSPLAY S A
XSTART:  WORD 0                    ; DISP  N-CHANNEL START
;
;        SUBROUTINE TO CHECK TOGGLES FOR DSP GP
;
DSPLY:   JSR PC,RSAVE
         JSR PC,DEVPLL             ; POLL DEV
         JSR PC,POLL               ; POLL SWP'S
         MOV  GRPNUM,R5            ; R5 = MAX#GPS
         MOV  @#SWR,R4             ; R4 HAS TOGGLE POSN
UP:      ROR  R4,                  ; SET BIT ?
         BCC  DOWN                 ; NO SO GET ANTHEER
         JSR  PC,DISP              ; YES SO DSP GP
DOWN:    ADD  DSPLEN,DSPLSA        ; MOV UP 1 GP
         DEC  R5                   ; DEC GRP CTR DONE?
         BNE  UP                   ; NO GET ANOTHER TOG
         JSR PC,RESTOR
         RTS  PC                   ; NORMAL EXIT
;
;        WILL CONTINUE FOR CHAR STRING INP TILL CR
BKGDI:   .TTINR
         MOV R0,R1                 ;MOVE CHAR TO R1
         BCC OUTBKG                ;RETURN IF CR
         JSR PC,DSPLY              ;DISPLAY ROUTINE
         BR BKGDI                  ;AND CHECK FOR CR
OUTBKG:  RTS PC                    ; RETURN
;
;        SUBROUTINE TO OUTPUT A CHAR DURING BKGD PGM
;        # IN R1 AND USES R0
;
BKGDO:   TST  WRFLG                ; IS IN WR MODE?
         BNE  PRNT1                ;NO SO PRINT
         MOVB R1,@IOTMP            ;PUT CHAR IN WR BUF
         INC  IOTMP                ; UPDAT PTR
         CMP  IOTMP,#IOEND         ; BUFFER FULL?
         BNE  DOWN1                ; NO SO GET NOTHER
         .WRITW #AREA,#0,#IOBUF,#400,BLOCK      ; WR BLK DATA ON DSK
         BCS  WTERR                ; BR IF WRITE ERROR OCCURED
         INC  BLOCK                ; INC BLK CTR
         MOV  #IOBUF,IOTMP         ; RESTOR BUF PTR
         MOV  #IOBUF,R1            ; SET UP TO CLR BUFFR
CLRLP:   CLR  (R1)+                ; CLR BUFFER
         CMP  R1,#IOEND            ; DONE?
         BMI  CLRLP                ; NO SO CLR
         BR   DOWN1                ; AND EXIT
PRNT1:   MOV  R1,R0                ; PRNT CHAR ROUTINE
         .TTOUTR
         BCC DOWN1                 ;BUFF READY FOR CHAR?
         MOV GTEFLG,GTETMP         ; STORE GATE FLAG
         MOV #1,GTEFLG             ; SET GATE FLG SO TS GATE IGNORED
         JSR PC,DSPLY              ;NO SO DISPLAY
```

```
            MOV GTETMP,GTEFLG       ; RESTORE GATE FLAG
            BR PRNT1                ;AND RECHECK BUFF
DONN1:      RTS  PC
GTETMP:     .WORD 0                 ; GATE FLAG TEMP STORE

; WRITE ERROR ROUTINE
WTERR:      PRINT #MSGT             ;PRINT ERROR MESSAGE
            JMP PEDO                ; GO TO BACKGROUND

;       SUBROUTINE TO SAVE REGS R1 TO R5
;
RSAVE:      MOV #STPTR,R0           ;R0 HAS STACK POITER
            MOV R1,(R0)+
            MOV R2,(R0)+
            MOV R3,(R0)+
            MOV R4,(R0)+
            MOV R5,(R0)+
            RTS  PC

;       SUBROUTINE TO RESTORE CONTENTS OF REGS
;
RESTOR:     MOV #STPTR,R0
            MOV (R0)+,R1
            MOV (R0)+,R2
            MOV (R0)+,R3
            MOV (R0)+,R4
            MOV (R0)+,R5
            RTS  PC
STPTR:      .WORD 0,0,0,0,0
;;          SUBR TO DISPLAY FROM DSPLSA FOR A LENGTH
;             OF DSPLEN IN DATA BUFFER (ADDR UNITS)
;
DISP:       MOV XSTART,@#XREG       ; SET XREG TO START
            MOV  DSPLSA,R3          ; R3 HAS DAT BUF S.A.
LOOP7:      MOV  (R3)+,@#YREG       ; LOAD YREG WITH DATA
            MOV #1,@#DSPSR          ; INTENSITY LO DATA
            INC  @#XREG             ; NEXT CHANNEL
            CMP  @#XREG,R2          ; LAST PT?
            BNE  LOOP7              ; NO SO RECYCLE
            MOV  @#MREG,R1          ; YES SO DSP MRKRS
            BIC  #K4,R1             ; CLR BITS OF VOID ADDR
            MOV  R1,@#XREG          ; LOAD XREG WITH CHAN#
            ASL  R1                 ; EVEN ADDR ONLY
            ADD  DSPLSA,R1          ; CALC DATA ADDR
            MOV  (R1),@#YREG        ; LOAD Y REG
            MOV  #3,@#DSPSR         ; INTENSITY HI ON MRKRS
            RTS  PC                 ; NORMAL EXIT
;
;       ROUTINE TO POLL T/S GATE AND INT BUFF ERASE
;       WILL PRINT WINDOW CONTENTS ON T/S GATE IN
;
DEVPLL:     BIT #4,@#DSPSR          ; T/S GATE IN
            BEQ GATE                ; YES SO SERVICE
            CLR GTEFLG              ; NO SO CLR FLG
            BR DEVOUT               ; AND EXIT
GATE:       TST GTEFLG              ; IS GATE FLG SET?
            BNE DEVOUT              ; YES SO EXIT
```

```
          JSR PC,TSGATE          ; NO SO SERVICE
DEVOUT    BIT #40,@#MRCSR        ;       ERASE T/S?
          BEQ EPAOUT             ; NO SO EXIT
          CLR INTLO              ; CLEAR LO ORDER INTEG SUM
          CLR INTHI              ; AND HIGH ORDER SUM
          JSR PC,WINSUM          ; UPDATE WINDOW SUMS
          BIC #40,@#MRCSR        ;       RESET RESET
EPAOUT    RTS PC                 ; RETURN
GTEFLG    WORD 0                 ; GATE FLG
;
;         ROUTINE TO PRINT T/S VALUE AND WINDOWS
;
TSGATE:   MOV #1,WRFLG           ; INIT FLG FOR PRINT ONLY
          .TTYOUT #15            ; OUTPUT CR/LF
          .TTYOUT #12
          MOV INTLO,R4           ; R4 HAS T/S VALUE
          MOV INTHI,R5           ; R5 HAS HI ORDER
          JSR PC,PRNTDP          ; DOUBLE PREC. PRINT IT
          BIT #104,@#ADCSR       ; ADC ON?
          BEQ TSEXIT             ; NO SO EXIT
          BR TSG1                ;       BRANCH OVER ERASE ENTRY
TSERAS:   CLR WRFLG              ; ERASE ENTRY.CLR WRFLG
TSG1:     MOV #30,TSCTR          ; YES SO SET CTR
          MOV #WINBUF,R3         ; R3 PNTS TO WINDOW ADDR  BUFF S A
          MOV #WINTMP,R4         ; R4 PNTS TO TMP STORAGE BUFFER
TRANS:    MOV (R3)+,(R4)+        ;       MOVE ADDR  TO TMP STORAGE
          DEC TSCTR              ;       FINISHED?
          BNE TRANS              ; NO SO LOOP
          JSR PC,WINSUM          ; SET UP WINDOW SUMS
          MOV #WINBUF,R1         ; R1 IS SUM PNTR AGAIN
          MOV #WINTMP,R2         ; R2 PNTS TO TMP STORE AGAIN
          MOV #60,WINNUM         ; SET WINDOW #
          MOV #10,TSCTR          ; RESET CTR
          MOV #MRKBUF,MRKLOC     ; SET PTR TO MIDDW ADDR  BUFF
          ADD #2,MRKLOC          ; PNT TO FIRST END ADDR
TSTST:    TST @MRKLOC            ; IS IT ZERO?
          BNE SCAN               ; NO SO OUTPUT WINDOW
          ADD #4,R1              ; YES SO INC PTRS
          ADD #4,R2
          BR NOSCAN              ; AND BRANCH
SCAN:     MOV (R1)+,R4           ; STORE LOW ORDER SUM
          MOV (R1)+,R5           ; AND HI ORDER
          SUB (R2)+,R4           ; SUB LO ORDER SUMS
          SBC R5                 ; WATCH CARRY
          SUB (R2)+,R5           ; SUB HI ORDER SUMS
          TST WRFLG              ; WHICH MODE?
          BNE TSG2               ; WRITE SO BRANCH
          COM R4                 ; ERASE SO NEG LO ORDER SUM
          COM R5          ; AND HI ORDER
          ADD #1,R4              ; TWO'S COMPLEMENT
          ADC R5
          MOV R5,-(R1)           ; STORE HI ORDER
          MOV R4,-(R1)           ; AND LO ORDER
          ADD #4,R1              ; RESET PTR
          BR NOSCAN              ; AND BRANCH
TSG2:     .TTYOUT WINNUM         ; PRINT WINDOW #
          .TTYOUT #':            ; AND ":"
```

```
            MOV P1,TSTMP1           ; TMP STORE P1
            MOV R2,TSTMP2           ; AND R2
            JSR PC,PRNTDP           ; DOUBLE PREC PRINT
            MOV TSTMP1,P1           ; RESTORE R1
            MOV TSTMP2,R2           ; AND R2
NOSCAN      ADD #4,MPNLOC           ; UPDATE ADDR PTR
            INC WINNUM              ; AND WINDOW #
            DEC TSCTR               ; FINISHED?
            BNE TSTST               ; NO SO LOOP
TSEXIT      .TTYOUT #15             ; OUTPUT CR,LF
            .TTYOUT #12
            INC GTEFLG              ; INC GATE FLAG
            RTS PC          ; RETURN
WINTMP:     .BLKW 20                ; TMP SUM STORAGE
TSCTR:      .WORD 0                 ; CTR
MPNLOC:     .WORD 0                 ; WINDOW ADDR PTR
WINNUM:     .WORD 0                 ; WINDOW ASCII #
TSTMP1:     .WORD 0                 ; TMP STORE
TSTMP2:     .WORD 0                 ; TMP STORE
;
;           ROUTINE TO SUM WINDOWS
;
WINSUM:     MOV #10,WINCNT          ; SET WINDOW CTR
            MOV #MPNBUF,P1          ; P1 PNTS TO WINDOW ADDR BUFF
            MOV #WINBUF,R2          ; R2 PNTS TO WINDOW SUM BUFF
WIND:       MOV (P1)+,R4            ; R4 HAS WINDOW S A
            MOV (R1)+,R5            ; R5 HAS END ADDR
            TST R5                  ; IS END ADDR ,ZERO?
            BEQ SUMEND              ; YES SO DON'T ADD
            ADD ADDSA,R4            ; ADD OFFSET
            ADD ADDSA,R5
            CLR (R3)+               ; CLEAR SUM STORE
            CLR (R3)                ; DOUBLE PRECISION
            SUB #2,R3               ; PNT TO START OF SUM STORE
WINADD:     CMP R5,R4               ; FINISHED SUM?
            BMI SUMEND              ; YES SO BRANCH
            ADD (R4)+,(R3)+                 ; ADD LO ORDER WORDS
            ADC (R3)                ; AND WATCH OVERFLOW
            SUB #2,R3               ; POINT TO START OF SUM STORE
            BR WINADD               ; ADD MORE
SUMEND:     ADD #4,R3               ; PNT TO NEXT SUM LOC
            DEC WINCNT              ; FINISHED?
            BNE WIND                ; NO SO LOOP
            RTS PC                  ; RETURN
WINBUF:     .BLKW 20                ; SUM SORAGE
WINCNT:     .WORD 0                         ; CTR
;
;
;
;           SUBROUTINE TO POLL THE DEVICES
;
POLL:       TST DSPFLG              ; IN EXPAND DISP MODE?
            BNE NOSA                ; YES SO S.A 'S ALREADY INIT
            MOV #BUFSA,DSPLSA               ; INIT DISP S.A.
            CLR XSTART              ; READY X-CHANNEL START
            MOV GPWDTH,R2           ; INIT DISP END ADDR.
            BR PLLSET
```

```
NOSH    MOV DSPTMP,DSPLSH           ; SET DISP S A  FOR EXP MODE
        MOV LTMPR,XSTART            ; SET X START CHANNEL
        MOV PTMPR,R2                ; SET X END CHANNEL
        INC R2
PLLSET  BIT #200,@#DSPSR            ; DISPLAY MODE ON?
        BEQ PLOUT                   ; NO SO EXIT
        MOV LTMPR,@#XREG            ; SET XREG TO LEFT MPR POS
        CLR R5                      ; CLR SWEEP CTR
SWP1    MOV #40,R1                  ; READY DOT POS
        MOV #1,R3                   ; AND DOT INC
        MOV #12,R4                  ; AND DOT CTR
SWEEP   MOV R1,@#YREG               ; MOVE DOT POS TO YREG
        MOV #1,@#DSPSR              ; AND INTENSITY HI
        ASL R1                      ; DOUBLE DOT POS
        SUB R3,R1                   ; AND SUB DOT INC
        ADD #1,R3                   ; INC DOT INC
        DEC R4                      ; FINISHED SWEEP?
        BNE SWEEP                   ; NO SO CONT SWEEP
        TST R5                      ; LEFT AND RIGHT SWEEP DONE
        BNE POLE1                   ; YES SO EXIT FROM SWEEP
        INC R5                      ; INC SWEEP CTR
        MOV PTMPR,@#XREG            ; MOVE RIGHT MRK POS TO XREG
        BR SWP1                     ; AND SWEEP AGAIN
POLE1   DEC MPRCTR                  ; UPDATE ONLY EVERY 10 SWEEPS
        BNE POLE1                   ; NO SO EXIT
        TST DSPFLG                  ; IN EXPAND MODE?
        BNE DSPEXP                  ; YES SO BRANCH
        JSR PC,MRKPOS               ; NO SO UPDATE MARKER POS
        MOV #12,MPRCTR              ; RESET SWEEP CTR
        BR POLE1                    ; AND EXIT
DSPEXP  JSR PC,EXPAND               ; EXPAND DISPLAY
        MOV #12,MPRCTR              ; RESET SWEEP CTR
        BR POLE1
PLOUT   CLR DSPFLG                  ; NOT IN DISP MODE SO CLR FLG
POLE1   RTS PC                      ; RETURN

LTMPR:  WORD 0                      ; LEFT MARKER POSITION
PTMPR   WORD 0                      ; RIGHT MARKER POSITION
DSPFLG  WORD 0                      ; DISPLAY MODE FLAG
MPRCTR  WORD 12                     ; SWEEP CTR

;       SUBR TO UPDATE MARKER POSITIONS

MRKPOS  BIT #40,@#DSPSR             ; LEFT MOTION?
        BEQ TSTPT                   ; NO SO TST FOR RIGHT MOTION
        BIT #100,@#DSPSR            ; LT MOT-WHICH MARKER?
        BEQ LTMLT                   ; LEFT
        DEC PTMPR                   ; RIGHT SO MOVE 1 LEFT
        CMP LTMPR,RTMPR             ; MARKER OVERLAP?
        BNE TSTPT                   ; NO SO OK
        INC PTMPR                   ; YES SO RESTORE
        BR TSTPT
LTMLT   TST LTMPR                   ; LEFT MPR AT ZERO?
        BEQ  TSTRT                  ; YES SO DON'T MOVE
        DEC LTMPR                   ; NO SO MOVE 1 LEFT
TSTPT   BIT #10,@#DSPSR             ; RIGHT MOTION?
        BEQ NOMOT                   ; NO SO EXIT
```

```
        BIT #100,@#DSPSR        ; YES SO WHICH MARKER
        BEQ LTMPT               ; LEFT
        INC RTMP1               ; RIGHT SO MOVE 1 RIGHT
        CMP GRWDTH,RTMP1        ; BEYOND BUFFER?
        BNE NOMOT               ; NO SO OK
        DEC RTMP1               ; YES SO RESTORE
        BR NOMOT
LTMPT   INC LTMP1               ; MOVE LEFT MKR 1 RIGHT
        CMP LTMP1,RTMP1         ; MKRS OVERLAP?
        BNE NOMOT               ; NO SO OK
        DEC LTMP1               ; YES SO RESTORE
NOMOT   RTS PC          ; RETURN
;
;       ROUTINE TO DISPLAY ONLY BETWEEN MARKERS
;
EXPAND  BIT #10,@#DSPSR                 ; MOVE DISPLAY LEFT?
        BEQ TSTRT1              ;NO SO TST RIGHT
        CMP DSPTMP,#BUFSA       ; YES SO AT START OF BUFFER
        BEQ TSTRT1              ; YES SO DO NOTHING
        DEC DSPTMP              ; NO SO DEC S A BY 1
        DEC DSPTMP
TSTRT1  BIT #40,@#DSPSR                 ; MOVE DISPLAY RIGHT?
        BEQ EXEND               ; NO SO EXIT
        MOV DSPTMP,R1           ; POINT TO DISP S A
        SUB  #BUFSA,R1          ; SUBR BUF S A
        ASR R1                  ; PUT IN #WRDS
        ADD RTMP1,R1            ; PNT TO END OF DISP
        SUB LTMP1,R1            ; R1 IS PTR
        INC R1
        CMP R1,GRWDTH   ; BEYOND BUFFER?
        BEQ EXEND               ; YES SO EXIT
        INC DSPTMP              ; NO SO MOVE S A  1 WORD
        INC DSPTMP
EXEND   RTS PC
;
;
;       SUBR TO INPUT GR WIDTH
;
INPT1   CLR  ERFLG              ;RESET ERR FLAG
        JSR  PC,INBIN           ; INPUT THE CHAR STRING
        MOV #TTBUF,TEMP1        ;TEMP1 HAS BUFF S A
        JSR PC,INBIN            ; CONV TO #
        CMP  #0,ERFLG           ; LEGAL #
        BEQ  CONT1              ; YES SO CNTUE
RSTRT1   RPRINT #MSGG           ; NO SO "?"
        BR  INPT1               ; RESTART
CONT1   CLR  R1                         ; IS # MULTPL OF 2
        MOV SISTN,R2            ; R2 HAS 16 BITS
        MOV BINNB,R4            ;R4 HAS #
        MOV R4,R3               ;SO DOES R3
RSTRT2  ASL  R3                 ; LEFT SFT #
        BCC  HERE               ; CARRY?
        INC R1                  ;YES SO CNT IT
HERE    DEC  R2                         ; DEC CTR & DONE?
        BNE  RSTRT2             ; NO SO CHECK NOTHR
        CMP  R1,#1              ; PWR OF 2?
        BNE  RSTRT1     ; NO SO REINPT#
```

```
        MOV   R4,PC                 ; YES SO R3=#CHANGE
        ASL   R4                            ; R4 = # BYTES
        CMP   #BUFLEN,R4                    ; BEYOND BUFFR
        BMI   RSTRT1                ; YES SO REINPT #
        RTS   PC                    ; NORMAL RETURN

;       CMND STRING INPUT ROUTINE

;
INBIN   CLR   DCTR                  ; CLR DIGIT CTR
        MOV   #TTBUF,R1             ; SET PTR TO BUFFER
LOOP1    TTYIN  ,R1)+               ; INPT CHAR
        INC   @CTR                  ; BUMPP CTR
        CMPB   #12,R0               ; LAST CHAR ?
        BNE   LOOP1                 ; NO SO GET ANOTHER
        SUB   #2,DCTR               ; SUB CR,LF #
        RTS   PC                    ; RETURN NORMALLY

;       SUBR TO CNVRT ASCII CHARS TO BIN NUMBER

;
INBIN   MOV DCTR,R2                 ; R2 = # DIGITS
        CMP   #5,R2                 ; TOOO BIG?
        BMI   ERR1                  ; YES SO "?"
        MOV   #BUFPTR,TMPTR         ; SET UP TMP PTR
        CMP   #0,R2                         ; TOO SMALL?
        BEQ   ERR1                  ; YES SO "?"
        MOV TEMP1,R1                ; R1 PTS TO BUFFR
LOOP2   CLR R4
        MOVB   (R1)+,R4             ; GET #
        SUB   #60,R4                ; # FROM ASCII
        BMI ERR1
        CMP #11,R4
        BMI ERR1                    ;VALID # ? NO SO ERROR
        MOVB  R4,(R1)+              ;STORE ASCII AS #
        DEC   TMPTR                 ; DEC TMP PTR
        DEC   TMPTR                 ;  2'S FOR ADDR
        DEC   R2                            ; FINI?
        BNE   LOOP2                 ;NO SO GET MORE
        CLR   BINNB                 ; PREP # LOC
        MOV TEMP1,R1        ; YES SO CONVERT
LOOP5   CLR R3
        MOVB (R1)+,R3               ; GET DIGIT
        INC   R2                            ;BUMP CTR
        CLR R4                      ;READY COEFF CTR
LOOP4   DEC R3                      ;DEC PWR CTR
        BMI LOOP6                   ;FINI?
        ADD @TMPTR,R4               ;NO,ADD NTHER 10PWR
        BR LOOP4                    ;AND GO AGAIN
LOOP6   INC TMPTR                   ;YES SO SCALE 10 PTR
        INC TMPTR                   ;2'S FOR ADDR
        ADD R4,BINNB                ;ADD TO PREV #
        CMP R2,DCTR                 ;GOT ALL DIGITS?
        BEQ QUIT                    ;YES SO EXIT
        BR LOOP5                    ;CNVRT NEXT DIGIT
ERR1    INC   ERFLG                 ; ERROR SO NOTE IT
QUIT    RTS   PC                            ; EXIT

TEMP1    WORD  0            ; TEMP STOR
```

```
TEMP1     WORD  0          ; TEMP STOR TOO
TEMP2     WORD  0
LOPTR     WORD  0                              ; PTR TO LO ORDER 16 BNR #
HIPTR     WORD  0                              ; PTR TO HI ORDER 16 BNR #
TNPHI     WORD  17,1,0,0,0,0,0                 ; HI ORDER 16 BNR #
TNPLO     WORD  41100,10240,23420,17500,144,12,1  ;SCALE FACTS
BUFPTR    WORD  0,0                            ;BUFF PTR
TTBUF     BLKW  50              ; TTY INPUT BUFFER
BINNB     WORD  0               ; CONVRTD BIN NUMB
ADDSW     WORD  0               ; ADD = M
TNPTR     WORD  0                              ;PTR TO TN PTR
DCTR      WORD  0               ; DIGIT CTR
ERFLG     WORD  0               ; ERROR FLAG ON INPUT
```

```
;       SUBR TO OUTPUT DOUBLE PREC  OR SINGLE PREC  # IN ASCII DEC

;DOUBLE PREC  ENTRY-7 DIGIT OUTPUT
PRNTDP  MOV #7,DCTR             ; SET DIGIT CTR TO 7
        MOV #TNPLO,LOPTR        ; PNT TO LO 10 PWR =
        MOV #TNPHI,HIPTR        ; AND HI 10 PWR =
        BR OPENT                ; AND BRANCH
;SINGLE PREC  ENTRY-5 DIGITS
PRNTSC  MOV #5,DCTR             ; SET DIGIT CTR TO 5
        MOV #TNPLO+4,LOPTR      ; PNT TO SINGLE PREC  LO 10 PWR =
        MOV #TNPHI+4,HIPTR      ; AND HI 10 PWR =
        CLR R5                  ; CLEAR HI ORDER WORD
OPENT   CLR R1                  ; READY UNIT CTR
LOOPC   SUB @LOPTR,R4           ; SUB LO ORDER
        SBC R5                  ; WATCH CARRY
        SUB @HIPTR,R5   ; SUB HI ORDER
        BMI FOUND               ; BRANCH IF MINUS
        INC R1                  ; INC UNIT CTR
        BR LOOPC                ; AND LOOP
FOUND   ADD #60,R1              ; CNVT TO ASCII
        JSR PC,BIGDO            ; AND OUTPUT
        ADD @LOPTR,R4           ; RESTORE LO ORDER
        ADC R5                  ; WATCH CARRY
        ADD @HIPTR,R5           ; RESTORE HI ORDER
        ADD #2,LOPTR            ; PNT TO NEXT LO ORDER IN PWR
        ADD #2,HIPTR            ; AND HI ORDER IN PWR
        DEC DCTR                ; FINISHED?
        BNE OPENT               ; NO SO DO ANOTHER DIGIT
        MOV #  ,R1              ; YES SO PRINT SPACE
        JSR  PC,BIGDO           ; NOW
        RTS PC          ; YES SO EXIT

;       SUBROUTINE TO OUTPUT A LINE OF SPECTRUM PRINT OUT
;       ADDRESS IN R2,CHANN # IN INDEX, END ADDR IN STADDR

PRNTLN  TST  WRFLG              ; WRIT ON DSK?
        BEQ  OVER1              ; YES SO IGNOR KYBD
        .TTINR                  ; CHAR ON KYBD?
        BCC  FINIS              ; YES SO ABORT
OVER1   MOV  INDEX,R4           ;R4 HAS CHAN #
        JSR  PC,PRNTDC          ; PRNT IT OUT
        MOVB  #' ,R1            ; PRNT OUT SPACE
        JSR  PC,BIGDO           ; DO IT
        MOV  #12,CHNCNT                 ; SET UP CTR 10CHAN/LN
LOOP20  MOV  (R2)+,R4           ; PICK CHANN CONTNTS
        JSR  PC,PRNTDC          ; PNT IT OUT
        CMP  R2,STADDR          ; FINISHED SPECTRUM?
        BNE LOOP50              ; NO SO CONTINUE
FINIS.  CLR STADDR              ; YES SO CLR FINISH FLAG
        BR LOOP60               ; AND OUTPUT CR/LF AND EXIT
LOOP50  DEC  CHNCNT                     ; FINISHED LINE?
        BNE  LOOP20             ; NO SO DO MOR
LOOP60  MOVB  #15,R1            ; YES SO CR/LF
        JSR  PC,BIGDO
        MOVB  #12,R1
        JSR  PC,BIGDO
        RTS  PC                         ; FLG FINISH
```

```
CHNCNT    WORD 0
;
;         SUBROUTINE TO PRINT OUT PL FRAMES OF PRF TAP
;
LOP       MOV  #0,P1              ; PUT IN HALF NULL
LOP15     JSR  PC,@#GDD           ; PRINT IT
          DEC  P1                 ; DONE
          BNE  LOP15              ; NO SO MORE
          RTS  PC                 ; YES SO EXIT
;
INDEX     .WORD  0          ; CHAN # FOR PNT CMND
STRDOP    .WORD  0          ; END ADDR FOR PNT CMND
;
;
;         COMMAND SERVICE ROUTINES
;
;         ADC START ROUTINE
;
ADCST     CMP GRCOM,#0      ;CHECK GRP COMM
          BMI  ERR3               ; YES SO ERROR
          BIT  #104,@#ADCSR       ; CHECK IF ADC ON
          BNE  ERR2               ; GET BUFFER LENGTH
          JSR PC,FETCH            ;GET ADC S R
          MOV P4,ADCSR            ;AND STORE IT
          JSR PC,WINSUM           ; STORE WINDOWS
          BIS  #104,@#ADCSR       ; OF SO ADC ON
          JMP  FINI               ; FINISHED SO !
;
;         SECTION TO STOP THE ADC
;
STOP      CMP #0,GRCOM            ;CHECK GRP COMM
          BMI ERR2                ;NOT -1 SO ERROR
          BIT  #104,@#ADCSR       ; YES SO ADC ON ?
          BEQ  ERR2               ; YES SO ERROR
          BIC  #104,@#ADCSR       ; NO SO TURN OFF
          JMP  FINI               ; FINISHED SO.
;
;         GRP ERASE ROUTINE
;         WILL ERASE CORRESPONDING TITLE BUFFER AS WELL
;
ERASE     CMP  GRCOM,#0           ; PICK UP GP #
          BMI  ERR2               ; IS -1 SO ERROR
          BIT #104,@#ADCSR        ; ADC ON?
          BEQ NORMAL              ; NO SO BRANCH
          JSR PC,FETCH            ; GET ERASE GROUP S R
          CMP ADCSA,P4            ; CMP TO ADC S R
          BNE NORMAL              ; NOT = SO BRANCH
          JSR PC,TSERAS           ; YES SO UPDATE WINDOWS
NORMAL    JSR  PC,FETCH           ; P4 NOW HAS DSPLSA
          MOV  DSPLEN,R2          ; GET DSP LENGHT
          ADD  R4,R2              ; R2 HAS END ADDR
LOOP15    CLR  (R4)+              ; CLEAR CHANNEL
          CMP  R4,R2              ; DONE?
          BNE  LOOP15             ; NO SO LOOP
          JSR PC,TITPTR           ; R2 HAS TITLE BUFF S R
          MOV #100,R3             ;  HAS 100 BYTES
          ADD R2,R3               ; R3 PTS TO TITLE BUFF END
```

```
TITLOP  CLR (R2)+               ; CLR BUFFER
        CMP R5,R2               ; END OF BUFF?
        BNE TITLOP              ; NO SO CONT CLR
        JMP  FINI               ; FINISHED SO
ERR1    JMP  PSTPT4         HOOP LINES

        GPP PRINT OR WRITE ON FLOPPY ROUTINE
        WRFLG=0 IS WRITE ON FLOPPY
        WRFLG=1 IF PRINT ENTIRE SPECTRUM
        WRFLG=2 IF PRINT BETWEEN MARKERS

WRITE   CMP GPCOM,#0            ; LEGAL COMMAND?
        BMI ERR1                ; NO SO ERROR
        CLR  WRFLG
        CLR  BLOCK              ; CLR BLOCK CTR
        MOV  #IOBUF,IOTMP       ; SET BUFF PTR
         PRINT #MSG             ; PRNT FILENAME?
        JSR  PC,BLOCK           ; GET CHAR STRING
        MOV  #MSG+4,R5                  ; INSERT IN CSIGEN CALL
        MOV  #7,R1              ; USE R1 AS CHAR CNT
        BR GETC1
GETCHR   TTYIN  R1          ; CHAR OUT IN R1
GETC1   CMPB  #15,R1            ; HAVE CR?
        BEQ  CSI                ; YES SO HAVE FILENAM
        DEC  R1                         ; NO SO GET NOTHR
        BNE  GETC11             ; DONE?
        JMP  ERR2               ; NO SO ERROR
GETC11  MOVB R1,(R2)+           ; STORE CHAR
        BR GETCHR               ; AND GET ANOTHER
CSI     MOVB # =,(R2)+
        CLRB (R2)
         CSIGEN #DEVSPC,#DEFENT,#MSG6   ; CREATE FILE
        BCC  NO                         ; MOV OVER PNT FLG IF NO ERROR
        JMP CSIERR              ; CSI ERROR SO BRANCH
PRNT    MOV  #1,WRFLG           ; SET UP WRFLG FOR PNT
        BIT #200,@#DSPSR        ; IN MARKER MODE?
        BEQ NO                  ; NO SO WRFLG=1
        MOV #2,WRFLG            ; YES SO WRFLG=2
NO      CMP GPCOM,#0            ; LEGAL GPP #?
        BMI  ERR1               ; YES SO ERR EXIT
        JSR PC,TITPTR           ; FETCH TITLE BUFF S A  FOR GPP
        CMP  #1,WRFLG           ; IS WR CMND?
        BNE  OVER               ; YES SO NO LOP
        MOV  #50,R1             ; DO LEADER
        JSR  PC,LOP             ; SO ::
OVER    MOVB  (R2)+,R1          ; PICK UP CHAR IN R1
        JSR  PC,BNGDO           ; PRNT OUT CHAR
        CMPB  (R2),#0           ; ZERO? (LST CHAR)
        BNE  OVER               ; NO SO DO MOR
        JSP  PC,FETCH           ; YES SO TO SPECTRUM
        MOV  R4,R2              ; R2 HAS S A
        CMP #2,WRFLG            ; IN MARKER MODE?
        BEQ PNTEXP              ; YES SO BRANCH
        ADD  DSPLEN,R4          ; SET UP LST PT
        MOV  #1,INDEX           ; SET UP CHNL CTR
        BR SETAD                ; BRANCH
PNTEXP  TST DSPFLG          ; WHICH MARKER MODE?
```

```
          BNE PNTSOM                  ; EXPAND MODE SO BRANCH
          MOV LTMP1,P2                ; NORMAL MANTER MODE
          ASL P2                      ; P2 HAS BYTE S H OFFSET
          ADD P2,P2                   ; ADD TO S H
          MOV PTMP1,P2
          INC  P2                             ; INCL MAP P1 IN DSP
          ASL P2                      ; P2 HAS BYTE END ADDR
          ADD P2,P4                           ; ADD TO S H
          MOV LTMP1,INDEX                     ; SET UP CHANNEL PTR
          INC INDEX
          BR SETAD                    ; DONE
PNTSOM    SUB #BUFSH,P2               ; SET UP FOR OFFSET
          ADD DSPTMP,P2               ; P2 HAS EXP MODE S H
          MOV PTMP1,P4      ; P4 HAS PT MAP
          SUB LTMP1,P4                ; P4 HAS LT-PT
          INC  P4                             ; INCL MAP PT IN DSPLY
          ASL P4            ; PUT IN BYTES
          ADD P2,P4                   ; P4 HAS END ADDR
          MOV DSPTMP,P1               ; SET UP CHANNEL INDEX
          SUB #BUFSA,P1               ; SUB BUFF S H
          ASR P1
          INC  P1                             ; INCL MAP IN DSPLY
          MOV R1,INDEX
SETAD     MOV P4,STADDR               ; STORE END ADDR
LOOP19    JSR  PC,PRNTLN              ; PRNT 10 CHANNELS
          CMP  #0,STADDR              ; CHECK IF DONE
          BEQ OUT1                    ; DONE IF 0
          ADD  #12,INDEX              ; INC CHNL INDEX
          BR  LOOP19                  ; DO MORE
OUT1      TST  WPFLG                  ; HAVE WP CMND?
          BNE  DONE1                  ; YES SO NO LOP
           WRITW  #AREA,#0,#IOBUF,#400,BLOCK        ; WRITE LAST BLOCK
          CLOSE #0                    ; CLOSE OUTPUT FILE
          BCS WTERR2                  ; BR IF ERROR ON WRITE
          JMP  FINI                   ; EXIT
DONE1     CMP#1,WPFLG                 ; TRAILER IF FULL PRNT MODE
          BEQ TRAIL
          JMP FINI                    ; NO TRAILER SO EXIT
TRAIL     MOV  #20,R2                 ; DO TRAILER
          JSR  PC,LOOP                ; 20 ::
          JMP  FINI                   ; FINISHED SO ;
WTERR2    JMP WTERR

;         ROUTINE TO SET FLAG IF IN DISP MODE
;         WILL CAUSE DISPLAY ONLY BETWEEN MARKERS

DSPMRK    CMP #0,GPCOM                ; LEGAL COMMAND?
          BMI ERR4                    ; NO SO EPROR
          BIT #200,@#DISR             ; IN DISPLAY MODE?
          BEQ ERR4                    ; NO SO EPROR
          INC DSPFLG                  ; YES SO SET DISP FLAG
          MOV #BUFSA,DSPTMP           ; SET DISP S.A
          MOV LTMP1,P1                ; INDEX BY 2XLEFT MRK POS
          ASL R1
          ADD R1,DSPTMP
          JMP REDO                    ; AND GO TO BACKGROUND
ERR4      JMP RSTRT4                  ; ERROR RETURN
```

```
DSPTMP    WORD 0                    ; TMP DISP S A  FOR EXPAND MODE

          GPP TITLE STORAGE ROUTINE

TITLE     CMP  GPCOM,#0             ; GET GP # , OK ?
          BMI  ERR4                 ; NO SO ERROR
          JSR PC,TITPTR             ; FETCH TITLE BUFF S A  FOR GPP
          MOV R2,TEMP1              ;STORE TITLE BUFF PTR
          MOV #75,TEMP2             ;SET CHAR CTR
SET1      JSR PC,BKGDI              ;CONT BKGD TILL CR
          CMP R1,#33                ;ESC ?
          BEQ THTALL                ;YES SO EXIT
          DEC TEMP2                 ;NO SO TOO MANY CHARS ?
          BEQ THTALL                ;YES SO EXIT
          MOVB R1,@TEMP1
          INC TEMP1                 ;UPDTE TILE PTR
          BR SET1                             ;AND CONT INPUT
THTALL    MOV TEMP1,R4              ;R4 HAS TITLE PTR
          MOVB #15,(R4)+            ;STORE CR
          MOVB #12,(R4)+            ;STORE LF
          CLRB @R4                  ;CLR LAST CHAR
          JMP FINI                  ;RETURN

          SUBROUTINE TO ENTER THE RATIOMETER MODE OF OPERATION
          CALL ONCE-ON, CALL AGAIN RMTR OFF

RATIO     MOV  GPCOM,R4             ; PICK UP GP #
          CMP  #0,R4                ; -1 ? NO #
          BMI  ERR4                 ; NO SO ERROR
          TST  RFLAG                ; SECOND CALL ?
          BNE  TOFF                 ; YES SO TURN OFF
          BIC #40000,@#MRCSR        ; DISABLE INTEG INTERRUPT
          MOV #GRATE,R4             ; MOV RATIO SERVICE ADDR  TO VEC
          .PRINT #MSG16             ; ASK FOR DIGITIZER SAMPLE FREQ
RATTRY    JSR PC,BKGDI              ; WAIT IN BACKGRND FOR INPUT
          MOVB R1,TTBUF-1                   ; STORE FIRST CHAR OF CHAR STRING
          JSR PC,KBIN               ; INPUT CHAR STRING
          INC DCTR                  ; ADD ON FIRST CHAR TO CHAR CNT
          MOV #TTBUF-1,TEMP1        ; TEMP1 HAS CHAR BUFF S A
          JSR PC,INBIN              ; CNVRT ASCII TO DEC
          TST ERFLG                 ; LEGAL # ?
          BEQ NORTER                ; YES SO BRANCH
           TTYOUT #'?               ; PRINT ?
          CLR ERFLG                 ; RESET ERROR FLAG
          BR RATTRY                 ; AND TRY AGAIN
NORTER    MOV  BINNB,DIGFRQ         ; STORE DIG SAMP FREQ
          .PRINT #MSG17             ; READY RATIOMETER WINDOW
          JSR PC,BKGDI      ; WAIT IN BKGD TILL WINDOW SET
          MOV LTMRK,GRSML                   ; STORE LTMRK
          ASL GRSML                 ; IN BYTES
          MOV RTMRK,GRSMH                   ; STORE RTMRK
          ASL GRSMH                 ; IN BYTES
          CLR RATSHF                ; CLR RATIO MULT CTR
          BIS #40000,@#MRCSR        ; ENABLE INTERRUPT
          INC RFLAG                 ; SET FLAG FOR RATIO MODE
          CLR INTLO                         ; CLR INTEG BUFF
```

```
        JMP FINI                        ; AND RETURN
TOFF    CLR PFLAG                       ; RESET FLAG FOR EXIT FROM RATIO MODE
        BIC #400000,@#MFCSR             ; DISABLE INTER6 INTERRUPT
        MOV #INTE6,M4                   ; MOV NORMAL INTE6 SERV ADDR TO VEC
        BIS #400000,@#MFCSR                     ; ENABLE INTERRUPT
        JMP FINI                        ; AND RETURN TO BASIC
DIGFRQ  .WORD 0                                 ; DIGITIZER SAMPLE FREQUENCY
GPSML   .WORD 0                                 ; LOWER WINDOW ADDR
GPSMH   .WORD 0                                 ; HIGH WINDOW ADDR
RATSMF  .WORD 0                         ; RATIO SUM MULTIPLIER
RFLAG   .WORD  0                        ; FLAG=1 IF RATIOMTR ON
;
;
;       SECTION TO RESTART THE PROGRAM AND TO
;         RESET GROUP WIDTH AND CONV GAIN
;
GAIN    CMP #0,GPCOM                    ;CHECK GPH COM
        BMI ERR2                        ;NOT -1 SO ERROR
        BIT  #104,@#ADCSR               ; ADC ON ?
        BNE ERR2                        ; YES SO ABORT
        JMP  RSTRT                      ; NO SO RESTART
ERR2    JMP  RSTRT4                     ; ERROR SO RESTART
;
;       ROUTINE TO READ FILE FROM DK:1 TO DISPLY BUFF
;
READ    CLR EOFFLG                      ; CLR EOF FLAG
        CMP  GPCOM,#0                   ; LEGAL GP #
        BMI  ERR2                               ; YES S ERR
         PRINT  #MSG1                           ; PRNT FILE NAM
        JSR  PC,BNGDI                   ; WAIT IN THE BNGD
        MOV  #MSG8+5,R2                         ; PT TO WHERE NAM GOS
        MOV  #7,R3                      ; 6 CHAR CTR
        BR  READ2                       ; 1ST CHAR THERE
RDCHR   .TTYIN  R1                      ; GET A CHAR
READ2:  CMPB  #15,R1                    ; CR?
        BEQ  CSIRD                      ; YES SO EXIT
        MOVB  R1,(R2)+  ; NO SO STOR CHAR
        DEC  R3                                 ; MOR THAN 6 CHR?
        BNE  RDCHR                      ; NO SO GET NOTHR
        JMP  ERR2                       ; YES SO ERROR
CSIRD   CLRB (R2)+                      ; CLEAR LAST BYTE OF COMMAND STRING
        .CSIGEN  #DEVSPC,#DEFEXT,#MSG8  ; READY FOR RD
        BCC NREPR                       ; BRANCH IF NO CSI ERROR
        JMP CSIERR                      ; BRANCH IF ERROR
NRERR   CLR BLOCK                       ; CLR BLK CTR
        JSR PC,RDNBLK                   ; READ A BLOCK ON CHNL #1
        CLR CTR5                        ; CLEAR TITLE CTR
RD10    MOV  #10,R2                     ; SET UP MSSGE CTR
        MOV  #MSGT,R3                   ; PT TO ASCII CHECK
RD11    INC CTR5                        ; INC CHAR CTR
        DEC  R2                                 ; DEC CTR, 0?
        BEQ RD12                        ; YES SO BEYOND TITLE ,EXIT
        CMPB (R3)+,(R5)+                ; CHAR=?
        BEQ RD11                        ; YES SO CHECK NEXT
        BR RD10                         ; NO SO START AGAIN
RD12    SUB #10,CTR5                    ; SUB 8FROM CTR
        MOV #IOBUF,R5                   ; R5 POINTS TO DATA BUFFER
```

```
          JSR PC,TITPTR          ; PC HAS TITLE BUFFER
RD1:      DEC CTR5               ; TITLE STORED?
          BMI RDOUT              ; YES SO EXIT
          MOVB (R5)+,(R2)+       ; NO SO STORE CHAR
          BR RD1:                ; AND GET ANOTHER
RDOUT     CLRB (R2)              ; CLEAR LAST BYTE
          JSR PC,FETCH     ; FETCH GRP S H  IN R4
          MOV R4,TEMP2           ; MOV S H  TO TEMP2
          ADD #SPLEN,R4          ; SET UP PTR TO END OF GRP
          MOV R4,TEMP1           ; AND STORE AT TEMP1
          MOV #5,CTR             ; CHAR CTR
          MOV #TMPBLK,TEMP1      ; TEMP1 PTS TO TMP CHAR STORAGE
          MOV #12,CTR10          ; SET UP DECODE CTRS
          MOV #7,CTR9
          MOV #5,CTR5
DECOD     CMP R5,IOTMP      ; AT END OF I/O BUFFER
          BNE STORE              ; NO SO DECODE CHAR
          TST EOFFLG             ; PAST END OF FILE?
          BNE RDCLSE             ; YES SO CLOSE READ CHANNEL
          JSR PC,RDNBLK          ; NO SO READ ANOTHER BLOCK
STORE     DEC CTR9               ; LEGAL #?
          BPL EXIT9              ; NO SO IGNORE
          MOVB (R5)+,@TEMP1      ; YES SO TEMP STORE
          INC TEMP1              ; INC TEMP STORE PTR
          DEC CTR5               ; END OF #?
          BNE DECOD              ; NO SO GET NEXT CHAR
          JMP BINCON
RTNBIN    MOV #5,CTR5            ; RESTORE CTR
          DEC CTR10              ; END OF LINE?
          BNE EXIT8              ; NO SO IGNORE SPACE
          MOV #12,CTR9           ; RESET DECODE CTR
          MOV #12,CTR10          ; RESET #/LINE CTR
          BR DECOD               ; AND LOOP AGAIN
EXIT8     MOV #1,CTR9            ; SET TO IGNORE SPACE
          BR DECOD
EXIT9     INC R5                 ; POINT TO NEXT CHAR
          BR DECOD               ; AND LOOP
RDCLSE    CLOSE #2          ; CLOSE INPUT CHANNEL
          JMP REDO               ; AND GO TO BNGD

EOFFLG    WORD 0                 ; EOF FLAG
CTR5      WORD 0                 ; DECODE CTR STORAGE
CTR9      WORD 0
CTR10     WORD 0
TMPBLK:   WORD 0,0,0             ; TMP CHAR STRING STORAGE

;         LOOP TO CONVERT ASCII STRING AT TMPBLK TO BIN#
;         AND STORE IN PROPER GRP LOC

BINCON    MOV #TMPBLK,TEMP1      ; POINT TEMP1 TO START OF TEMP STORE
          JSR PC,INBIN           ; PREFORM CONV
          TST ERFLG              ; WAS ILLEGAL CHAR READ?
          BEQ NOERR              ; NO SO STORE #
          PRINT #MSG9            ; YES SO PRINT ERROR MESSAGE
          JMP RDCLSE             ; AND CLOSE INPUT CHANNEL
NOERR     MOV BINNB,@TEMP2       ;AND STORE IN GRP
          INC TEMP2              ; INC GRP PTR
```

```
        INC TEMP2
        CMP TEMP1,TEMP2                 ; END OF GRP
        BEQ PCLSE                       ; YES SO CLOSE READ
        BR RTNEIN                       ; CONTINUE

        ROUTINE TO READ BLOCK ON CHANNEL #1
        WILL EXIT IF PREVIOUS READ REACHED EOF

RDNEL1  .READW #AREA,#1,#IOBUF,#400,BLOC1       ;DO READ
        BCC NOERR
        MOV #1,EOFFLG                   ; IF READ ERROR SET EOFFLG
NOERR   ASL R0                          ; R0 HAS #BYTES READ
        ADD #IOBUF,R0                   ; PNT TO END OF I/O BUFF
        MOV R0,IOTMP                    ; AND STUFF AT IOTMP
        MOV #IOBUF,R5                   ; RESET R5 TO BUFF S/R
        INC BLOC1                       ; INC BLOCK COUNT
        RTS PC                          ; EXIT

        ROUTINE TO SET WINDOW BY MARKER SETTINGS
        MUST BE IN NORMAL MARKER MODE

MARKR   MOV #1,WRFLG                    ; ENTER PRINT MODE
        TST GRCOM                       ; WAS A # INPUT?
        BMI NOMPI                       ; NO SO PRINT MARKER CHANNELS ONLY
        MOV GRCOM,R1                    ; R1 HAS GRP #
        MOV #MRIBUF,R2      ; R2 POINTS TO MRI STOP BUFF
MRICHK  DEC R1                          ; DEC WINDOW CTR
        BMI MRIEND                      ; AT WINDOW STORAGE YET?
        ADD #4,R2                       ; NO SO INC R2 BY 4 LOC
        BR MRICHK                       ; AND CHECK AGAIN
MRIEND  MOVB TTBUF+2,R1                 ; R1 HAS MARKER CHAR COMMAND
        CMPB #15,R1                     ; IS IT CR?
        BEQ MRIPNT                      ; YES SO PRNT WINDOW CHANNELS
        CMPB # S,R1                     ; IS IT "S"?
        BEQ MRISET                      ; YES SO SET WINDOW
        CMPB #'E,R1                     ; IS IT "E"?
        BEQ MRKERS                      ; YES SO ERASE WINDOW
        CMPB # M,R1                     ; IS IT "J"?
        BEQ MRIMOV                      ; YES SO MOV MARKERS TO WINDOW
        JMP RSTRT4                      ; NO SO ILLEGAL COMMAND
MRIPNT  MOV (R2)+,R4    ; R4 HAS LEFT MARKER
        MOV (R2),R3                     ; R3 HAS RIGHT VALUE
        ASR R4          ; PUT IN BYTES
        ASR R3
        TST R3                          ; WAS WINDOW SET?
        BNE MRI02                       ; YES SO BRANCH
        .PRINT #MSG20       ; NO SO SAY SO
        JMP RSTRT4                      ; AND RETURN
MRI02   .PRINT #MSG21       ; PRINT "WINDOW LOCATION "
        INC R4                          ; INC R4
        JSR PC,PRNTDC       ; PRINT IT
        INC R3
        MOV R3,R4
        JSR PC,PRNTDC                   ; PRINT R3
        MOV #15,R0                      ; OUTPUT CR/LF
        .TTOUTR
        JMP REDO                        ; AND RETURN
```

```
MPI SET   MOV LTMPI,R4          ; R4 HAS LEFT MARKER
          MOV RTMPI,R5          ; R5 HAS RIGHT MARKER
          ASL R4                ; PUT IN BYTES
          ASL R5
          MOV R4,(R2)+          ; STORE THEM
          MOV R5,(R2)
          PRINT #MSG18          ; PRINT "WINDOW SET "
          BR NOMPI              ; AND PRINT CHANNELS
MPI ERS   CLR (R2)+             ; ERASE WINDOW
          CLR (R2)
          PRINT #MSG11          ; AND SAY SO
          JMP REDO              ; RETURN
MPI MOV   MOV (R2)+,R4          ; R4 HAS LEFT MARKER
          MOV (R2),R5           ; R5 HAS RIGHT MARKER
          ASR R4                ; PUT IN WORDS
          ASR R5
          TST R5                ; WAS A WINDOW SET?
          BNE MPI01             ; YES SO BRANCH
          PRINT #MSG20          ; NO SO SAY SO
          JMP RSTRT4            ; AND RETURN
MPI01     MOV R4,LTMPI          ; SET LEFT MARKER
          MOV R5,RTMPI          ; AND RIGHT MARKER
          PRINT #MSG19          ; AND SAY SO
NOMPI     MOV LTMPI,R4          ; R4 HAS LEFT MARKER
          INC R4                ; INC R4
          JSR PC,PRNTOC         ; PRINT IT
          MOV RTMPI,R4          ; R4 HAS RIGHT MARKER
          INC R4                ; INC R4
          JSR PC,PRNTOC         ; PRINT IT
          MOV #15,R0            ; OUTPUT CR,LF
          TTOUTR
          JMP REDO              ; AND RETURN

MPIBUF            WORD 0,0,0,0,0,0,0,0,0,0,0,0,0,0,0,0,WINDOW BUFF

          FINI -  JMP  REDO                 ; NORMAL EXIT TO BKGD
;
;         ROUTINE TO POINT TO TITLE BUFFER S A  FOR GIVEN GRP
;         R2 RETURNED AS PTR
;         R2,R1 USED
;
TITPTR    MOV GRCOM,R1            ; R1 HAS GRP #
          MOV #TITSA,R2           ; R2 HAS TITLE BUFF S A
ADDMOR    DEC R1                  ;RIGHT GRP?
          BMI SETUP               ; YES SO RETURN
          ADD #100,R2             ; NO SO PNT TO NEXT GRP BUFF
          BR ADDMOR               ; AND CHECK IT
SETUP     RTS PC                  ;NORMAL EXIT
```

```
        ROUTINE TO TURN OFF INTERRUPTS AND EXIT

DUMP    CMP GPCOM,#0        ; ILLEGAL COMMAND?
        BMI DUMP1           ;NO, SO BRANCH
        JMP PSTPT4          ; YES SO ERROR
DUMP1   CLR R0              ; RESET INTERRUPTS
        EXIT                ; AND EXIT


        INTERRUPT HANDLERS

SCALE   INTEN  SLPPRI       ; RUN AT LEVEL 5
        INC  SCLPO          ; STOPE UFLO
        RTS  PC             ; NORMAL RETURN


        ROUTINE TO SEVICE INTEG IN RATIOMETER MODE

GRATE   INTEN  GTPPRI       ; RUN AT LEVEL 7
        INC  INTLO          ; UPDATE RUNNING SUM
        BIT #10000,@#MRCSR  ; MULT = 2?
        BEQ PB1             ; NO SO BRANCH
        INC RATSHF          ; YES SO INC MULT
        BIC #10000,@#MRCSR  ; CLEAR PB
PB1     BIT #20000,@#MRCSR  ; DIVIDE BY 2?
        BEQ PB2             ; NO SO BRANCH
        DEC RATSHF          ; YES SO DEC MULT
        BIC #20000,@#MRCSR  ; CLEAR PB
PB2     CMP INTLO,DIGPRD    ; TIME TO SAMPLE?
        BNE QUIT2           ; NO SO EXIT
        MOV GPSML,R4        ; R4 HAS LOW WINDOW ADDR
        MOV GPSMH,SUM11     ; SUM11 HAS HI WINDOW ADDR
        ADD ADCSA,R4        ; ADD OFFSET
        ADD ADCSA,SUM11
        CLR R5              ; CLEAR SUM
GRTSM   ADD (R4),R5         ; ADD
        CLR (R4)+           ; CLEAR CONTENTS
        CMP R4,SUM11        ; FINISHED?
        BMI GRTSM           ; NO SO LOOP
        MOV RATSHF,R4       ; R4 HAS SUM MULT
        BEQ GRTE1           ; ZERO SO NO MULT
        BMI GRTMI           ; MINUS SO BRANCH TO DIVIDE
MULT1   ASL R5              ; PLUS SO MULT X 2
        DEC R4              ; FINISHED?
        BNE MULT1           ; NO SO LOOP
        BR GRTE1            ; YES SO EXIT
GRTMI   ASR R5              ; DIV BY 2
        INC R4              ; FINISHED?
        BNE GRTMI           ; NO SO LOOP
GRTE1   CMP R5,#7777        ; IS # > DAC?
        BMI GRTOK           ; NO SO BRANCH
        MOV #7777,R5        ; YES SO SET DAC TO MAX VALUE
GRTOK   COM R5              ; COMPLEMENT SUM
        MOV R5,@#MTREG      ; MOVE TO RATIOMETER
        CLR INTLO           ; CLR INTEG BUFFER
QUIT2   BIC #100000,@#MRCSR ; RESET INTEG
        RTS PC              ; AND RETURN
```

```
SUM11   .WORD 0                 ; END WINDOW ROUT  TMP STUFF

        ROUTINE TO SERVICE INTEGRATOR INTERRUPT
        IN NORMAL MODE

INTEG   .INTEN GTPRI            . RUN AT LEVEL 6
        ADD #1,INTLO            . INC INTEGRATOR BUFFER
        ADC INTHI               . WATCH CARRY
        BIT #100000,@#INCSR     . RESET INTEG
        RTS PC                  . RETURN


        ADC HANDLER

ADCI    .INTEN ADCPRI           . RUN AT LEVEL 7
        MOV @#ADCI,R4           . PU HRS UNWTD DATA
        CMP GPWDTH,R4           . BEYOND BUFFER
        BMI ADCI1               . YES SO IGNORE DATA
        ASL R4                          . EVEN ADDR ONLY
        ADD ADCSA,R4            . CALC CHANNEL #
        INC (R4)                ; +1 AT CHANNEL
ADCI1   INC @#ADCSR             . CLEAR THE ADC
        RTS PC                          . RETURN NORMALLY

        ROUTINE TO POINT TO START OF BUFFER FOR GPR #
        POINTER RETURNED IN R4
        R2,R4 USED

FETCH   CLR R2                  ;SET UP CTR
        MOV #BUFSA,R4           ;MOV BUFF S A  TO R4
BACK1   CMP GPCOM,R2            ;RIGHT GPR?
        BEQ BACK2               ;YES SO EXIT
        ADD DSPLEN,R4           ;MOVE TO NEXT GPR S A
        INC R2                  ;AND INC CTR
        BR  BACK1               ; LOOP AGAIN
BACK2   RTS PC                  ;NORMAL EXIT

        DATA BUFFER FOR HNDLRS

SCLR0   .WORD 0                 . OFLO WORD FOR SCLR
INTHI   .WORD 0                 ; MSW  FOR INTGRTR SUM
INTLO   .WORD 0                 ; LSW FOR INTEGRATER SUM

        CSI ERROR SERVICE ROUTINE
        CONTROL RETURNS TO USER ON ERROR

CSIERR  TSTB @#ERRWRD           . IS ERROR BYTE=0?
        BNE CSI1                ; NO SO TEST MORE
        .PRINT #MSG12           . YES SO PRINT MESSAGE
        BR CSIEX                        . AND RETURN CONTROL
CSI1    CMPB #1,@#ERRWRD        . IS ERROR BYTE=1?
        BNE CSI2                ; NO SO TEST MORE
        .PRINT #MSG11           ; YES SO PRNT MESS
        BR CSIEX                ; AND RETURN CONTROL
CSI2    CMPB #3,@#ERRWRD        ; IS ERROR BYTE =3?
        BNE  CSI4               ; NO SO TES MOR
```

```
            PRINT   #MSG14              ; PRINT ERROR MESS
            BR      LSIE.                 AND RETURN CNTRL
CI14        CMPB    #4,@#ERRNFD           IS ERRBYTE=4
            BNE     CSIE'                 ; YES SO PRNT ERR MESS
            PRINT   #MSG1'                ; YES SO PRNT ERR MESS
CSIE'       JMP     @STAT4                ; RETURN CNTRL
.
.
.           MESSAGE BUFFER
.
            NLIST
MSG6        ASCII   '%'
MSG0        ASCII   <7><200>
MSG1        ASCII  /PRM PGM V5.N 01-10-76.'
MSG2        ASCII  /GROUP WIDTH:'<200>
MSG3        ASCII  /INPUT FILENAME (MAX 6 CHAR) :'
MSG4        ASCII  /MAXIMUM NUMBER OF GROUPS IS :'<200>
MSG5        ASCII  <15><12>/CLEAR SPECTRM BUFFER? YES=Y :'<200>
            EVEN
MSG6        ASCII  /DK1:       =.'
MSG7        ASCII  /WRITE ERROR HAS OCCURED -ABORT WRITE.'
MSG8        ASCII  /=DK1       .'<200>
MSG9        ASCII  /ILLEGAL CHAR READ-ABORT READ.'
MSG11       ASCII  /WINDOW ERASED.'
MSG12       ASCII  /ILLEGAL FILENAME.'
MSG13       ASCII  /DISK #1 NOT READY.'
MSG14       ASCII  /DISK #1 DIRECTORY FULL.'
MSG15       ASCII  /FILE NOT FOUND.'
MSG16       ASCII  /INPUT DIGITIZER SAMPLE FREQUENCY :'<200>
MSG17       ASCII  /SET POTIOMETER WINDOW AND PRESS CR.'
MSG18       ASCII  /WINDOW SET..'<200>
MSG19       ASCII  /MAP EPS MOVED TO :'<200>
MSG20       ASCII  /NO WINDOW SET.'<200>
MSG21       ASCII  /WINDOW LOCATION :'<200>
MSGT.       ASCII  /00001  .'
            LIST
            EVEN
TITSA:      BLKW 1100
IOTMP       WORD 0                        ; PTR TO I/O BUFFER
AREA        BLKW 10                     ; EMT ARG LIST FOR  WRITW
IOBUF       = +1000                       ;  , RESERVE 256 WORD BUFFER
IOEND       WORD 0                      ; END OF I/O BUFFER
DEFEXT      RAD50 "DAT"                 ; INPUT #2 DEFAULT EXT
            RAD50 "DAT"                 ; OUTPUT #0 DEFAULT EXT .
            WORD 0,0
BLOCK       WORD 0                      ; WR BLOCK # CTR
WRFLG       WORD 0                      ; WR FLG FOR FLOPPY WRITE
DEVSPC      WORD 0                      ; DEVICE HANDLER AT END OF BUFFER
.
.           END OF THE PROGRAM THANK  GOD !!!!!!
;
            END START
```

REFERENCES

1. G. Dearnaley, J.H. Freeman, R.S. Nelson and J. Stephen, Ion Implantation, American Elsevier, New York (1973).
2. K.B. Winterbon, Ion Implantation Range and Energy Deposition Distributions, Vol. 2, Plenum, New York (1975).
3. P. Sigmund, Rev. Roum. Phys. 17, no. 7, 823 (1972).
4. F. Seitz and J.S. Koehler, Sol. State Phys. 2, 327 (1956).
5. J. Lindhard, V. Nielson, M. Scharff and P.V. Thomson, Kgl. Dan. Vid. Selsk. Mat. Fys. Medd. 33, no. 10 (1963).
6. J. Lindhard, M. Scharff and H.E. Schiott, Kgl. Dan. Vid. Selsk. Mat. Fys. Medd. 33, no. 14 (1963).
7. J. Lindhard, V. Nielson and M. Scharff, Kgl. Dan. Vid. Selsk. Mat. Fys. Medd. 36, no. 10 (1968).
8. K.B. Winterbon, P. Sigmund and J.B. Sanders, Kgl. Dan. Vid. Selsk. Mat. Fys. Medd. 37, no. 14 (1970).
9. O.B. Firsov, Sov. Phys. JETP 36(9), 1076 (1959).
10. J. Lindhard and M. Scharff, Phys. Rev. 124, 128 (1961).
11. K.B. Winterbon, Rad. Effects 30, 199 (1976).
12. H. Goldstein, Classical Mechanics, Addison-Wesley, Cambridge, Mass. (1958).
13. D.R. Hartree, Calculations of Atomic Structures, Wiley & Sons, N.Y. (1957).
14. M. Born and J.E. Mayer, Z. Physik 75(1), 96 (1932).
15. N. Bohr, Kgl. Dan. Vid. Selsk. Mat. Fys. Medd. 18, no. 8 (1948).
16. J. Lindhard, Kgl. Dan. Vid. Selsk. Mat. Fys. Medd. 34, no. 14 (1965).
17. G. Molière, Z. Naturforsch 2a, 133 (1947).

18. O.B. Firsov, Sov. Phys. JETP 6(33), 534 (1958).

19. P. Gombas, Handbuch der Physik, Ed XXXVI (1956).

20. P. Sigmund, Phys. Rev. 184, 383 (1969).

21. J. Böttiger and K.B. Winterbon, Rad. Effects 20, 65 (1973).

22. D.K. Brice, Ion Implantation Range and Energy Deposition Distributions, Vol. 1, Plenum, New York (1975).

23. E.M. Baroody, J. Appl. Phys. 36, 3562 (1965).

24. M.G. Kendall and A. Stuart, The Advanced Theory of Statistics, Vol. 1, Third Edition, Griffin, London (1969).

25. P. Sigmund, G.P. Scheidler and G. Roth, BNL 50083 (C-52), 374 (1968).

26. J.E. Westmoreland and P. Sigmund, Rad. Effects 6, 187 (1970).

27. G.H. Kinchin and R.S. Pease, Rep. Prog. Phys. 18(1), 143 (1955).

28. M.T. Robinson, Phil. Mag. 12, 741 (1965).

29. M.T. Robinson, Phil. Mag. 17, 639 (1968).

30. P. Sigmund, Rad. Effects 1, 15 (1969).

31. P. Sigmund, Appl. Phys. Letts. 14, no. 3, 114 (1969).

32. F.H. Eisen, Can. J. Phys. 46, 561 (1968).

33. W.K. Hofker, D.P. Oosthoek, N.J. Koeman and H.A.M. DeDrefte, Rad. Effects 24, 223 (1975).

34. A.H. Andersen, J. Böttiger and H. Wolder-Jorgensen, Appl. Phys. Letts. 26, 678 (1975).

35. W.A. Grant, J.S. Williams and D. Dodds, Rad. Effects 29, 189 (1976).

36. E. Bögh, P. Högild and I. Stensgaard, Rad. Effects 7, 115 (1971).

37. R.S. Walker and D.A. Thompson, J. Nucl. Instrum. Methods 135, 489 (1976).

38. D.A. Thompson, J.E. Robinson and R.S. Walker, Rad. Effects 32, 169 (1977).

39. M.W. Thompson, Phil. Mag. 18, 377 (1968).

40. W. Kohler and W. Schilling, Nucleonik 7, 389 (1965).

41. W. Schilling and J. Völke, Kernsforschungsanlage Jülich Rept., Jül-464RW (1967).

42. J.B. Mitchell, J.A. Davies, L.M. Howe, R.S. Walker, K.B. Winterbon, G. Foti and J.A. Moore, in Ion Implantation in Semiconductors, ed. S. Namba, Plenum, New York (1975).

43. D.A. Thompson and R.S. Walker, J. Nucl. Instrum. Methods 132, 281 (1976).

44. D.A. Thompson, R.S. Walker and J.A. Davies, Rad. Effects 32, 135 (1977).

45. K.J.R. Parsons, Phil. Mag. 12, 1159 (1965).

46. D.J. Mazey, R.S. Nelson and R.S. Barnes, Phil. Mag. 17, 1145 (1968).

47. E.C. Baranova, V.M. Gusev, Yu. V. Martynenko, C.V. Starinin and I.B. Hailbullin, Rad. Effects 18, 21 (1973).

48. M.L. Swanson, J.R. Parsons and C.W. Hoekle, Rad. Effects 9, 249 (1971).

49. F.L. Vook and H.J. Stein, Rad. Effects 2, 23 (1969).

50. G.H. Vineyard, Disc. Farad. Soc. 31, 7 (1961).

51. P. Sigmund, Appl. Phys. Letts. 25, no. 3, 169 (1974).

52. Yu. N. Knyzhnikov, Rad. Effects 25, 41 (1975).

53. J.A. Brinkman, J. Appl. Phys. 25, 961 (1954).

54. J.B. Gibson, A.N. Goland, M. Milgram and G.H. Vineyard, Phys. Rev. 120, 1229 (1960).

55. G.K. Wehner, Phys. Rev. 102, 690 (1956).

56. M.W. Thompson and R.S. Nelson, Phil. Mag. 7, 2015 (1962).

57. R.S. Nelson, Phil. Mag. 11, 291 (1965).

58. H.H. Andersen and H.L. Bay, Rad. Effects 19, 139 (1973).

59. H.H. Andersen and H.L. Bay, J. Appl. Phys. 45, 953 (1974).

60. H.H. Andersen and H.L. Bay, J. Appl. Phys. 46, 2416 (1975).

61. S.S. Johar, private communication.

62. H.H. Andersen, Rad. Effects 3, 51 (1970).

63. M. Kopcewicz, I. Sosnowska and J. Tatapkiewicz, Rad. Effects 30, 207 (1976).

64. D.K. Holmes, G. Leibfried, O.S. Oen and M.T. Robinson, in Radiation Damage, p.3, Conf. Proceed. (I.A.E.A., Vienna), (1962).

65. M.T. Robinson and O.S. Oen, Phys. Rev. 132, 2385 (1963).

66. M. Yoshida, J. Phys. Soc. Jap. 16, 44 (1961).

67. I.M. Torrens and M.T. Robinson, in Interatomic Potentials and Simulation of Lattice Defects, ed. P.C. Gehlen et.al., Plenum, New York, p.423 (1972)

68. M.T. Robinson, I.M. Torrens, Phys. Rev. 9B, no. 12, 5008 (1974).

69. T. Ishitani, R. Shimizu and K. Murata, Jap. J. Appl. Phys. 11, 125 (1972).

70. J.E. Robinson, Rad. Effects 23, 29 (1974).

71. G. Nabil, Masters Thesis, McMaster University (1975).

72. W.S. Synder and J. Neufeld, Phys. Rev. 97, 1636 (1955).

73. J.A. Davies, J. Denhartog, L. Eriksson and J.W. Mayer, Can. J. Phys. 45, 4053 (1967).

74. Ion Implantation in Semiconductors and Other Materials, ed. B.L. Crowder, Plenum, New York (1973).

75. J. Stark, Z. Phys. 13, 973 (1912).

76. G.R. Piercy, F. Brown, J.A. Davies and M. McCargo, Phys. Rev. Letts. 10, 399 (1963).

77. H.O. Lutz and R. Sizman, Phys. Letts. 5, 113 (1963).

78. D.S. Gemmel, Rev. Modern Phys. 46, 129 (1974).

79. D.V. Morgan, Channeling-Theory, Observation and Applications, J. Wiley and Sons, London (1973).

80. L. Eriksson, J.A. Davies and P. Jespersgård, Phys. Rev. 161, 219 (1967).

81. J.U. Andersen, Kgl. Dan. Vid. Selsk. Mat. Fys. Medd. 36, no. 7 (1967).

82. J.H. Barrett, Phys. Rev. 3B, 1527 (1971).

83. H. Matsumura and S. Furukawa, Rad. Effects 27, 245 (1976).

84. (a) F.H. Eisen, G.J. Clark, J. Böttiger and J.M. Poate, Rad. Effects 13, 93 (1972).

(b) J. Böttiger and F.H. Eisen, Thin Solid Films 19, 239 (1973).

85. J.F. Ziegler, IBM Rept. No. RC 3551 (1971).

86. J.F. Ziegler and W.K. Chu, Atomic and Nucl. Data Tables 13, 463 (1974).

87. D.V. Morgan and D. Van Vliet, Rad. Effects 12, 203 (1972).

88. E. Bøgh, Can. J. Phys. 46, 653 (1968).

89. L.C. Feldman and J.W. Rodgers, J. Appl. Phys. 41, 3776 (1970).

90. R.R. Hart, Rad. Effects 6, 69 (1970).

91. J.E. Westmoreland, J.W. Mayer, F.H. Eisen and B. Welch, Rad. Effects 6, 161 (1970).

92. S.U. Campisano, G. Foti, F. Grasso and E. Rimini, Atomic Collisions in Solids, Vol. 2, Ed. S. Datz et al., Plenum, New York (1975), p.905.

93. F. Kiel, E. Zietler and W. Zinn, Z. für Naturforsch 15a, 1031 (1960).

94. L. Meyer, Phys. Stat. Sol. 44, 253 (1971).

95. J. Mory and Y. Quéré, Rad. Effects 13, 57 (1972).

96. Z.F. Ziegler and J.E.E. Baglin, J. Appl. Phys. 42, 2031 (1971).

97. K. Schmid, Rad. Effects 17, 201 (1973).

98. R.S. Walker, D.A. Thompson and S.W. Poehlman, Rad. Effects, in press.

99. J.U. Andersen, O. Andreasen, J.A. Davies and E. Uggerhoj, Rad. Effects 7, 25 (1971).

100. G.D. Watkins, in Radiation Effects in Semiconductors, ed. F.L. Vook, Plenum, New York, p.67 (1970).

101. F.H. Eisen, in ref. 79, p.415.

102. Y. Quéré, Rad. Effects 28, 253 (1976).

103. L.T. Chadderton, Rad. Effects 27, 13 (1975).

104. H.J. Pabst and D.W. Palmer, Proc. 5th Int. Conf. on Atomic Collision Phenomena in Solids, Plenum, New York (1973).

105. S.T. Picraux and F.L. Vook, Rad. Effects 11, 179 (1971).

106. W.H. Bragg and R. Kleeman, Phil. Mag. 10, 5318 (1905).

107. J.U. Andersen, J.A. Davies, K.D. Nielson and S. Anderson, Nucl. Instrum. Methods 38, 210 (1965).

108. L. Rosenfeld, ed., Nuclear Physics, Vol. A214, North-Holland, Amsterdam (1973).

109. J.B. Marion, Revs. Mod. Phys. 33, 139 (1961).

110. J.B. Mitchell, S. Agamy and J.A. Davies, Rad. Effects 28, 133 (1976).

111. G.D. Watkins, in Radiation Damage in Semiconductors, Dunod, Paris, p.97 (1964).

112. S.T. Picraux, Rad. Effects 17, 261 (1973).

113. J. Böttiger and J.L. Whitton, Rad. Effects 19, 201 (1973).

114. D.A. Thompson and J.E. Robinson, Nucl. Instrum. Methods 132, 261 (1976).

115. J.H. Ormrod and H.E. Duckworth, Can. J. Phys. 41, 1424 (1963) and J.H. Ormrod, J.R. MacDonald and H.E. Duckworth, Can. J. Phys. 43, 275 (1965).

116. P. Baeri, S.U. Campisano, G. Gavialo, G. Foti and E. Rimini, J. Nucl. Instrum. Methods 132, 237 (1976).

117. P. Baeri, S.U. Campisano, G. Foti, E. Rimini and J.A. Davies, Appl. Phys. Letts. 26, 424 (1975).

118. D.A. Thompson and R.S. Walker, Rad. Effects 30, 37 (1976).

119. D. Van Vliet, Rad. Effects 10, 137 (1971).

120. F.F. Morehead, Jr. and B.L. Crowder, Rad. Effects 6, 25 (1970).

121. L.T. Chadderton, Rad. Effects 8, 77 (1971).

122. L.T. Chadderton and F.H. Eisen, Rad. Effects 7, 129 (1971).

123. A. Golanski, private communication.

124. G. Carter and J.L. Whitton, Rad. Effects 15, 143 (1972).

125. J.J. Loferski and P. Rappaport, Phys. Rev. 111, 432 (1958).

126. R. Bäuerlein, Z. Naturforsch, 14a, 1069 (1969).

127. E.C. Baranova, V.M. Gusev, Yu. V. Martynenko and I.B. Hailbullin, Rad. Effects 25, 157 (1975).

128. M.O. Ruault, B. Jouffrey, J. Chaumont and H. Bernas, in Application of Ion Beams to Metals, p.459, ed. S.T. Picraux et.al., Plenum, New York (1974).

129. F. Häussermann, Phil. Mag. 25, 537 (1972).

130. C.A. English, B.L. Eyre and M.L. Jenkins, Nature 263, 400 (1976).

131. J.A. Moore, G. Carter and A.H. Tinsley, Rad. Effects 25, 49 (1975).

132. J.A. Davies, G. Foti, L.M. Howe, J.B. Mitchell and K.B. Winterbon, Phys. Rev. Letts. 34, 1441 (1975).

133. J.B. Mitchell, G. Foti, L.M. Howe and J.A. Davies, Rad. Effects 26, 193 (1975).

134. M.O. Rault, J. Chaumont, H. Bernas and P. Sigmund, Phys. Rev. Letts. B6, no. 19 (1975).